INFRARED INTERFEROMETER SPECTROMETER AND RADIOMETER (IRIS) INSTRUMENT FOR MARINER/JUPITER/SATURN 1977 (MJS'77)

TEXAS INSTRUMENTS INCORPORATED
13500 North Central Expressway
Dallas, Texas 75222

October 1974

SECOND QUARTERLY REPORT FOR PERIOD

12 July - 12 October 1974

Prepared For

GODDARD SPACE FLIGHT CENTER
Greenbelt, Maryland 20771

TECHNICAL REPORT STANDARD TITLE PAGE

1. Report No.	2. Government Accession No.	3. Recipient's Catalog No.

4. Title and Subtitle	5. Report Date
Second Quarterly Report for Infrared Interferometer Spectrometer and Radiometer (IRIS) for the MJS'77 Spacecraft	10-31-74
	6. Performing Organization Code
7. Author(s)	8. Performing Organization Report No.
D.D. Vanous	U2-863919-1
9. Performing Organization Name and Address	10. Work Unit No.
Texas Instruments Incorporated 13500 North Central Expressway Dallas, Texas 75222	11. Contract or Grant No. NAS 5-20498
12. Sponsoring Agency Name and Address	13. Type of Report and Period Covered Quarterly Report 12 July–12 October 1974
NASA Goddard Space Flight Center Greenbelt, Maryland	14. Sponsoring Agency Code

15. Supplementary Notes

16. Abstract

This report documents the progress made during the period 12 July to 12 October 1974 in developing the MJS'77 IRIS subsystem design and in overall program activities.

The continuing efforts in the program cover designs in both opto-mechanics and electronics. Piece part fabrication has progressed on the Michelson motor. Vendor selection is complete for the telescope procurement. Fifty percent of the electronic designs are committed to PCB layout. Radiation testing at GSFC was performed.

17. Key Words (Selected by Author(s))		18. Distribution Statement
IRIS	data channel	
interferometer	phase locked loop	
Cassegrain telescope	beamsplitter	
radiometer		

19. Security Classif. (of this report)	20. Security Classif. (of this page)	21. No. of Pages	22. Price*
Unclassified	Unclassified		

*For sale by the Clearinghouse for Federal Scientific and Technical Information, Springfield, Virginia 22151.

PREFACE

Texas Instruments Incorporated is under NASA Contract NAS 5-20498 to design, develop, test, and deliver the Infrared Interferometer Spectrometer and Radiometer (IRIS) for the Mariner Jupiter/Saturn 1977 (MJS'77) deep space probe. This quarterly report is the second to be submitted in compliance with the subject contract, in accordance with the requirements of GSFC specification GSFC-S-250-P-1C.

TABLE OF CONTENTS

LIST OF ILLUSTRATIONS

LIST OF ILLUSTRATIONS (CON'T)

LIST OF ILLUSTRATIONS (CON'T)

LIST OF TABLES

SECTION I

INTRODUCTION

The second three month period of the MJS'77 program was marked by some activities of major import - chiefly the Preliminary Design Review and the telescope procurement. Other milestone activities were: beginning layouts of five printed wiring boards; and completion of the fabrication of the Michelson motor test model parts.

Progress in the opto-mechanical design encompasses detail design complete on 22 beryllium parts, optical design and mounting concept of the calibration mirror, the establishment of techniques to control the temperature of the beamsplitter substrate during coating, completion of the preliminary design of the discrete step IR beamsplitter coating, and combining the separate thermal computer models into one.

During the reporting period, the detail design, breadboard, and test of the electronics circuits and subsystems have continued. Three of the six multilayer printed circuit boards (PCB's) included in the electronics package and the two power supply PCB's have been released for PCB layout. Circuits included on the three multilayer PCB's consist of the programmer logic, summation unit, delay generator, and HK multiplexer on one of the boards; the IR analog data channel and the analog-to-digital converter on another; and many of the phase lock loop circuits on the third. In addition to these circuits, the design of the radiometer electronics and the position control loop electronics is nearing completion.

Information presented in this second quarterly report follows the same general outline as the first report. Section II contains the technical discussion of the electronic and electro-mechanical design areas as well as Reliability and Quality Assurance activities, a program management overview is presented in Section III, with planned activities for the next reporting period in Section IV.

SECTION II

TECHNICAL DISCUSSION

A. ELECTRONIC DESIGN

The system design, analysis, and specification have continued during the present reporting period. Much of this analysis was completed through use of the data channel computer model discussed in detail in the first Quarterly Report. Some of the results obtained through use of the model are discussed in paragraph 1.0 of this Section of the report.

During the reporting period, the detail design, breadboard, and test of the electronics circuits and subsystems have continued. Three of the six multilayer printed circuit boards (PCB's) included in the electronics package and the two power supply PCB's have been released for PCB layout. Circuits included on the three multilayer PCB's consist of the programmer logic, summation unit, delay generator, and HK multiplexer on one of the boards; the IR analog data channel and the analog-to-digital converter on another; and many of the phase lock loop circuits on the third. In addition to these circuits, the design of the radiometer electronics and the position control loop electronics is nearing completion. The design and technical status of these circuits are discussed in the following paragraphs of this report.

The results of two dynamic radiation tests run during the second quarterly reporting period are included in Appendices B and C. The first test series used gamma ray irradiation from cobalt-60. Test results are in Appendix B. The radiation source intended for the second test series was a 2 Mev Van de Graaff. When the Van de Graaff was beset by a number of malfunctions, tests were conducted with strontium - 90/yttrium - 90 instead. Test results are in Appendix C. All tests were run in air.

1. Data Channel Simulation Results

The following paragraphs discuss the results obtained from the data channel simulation during the present reporting period. The results discussed include the effects on system noise equivalent radiance (NER) of delay generator (shift register) resolution, reference interferometer (neon) signal to noise ratio, and modulation inputs (with and without delay error).

Figure 2-1 indicates the sensitivity of system NER to delay generator clock frequency. Essentially this figure shows the requirement for a 400 KHz shift register clock. The set of information used is for a 0.5 radian @ 20 Hz modulation condition. Similar results occur for other modulation levels and frequencies; the main difference being a change in the NER asymptote. It should be noted that this figure represents a change from that data presented in the first quarterly report as Figures 2-8, 2-9, 2-10, 2-11, and 2-12. A program error was discovered which invalidates the data presented in those figures.

Figure 2-2 relates NER to the reference channel (neon) signal to noise ratio. The simulation assumes white Gaussian noise and shortens the interferogram to 2 seconds duration. In the actual system the lengthened interferogram (45 seconds) will provide more averaging which should enhance the NER. Taking into account the longer interferogram time, the required signal to noise ratio is on the order of 50 db. Based on previous data, approximately an order of magnitude improvement is needed in the neon signal to noise ratio. This will be achieved through the closer coupling of the reference interferometer and through an improved optical design of the reference interferometer.

Figure 2-3 shows the effects of modulation (vibration inputs) on the system. To acquire the data, the simulation was set up with a particular data channel bandwidth. Then, under modulation (with and without delay error) the modulation index (jitter) was

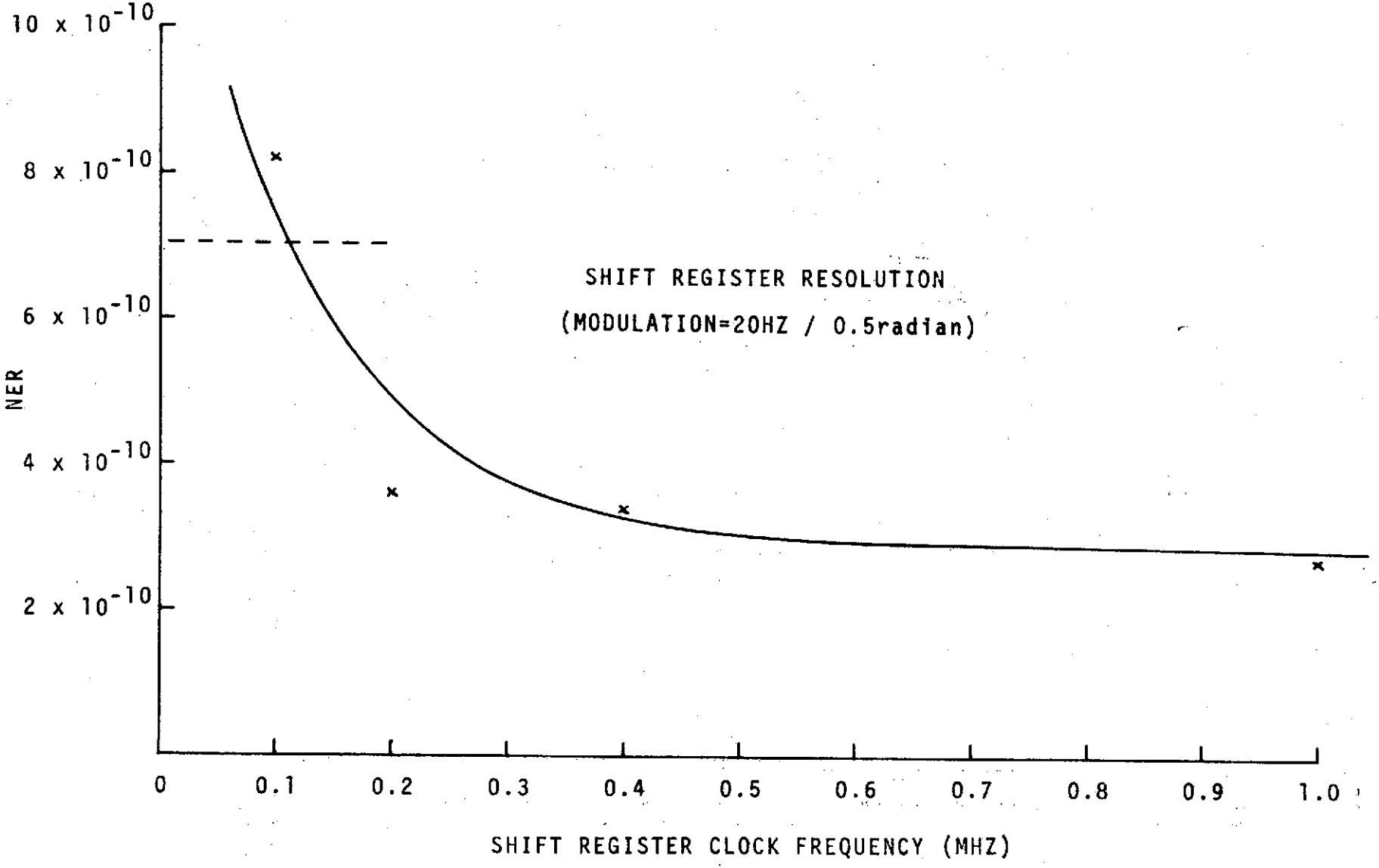
10 x 10^-10
8 x 10^-10
6 x 10^-10
4 x 10^-10
2 x 10^-10
NER
SHIFT REGISTER RESOLUTION
(MODULATION=20HZ / 0.5radian)
0
0.1
0.2
0.3
0.4
0.5
0.6
0.7
0.8
0.9
1.0
SHIFT REGISTER CLOCK FREQUENCY (MHZ)

Figure 2-1

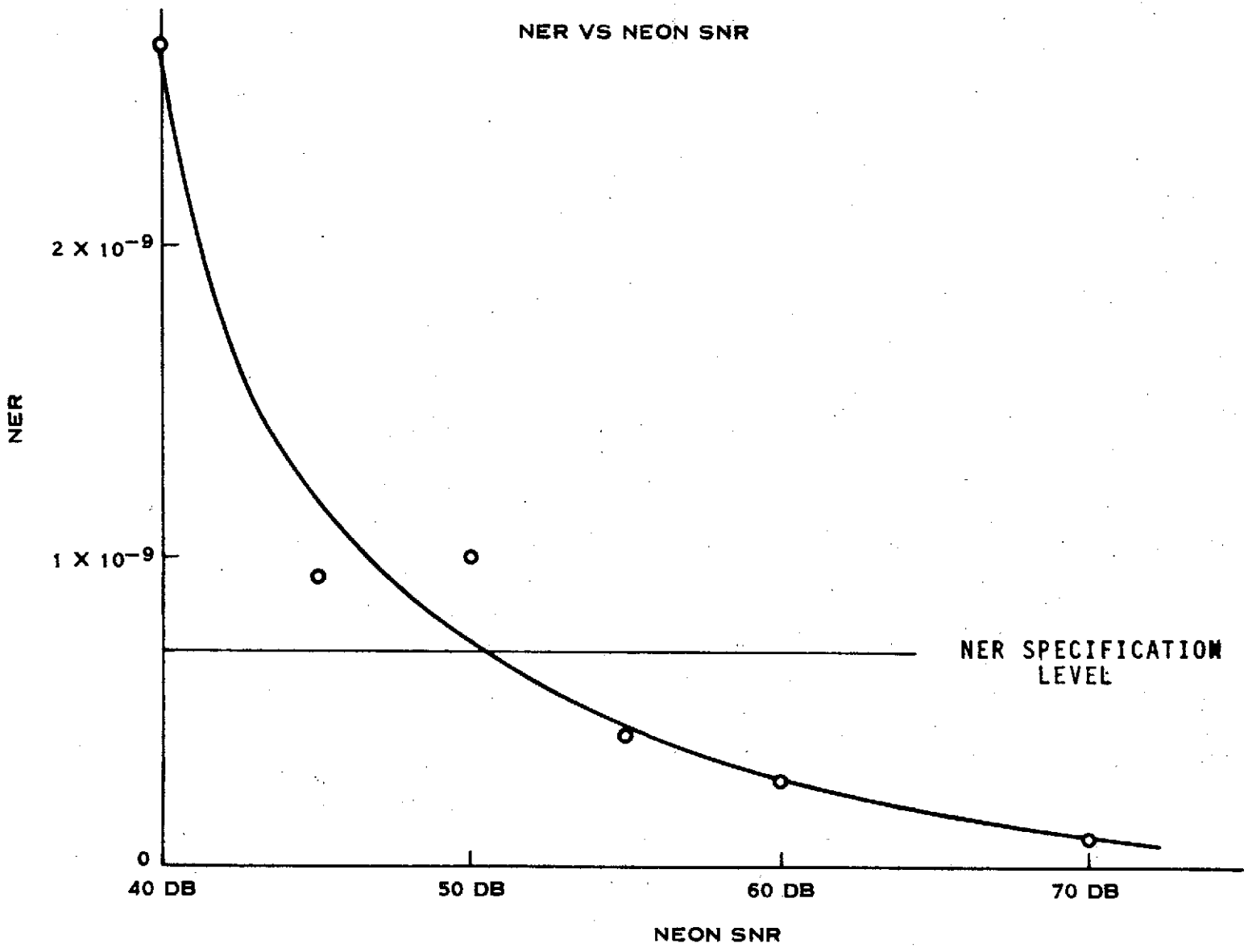
NER VS NEON SNR
2 X 10⁻⁹
1 X 10⁻⁹
0
NER
NER SPECIFICATION LEVEL
40 DB
50 DB
60 DB
70 DB
NEON SNR

FIGURE 2-2

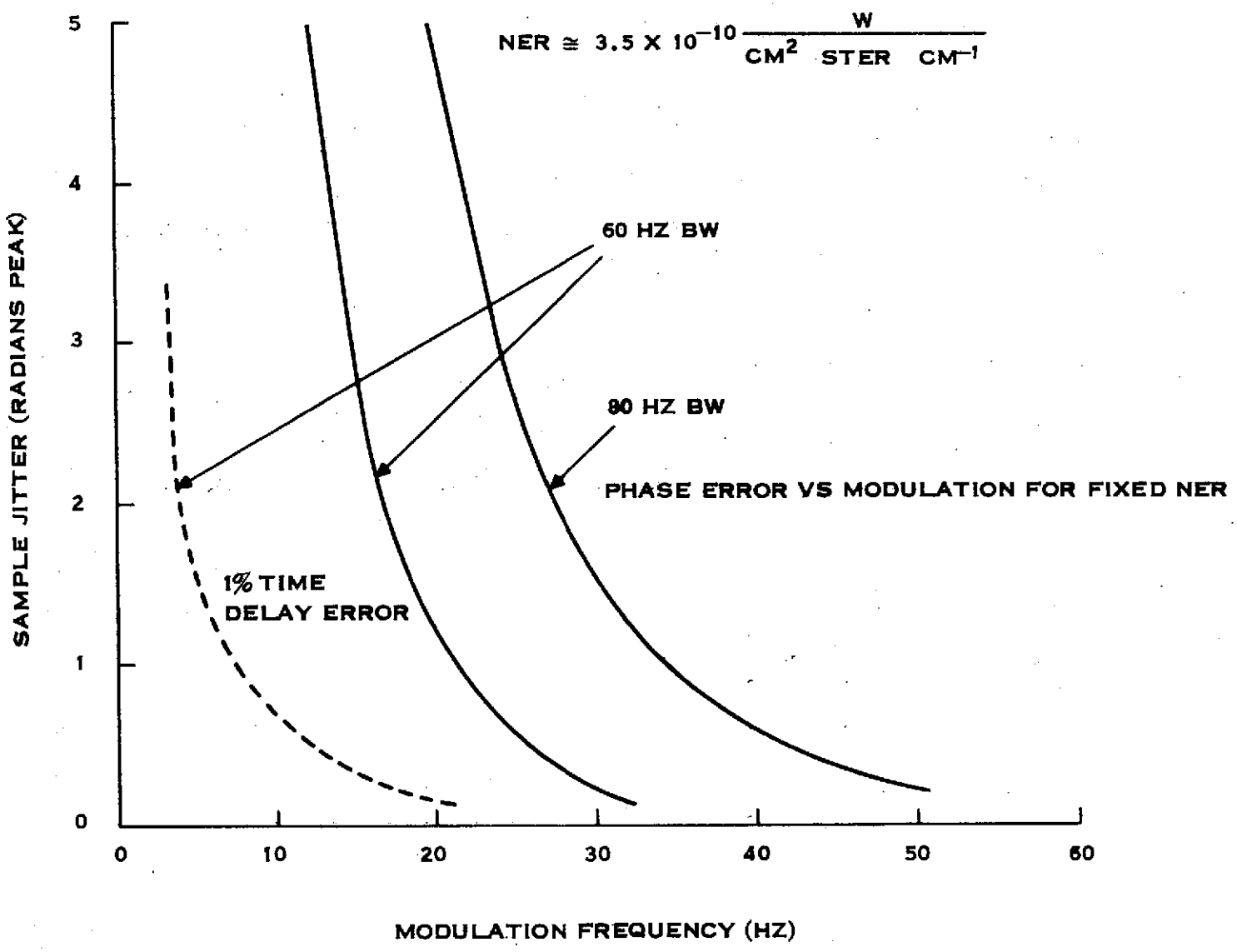
NER ≅ 3.5 X 10⁻¹⁰ W / CM² STER CM⁻¹
60 HZ BW
80 HZ BW
PHASE ERROR VS MODULATION FOR FIXED NER
1% TIME DELAY ERROR
SAMPLE JITTER (RADIANS PEAK)
MODULATION FREQUENCY (HZ)
0
1
2
3
4
5
0
10
20
30
40
50
60

Figure 2-3

varied to achieve 3.5×10^{-10} NER (one half of the specification value). Note should be taken of the degradation caused by a 1% time delay error. This is about the best time delay accuracy expected and therefore puts a serious limitation on the performance. The curves to be meaningful must be related back to vibration input levels which requires the mechanical transfer function from the spacecraft to the Michelson motor and the Michelson motor drive phase lock loop performance for the specified vibration input. Figure 2-4 shows the data from Figure 2-3 superimposed on a plot of expected phase error due to a 0.01G sinewave vibration applied to the spacecraft/instrument interface. For a data channel bandwidth of 80Hz and an assumed 1% time delay error, it can be determined from Figure 2-4 that a 0.01G vibration level may be applied to the instrument for vibration frequencies up to 25 Hz without severe degradation of system NER.

Figure 2-5 is a verification that previous specification of the number of quantization bits is correct and a check on the simulation performance. The curves do not include the effect of chirping and thus are 1 to 2 bits higher than is required in the actual system for a given contribution to system NER.

In retrospect the data channel simulation has been a valuable tool. The ability to evaluate error sources independently has led to invaluable insight into the system requirements and limitations.

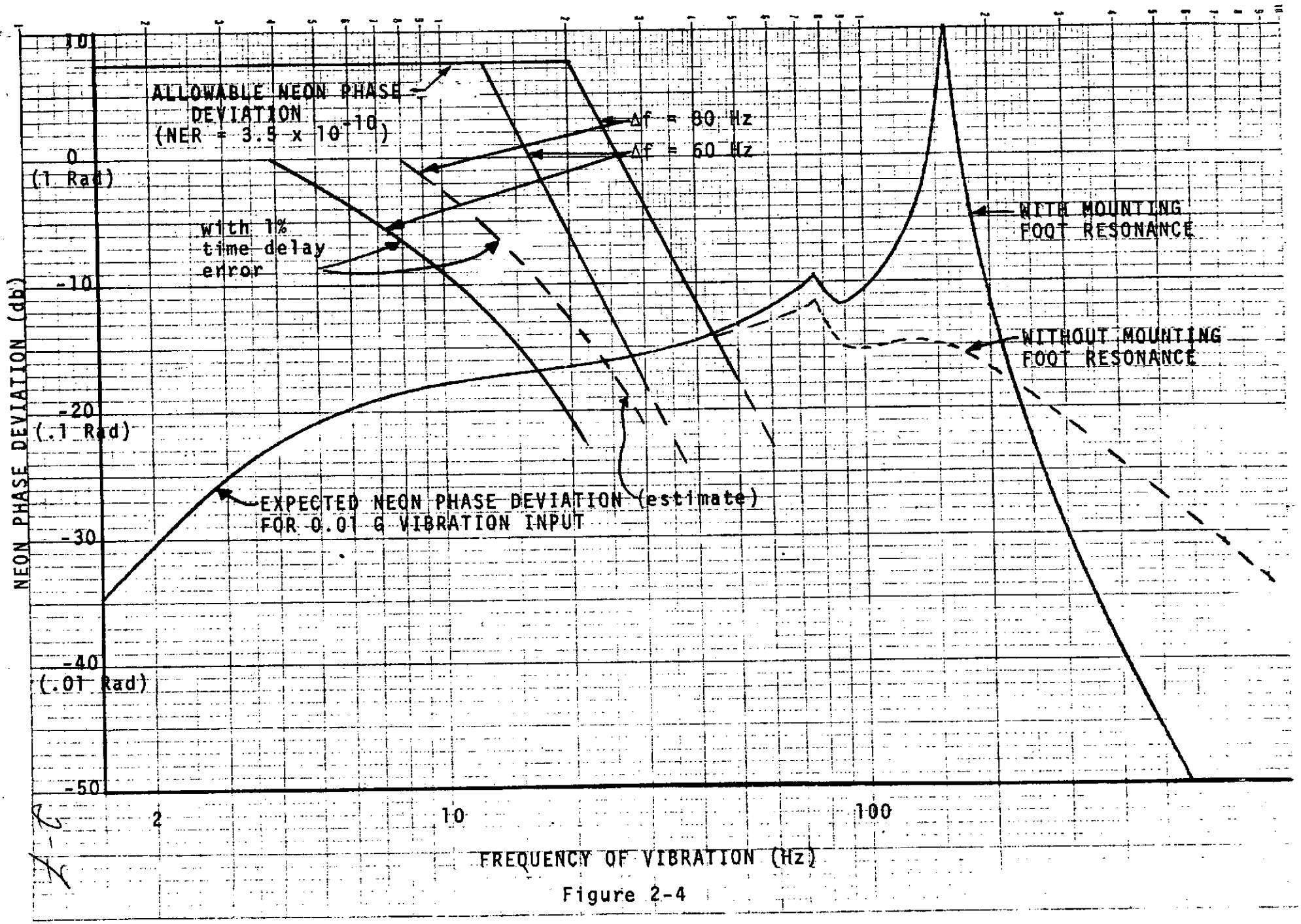
SEMI-LOGARITHMIC 3 CYCLES X 70 DIVISIONS AD-0837-07
10
0
(1 Rad)
-10
-20
(.1 Rad)
-30
-40
(.01 Rad)
-50
NEON PHASE DEVIATION (db)
ALLOWABLE NEON PHASE DEVIATION (NER = 3.5 x 10^-10)
Δf = 80 Hz
Δf = 50 Hz
with 1% time delay error
WITH MOUNTING FOOT RESONANCE
WITHOUT MOUNTING FOOT RESONANCE
EXPECTED NEON PHASE DEVIATION (estimate) FOR 0.01 G VIBRATION INPUT
2
10
100
FREQUENCY OF VIBRATION (Hz)

Figure 2-4

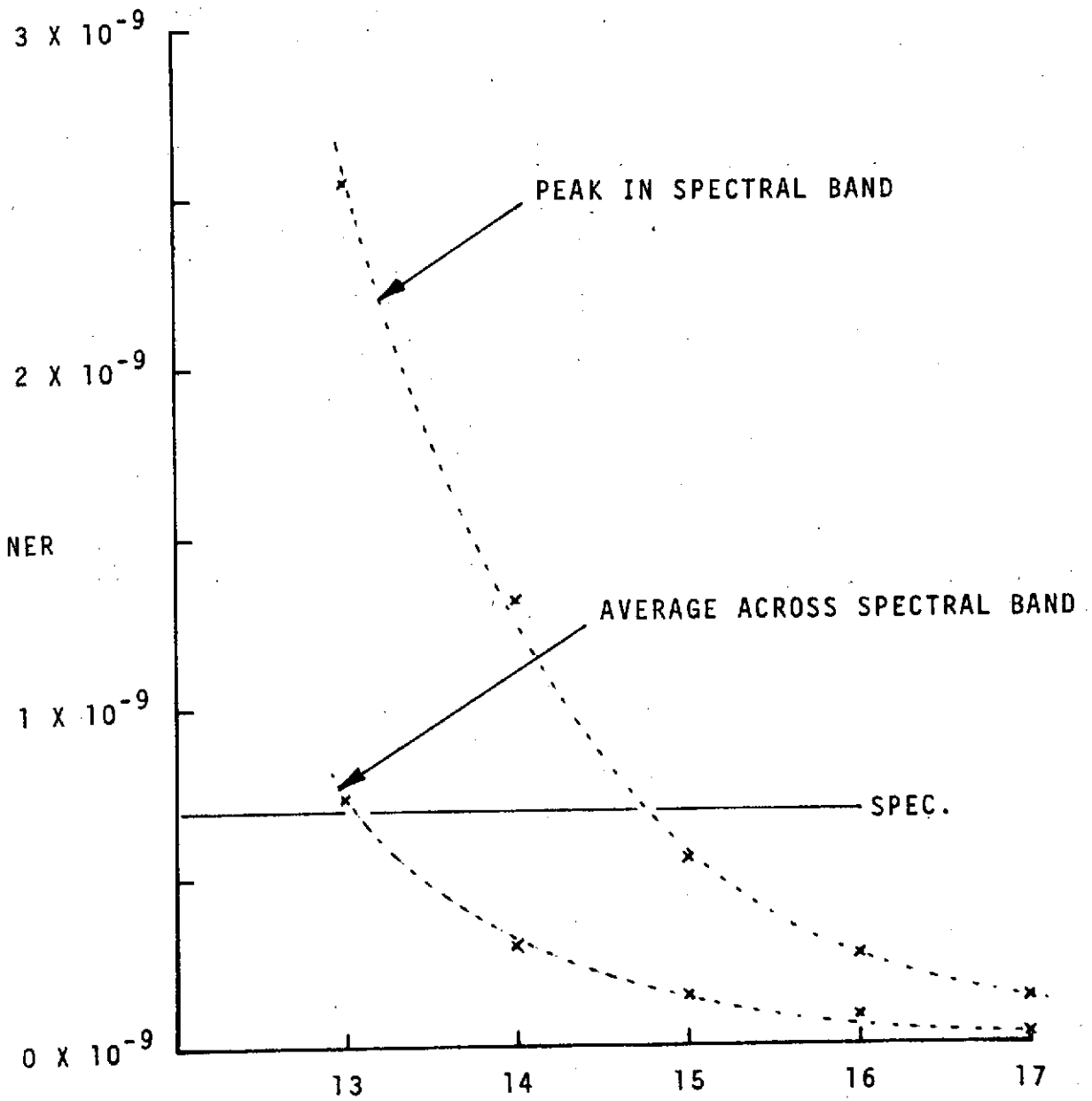
3 X 10-9
2 X 10-9
NER
1 X 10-9
0 X 10-9
PEAK IN SPECTRAL BAND
AVERAGE ACROSS SPECTRAL BAND
SPEC.
13
14
15
16
17
QUANTIZATION BITS

Figure 2-5

2. DATA CHANNEL

a. Detector and Preamp

Two types of IR detectors have been investigated for use in MJS-IRIS, a lithium tantalate pyroelectric detector, and a thermopile detector. Radiation tests have shown, however, that the pyroelectric detector proved noisy in a radiation environment thus dictating the selection of the thermopile detector. The major thermopile specifications required to meet system specifications are listed in Table 2-1.

Since the noise level of this detector is on the order of 0.5 $nV/\sqrt{Hz}$, a preamplifier with a noise level of $\simeq$ 0.2 $nV/\sqrt{Hz}$ is required to maintain a detector noise limited system. To achieve this, three methods of preamplifier implementation have been investigated. These methods are a magnetic amplifier, a modulation/demodulation scheme, and a transformer coupled preamp. Of these, only the transformer coupled preamp proved feasible as far as meeting the stringent noise level requirements. The disadvantages of this approach, however, are the transformer size and weight requirements needed for such low frequency coupling ($\simeq$ 1 Hz), and the degradation to the data channel phase linearity at low frequencies. This phase linearity degradation results in a degradation to the system NER at low data frequencies in a vibration or modulating environment. A compensating technique for this latter problem is discussed in the next section.

b. Compensation Amplifiers and Filter

The overall desired response of the data channel is flat amplitude with linear phase over the bandwidth 1 Hz - 80 Hz. This response characteristic allows passing the entire data band (1-28 Hz) and enough of the data side bands, resulting from any vibration frequencies, with minimum distortion to assure proper demodulation at the sample and hold. Thus, any phase non-linearities in this band gives rise to distortion of modulation sidebands resulting in system NER degradation.

TABLE 2-1

MAJOR THERMOPILE DETECTOR SPECIFICATIONS

●	NOISE EQUIVALENT POWER (AT 200°K)	: $\leq$ 1 X 10^{-10} WATTS (1000°K, 28 Hz, 1 Hz)
●	SPECTRAL RANGE	: 2.5 TO 50 MICROMETERS
●	ACTIVE AREA	: 2.5 X 2.5 MM
●	TIME CONSTANT	: $\leq$ 5 MSEC
●	RESPONSIVITY	: $\geq$ 10 VOLTS/WATT
●	RESISTANCE	: 10 TO 30 OHMS

Figure 2-6 is a block diagram of the entire data channel with associated frequency responses to indicate how the desired overall response is achieved. Since the thermopile detector has a pole at approximately 30 Hz, a detector compensation amplifier with a zero at 30 Hz has been added. Likewise, a compensating amplifier has been added to compensate for the transformer's 1 Hz coupling frequency. The detailed description of these amplifiers and also the remainder of the data channel is shown in schematic form in Figure 2-7 . Also, the measured frequency response of the breadboard detector compensation amplifier and the transformer compensation amplifier is shown in Figures 2-8 and 2-9 respectively.

Due to the high gain (≃ 120 db) required in the data channel, it is necessary to AC couple at selected places to remove any DC bias or amplifier offsets. However, this AC coupling can add phase shift to the low frequency portion of the data band and thus create phase non-linearities. Therefore, from a phase linearity or system NER standpoint it is desirable to couple at as low a frequency as physically possible with perhaps capacitor size being the limiting constraint. However, the disadvantage of this low frequency coupling is the data channel step response. Since any abrupt change in targets in the instrument field of view, such as deep space calibration, represents an input step function, it is desireable to minimize the data channel step response. To evaluate this trade-off and thus select the optimum AC coupling frequency, the data channel system model program was used to evaluate system NER for a fixed vibration input (20 Hz/.15 Radians) at four different coupling frequencies. The results of this trade-off study are shown in Table 2-2. The DC coupling entry is included to establish a reference point and indicates the error due to the non-linearities in the filter section of the data channel as described below. From the results of the table a coupling frequency of 0.025 Hz was selected as the optimum trade-off between NER and system step response.

IR DATA CHANNEL
FREQUENCY RESPONSE CHARACTERISTICS

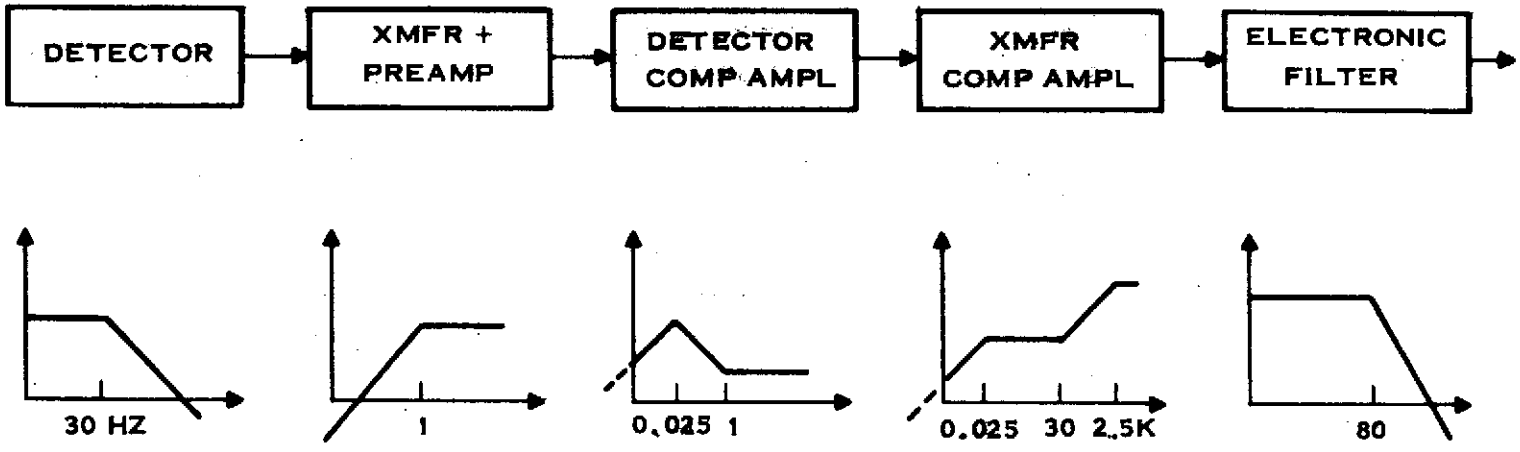

Figure 2-6

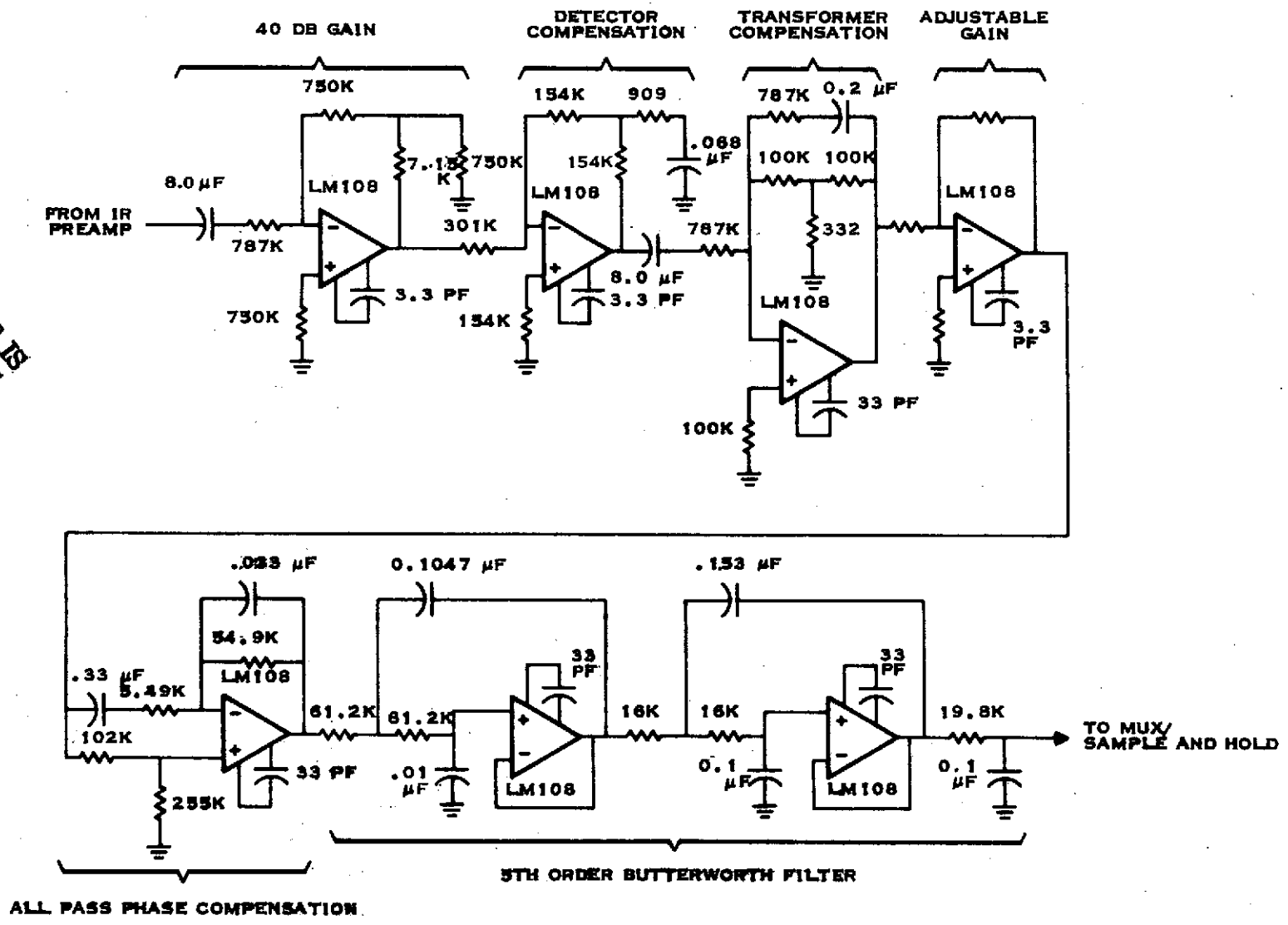

IR DATA CHANNEL SCHEMATIC
FIGURE 2-7

DETECTOR COMPENSATION AMPLIFIER
BREADBOARD FREQUENCY RESPONSE

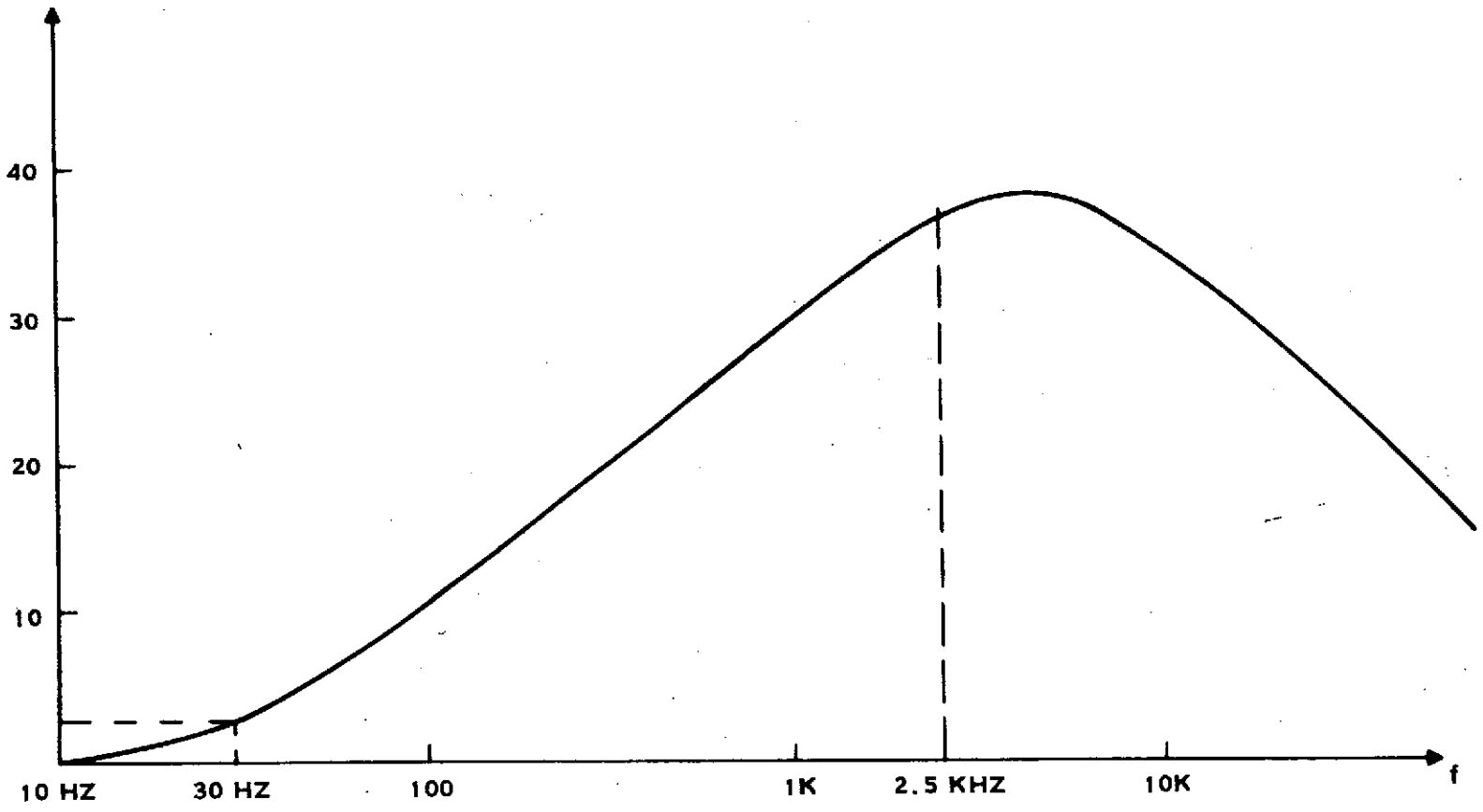

Figure 2-8

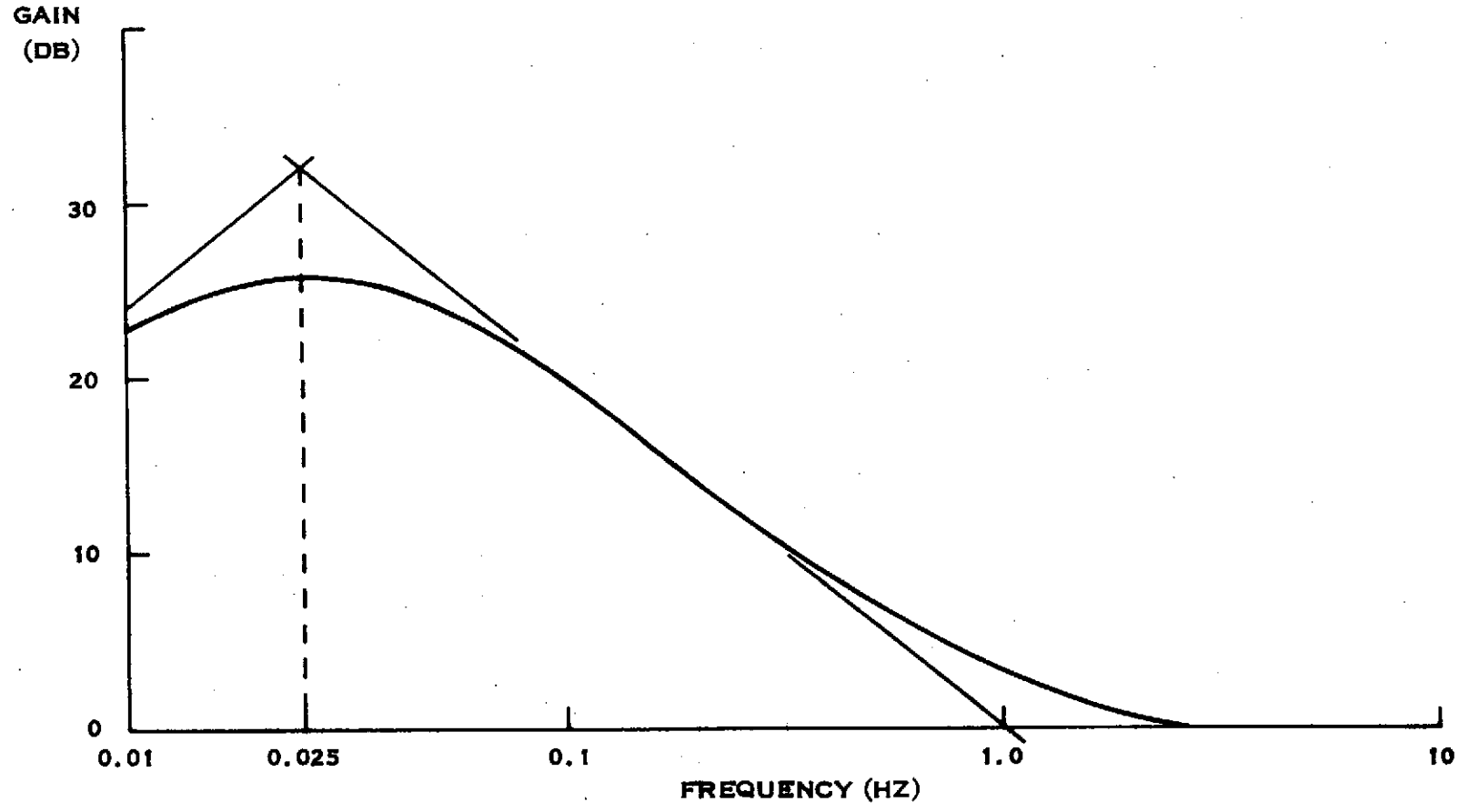

Transformer Compensation Amplifier
Breadboard Frequency Response

Figure 2-9

TABLE 2-1 A.C. COUPLING TRADE-OFF

A.C. COUPLING FREQ	AVERAGE VALUE NER ($X10^{-9}$)	MAX. VALUE NER ($X10^{-9}$)	TIME CONSTANT
D.C	.220	.577	≃ 0
.01 Hz	.198	.660	120 SEC
.025	.212	.805	48 SEC
.05	.375	1.104	24 SEC
.10	.754	2.044	12 SEC

NOTES:

1. NER VALUES ARE FOR VIBRATION LEVELS OF 20 Hz/0.15 RADIANS.

2. TIME CONSTANT IS THE TIME FOR A STEP INPUT TO DECAY TO WITHIN 99% OF FINAL VALUE.

Investigations of data channel performance, utilizing the system model program, uncovered an unexpected problem with the electronic filter. A Bessel configuration had been originally selected for this application, primarily on the merit of its superior phase linearity. However, it was discovered that the small amplitude response variations of the Bessel type filter would introduce minute distortions of signal sidebands during vibration. While the order of magnitude of this distortion would not have been a problem on previous instruments, it would impose serious limitation on the sensitivity of the MJS instrument. Accordingly, the Bessel filter design was supplanted with a fifth order Butterworth implementation with added phase correction circuitry.

The Butterworth filter configuration chosen is shown in Figure 2-7. This implementation provides an amplified response which is virtually frequency insensitive throughout the data bandwidth. Similarly, a second order all pass network assures a phase response linear to within 1% across the 1 to 80Hz band. This linear phase characteristic results in a constant time delay of all data band frequencies. Breadboard test results are displayed in Figure 2-9a. Deviations from the ideal case reflect the errors resulting from the channel coupling trade-off previously discussed.

Attaining the desired phase response of the Butterworth filter required an increase in the slope of the phase curve, or an increase in the constant time delay. This, in turn, necessitated a redesign of the delay generator to expand its nominal time delay.

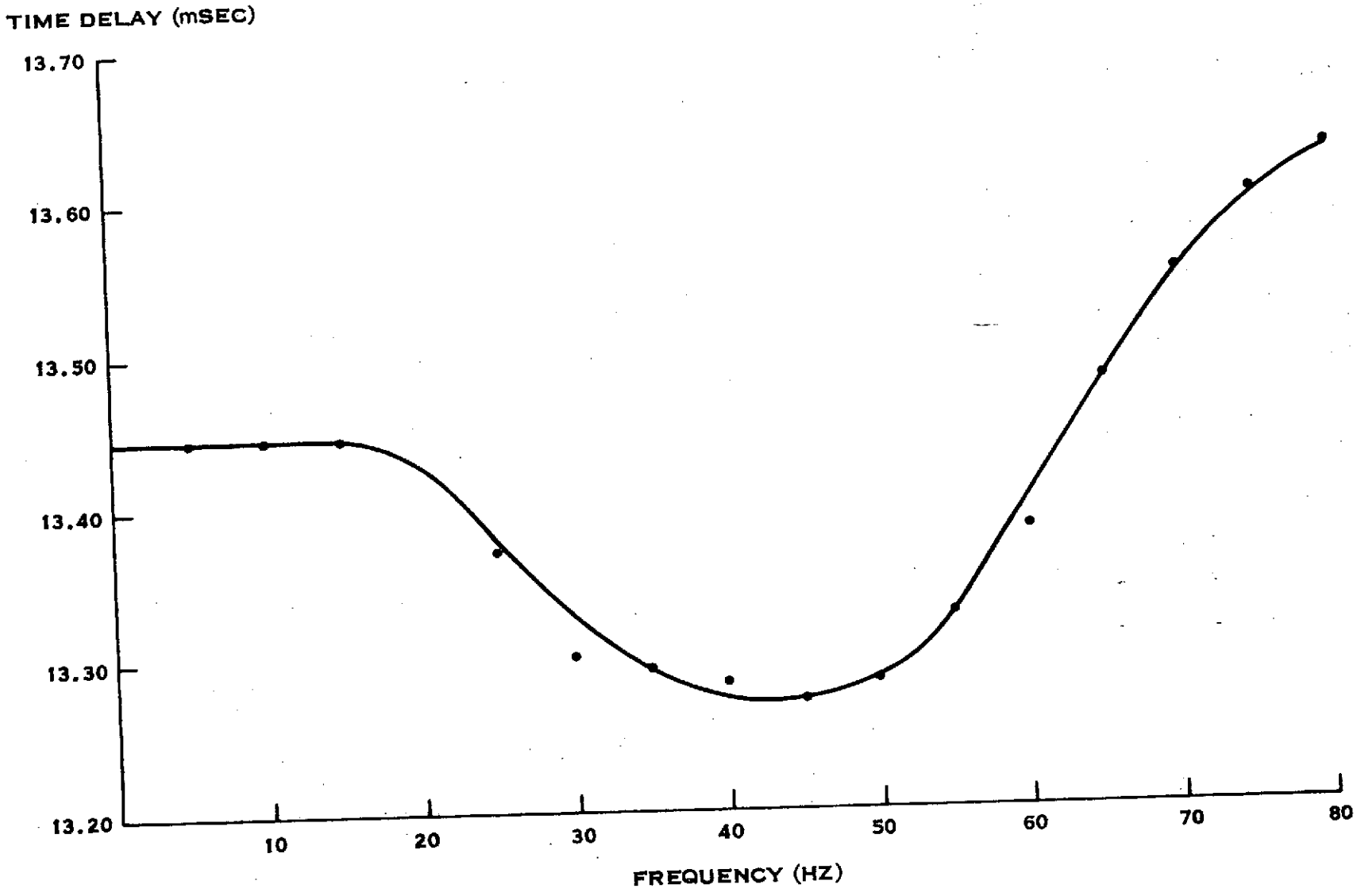

BUTTERWORTH FILTER/COMPENSATION TIME DELAY

Figure 2-9a

3. Phase - Lock Loop

A block diagram of the phase-lock loop (PLL) is shown in Figure 2-10. This diagram differs from the PLL block diagram shown in the first quarterly report by presenting the relationship of the bessel filter and zero crossing detector to the PLL. These circuits will be discussed in more detail in following paragraphs. This discussion will also include the neon preamplifier, AGC amplifier and amplitude detector, Michelson motor drive circuit, and the interface between the extended range phase comparator and the first integrator. The low pass (reference) filter, single sideband modulator, carrier generator, extended range phase comparator, and neon source driver were discussed in the first quarterly report.

a. Neon Preamplifier

As shown in the first quarterly report, the frequency of the neon preamplifier output is directly related to the velocity of the Michelson motor. The neon signal is phase-locked to a 120 Hz reference signal to achieve mirror velocity control. Figure 2-11 is a schematic diagram of the neon preamplifier.

A FET input stage followed by an operational amplifier provides a low noise, high open-loop gain, amplifier. This amplifier is used as a noninverting voltage amplifier, taking advantage of the FET's high input impedance to make the load on the silicon detector relatively independent of amplifier input impedance. Feedback is provided by R7, 8, 9, 10 and C3. DC gain is 2 and AC gain is 300 (50 db). R11 is used to control the bandwidth of the silicon detector. Q2 and R4, R5, and R6 provide a constant current source to the FET input stage.

Radiation induced degradation of operational amplifiers(1) and of silicon detectors was a large factor in the design of the neon preamp. A combination of the amplifier offset current and offset voltage changes under radiation, and the results of radiation tests on silicon photodiodes, dictated the high AC to DC gain ratio.

(1) Based on MJS radiation test results, San Diego, Calif., May 8, 9, and 10, 1974.

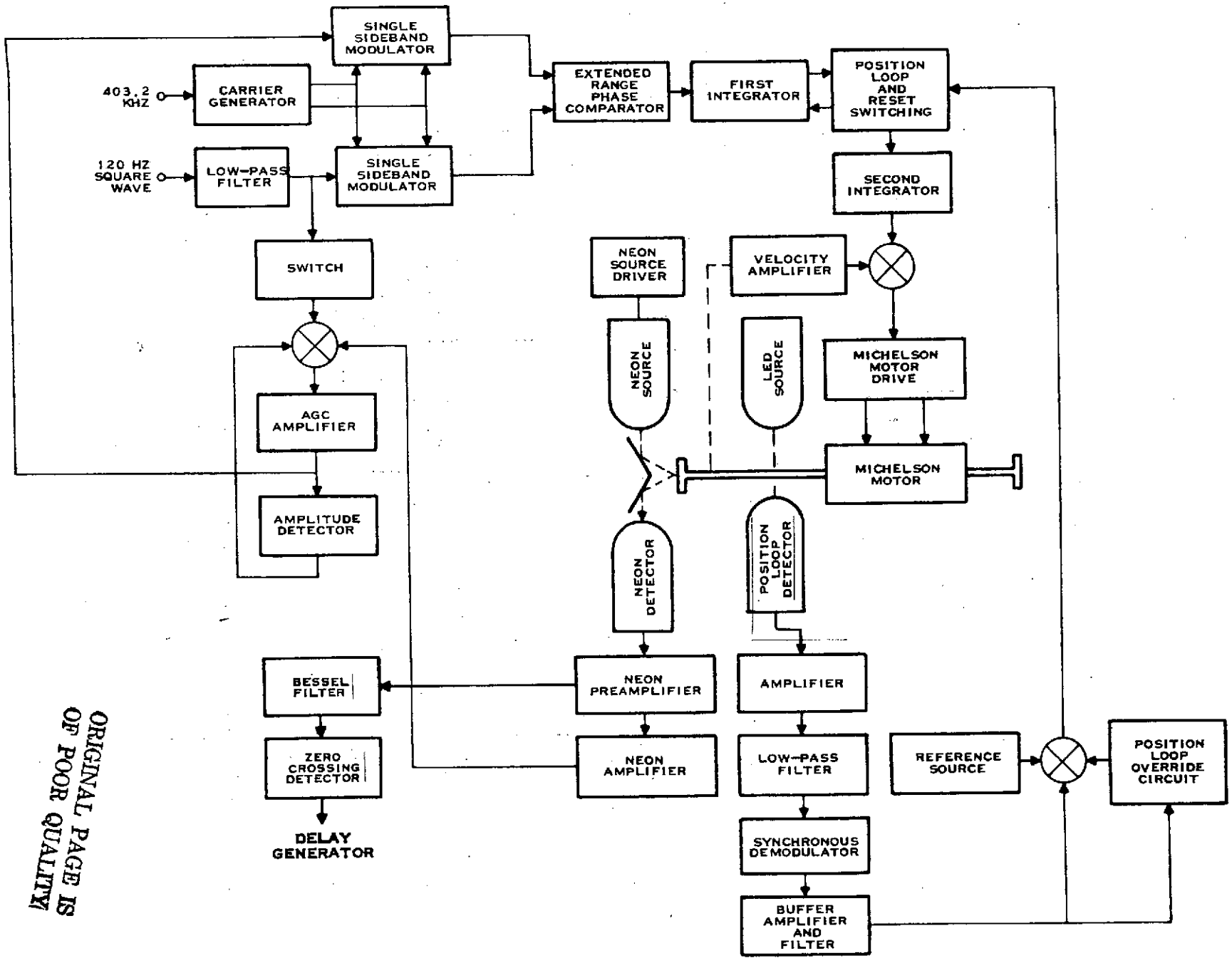

PLL AND POSITION LOOP BLOCK DIAGRAM

FIGURE 2-10

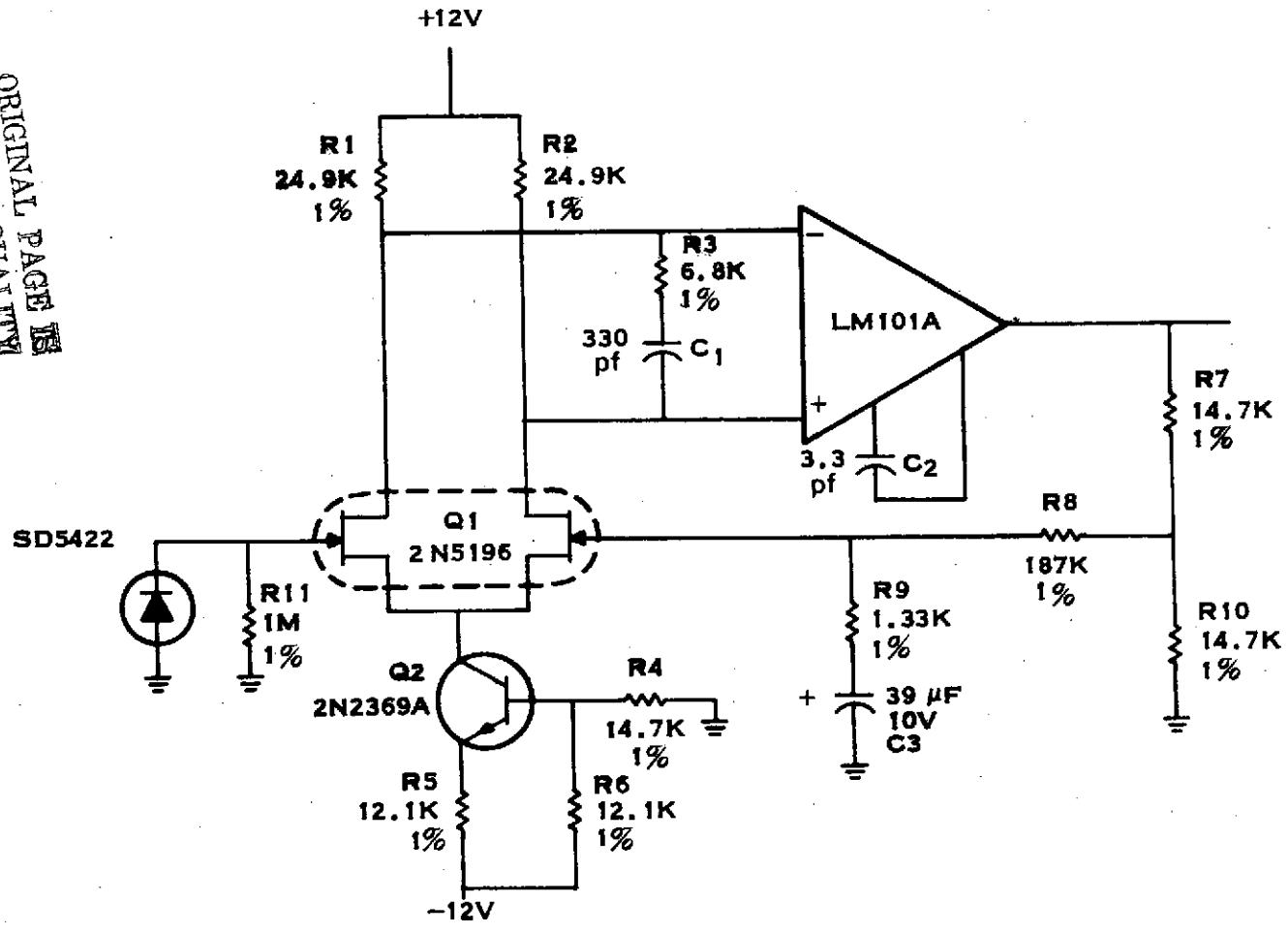

NEON PREAMPLIFIER

Figure 2-11

A more severe constraint was imposed by the degradation of open loop gain. Because of this constraint, an LM101A was used instead of the lower power LM108, and the closed loop gain was limited to 50 db. To keep the neon signal phase shift at near zero degrees, a bandwidth of 4 KHz was selected. This low phase shift is required in order to maintain equal time delays in the reference and infrared channels. Additionally, significant phase shift in the neon signal could cause instability in the phase lock loop. Figure 2-12 illustrates the lower closed loop gain necessary because of radiation, to ensure the closed loop response has its first break point at a frequency greater than 4 KHz.

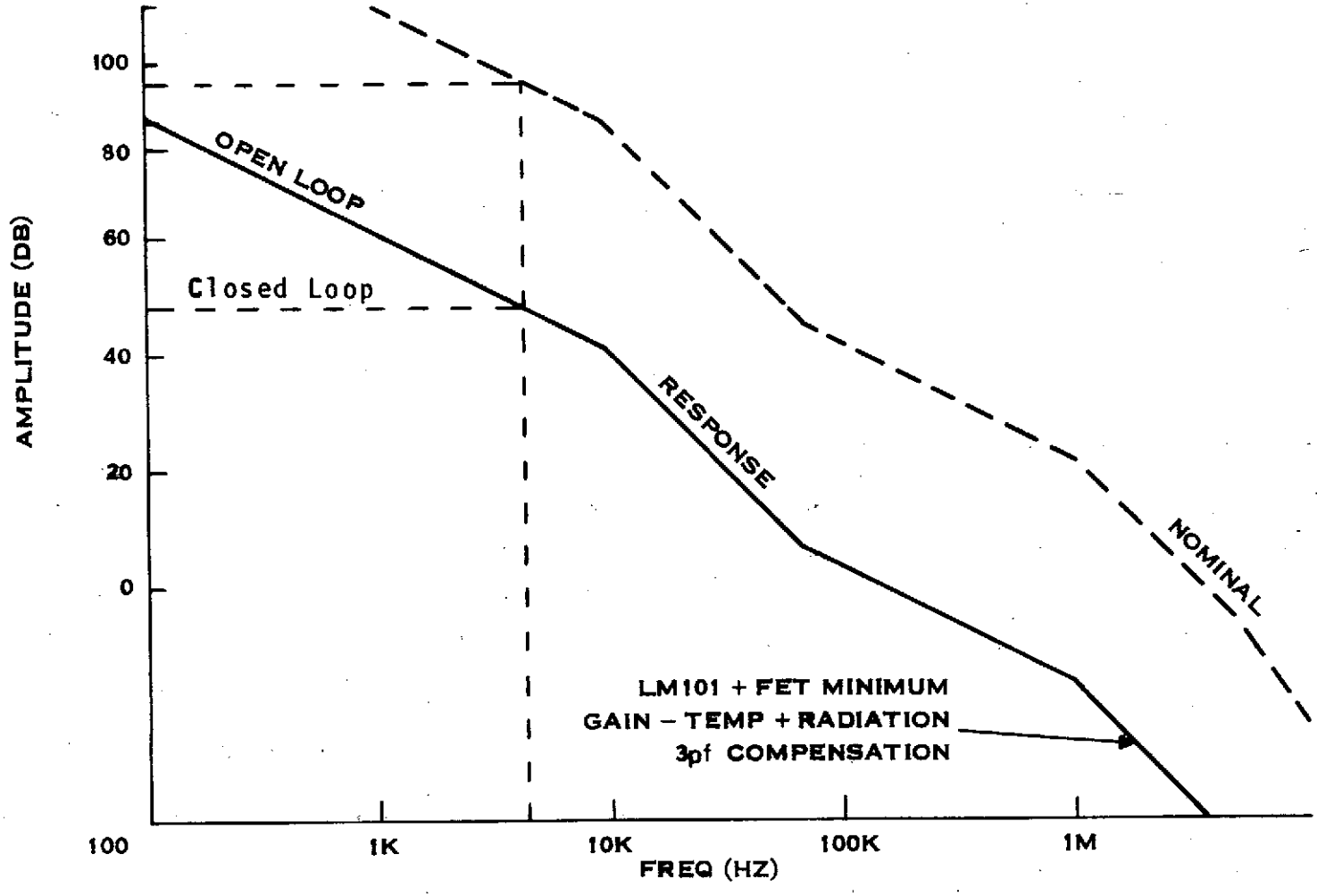

NEON PREAMP RADIATION CONSTRAINT

Figure 2-12

b. AGC Amplifier - Amplitude Detector

The AGC amplifier (Figure 2-13) is used to minimize noise induced jitter at the phase detector output by presenting a constant-amplitude signal to the single sideband (SSB) modulator in the neon channel. The amplitude of the neon signal is expected to vary over the duration of an interferogram, and also due to time, temperature, and radiation effects. The modulator has a relatively limited range of input signal amplitude (about $\pm$ 20%) for which optimum signal to carrier, signal to undesired sideband, and signal to intermodulation product ratios are maintained. As these ratios decrease, the effective signal to noise ratio is lowered.

During off time, an attenuated reference signal is switched into the AGC to reduce loop aquisition time. R1 will be selected to set the input magnitude of the reference signal. AGC gain control is accomplished by a resistor voltage-divider formed by R5 (R6 during off-time) and Q1. Radiation constraints dictated the use of the wide-bandwidth HARRIS 2520 op amp rather than the lower power LM108, and also limited the closed loop gain of the amplifier stage to 44 db. Higher closed loop gain in this stage would be desirable since second harmonic distortion, caused by signal at the drain of Q1, is an inverse function of the gain of the following stage. A level detector (Q2, Q3 and associated components) and a filter (R12, R13, C8, and C9) provide the control voltage for Q1. As shown in Figure 2-14 the AGC amplifier provides an essentially constant output for input signal levels from 30 MV to 10V RMS.

c. Bessel Filter and AGC Switches

Because of the high signal to noise ratios required, and because of the expected noise input to the neon preamp due to radiation, it is desireable to filter the neon signal as much as possible before presenting it to the zero crossing detector (ZCD). Additionally, all frequency components of the modulated neon signal must be passed through the filter with equal time delay. The 3rd order filter shown in Figure2-15 will accomplish these design goals. The -3 db frequency of the filter is 427 Hz, and the time delay for the modulated neon signal is .66 ms.

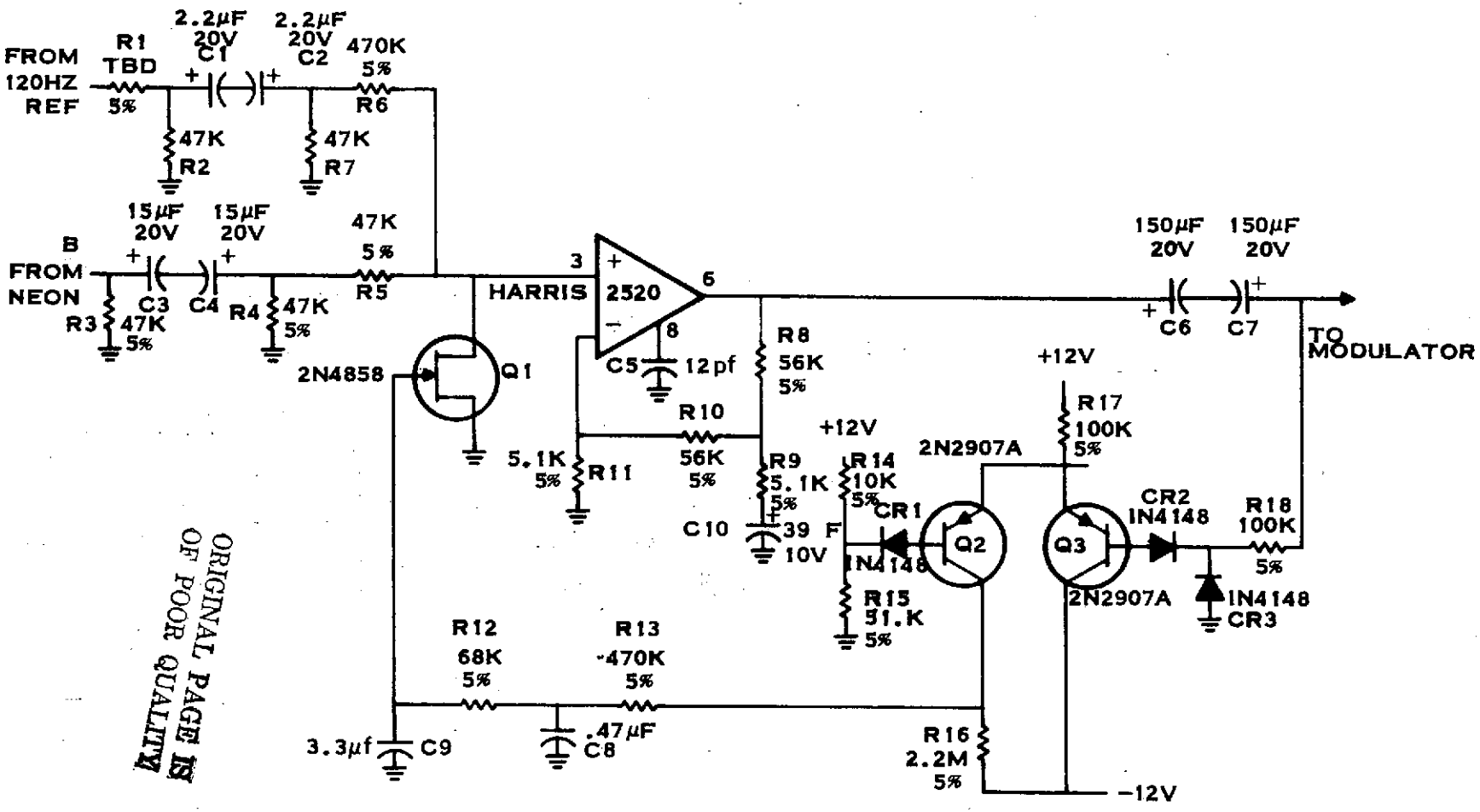

AGC AMPLIFIER

Figure 2-13

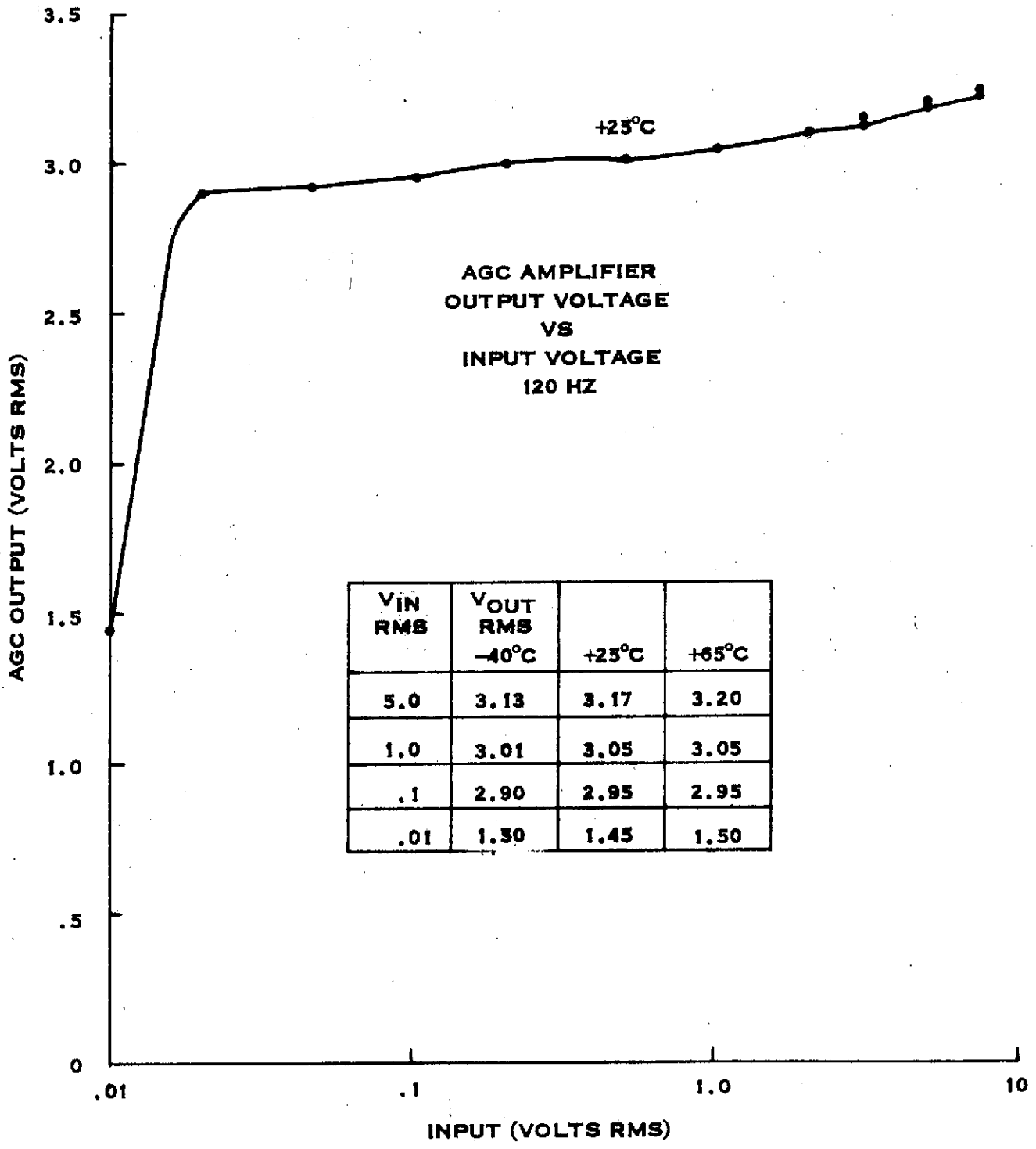

V_{IN} RMS	V_{OUT} RMS −40°C	+25°C	+65°C
5.0	3.13	3.17	3.20
1.0	3.01	3.05	3.05
.1	2.90	2.95	2.95
.01	1.50	1.45	1.50

Figure 2-14

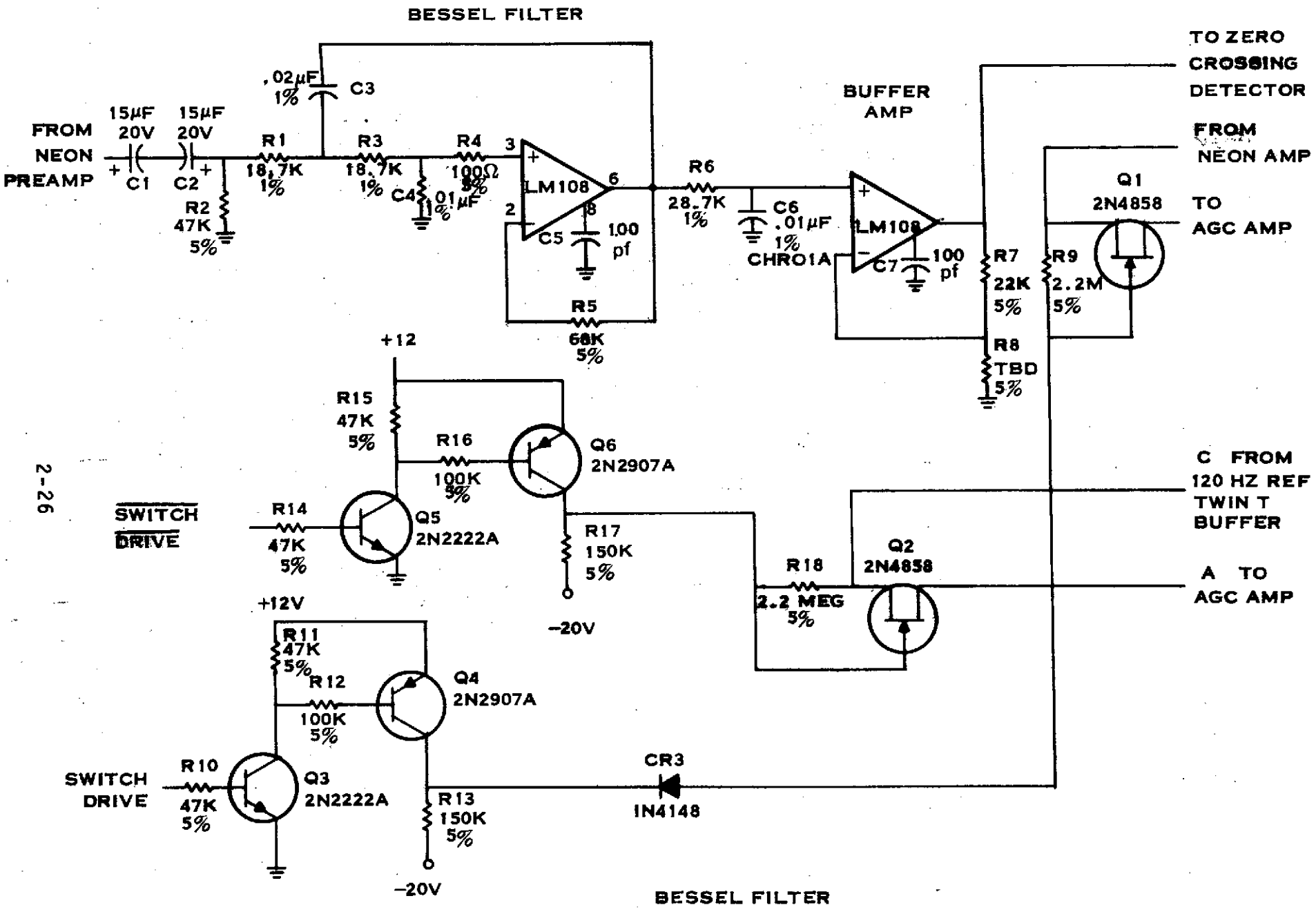
BESSEL FILTER
FROM NEON PREAMP
15µF 20V
C1
15µF 20V
C2
R2 47K 5%
R1 18.7K 1%
.02µF 1% C3
R3 18.7K 1%
C4 .01µF 1%
R4 100Ω 5%
LM108
C5 100 pf
R5 68K 5%
R6 28.7K 1%
C6 .01µF 1% CHRO1A
BUFFER AMP
LM108
C7 100 pf
R7 22K 5%
R8 TBD 5%
R9 2.2M 5%
Q1 2N4858
TO ZERO CROSSING DETECTOR
FROM NEON AMP
TO AGC AMP
+12
R15 47K 5%
R16 100K 5%
Q6 2N2907A
SWITCH DRIVE
R14 47K 5%
Q5 2N2222A
R17 150K 5%
-20V
C FROM 120 HZ REF TWIN T BUFFER
R18 2.2 MEG 5%
Q2 2N4858
A TO AGC AMP
+12V
R11 47K 5%
R12 100K 5%
Q4 2N2907A
SWITCH DRIVE
R10 47K 5%
Q3 2N2222A
CR3 IN4148
R13 150K 5%
-20V
BESSEL FILTER

Figure 2-15

Also shown in Figure 2-15 are the series FET switches (Q1 and Q2) which gate the neon signal and an attenuated reference signal into the AGC amplifier during mirror forward travel and during off time respectively. The switch drivers (Q3 through Q6) and associated components are driven from CMOS logic gates.

d. Zero Crossing Detector

The zero crossing detector (ZCD) provides a logic signal from which the ADC sampling signal is derived. The ZCD (Figure 2-16) will use an LM111 voltage comparator. Radiation induced changes of the same order of magnitude as experienced by LM101A's were assumed in the design of this circuit. R4 and R5 will be used to set the initial comparator offset. Time hysteresis in the ADC logic, as well as the relatively slow speed of the LM111 and the large magnitude of the input signal, eliminate the need for voltage hysteresis in this circuit.

e. Phase Detector Interface

An interface circuit is necessary between the CMOS output of the phase detector and the first integrator input. The first integrator will present a load impedence on the order of 3 KΩ and requires a voltage swing symmetrical about ground. The circuit shown in Figure 2-17 converts the logic level input to levels of +5V and -5V. Q3 and Q4 are inverted mode switching transistors with low $V_{CE_{SAT}}$. The +5 VDC supply for this circuit is derived from the -5 VDC supply to ensure that the supplies track.

f. Michelson Motor Drive

A schematic of the motor drive circuit is shown in Figure 2-18 . The MJS motor driver will be the same basic transconductance amplifier as was used in IRIS'71. Because of the reduced motor current required for the MJS Michelson motor, a number of component types and values have been changed from previous values.

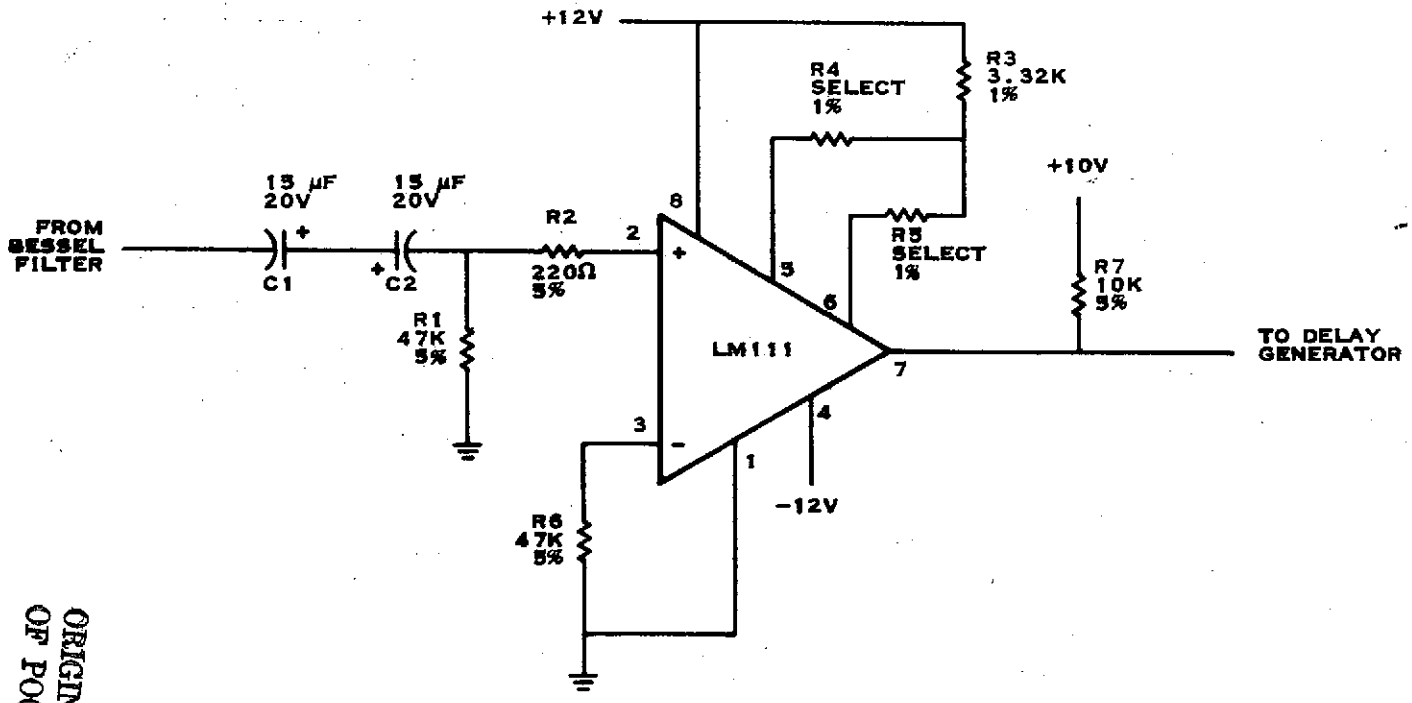

ORIGINAL PAGE IS
OF POOR QUALITY

Zero Crossing Detector Schematic

Figure 2-16

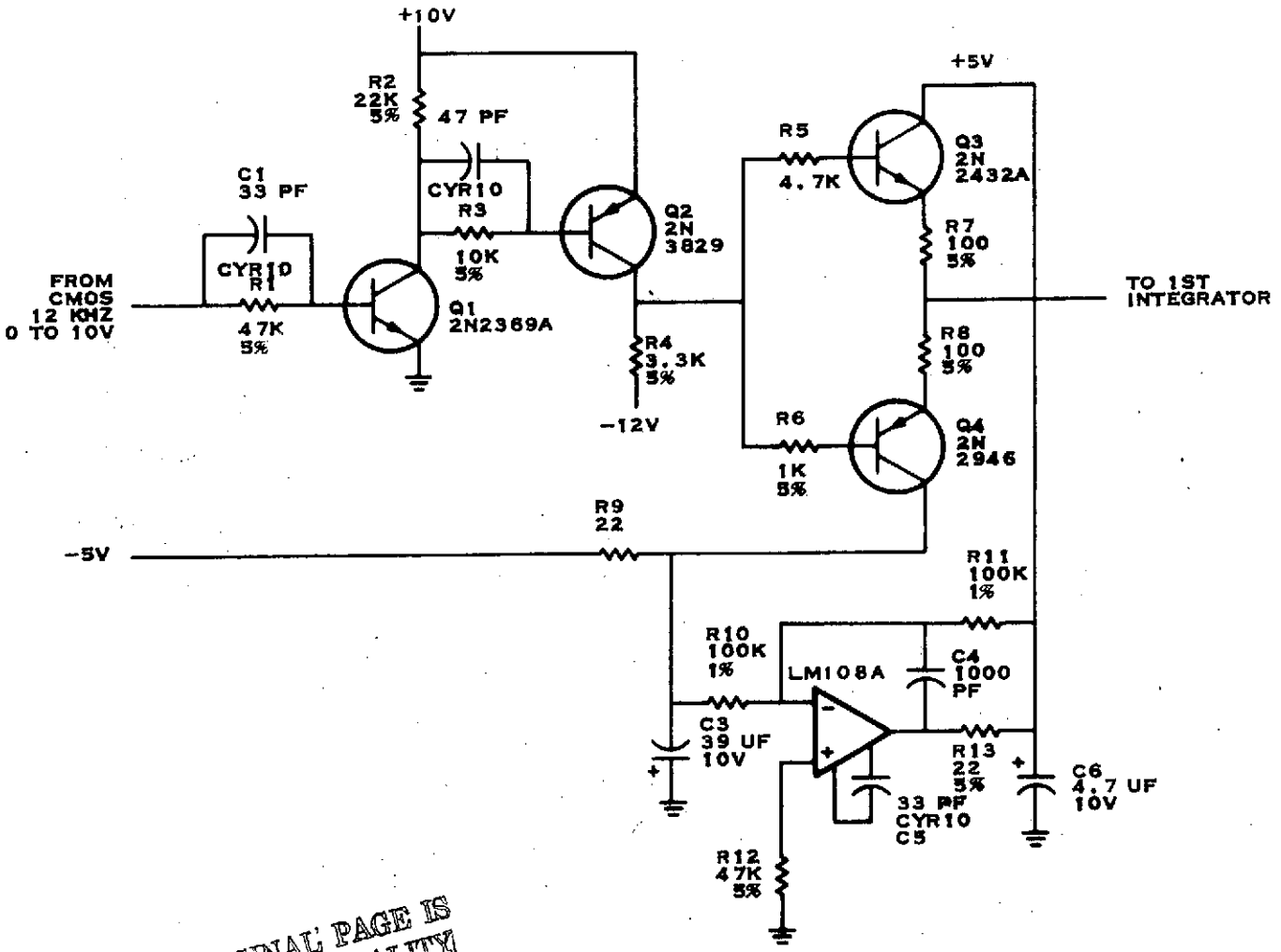

PHASE DETECTOR AND 5 V SUPPLY SCHEMATIC

FIGURE 2-17

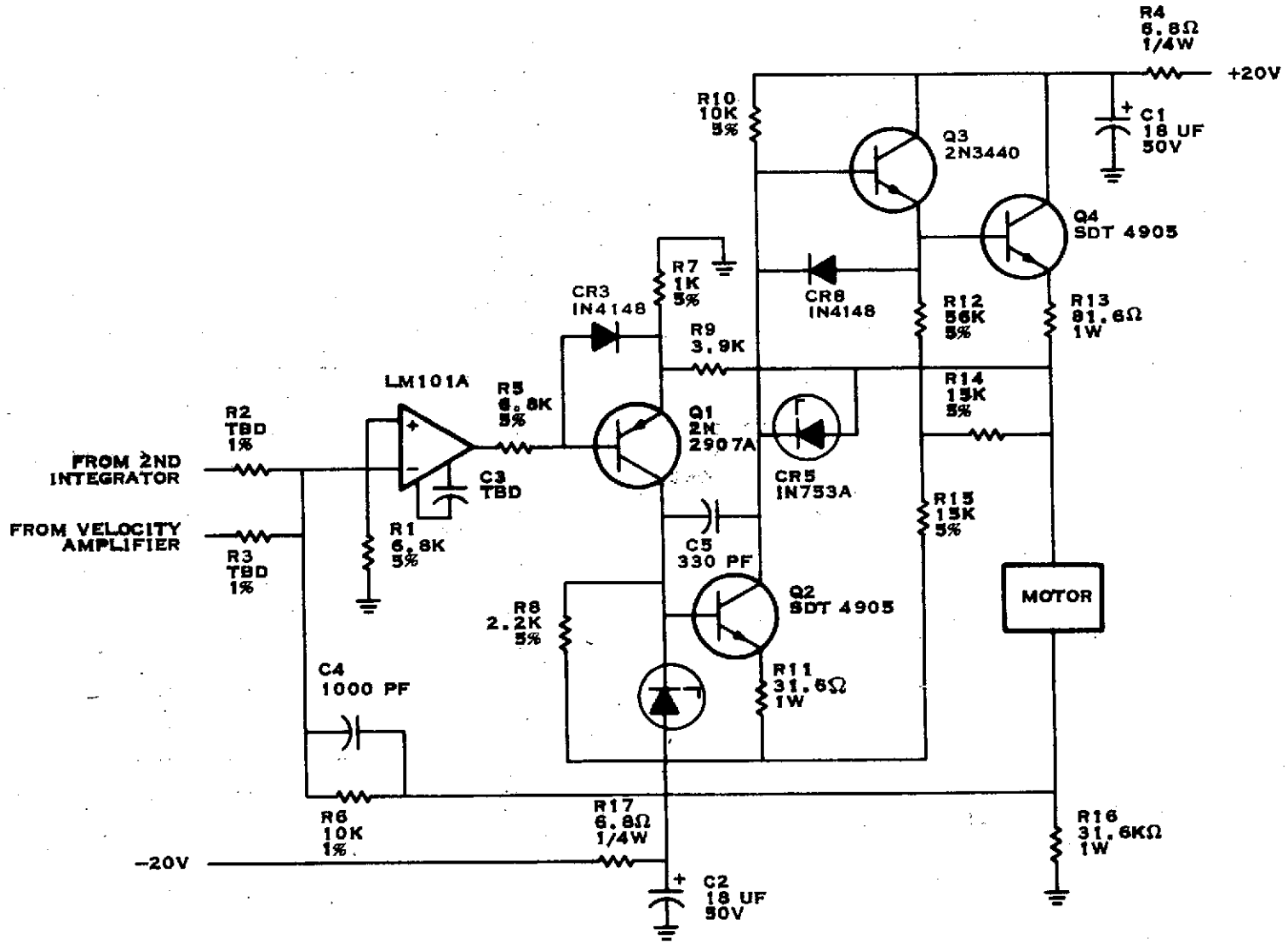

MOTOR DRIVE SCHEMATIC

FIGURE 2-18

g. 120 Hz Reference Filter

The purpose of the reference filter is to remove harmonic frequencies from the reference signal input. Figure 2-19 is a schematic of this circuit which was discussed in more detail within the 1st quarterly report.

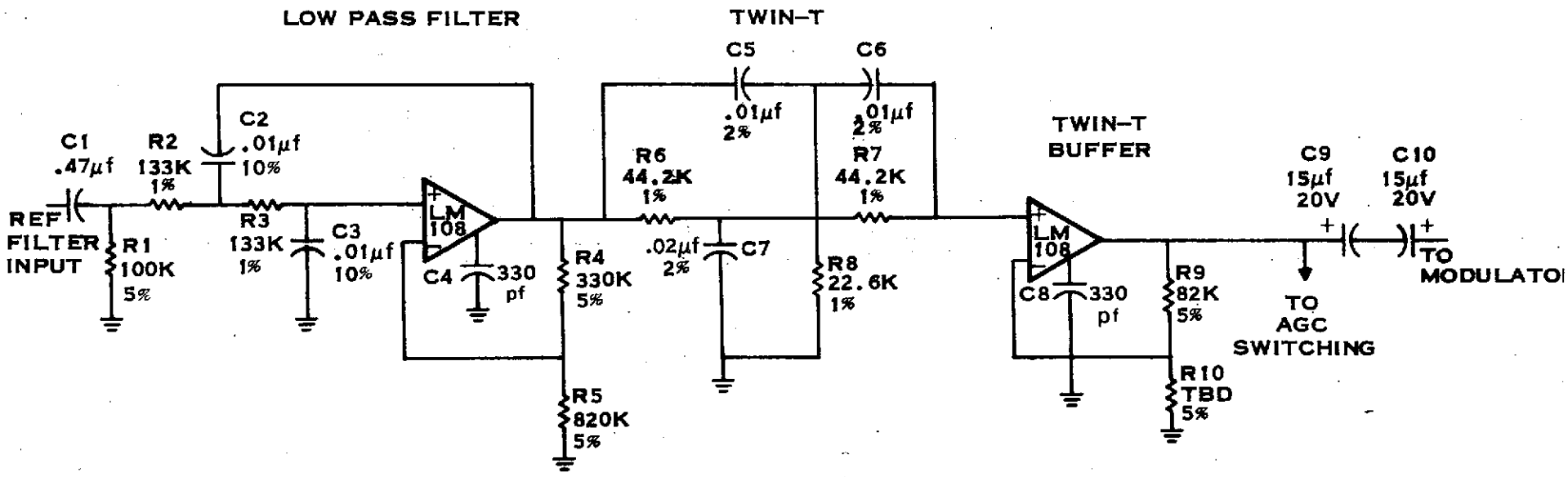

120 HZ REFERENCE FILTER

Figure 2-19

2-22

4. Michelson Mirror Position Control Loop

The Michelson mirror position control loop returns the Michelson mirror to its start position after each forward scan is complete. It is required that the accuracy of this start position be controlled to within ± 8 digital words (≈0.00014 inch). A block diagram description of the position loop was included in the first quarterly report.

During this reporting period detail design has been completed for the Light Emitting Diode (LED) current source, detector preamplifier, buffer amplifiers, synchronous detector and low pass filter. Breadboard testing was accomplished using the Texas Instruments SL 1466 GaAs emitter and a ENL626B silicon detector which was used on the NIMBUS IV IRIS. The ENL626B detector is no longer manufactured but closely matches the ENL PVS010 which will be used in the new design. The emitter and detector were mounted in a split doughnut assembly used in the NIMBUS IV IRIS engineering model. The assembly has a slit aperture in front of the detector and the emitter and is designed so that the slit width can be varied by placing different width shims between the two halves.

Measurements were made to determine the output of the detector as a function of emitter current and aperture width. Results of these measurements shown in Figure 2-20 indicate that over the 5 to 30 ma range, the detector output current is linear with respect to emitter current but non-linear with respect to slit width. The non-linearity with respect to slit width is to be expected since the incident radiant power on the detector is limited by the aperture in front of the emitter and by another aperture in front of the detector.

The selection of current drive and slit width involves a trade-off involving several parameters including carrier frequency, signal-to-noise ratio, amplifier bandwidths and loop sensitivity. As a result of room temperature testing a peak drive current of 30 ma (15 ma average), a two mil slit width (118 digital words) and a 1.8KHz carrier frequency were selected to provide a good signal-to-noise ratio and a high sensitivity without consuming excessive power.

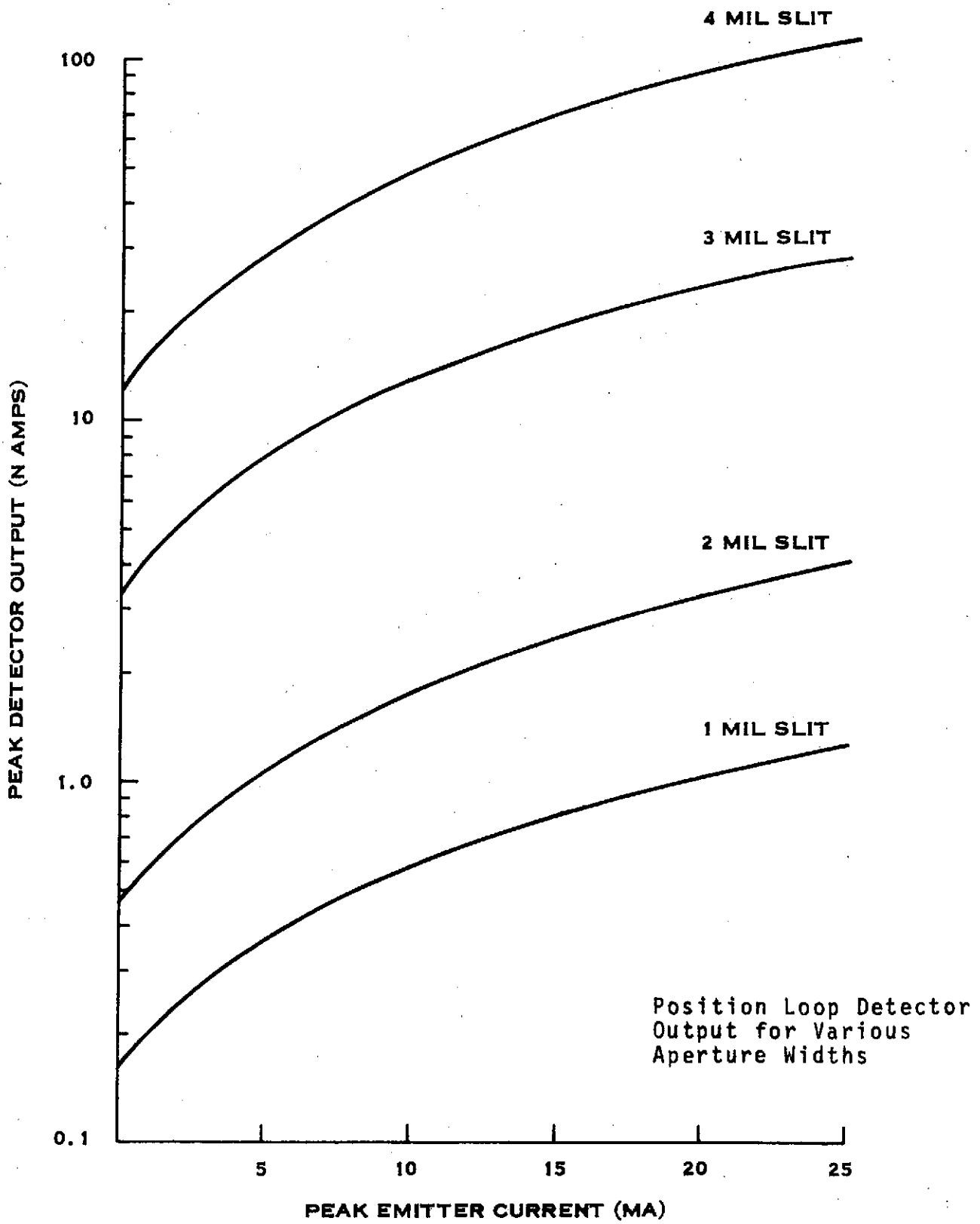
4 MIL SLIT
3 MIL SLIT
2 MIL SLIT
1 MIL SLIT
100
10
1.0
0.1
PEAK DETECTOR OUTPUT (N AMPS)
5
10
15
20
25
PEAK EMITTER CURRENT (MA)
Position Loop Detector
Output for Various
Aperture Widths

Figure 2-20

The 15 ma average emitter current is 7.5% of the rated level which assures negligible degradation in emitter output over the life of the mission. The emitters will be burned-in to eliminate the initial higher rate of change in output as recommended in Goddard Space Flight Center Pacer #08-005.

The two mil slit emitter/detector assembly was cooled to 200°K and the emitter current was varied over the same room temperature range to determine the change in detector output at the expected mission operating temperature. As shown in Figure 2-21 , for a given emitter current the detector output at the 200°K level was approximately 21% greater than the room temperature values. The detector capacitance as measured by the rise time also decreased by 25% at the lower temperature. In order to maintain a constant signal level over temperature the increase in emitter efficiency at 200°K is compensated for by reducing the output of the current source shown in Figure 2-22 . The current source operates from -5VDC so that the anode of the SL 1466 emitter which is electrically connected to the case can be at ground potential. This eliminates any capacitive feed through of the emitter drive signal into the detector amplifier. The output of the current source is controlled by the voltage at the base of Q_1 which is determined by the R_1, R_3, and R_4 resistor network and the emitter resistor R2. At room temperature the thermistor (R4) is approximately 2.25KΩ and the resulting collector current is 2.8 ma; at 200°K the value of R4 increases to a negligible value compared to R3 and the current drops to 24 ma.

The GaAs emitter is switched at a 1.8KHz rate by shunt transistor Q2. Shunt switching of the emitter current was chosen rather than switching the current on-and-off to eliminate the possibility of switching current transients disturbing the other sensitive circuit consisting of Q3, CR1 and CR2.

The PVS010 detector is used in the voltage mode by loading the output with a 487KΩ resistor. This value represents a trade off between output signal level and rise time. The detector signal developed across the load resistor is amplified by a LM108 used in a noninverting mode, which provides 28dB of gain. This is the maximum allowable closed loop gain (for a

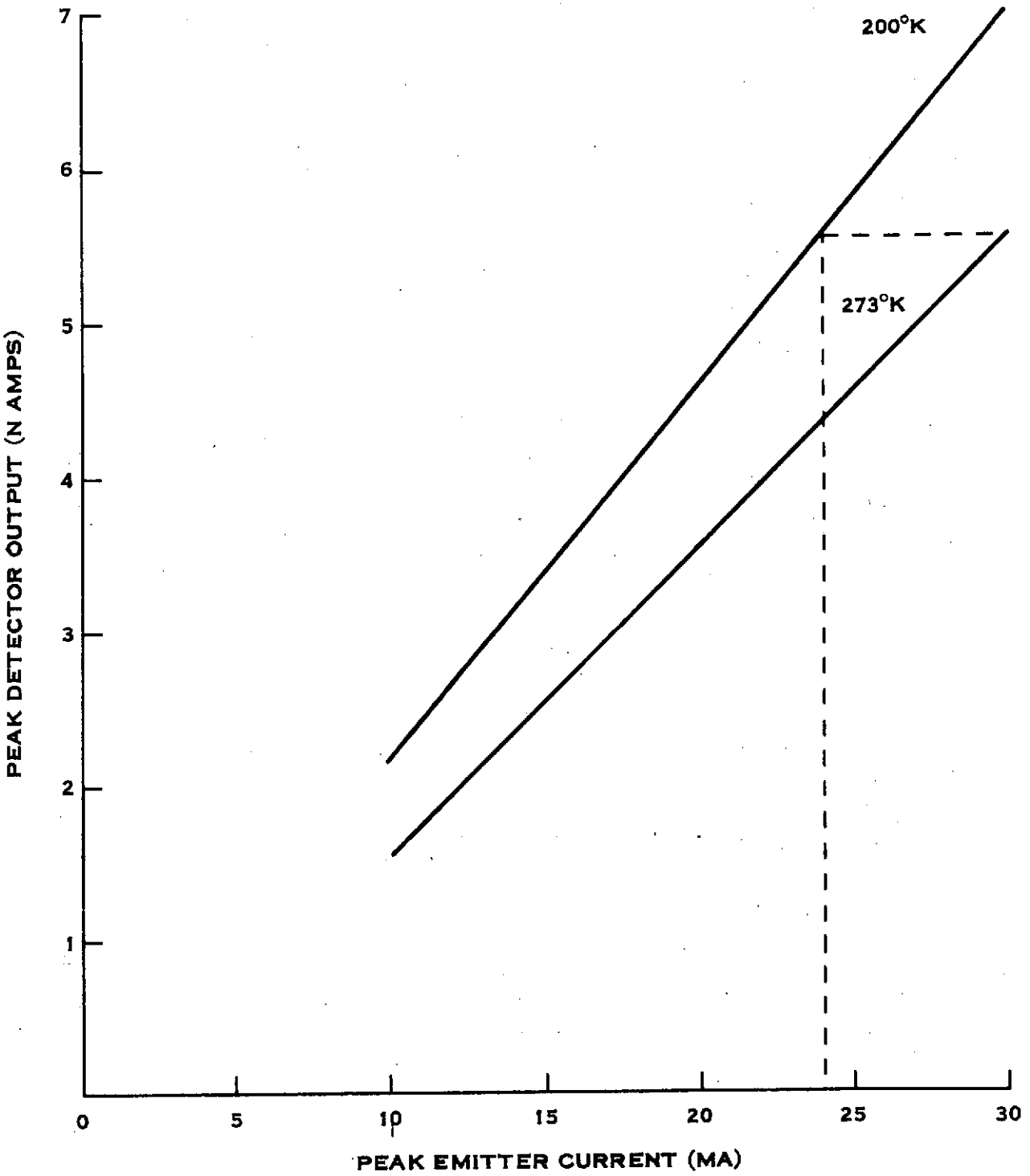

Position Loop Detector Output for Two Temperatures

Figure 2-21

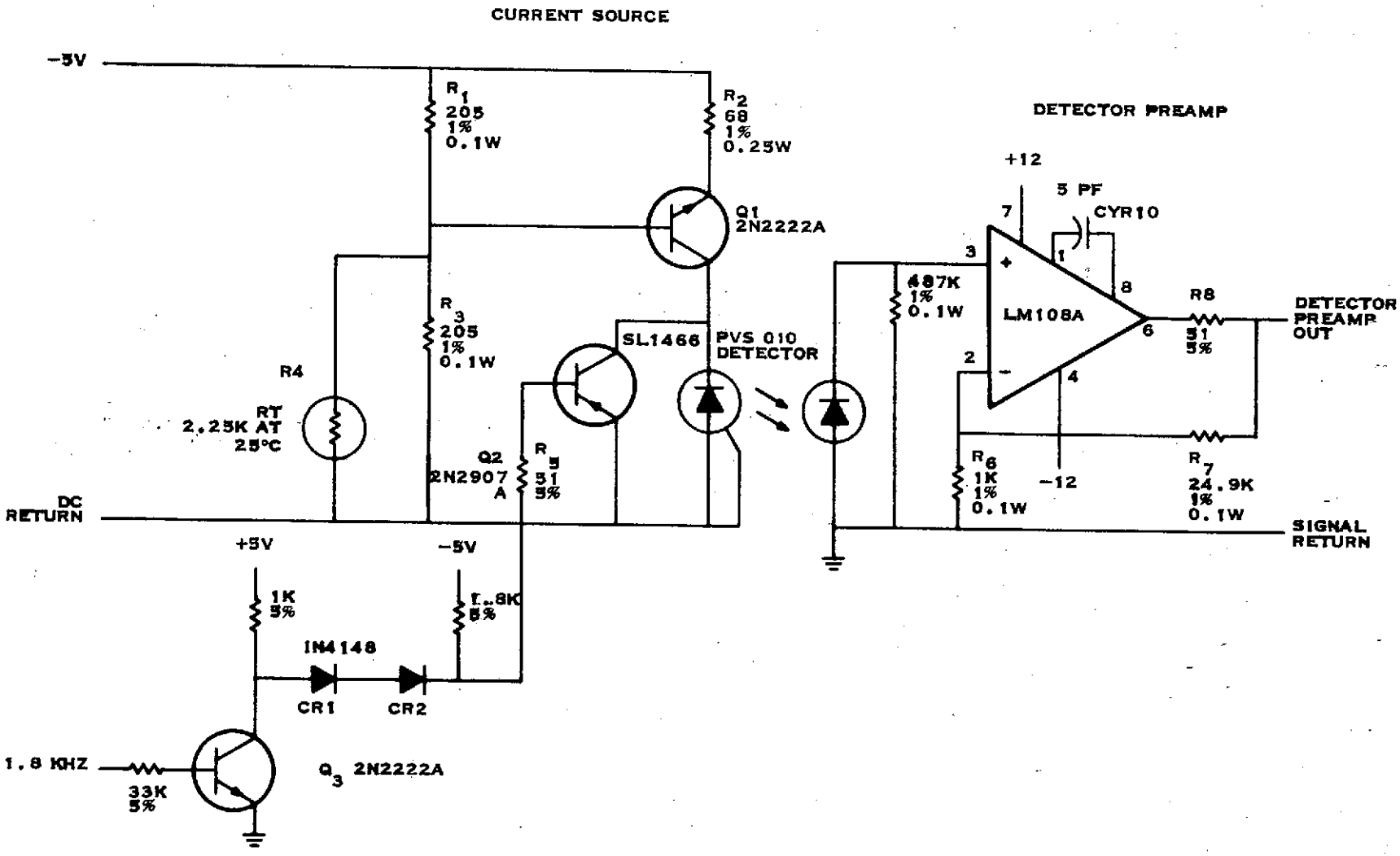

POSITION LOOP EMITTER DRIVER
AND
DETECTOR PREAMPLIFIER

FIGURE 2-22

radiation imposed minimum open loop gain of 80dB) that will insure that the amplifier rise time does not become significant. The signal level at the output of the amplifier is on the order of 50mv pp. To minimize noise pick-up, detector signal ground will be isolated from the DC return carrying the emitter current and the signal will be transmitted to the electronic module by a twisted-shielded pair.

The buffer amplifiers shown in Figure 2-23 located in the electronic module provide an additional 44dB of gain so that the input to the synchronous detector is a 6 vpp square wave when the detector is fully illuminated. The preamp output is ac coupled into the first buffer amplifier which provides 20dB of gain. The second buffer amplifier is a LM101 A with a selectable gain to meet the 6 vpp requirement. Slew rate requirements for the larger output signal make the LM101 A the preferred choice for the second amplifier. The gain of both buffer amplifiers is set to allow for minimum 80dB open loop gain without significantly affecting signal rise times.

The output of the second amplifier is ac coupled to the FET shunt demodulator through a series resistor. The FET gate signal is synchronous with the signal that switches the emitter. The FET drain is clamped to ground during the period when the emitter is off.

The synchronous demodulator is followed by a two pole active low pass filter which reduces the peak carrier frequency ripple to 50dB below the DC level. The low pass filter has a fo = 100Hz with a 0.5 damping ratio. The 50dB reduction in the peak carrier ripple corresponds to 0.5 digital words which compares favorably with the 8 word short term repeatability specification. The demodulator and filter were temperature tested over the extremes of +65°C to -45°C. The demodulator output exhibited a 3% decrease in output from the room temperature level at the two temperature extremes. This change is equivalent to two digital words for a two mil slit.

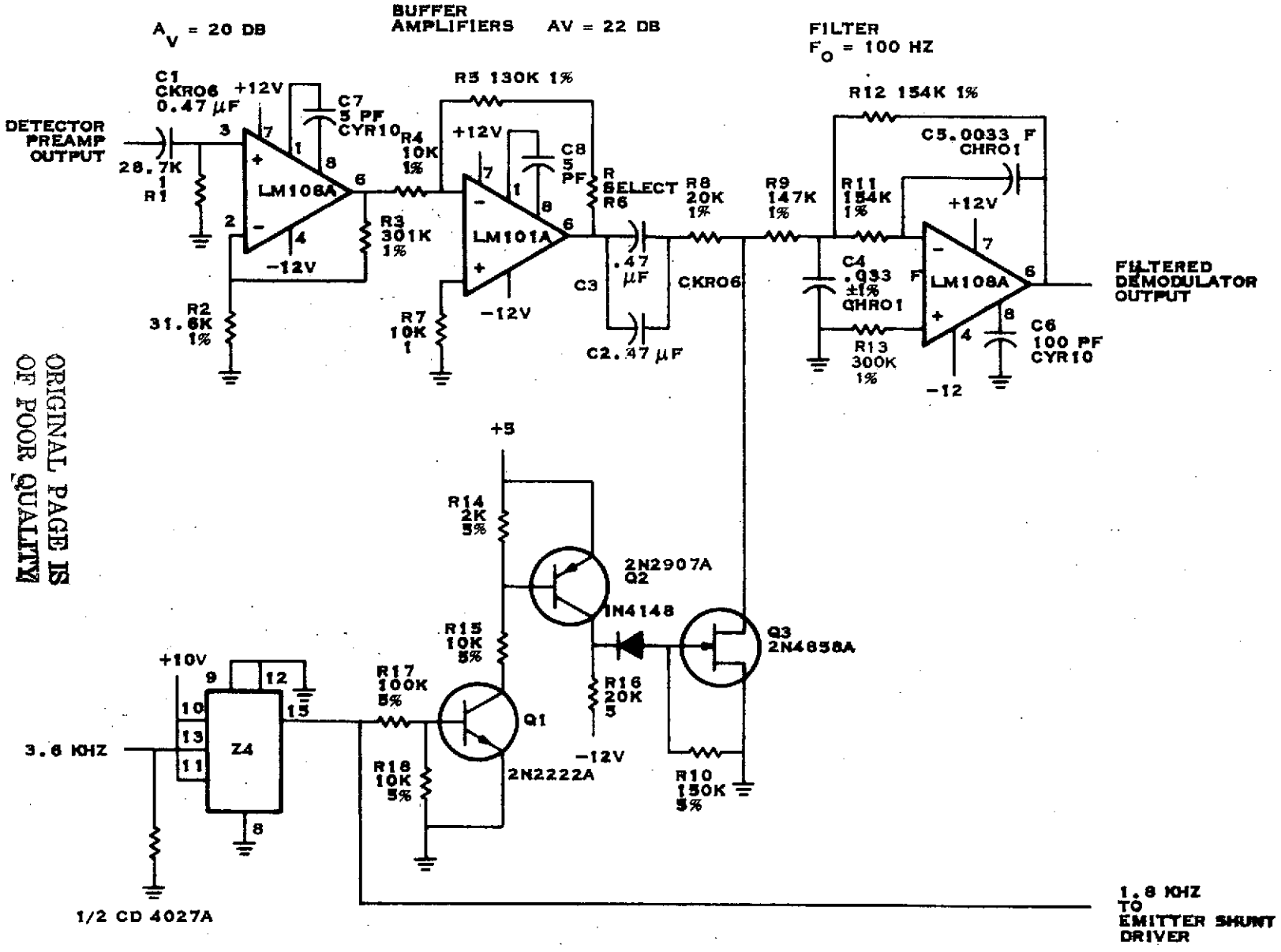

POSITION LOOP BUFFER AMPLIFIER, DEMODULATOR AND FILTER

FIGURE 2-23

5. Programmer and Summation

The logic design of the programmer and summation unit was discussed in detail in the first quarterly report. During the current reporting period, this logic has been breadboarded and checked out. This breadboard logic has been successfully integrated with the housekeeping multiplexer and the analog-to-digital converter (ADC). The schematic diagram of this logic has been completed and has been input to drafting for printed wiring board (PWB) layout.

A test set has been built and used for check out of the breadboard logic. This test set has the capability to test the programmer, summation, delay generator, and HK multiplexer, all of which will be on the same printed circuit board in the Engineering model and flight systems. Thus, the test set will be used to unit test this printed circuit board on all systems.

6. Delay Generator

The major part of the logic not discussed in the first quarterly report is the delay generator circuit. Figure 2-24 shows a block diagram of the delay generator logic. The function of this circuit is to provide a delay of the 120 Hz neon sq. wave signal (IR sampling signal) equal to the delay in the IR data channel circuits. Operation of the delay generator is described below.

The 120 Hz neon sq. wave signal from the neon detection circuit is first shifted through a 6-bit register by the 403.2 KHz clocks. When a transition (either positive or negative) occurs in the 120 Hz neon sq. wave, a positive pulse is generated by the exclusive-or circuit, G1. As shown, one input to G1 is selected from Q_2 through Q_5 of the 6-bit register. This allows for a fine adjustment of the overall delay time to one period of the 403.2 KHz clocks.

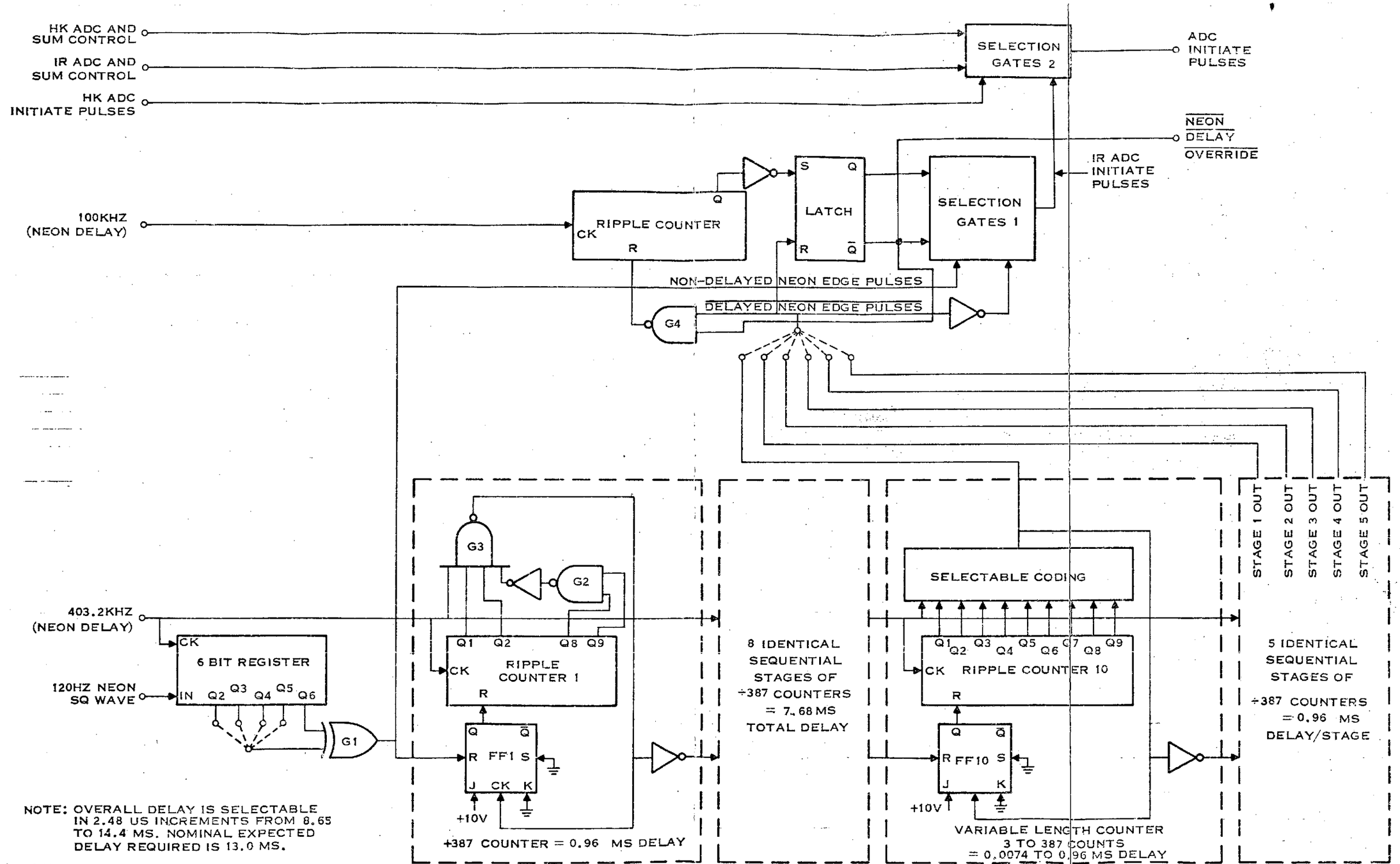

NOTE: OVERALL DELAY IS SELECTABLE IN 2.48 US INCREMENTS FROM 8.65 TO 14.4 MS. NOMINAL EXPECTED DELAY REQUIRED IS 13.0 MS.

MJS iRIS NEON DELAY BLOCK DIAGRAM

FIGURE 2-24

When a pulse occurs out of G1, FF1 is reset which releases the reset on ripple counter 1. Ripple counter 1 is advanced by the 403.2 KHz clocks until gate G3 detects count 383 (a period of 0.96 milliseconds). Gate G3 is inverted and resets FF2 in the next delay stage. Gate G3 also clocks FF1 back to the set state, which in turn resets ripple counter 1. It should be noted that all the counter stages (including the variable length counter in stage 10) are gated so that their count ends with Q_1 and Q_2 high. This allows time for ripple delays in the counter to settle before the final count is detected. It is because of this inability to selectively program Q_1 and Q_2 that programming of G1 off the 6-bit register is necessary.

Each counter stage in turn initiates the next counter stage at the end of its count. The overall delay circuit is in effect a series of sequential digital one-shots. As shown, the 10th counter stage is selectable from 3 to 387 counts and allows adjustment of the overall delay to within 4 periods of the 403.2 KHz clock. The next 5 stages are selectable through terminals and form a coarse adjustment (in increments of 0.96 milliseconds) of the overall delay to be adjusted in 2.48 microsecond increments from 8.65 to 14.4 milliseconds.

Several stages (as opposed to one long counter) are required because the amount of delay (approximately 13 milliseconds) is longer than the period (4.16 milliseconds) between neon transitions. Hence, a single stage counter would cause transitions to be missed. In addition, the length of each counter stage needs to actually be much shorter than the normal transition period to allow for the possibility of vibration induced motion in the interferometer. The maximum counter length of 0.96 milliseconds will allow for a greater than 4 to 1 compression of the neon transitions due to vibration before a transition edge will be missed. Also, the fact that the first counter stage will not respond to a second pulse out of G1 until its period of 0.96 milliseconds is completed, will act to filter out any noise spikes that might occur on a neon transition edge.

Figure 2-24 also shows a 12 stage ripple counter clocked by a 100 KHz signal. Normally the ripple counter is reset through gate G4 by the Delayed Neon Edge Pulses. If these pulses should stop because of a failure in some stage of the neon delay, ripple counter 16 would toggle Q_{12} to a logic "1" approximately 20.5 milliseconds following its last reset pulse. If Q_{12} becomes a logic "1" the latch is set, which allows the output of G1 (undelayed neon signal transitions) to be selected as the IR ADC initiate pulse, providing a back up for the delayed neon pulses. When the latch is set, it immediately resets the ripple counter through G4. This sets Q_{12} to "0" so that any Delay Neon Edge Pulse will be free to reset the latch.

The second set of selection gates are used to route the HK ADC Initiate Pulses to the ADC during HK channel times and to route the IR ADC Initiate Pulses to the ADC during the IR interferogram time.

7. Radiometer Channel Electronics

A block diagram of the radiometer electronics is shown in Figure 2-25 . The diagram is the same as that presented in the First Quarterly Report except in two respects. For one, the FDS interface for the low gain output to FDS has been moved out of the closed loop. Secondly, the DC amplifier and low-pass filter have been replaced by a double integrator. The descriptions of all other blocks are the same now as they were in the first report. (Note - the term "$f_c/2$" was inadvertently used for the Nyquist frequency in the first report. It should have been "$f_s/2$".)

a. AC Preamplifier

The current design of the AC preamp is shown in Figure 2-26 . Its gain at the 480 Hz chopping frequency (f_c) is 50 dB. Gain at DC has been lowered to 40 dB to reduce the possibility of saturation due to offset voltages. The frequency response includes a zero at 3.7 Hz and poles at 12 Hz and 1420 Hz ($\simeq 3\ f_c$). Dual FET Q_1 is the moderately low noise, high impedance, differential input stage. Since the common mode switching spikes will be much larger than the signals they accompany at the inputs, it is crucial for this stage to have very high common mode rejection. Current source Q_2/R_6 and the use of 0.1% resistors for the primary source and drain resistors of Q_1 help achieve the high CMRR.

b. AC Amplifier

The present AC amplifier design is shown in Figure 2-27 Its gain at f_c is 45 dB. Gain at DC (from E_1) has been lowered to 6 dB to reduce the undesired demodulator output f_c. Nulling of the AR_1 offset voltage also reduces this component. The frequency response includes zeros at 0 Hz, 0.8 Hz, and 51 KHz. There are two poles in the frequency response at 80 Hz ($=f_c/6$) and one

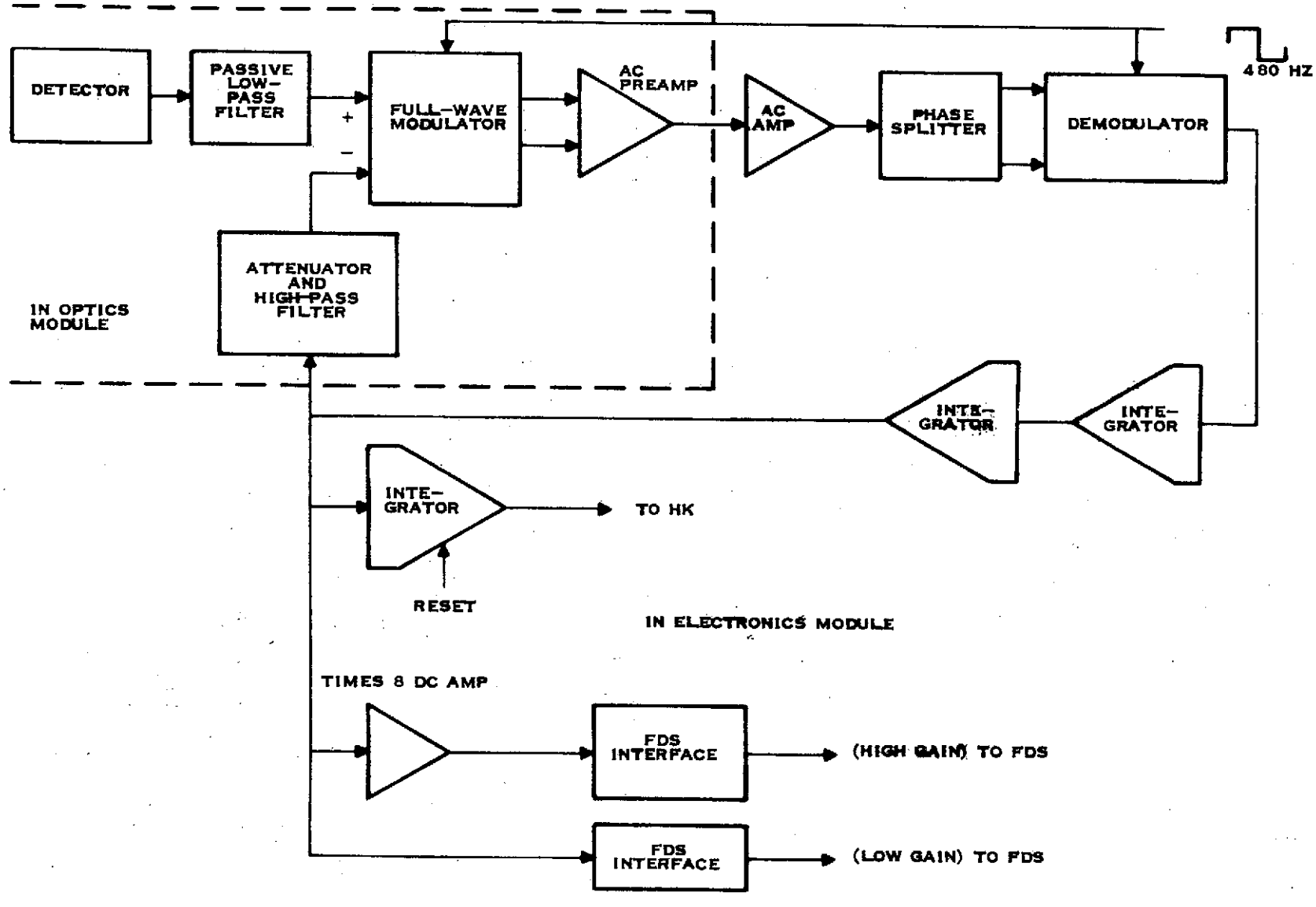

RADIOMETER CHANNEL BLOCK DIAGRAM

Figure 2-25

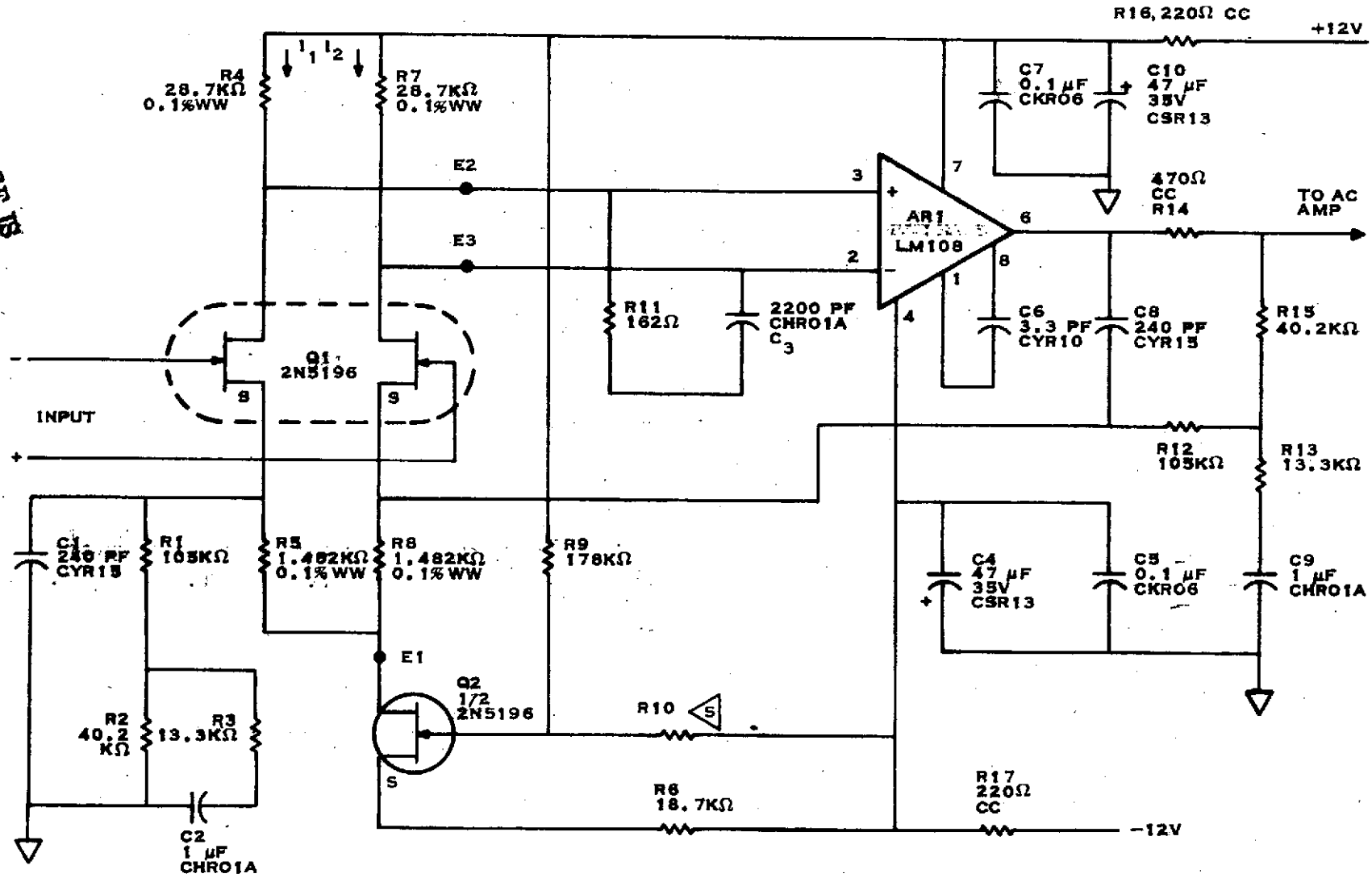

RADIOMETER PREAMPLIFIER

FIGURE 2-26

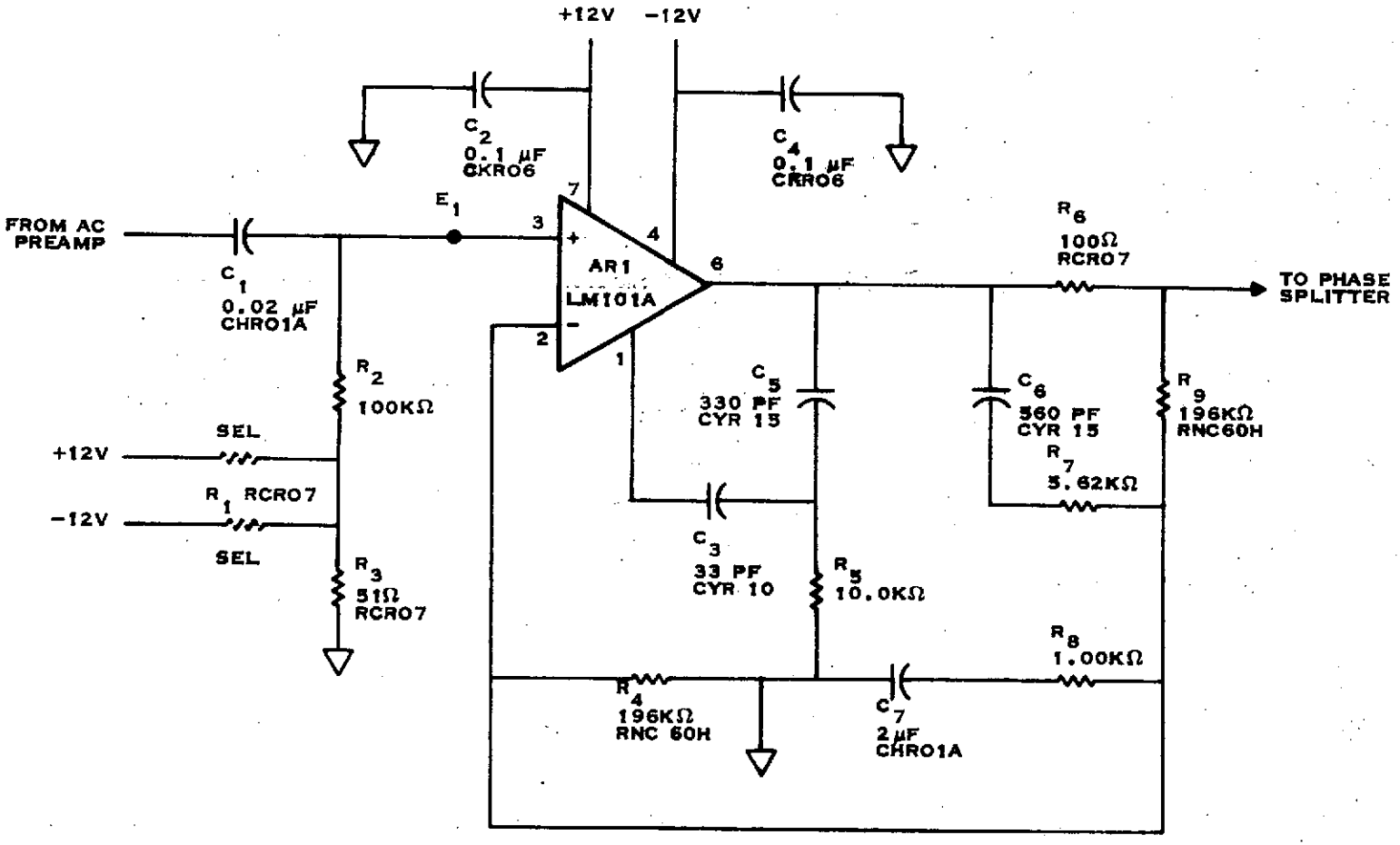

RADIOMETER AC AMPLIFIER

FIGURE 2-27

at 1410 Hz ($\simeq 3\ f_c$). The zero at 51kHz (a pole in the feedback) is used only to cancel out a zero in the op amp response for closed loop stability. "Two pole" op amp compensation is used to ensure good closed loop gain stability through $f = 3\ f_c$ by providing a loop gain $\geq$ 20 dB at this frequency.

c. Phase Splitter

The phase splitter has a non-inverted output hard-wired from the input and an inverted output produced by a unity gain inverting amplifier. The circuit is shown in Figure 2-28 . The amplifier offset is nulled to reduce offset at the demodulator output. Amplifier gain is held accurately to -1 by using 0.1% resistors for R_2 and R_5. This reduces demodulator output at f_c.

d. Double Integrator

The double integrator used in place of the DC amp and low-pass filter will provide better gain accuracy of the closed loop near DC. Its preliminary circuit design is shown in Figure 2-29 The gain of the circuit is basically,

$$\frac{X_{C_4}}{R_2} \quad \frac{X_{C_8}}{R_6}$$

Effective offset voltage is critical but only at the input of the first integrator. Resistors R_3 and R_7 are for op amp protection.

e. FDS Interface, Low Gain

The purpose of relocating this FDS interface was to assure that if FDS shorts this output, it will not automatically short the other two radiometer outputs.

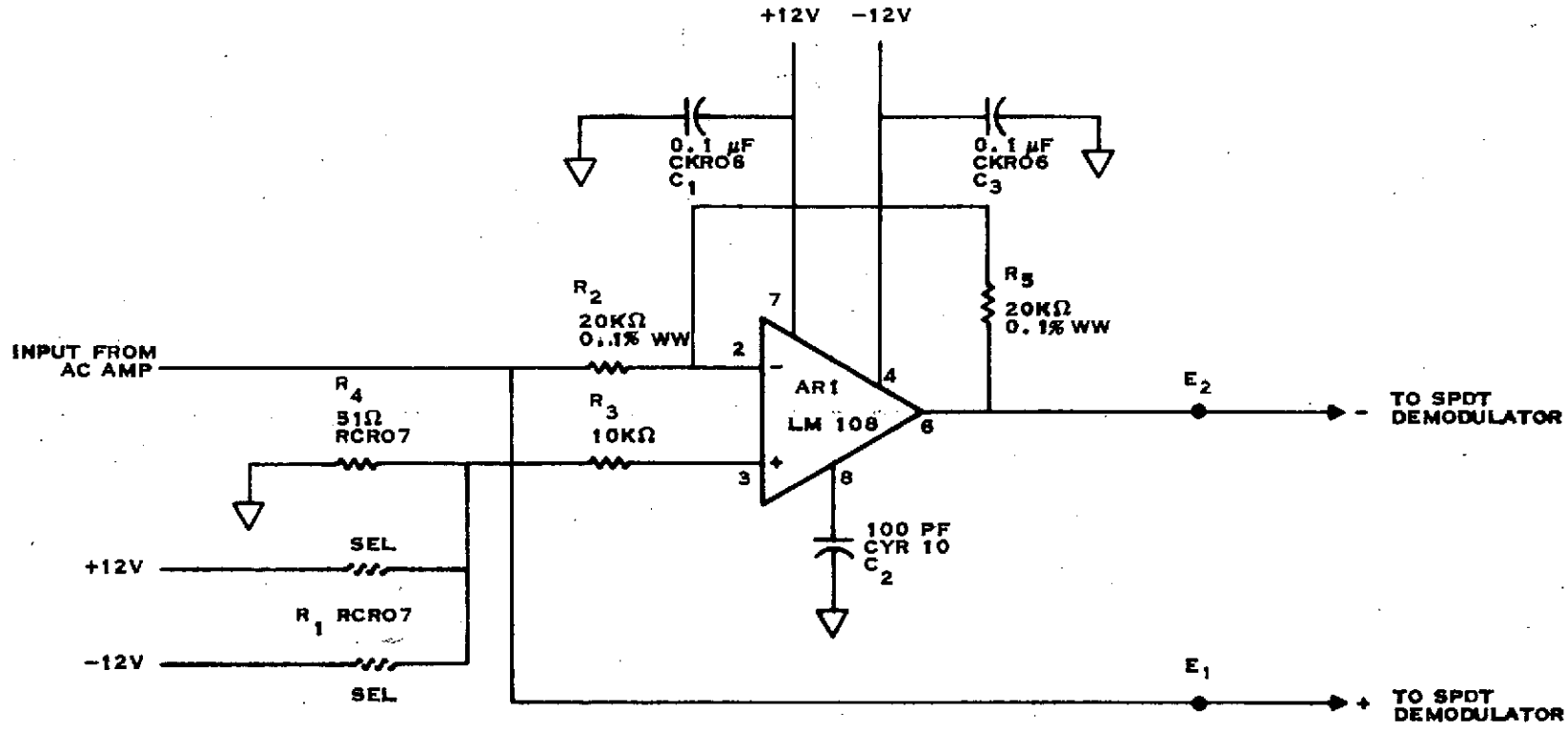

RADIOMETER PHASE SPLITTER
FIGURE 2-28

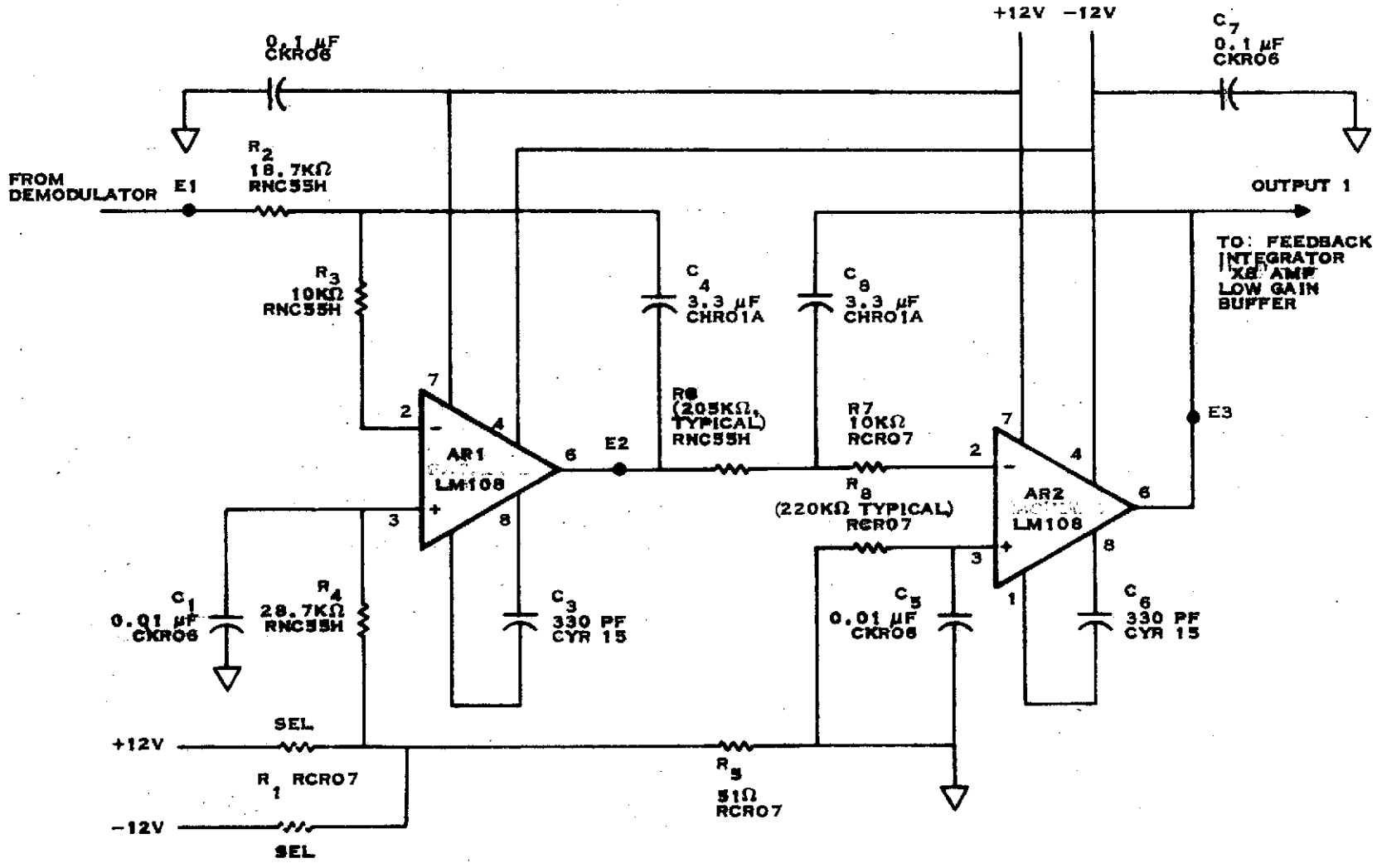

RADIOMETER DOUBLE INTEGRATOR

FIGURE 2-29

f. X 8 Amplifier

A simplified circuit is shown in Figure 2-30 for the amplifier used for the high gain output. Since gain accuracy is very important, 0.1% resistors are used for R_1 and R_5. Capacitor C3 is used to roll off the response above the channel bandwidth. In the final design, an offset nulling circuit will probably be added.

g. Integrator

The radiometer integrator design is shown in Figure 2-31 The integrator output voltage is,

$$V_o = - \frac{1}{2.787 M\Omega \times 9.9\ \mu F} \int_0^t V_i\ dt$$

The dual FET input stage is used in a source follower configuration due to the high impedances needed. The resetting switch JFET is protected from excessive current by a 470Ω resistor. In the final design, an offset nulling circuit will probably be added and a 2N4858 may be subsituted as the resetting switch.

h. Modulator

The design in the radiometer area which remains to be completed is the modulator circuitry. Design is in process on this item and will be discussed in the next quarterly report.

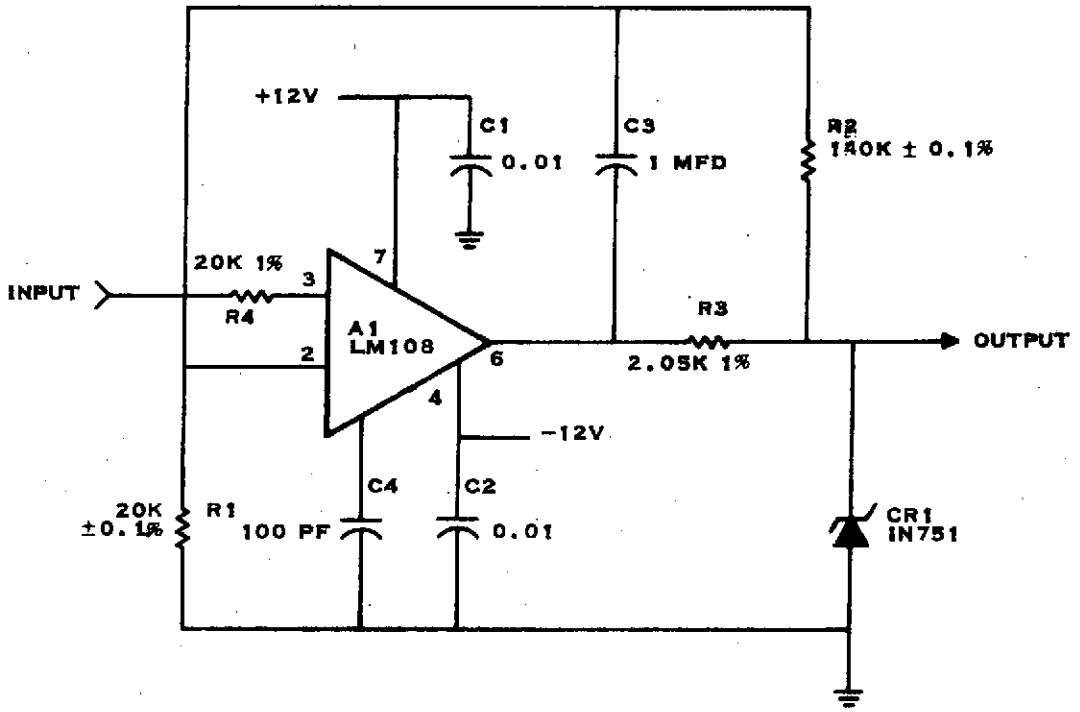

RADIOMETER X8 AMPLIFIER

FIGURE 2-30

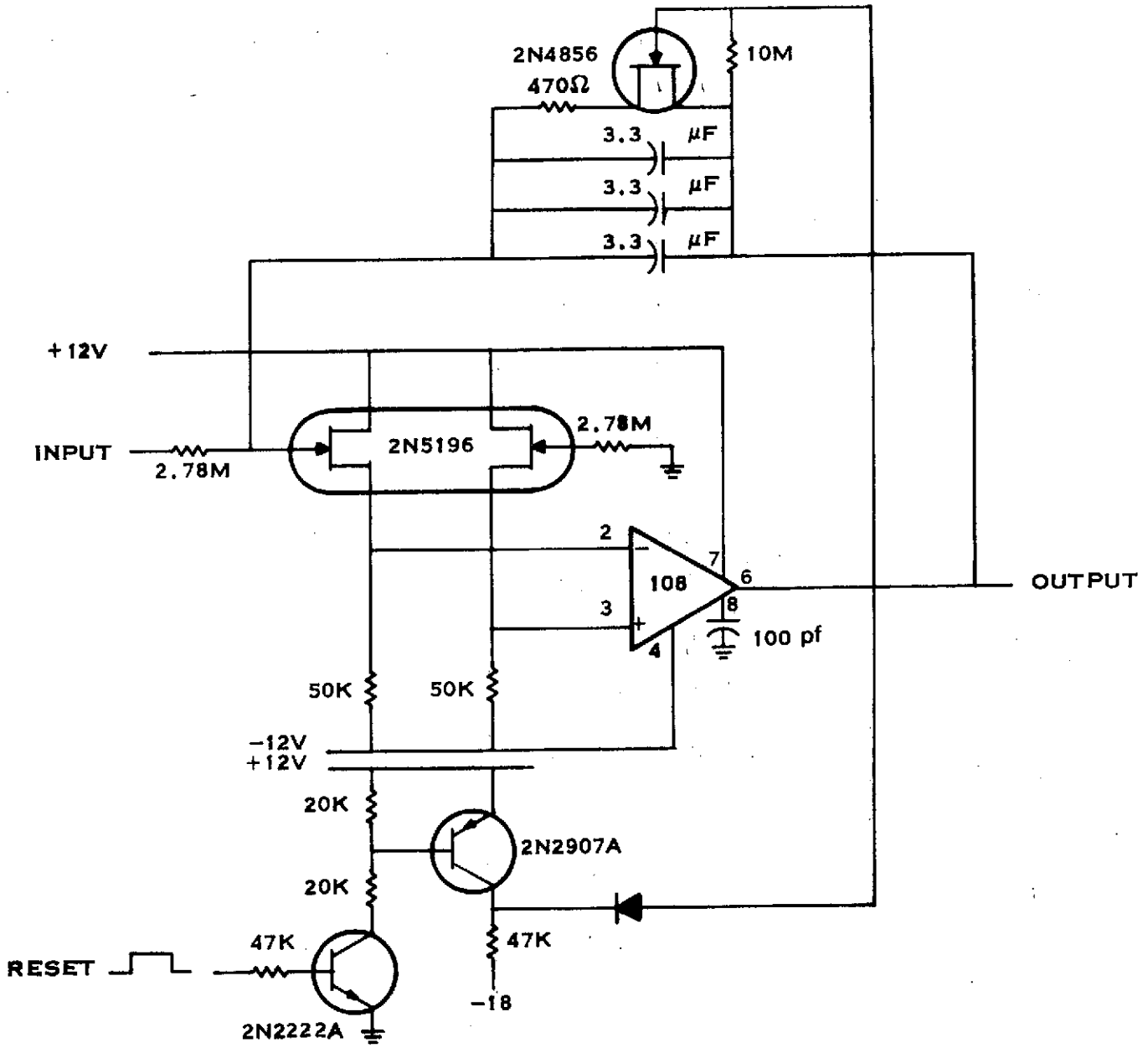

PRELIMINARY

INTEGRATOR, RADIOMETER CHANNEL

Figure 2-31

8. Power Supply

A detailed description of the power supply design was presented in the First Quarterly Report. During this reporting period the power supplies, including final transformer designs, have been breadboarded and successfully tested. Tables 2-3 and 2-4 summarize the measured test data.

The current limiter shown in Figure 2-32 has also been built and tested. The design requirement for turn-on surge limit from MJS 77-3-100 reads as follows: "Any change, including subsystem turn-on, shall not cause the peak power to exceed the subsequent steady state power by more than 25 W." The maximum allowable steady state primary power is specified at 13.7 watts. The total allowable peak surge power is then 13.7 + 25 = 38.7 W.

The current limiter is designed to limit turn-on surges to a maximum of 30 watts, or roughly 78% of the allowable. Photograph #1 of Figure 2-33 displays the measured primary power turn-on surge. The DC wave form shown is the power supply +10V output which is used as the voltage control source of the limiter. The magnitude of the turn-on surge is a function of the time constant controlled by R and C1 of Figure 2-32. Figure 2-34 illustrates this relationship.

Photograph #2 of Figure 2-33 displays the magnitude of the primary power supply turn-on surge without the limiter. As can be seen, the peak surge without limiting is roughly 1090% or 175 watts. While this is approximately 4.5 times allowable, its duration is extremely short. In fact, after 200 nano-seconds, the turn-on transient has decayed to a value well within specified levels.

The trade-off in question is summarized in Table 2-5. If the occasional turn-on surges without a limiter can be supplied by the spacecraft power subsystem and capacitor banks, three benefits can be derived. The instrument budgets could be reduced by 60 grams and 0.425 watts. Of greater importance to the scientific objectives of the instrument is the increased reliability. Deleting the current limiter eliminates ten components. The elimination of these components adds significantly to the overall instrument reliability since they are in effect in series with the power input. It has not been uncommon in

TABLE 2-3 MEASURED PERFORMANCE OF POWER SUPPLY

INPUT VOLTAGE: 2.4 KHz, 50.0 V_{RMS}

t_{rise} and t_{fall} = 4.0 µsec

INPUT CURRENT: 322 MA RMS

INPUT POWER: 16.1 Watts

OUTPUTS:

19.5V	@ 162.6 MA =	3.172 Watts	(270 mv Ripple)
-19.71V	@ 164.2 MA =	3.237 Watts	(200 mv Ripple)
+ 9.71V	@ 81 MA =	0.79 Watts	(100 mv Ripple)
+ 4.98V	@ 50 MA =	0.249 Watts	(60 mv Ripple)
- 4.97V	@ 50 MA =	0.249 Watts	(60 mv Ripple)
+158.8V	@ 4.8 MA =	0.762 Watts	(500 mv Ripple)
-17.53V	@ 78.6 MA =	1.38 Watts	(300 mv Ripple)
+12V	@120 MA =	1.44 Watts	(<5 mv Ripple)
-12V	@120 MA =	1.44 Watts	(<5 mv Ripple)
TOTAL OUTPUT PWR		12.705 Watts	

EFFICIENCY: = $\frac{12.705}{16.1}$ x 100 = 78.9%

± 12 Volt Line Regulation: ΔV_{out} < 1 mv for inputs from 47.4 to 55 volts RMS ▷

Power Factor: > 0.99 Lagging

Notes:

▷ ± 12 volt regulators drop out of regulation when input drops below 46.65 V_{RMS}

TABLE 2-4

MEASURED STANDBY POWER SUPPLY DATA

INPUT VOLTAGE:	50.0 V RMS
OUTPUT VOLTAGE:	23.23 @ 410 MA
OUTPUT RIPPLE:	200 mv Maximum
EFFICIENCY:	90%
OUTPUT REGULATION: (NO LOAD TO FULL LOAD)	21%

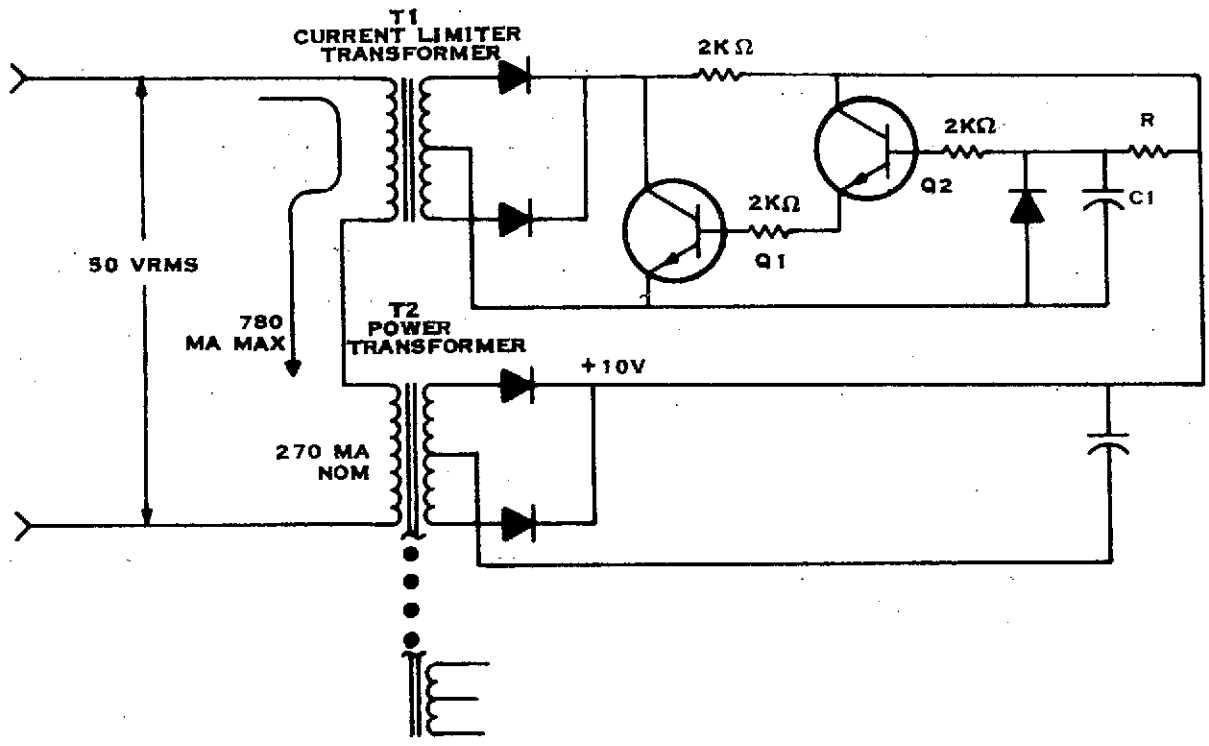

CURRENT LIMITER

Figure 2-32

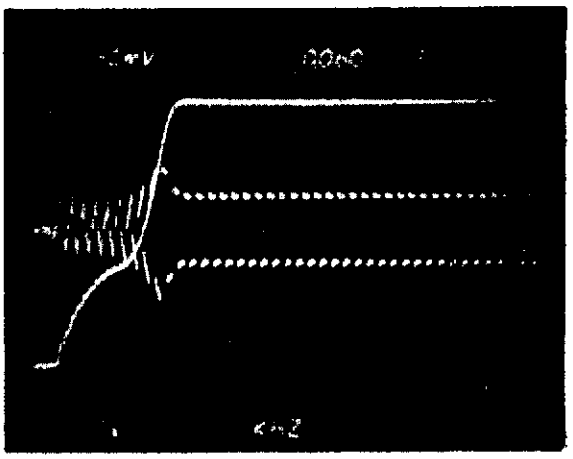

PHOTOGRAPH NO. 1

DESIGN TURN-ON SURGE
C = 1 μF
CURVE 1
VERT SCALE = 0.5 AMP/DIV
HORZ SCALE = 2 mSEC/DIV
CURVE 2 – +10V DC OUTPUT OF
POWER SUPPLY

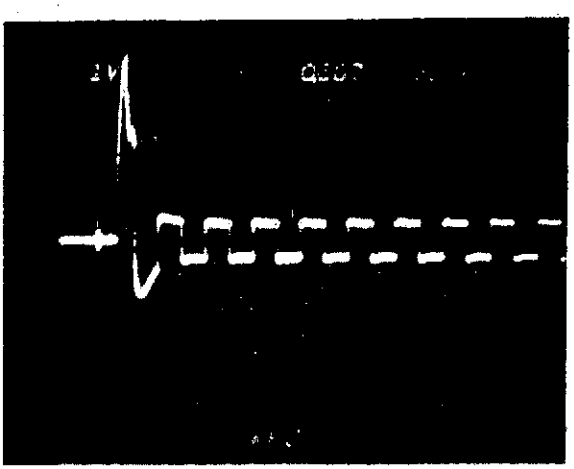

PHOTOGRAPH NO. 2

TURN-ON SURGE WITHOUT LIMITER
VERT SCALE = 1 AMP/DIV
HORZ SCALE = 0.5 μSEC/DIV

Current Limiter Performance
Figure 2-33

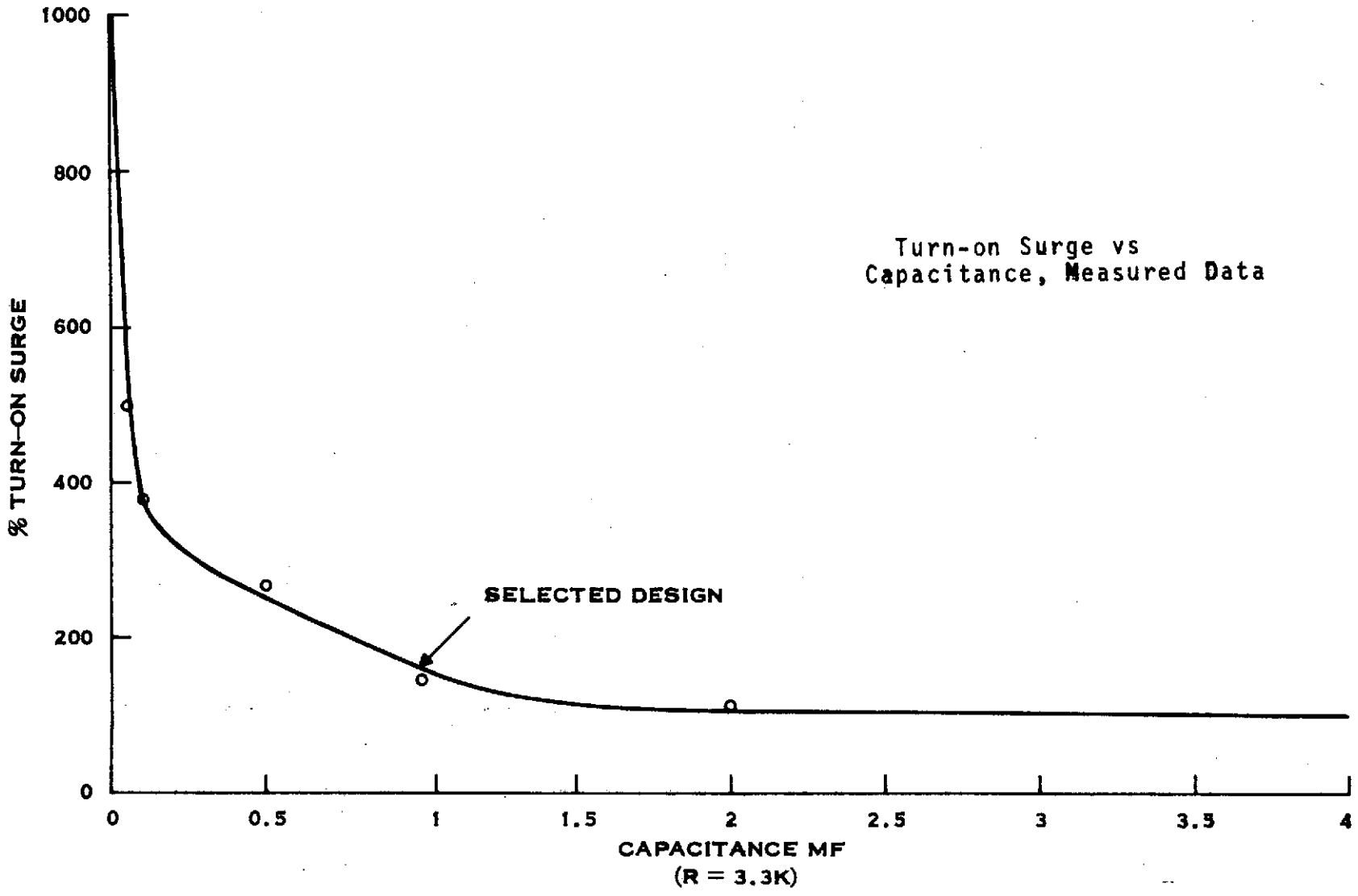
Turn-on Surge vs
Capacitance, Measured Data
% TURN-ON SURGE
1000
800
600
400
200
0
SELECTED DESIGN
0
0.5
1
1.5
2
2.5
3
3.5
4
CAPACITANCE MF
(R = 3.3K)

Figure 2-34

TABLE 2-5 TURN-ON SURGE CURRENT LIMITER TRADEOFF

PARAMETER	WITH CURRENT LIMITING	WITHOUT CURRENT LIMITING
MEET DESIGN REQUIREMENTS	YES	NO
RATIO TURN-ON SURGE AVERAGE CURRENT	200%	1090%
WEIGHT	60 GRAM	0
POWER LOSS*	425 MW	0
*AT 13.7 WATTS INPUT TO INSTRUMENT		
PARTS COUNT	+10	0

the past to provide parallel power inputs just to avoid this type of failure mode.

For the present, it is planned to include a current limiter in the engineering model power supply. Should it be decided in the future to eliminate the limiter, it would be a relatively simple task to modify the hardware accordingly. The converse would be a great deal more difficult.

Texas Instruments most current estimate of the power requirements for the MJS-IRIS subsystem is shown in Table 2-6.

This table indicates an average 2.4 KHz power of 19.29 watts and a peak 2.4 KHz power of 24.6 watts. The power baseline as established by the Statement of Work plus the quoted power increase due to radiation is 19.05 watts average and 24.7 watts peak.

TABLE 2-6

MJS'77 IRIS POWER ESTIMATE (WATTS)[1]

1.	PRIMARY POWER		
	A.	OPTICS	
		1. NEON SOURCE	0.310
		2. NEON DETECTOR PREAMPLIFIER	0.080
		3. INTERFEROMETER DETECTOR PREAMPLIFIER	0.250
		4. VELOCITY AMPLIFIER	0.150
		5. RADIOMETER PREAMPLIFIER	0.150
		6. MICHELSON MOTOR	0.200[2]
		7. POSITION SENSOR	0.200
		OPTICS TOTAL	1.340
	B.	ELECTRONICS	
		1. PHASE LOCK LOOP	4.000[3]
		2. ADC	0.600
		3. PROGRAMMER	0.260
		4. DATA CHANNELS	0.990
		5. INTERFACE CIRCUITS	0.090
		6. MULTIPLEXERS	1.100
		7. VOLTAGE REGULATORS	1.100
		8. SUMMATION	0.200
		9. POSITION LOOP	0.670
		ELECTRONICS TOTAL	9.010
	C.	POWER SUPPLY	
		1. TRANSFORMER LOSSES	1.300
		2. RECTIFIER LOSSES	0.550
		3. CURRENT LIMITER	0.500
		POWER SUPPLY TOTAL	2.350
	D.	CONTINGENCY	2.000

AVERAGE 2.4 KHz PRIMARY POWER = 14.7 WATTS

PEAK 2.4 KHz PRIMARY POWER = 16.3 WATTS

TABLE 2-6 (CON't)

MJS'77 IRIS POWER ESTIMATE (WATTS) (CON'T)

II.	STANDBY POWER[4]		
	A.	ELECTRONICS	
		1. CONTROLLERS	0.50
		2. HEATERS	3.35 (6.7 WATTS PEAK[5])
	B.	POWER SUPPLY	
		1. TRANSFORMER LOSSES	.54 (.80 WATTS PEAK[5])
		2. RECTIFIER LOSSES	0.20 (0.30 WATTS PEAK[5])
	AVERAGE STANDBY POWER = 4.59 WATTS		
	PESSIMISTIC PEAK = 8.30 WATTS[5]		
III	TOTAL 2.4 KHz AVERAGE POWER = 19.29 WATTS[6]		
	2.4 KHz PEAK POWER = 24.6 WATTS		

NOTES:

1. INCLUDES RADIATION IMPACT
2. 1.08 WATTS PEAK
3. 4.9 WATTS PEAK
4. ASSUMES THREE PROPORTIONAL TEMPERATURE CONTROLLERS WITH CONTROLLING DEVICES ON CONTROLLED SURFACE
5. BASED UPON A WORST CASE ESTIMATE OF 6.7 WATTS HEATER POWER CAPABILITY INCLUDING 1.5 WATT DESIGN MARGIN
6. BASELINE POWER IS 19.05 WATTS AVERAGE AND 24.7 WATTS PEAK.

9. Bench Checkout Equipment

The three MJS IRIS Bench Checkout Equipment consoles (BCE) will consist of a single bay rack similar to the MM'71 BCE. Two of the consoles are modifications of existing hardware. The third console will be rebuilt using the cabinet and blower assembly that was not required by the IRIS A/O program. Figure 2-35 shows a BCE rack layout and Figure 2-36 is a block diagram of the BCE.

The logic drawer for BCE #1 is complete. The original wiring was removed and the drawer rewired for the MJS timing. The timing logic, word and clock decoders, the input shift register, housekeeping register, HK status register, and the D/A register is contained in the logic drawer. The logic drawer has self check circuitry similar to that used in the Balloon Flight BCE. The mechanical portions of the drawer assembly have been utilized with a modification to the front panel to incorporate the self check switches.

The control drawer contains the displays and switches that reflect the instrument status, lamp drivers, and a D/A converter. A modular A/D converter replaces the old pulsewidth-to-analog circuitry for FDS analog monitoring. A partial logic panel is being installed in the control drawer to carry the A/D converter and additional circuitry required for the MJS system. The existing lamp driver and D/A circuit board assemblies will be used. The control drawer front panel has been replaced due to display function and switch groupings as seen in Figure 2-37 . A key lock switch has been added to lock out the REPLACEMENT and FLASHOFF heater functions during room temperature testing to prevent damage to the IRIS instrument.

Two additional relays have been installed in the AC power control assembly for switching of the standby power, primary power, and heater power to the instrument.

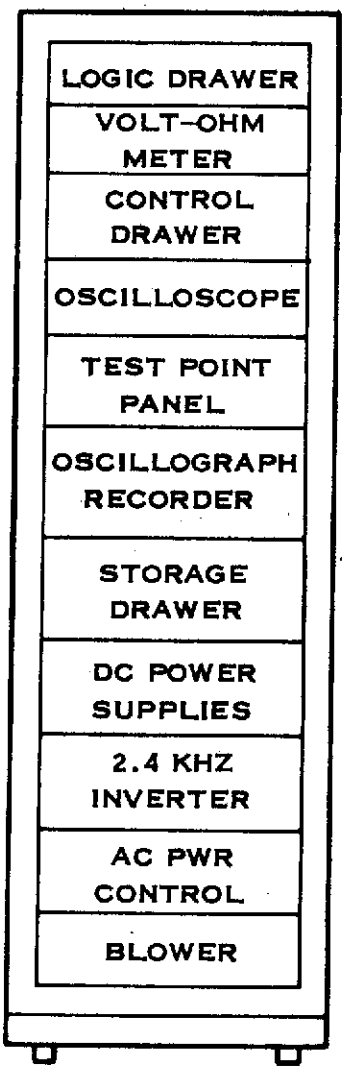

BENCH CHECKOUT EQUIPMENT (BCE)

Figure 2-35

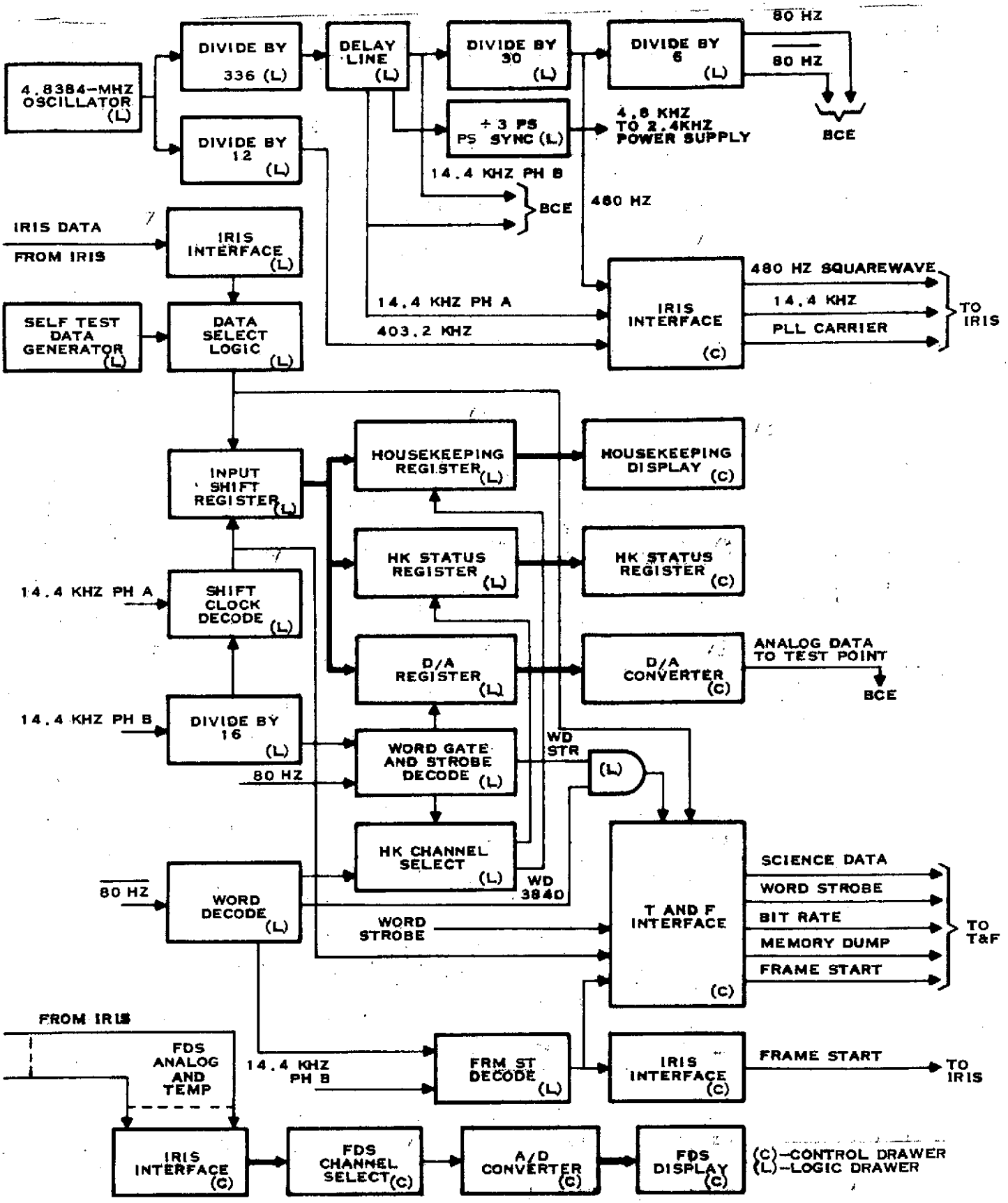

BCE BLOCK DIAGRAM

Figure 2-36

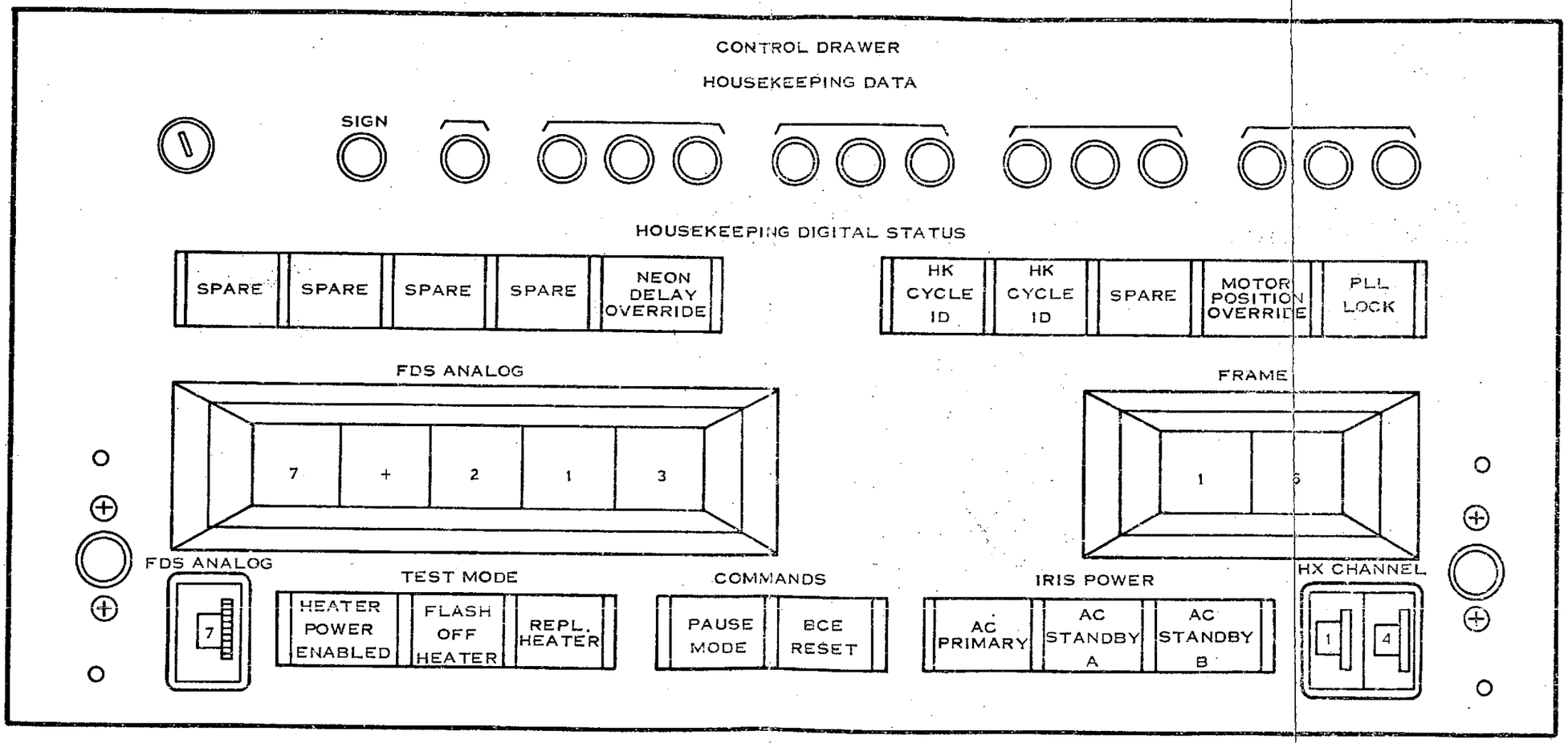

CONTROL DRAWER PANEL
FIGURE 2-37

A

B

Only two of the eleven cables internal to the console are being modified. The external cables from the BCE to the flight adapters are being rebuilt.

The oscilloscope and digital multimeter for one of the consoles will deviate from the models used in the other two consoles. A nonstorage oscilloscope will be used. The digital multimeter will be a DANA instrument similar to the model in the other two consoles as the original model is no longer being built.

B. Opto-Mechanical Design

1. GENERAL

During the second quarter, the MJS IRIS mechanical design has matured considerably in several areas. Generally, all mechanical parts which are critical (for optical or structural reasons, or because of machining complexity) have reached the detailed piece-parts drawing stage.

The following discussion addresses some of the activities pursued during the reporting period:

- Michelson Motor: All piece parts for the prototype have been fabricated. Delivery of the SmCo magnets is the pacing event in this area.

- Nickel Coating Tests: Sample beams of beryllium with low-stress nickel coatings have been subjected to vibration testing, and thermally-cycled between room temperature and 77° Kelvin. No damage is visible at 360 X magnification. Further testing and evaluation is planned.

- Telescope: The major technical consideration remaining in this area concerns the primary mirror optical coating. Applied Optics Center contends that aluminum/SiO coatings are not compatible with low-scatter mirror surfaces, due to the surface preparations needed to assure adhesion. AOC's recommendation is to use a gold overcoat, which in their experience will result in a low-scatter surface of sufficient durability that it can be cleaned without damage.

- Calibration Mirror: Optical design has been completed. A preliminary concept for mounting this mirror to the circular fin in front of the primary mirror has been developed.

- Other Beryllium Parts: 22 parts (mirrors, detector mounts, adjustment wedges, motor shaft, and interferometer optics housing) have been detailed and are out for quotations.

- Computer-Aided Study: During the quarter, the process of combining the various individual computer models (stress/vibration, PLL, Michelson Motor) into a system model was started.

2. Optical Design

a. Design Goals and Optical Methods for Achieving Design Goals

The Infrared Interferometer Spectrometer and Radiometer (IRIS) instrument for the Mariner Jupiter-Saturn (MJS) 1977 space mission is in fundamental concept an optical instrument. The purpose of IRIS is to gather "raw" light flux data in the wavelength band 0.3 to 2.0 μm and to obtain quantitative spectral data in the wavelength band 2.5 to 50.0 μm. To achieve these objectives, IRIS is basically two instruments in one: an energy-collecting optic and detector to gather short wavelength flux data (radiometer) and a Michelson interferometer spectrometer to obtain long wavelength spectral data. In addition, the IRIS optics must divide the two wavelength bands and route them to their respective portions of the instrument.

b. Requirements of Optical Methods

The optical design of IRIS must satisfy four basic requirements. First, to ensure that the radiometer and spectrometer receive radiation in amounts adequate to generate an acceptable signal level, there must be a means of obtaining adequate throughput of radiant energy. Second, based on throughput and spectral resolution requirements, the optics must provide the optimum instrument field of view and relay this into the proper spectrometer field of view. Third, the optical design must be compatible with the technological limitations of the IRIS instrument in-so-far as structure, thermal design materials, overall size, detector parameters, and spacecraft integrability are concerned. Finally, due to the performance parameters peculiar to IRIS, the optical design problem must be approached so as to yield a self-consistent optical system. Elaboration of this last point will follow.

c. Strategy for Satisfying the Requirements

The four requirements presented above yield the basic optional specifications to which the IRIS optical design must conform. To guarantee adequate throughput, a 20-inch aperture telescope must be included in addition to the "bare" radiometer and spectrometer. Throughput requirements, along with resolution and operational requirements for the spectrometer, establish the telescope field of view at $\pm$ 2.18 milliradians and the spectrometer field of view at $\pm$ 36.4 milliradians. This, in turn, sets the nominal angular magnification of the optical input to the spectrometer at 16.68 times.

When these optical specifications are achieved in a design which is also compatible with the technological limitations (of size, materials, etc.) of IRIS an optimal optical design begins to take shape, as shown schematically in Figure 2-38. In the interest of compactness, the 20-inch aperture telescope is given the Cassegrain configuration, with a fast primary mirror. The telescope forms an image of the observed scene at the field stop, the diameter of which sets the telescope field of view. The waveband divider for the instrument is located behind the telescope field stop and takes the form of a dichroic mirror. Again in the interest of compactness, the tilted dichroic folds and collimates the long wavelength radiation into the spectrometer, while transmitting the short wavelength band onto the radiometer collector mirror. Final attenuation of shorter wavelengths within the spectrometer is accomplished by dark mirrors integral to the spectrometer design.

In approaching the problem of establishing performance criteria and specifications for the IRIS optical design, an overall system viewpoint is important. IRIS is not a specular imaging system on the one hand, but on the other hand, image quality must be such as to make optimal use of detector size and response uniformity characteristics. In addition, while the quality of collimation of the input radiation to the spectrometer need not be perfect, it cannot degrade to such an extent that spectral response in the 2.5 μm region is unduly affected. By establishing performance specifications for the various segments of the IRIS optics based on these overall

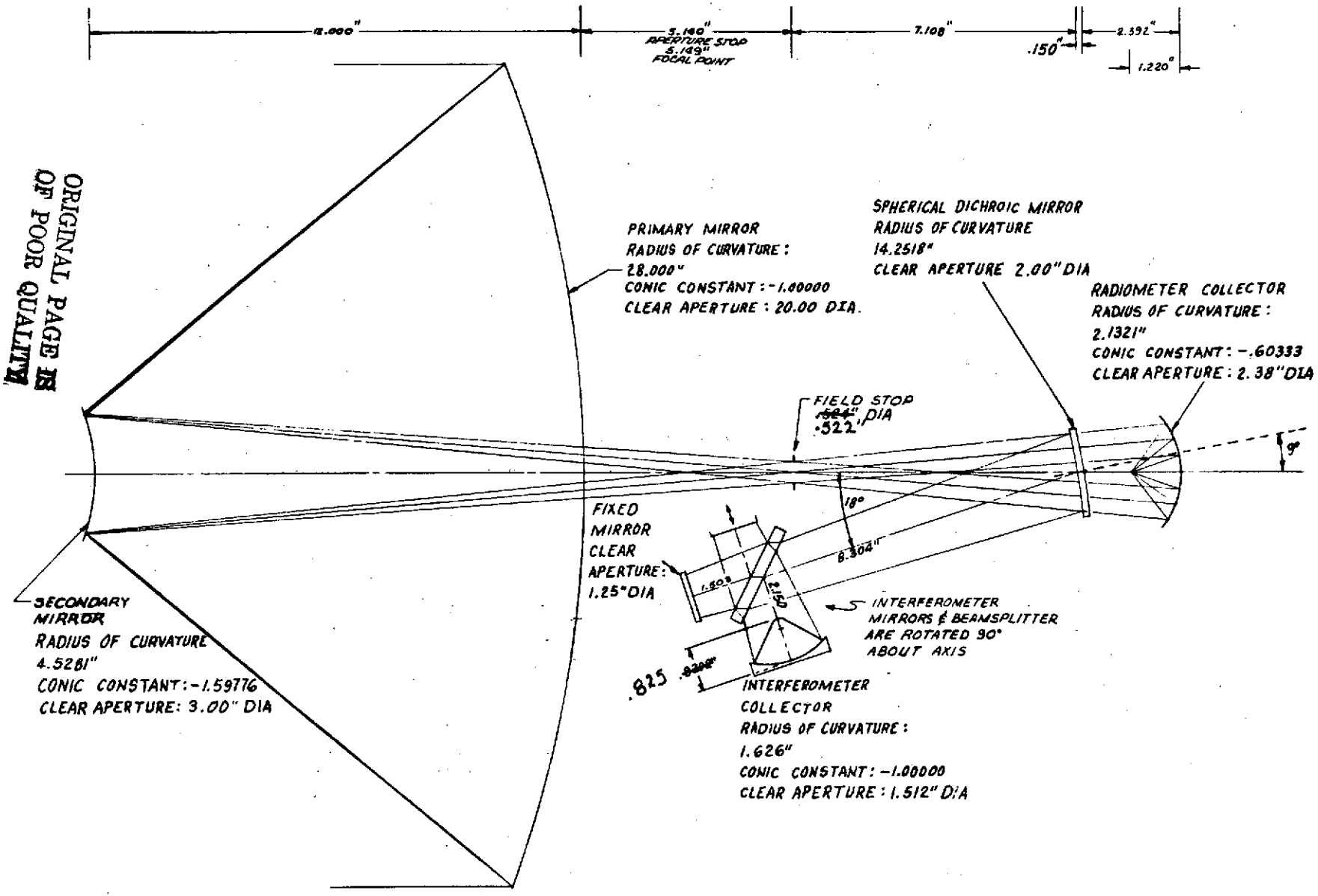

OPTICAL CONFIGURATION

FIGURE 2-38

systems considerations, the possibility of (needlessly) overspecifying or (undesirably) underspecifying any specific segment of the optics is reduced. An optically self-consistent design is the result. Several specific areas of the IRIS optical design are now examined.

d. Cassegrain Telescope and Dichroic Mirror

The IRIS Cassegrain telescope is fabricated entirely of beryllium, and is configured with a 20-inch diameter, 14-inch focal length (f/0.7) paraboloidal primary mirror and a 3-inch diameter hyperboloidal secondary mirror. The mirrors are a matched set with a separation of 12 inches. The focal point of the matched mirror set falls 5.15 inches behind the vertex of the primary mirror. A 0.522-inch diameter field stop is located at the telescope focal plane, which with the 119.5-inch effective focal length of the telescope permits a total telescope field of view of 4.364 milliradians.

Figure 2-39 presents a schematic of the IRIS telescope along with the values of several of its important optical parameters. The EFL, BFL, and the blur circle size at the telescope field stop are the three telescope parameters which have the greatest impact on the IRIS instrument as a whole. The EFL, in conjunction with the focal length of the dichroic mirror, determines the angular magnification of the telescope-dichroic combination. The BFL helps determine the axial length of the IRIS instrument. The angular subtense of the telescope blur circle at the dichroic mirror is largely responsible for the quality of collimation of the input radiation to the spectrometer. The maximum axial telescope blur circle of .035-inch diameter thus implies that the spectrometer input radiation will be collimated to within a ~5 milliradian maximum angular diameter. Additionally, the astigmatism introduced by the nine-degree tilt of the dichroic mirror causes a slightly elliptical spectrometer field of view, with a minor axis of 71.8 milliradians and a major axis of 74.3 milliradians.

In terms of the parameters of Figure 2-39 , the equation for the EFL is

$$EFL = \frac{PFL \times BFL}{PFL - S} = 120.05"$$

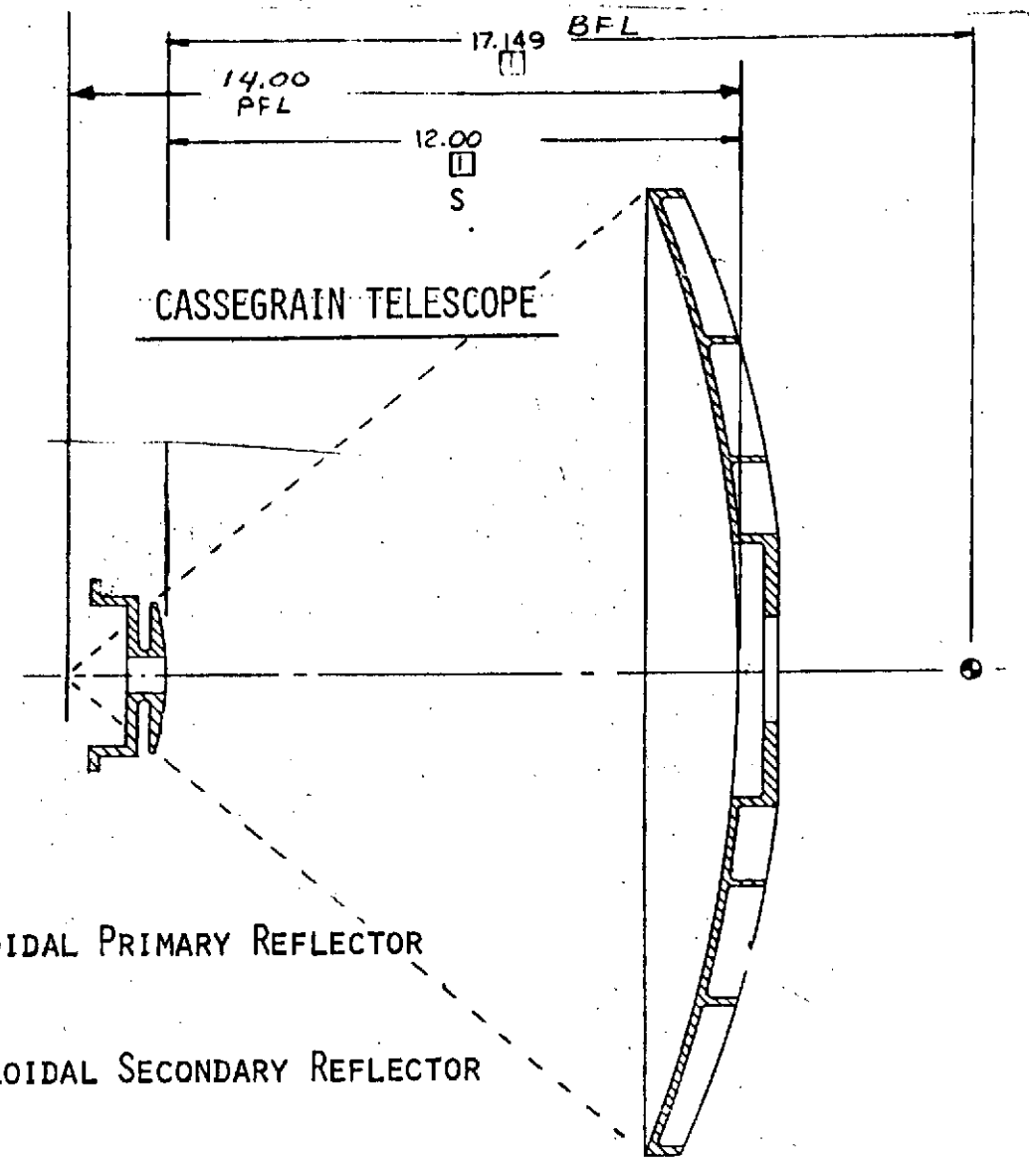

PARABOLOIDAL PRIMARY REFLECTOR

HYPERBOLOIDAL SECONDARY REFLECTOR

INVERTED IMAGE FORMED BEHIND PRIMARY

EFL = TELESCOPE EFFECTIVE FOCAL LENGTH

BFL = TELESCOPE BACK FOCAL LENGTH

PFL = TELESCOPE PRIMARY MIRROR FOCAL LENGTH

S = SEPARATION BETWEEN TELESCOPE PRIMARY AND SECONDARY MIRRORS

FIGURE 2-39

and thus:

$$\frac{\partial EFL}{\partial PFL} = BFL\left[\frac{1}{PFL - S} - \frac{PFL}{(PFL - S)^2}\right] = -51.45$$

$$\frac{\partial EFL}{S} = \frac{PFL \times BFL}{(PFL - S)^2} = 60.025$$

$$\frac{\partial EFL}{\partial EFL} = \frac{PFL}{PFL - S} = 7.00$$

In light of these equations describing the differential behavior of the EFL, it is clear that to specify a reasonable tolerance on the PFL ($\pm$ .030"), it is imperative that one have the freedom to respecity S and BFL once the PFL is actually measured, so that the EFL specification of 119.5 $^{+.5"}_{-1.0"}$ can be met. This iteration for the telescope design is provided for in the telescope procurement specification. Thus the 120.05" EFL of the present "paper" design is no cause for alarm.

In practice, it will be desirable to adjust the EFL to 119.5 inches by altering S and BFL in such a way that the axial focal point remains 5.149 inches behind the primary mirror vertex. With this constraing, the equations for establishing new values S' and BFL' once the PFL is known are

$$S' = 12.000" + x$$

$$BFL' = 17.149 + x$$

$$x = \frac{(PFL - 14.000")(51.45) - .55"}{67.025}$$

S' then becomes the axial separation at which the secondary mirror must be matched to the fabricated primary mirror, while BFL' $\pm$ .035" will become the new back focal length specification which the telescope must satisfy. (S' will have to be held to within $\pm$ .002".) For example, if PFL = 14.000", then S' = 11.9918" and BFL' = 17.141. S' and BFL' will need to be established in this way for each telescope fabricated.

e. Spectrometer Collector and Radiometer Collector

The radiation in the 2.5 μm -50.0 μm waveband which is reflected and collimated by the dichroic mirror is ultimately collected by a paraboloidal beryllium reflector after exiting from the interferometer portion of the spectrometer. This spectrometer collector focuses the radiation onto a thermopile detector with a .100-inch square sensitive area. Since the collector is quite fast and has a field of view of ~72.8 milliradians, its imagery exhibits aberration and the smallest total image size (~.080" dia.) occurs .007" outside its axial focal length which is specified at .813" ± .005. However, to ensure that variations in detector sensitivity over its active surface do not affect instrument performance, the spectrometer detector should be positioned .012" outside the measured axial focus of the spectrometer collector. This should produce an image (~.088 dia.) which is scrambled enough to smooth out detector variations, while providing adequate margin for the angular tolerances on the collector mirror obtainable without using a wedge ring tilt adjustment assembly.

Turning toward the radiometer, there is once again a fast collecting reflector-detector combination with defocusing employed for the sake of uniform detector response over the field of view. The radiometer collector is ellipsoidal in configuration with a distant axial focus (~9.65") located at the telescope field stop and a near axial focus (~1.20") which when measured should fall .020" inside the detector position so that proper image scrambling can be obtained. The (defocused) image size of ~.150" dia. on the .160" dia. detector active surface should again obviate the need for a wedge ring assembly. The passage of the short wavelength radiation through the tilted dichroic window does, however, cause a displacement of the radiometer optical axis by ~.0088" from the telescope optical axis. Both radiometer and spectrometer collector-detector assemblies can be decentered by ~.024" without affecting instrument performance, since the defocused images "track" almost exactly with decentrations of this magnitude.

f. Obscurations and Field of View

The field of view of IRIS is determined primarily by the diameter of the telescope field stop, as mentioned previously. Instrument response, however, is not uniform over the entire ± 2.18 milliradian nominal field of view for two main reasons. First, the nonzero blur circle of the telescope produces a steep but continous roll-off in response near the edge of the nominal field of view, rather than a discontinous drop from full response to no response. Secondly, due to the interplay between the various obscurations in the telescope, spectrometer, and radiometer, the instrument response profile as a function of field position is further modified.

The obscurations within the telescope itself are comprised of a central circular obscuration 8.2 inches in diameter due to the telescope secondary mirror and its associated shroud, and three symmetrically placed additional obscurations caused by the support legs for the secondary mirror. The total obscuration which these parts of the telescope create is shown to scale in Figure 2-40. In all, 21.6% of the total area of the primary mirror aperture is effectively obscured, 16.8% by the secondary mirror and shroud and 5.8% by the secondary mirror support legs.

Obscurations geometrically similar to those of the telescope exist in both the spectrometer and radiometer, and are due to the detector packages and their associated support legs. (See Figures 2-41 and 42). The detector packages are sized so as to produce obscurations which lie within the "shadow" of the telescope central obscuration, while the size and placement of the detector package support legs are selected to ensure maximum coincidence between their obscurations and the shadows of the secondary mirror support legs. In this way, obscurations in addition to those present in the telescope are held to a minimum. Nevertheless, as the field angle is increased, the increasing lack of overlap between the telescope obscurations and those in the spectrometer and radiometer causes the response in these areas of the instrument to have a more sloping roll-off than the telescope response. Quantitative results are displayed in Figures 2-43 and 2-44.

OBSCURATIONS - CASSEGRAIN TELESCOPE

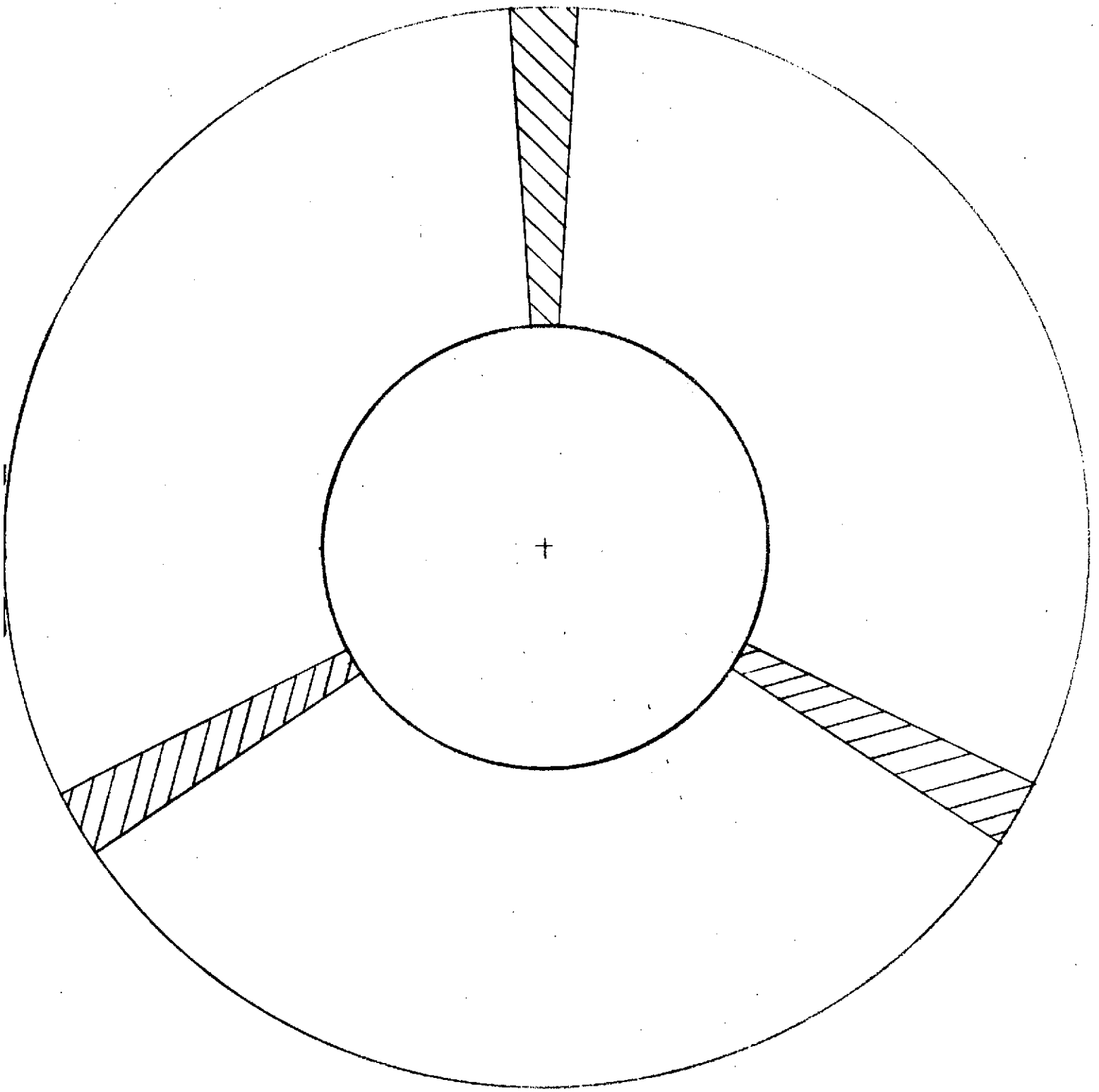

FIGURE 2-40

OBSCURATIONS – SPECTROMETER APERTURE

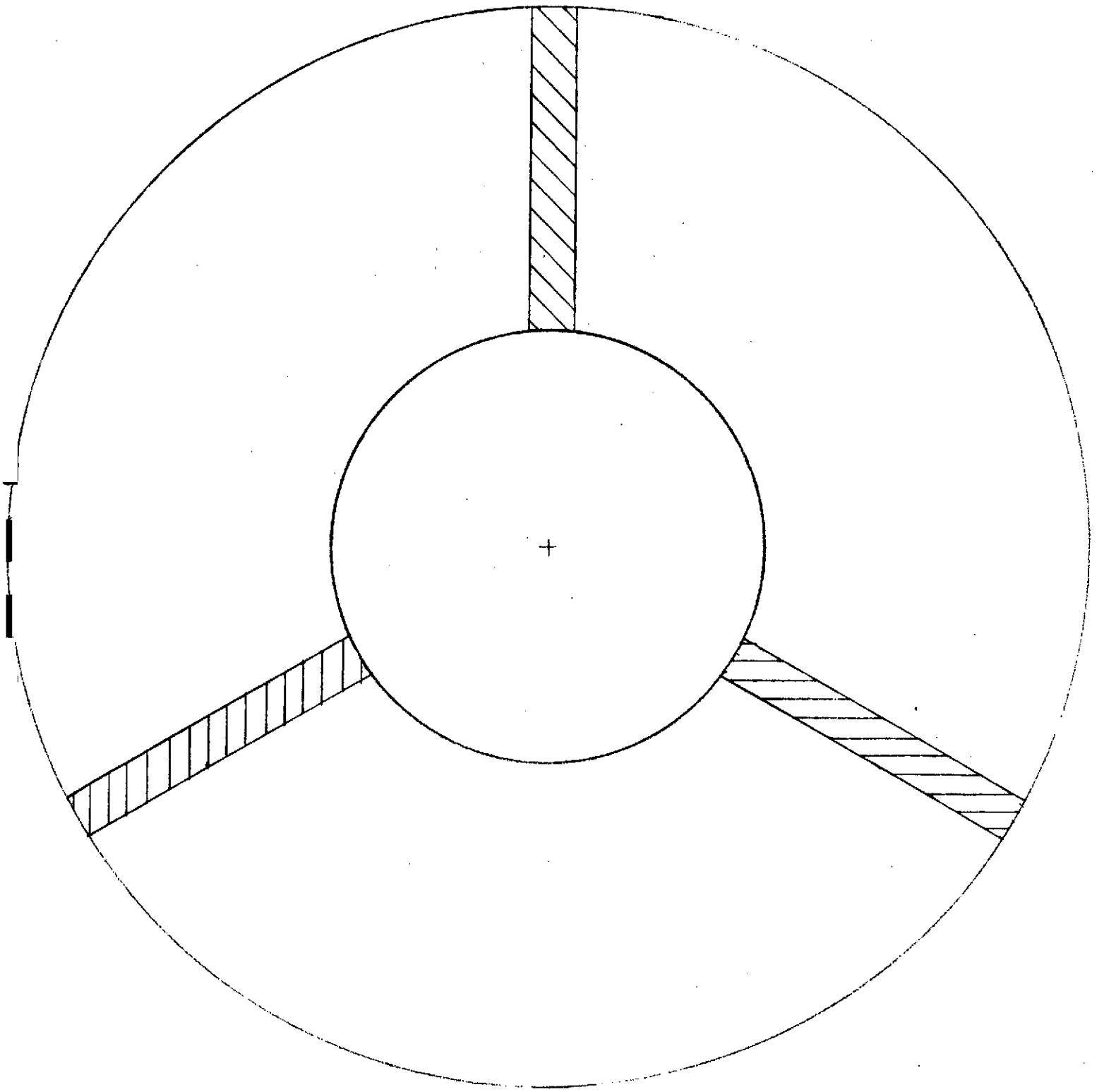

FIGURE 2-41

OBSCURATIONS- RADIOMETER APERTURE

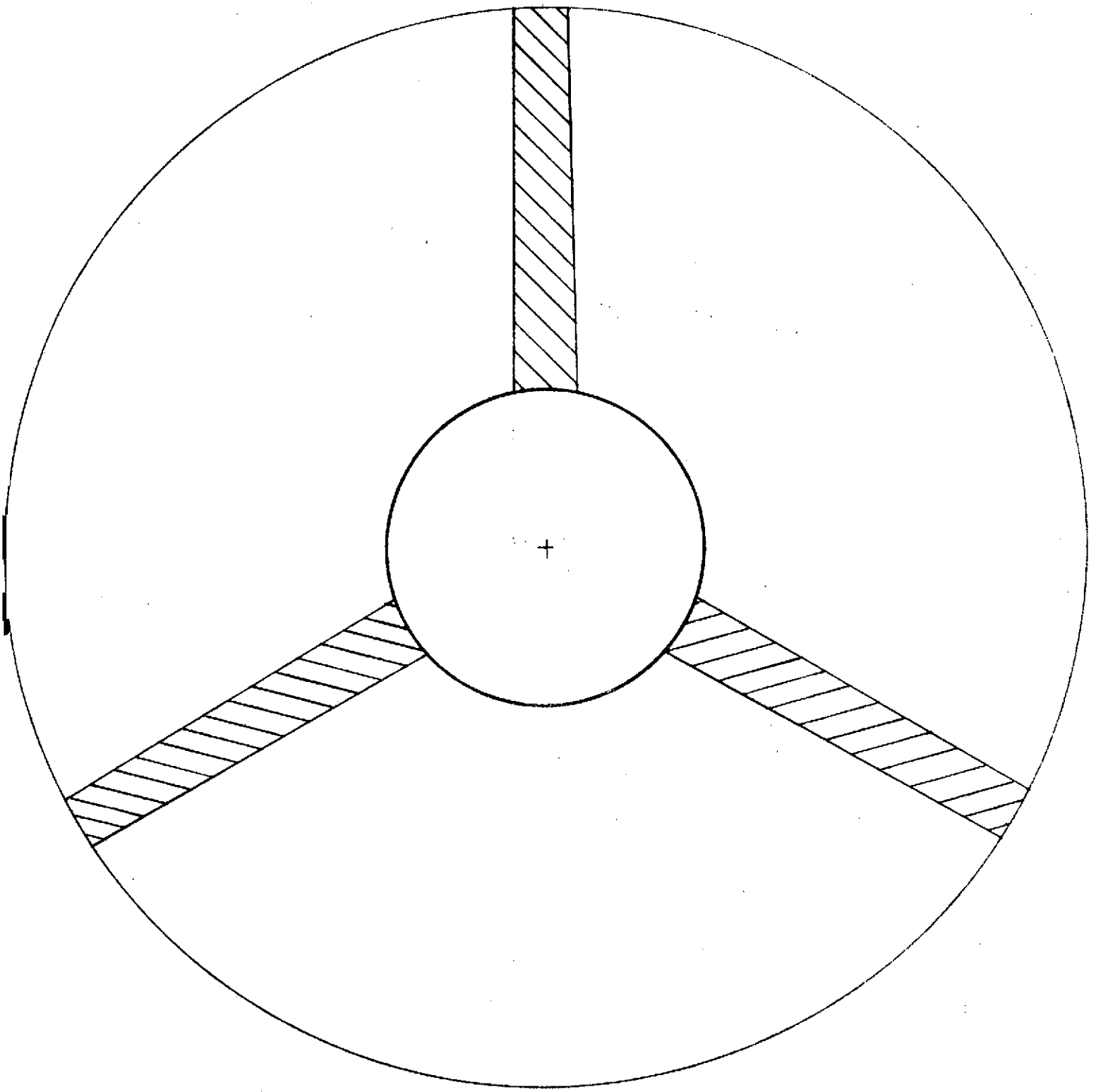

FIGURE 2-42

IRIS FIELD OF VIEW - ABSOLUTE

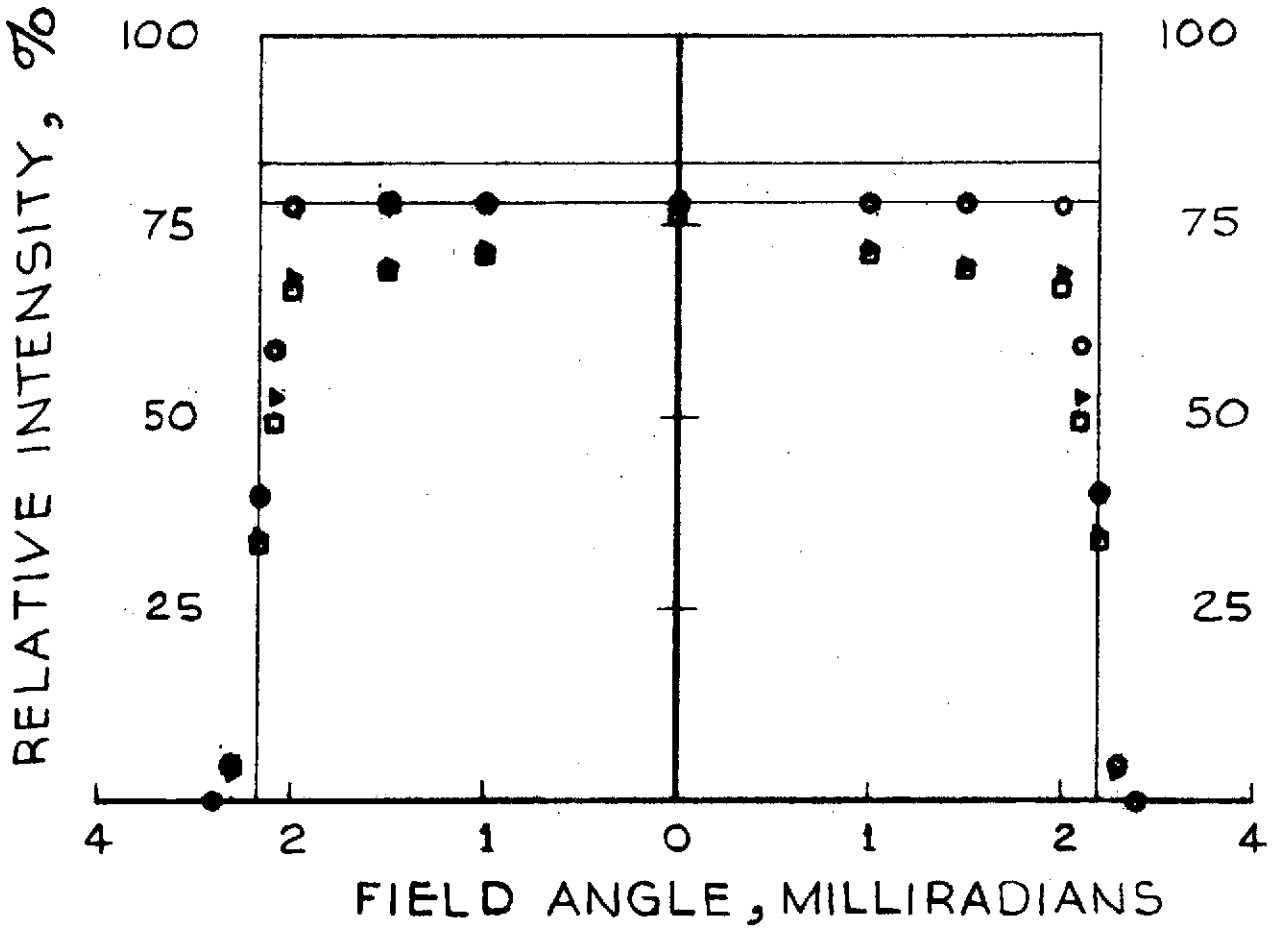

LEGEND

- ○ TELESCOPE FIELD STOP
- ▫ RADIOMETER DETECTOR
- ▸ SPECTROMETER DETECTOR

FIGURE 2-43

IRIS FIELD OF VIEW- NORMALIZED

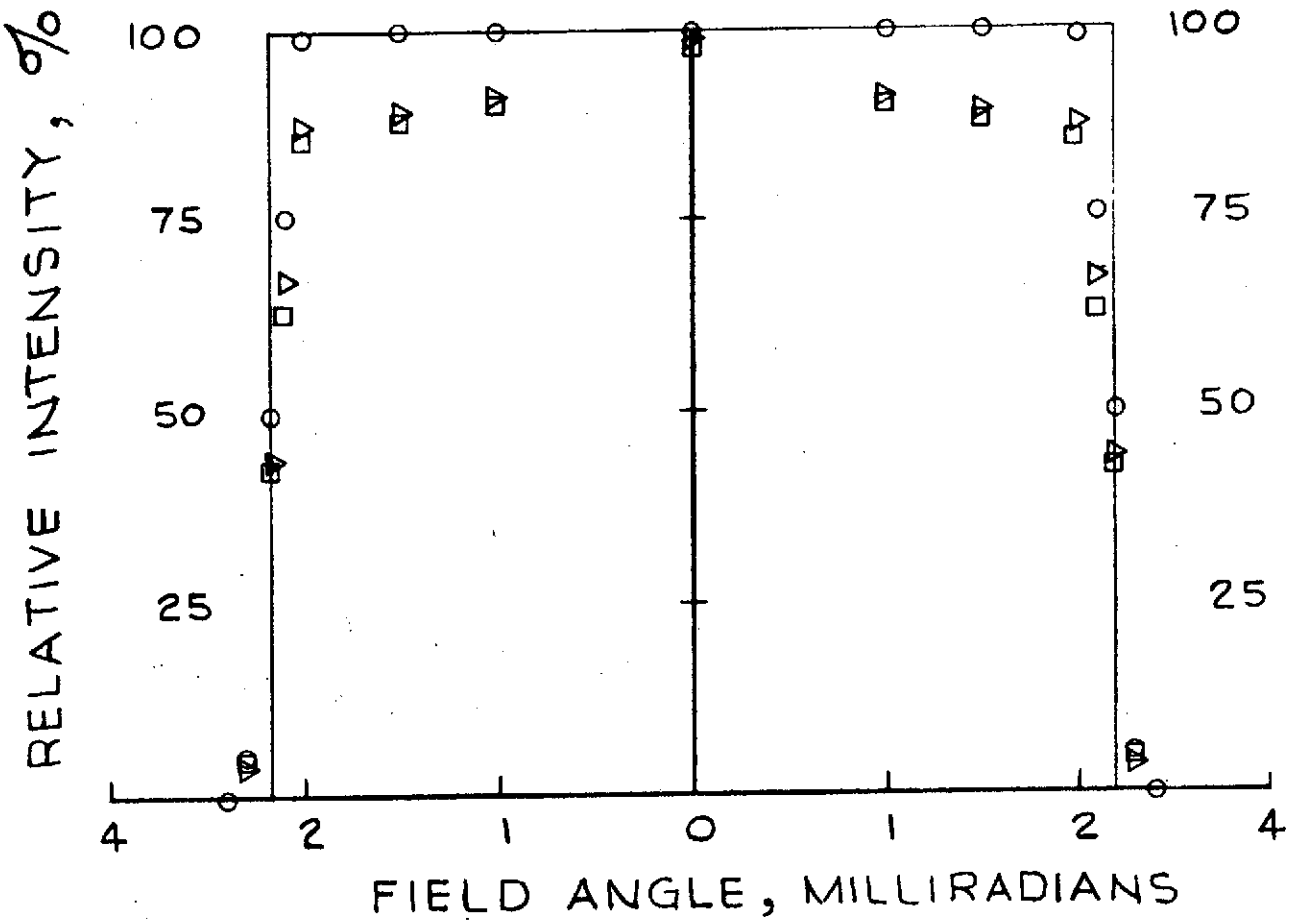

LEGEND

- ○ TELESCOPE FIELD STOP
- □ RADIOMETER DETECTOR
- ▷ SPECTROMETER DETECTOR

FIGURE 2-44

g. Optical System Tolerance Study

One of the important phases of the IRIS optical design effort has been the development of intelligent and realistic optical tolerances, which are in turn reflected in fabrication and structural tolerances. To this end, a detailed tolerance study of the IRIS optics has been performed, involving investigation of the effects of tilt, decentration, surface figure error, and axial displacement of every optical element. Figure 2-45 presents a summary of much of the data gathered during the optical tolerance study.

Several conclusions have become apparent from this study: (1) the performance of the spectrometer is the governing factor in establishing optical tolerance throughout IRIS, (2) each telescope primary-secondary combination must be an individually matched pair, since requiring interchangeability of primary and secondary mirrors would necessitate imposing unrealistically tight tolerances on these mirrors, (3) optical performance is not affected by small perturbations in the position and orientation of the dichroic mirror, and thus the dichroic can be used as an aid in spectrometer alignment as well as to provide a collimated spectrometer input, (4) use of defocused imagery and slightly oversized detectors in both the spectrometer and radiometer obviates the need for special (and rather expensive) wedge ring alignment assemblies in these areas, (5) failure of the (quartz) dichroic to "scale" exactly with the rest of the IRIS (beryllium) optics as temperature changes should have negligible effect on system performance, and (6) allowable system thermal perturbations in general are an order of magnitude below that needed to induce noticeable optical degradation, so long as the thermal coefficient of expansion is uniform throughout the system and expansion anisotropies are 1% or less.

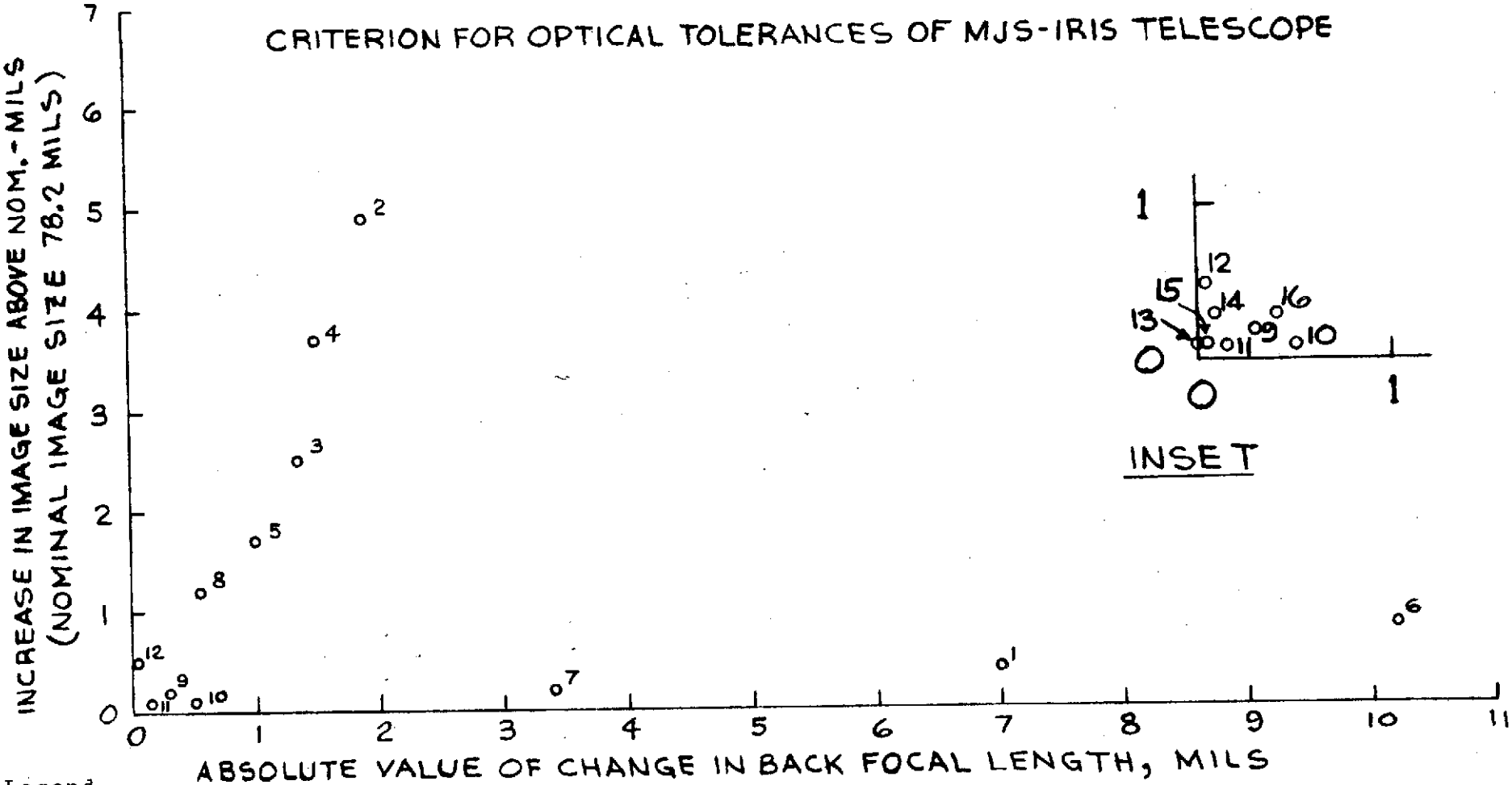

Legend

1. radius, primary, ±.014"
2. vertical decentration, primary, ±.015"
3. horizontal decentration, primary, ±.015"
4. tilt about horizontal, primary, ±.0005 rad
5. tilt about vertical, primary, ±.0005 rad
6. airspace, primary to secondary, ±.010"
7. radius, secondary, +.009"
8. tilt about horizontal, secondary, ±.002 rad
9. tilt about vertical, secondary, ±.002 rad
10. airspace, secondary to collimator, ±.030"
11. radius, collimator, +.028"
12. tilt about horizontal, collimator, 9°+.002 rad
13. tilt about vertical, collimator, ±.002 rad
14. vertical decentration, collimator, ±.020"
15. horizontal decentration, collimator, ±.020"
16. airspace, collimator to beamsplitter, ±.300"

FIGURE 2-45

3. Dichroic and Beamsplitter

a. Summary

CsI substrates and beryllium beamsplitter mounts have been ordered. The bonding materials evaluations point to DC 93-500 as a viable bonding material. To achieve a sufficient reduction in the low temperature stresses on the CsI substrates, it is anticipated that the bond line thickness will have to be increased to around .030 inch. Additional evaluations are underway to establish the optimum bond line thickness.

Techniques have been established to control the temperature of the CsI substrate during evaporation of the IR beamsplitter coating and the design of the production cooling fixture is complete. Tests were initiated to establish the technique for controlling the material deposition rates required to produce a graded index IR beamsplitter coating. Further work is still required to establish the feasibility of using this technique to produce an IR beamsplitter coating.

The preliminary design of the discrete step IR beamsplitter coating is complete. An analysis of the discrete step beamsplitter coating shows it to be relatively insensitive to deposition errors. The graded index beamsplitter coating has been optimized for reduced physical thickness; however, finalization of the preliminary design will require further data on the optical constants of the material combinations required to produce the graded index coating.

A single surface dichroic coating has been designed analytically. However, due to adhesion problems between the films in the coating, it is recommeded that a commercially available dichroic with a second surface coating be used for the dichroic.

Dark mirror work has been directed primarily at deposition and evaluation of modified published dark mirror designs. Coatings suitable for use on a beryllium substrate have been developed and a sharp reflectance cut-on has been achieved. Further data on the optical constants of thin metal films is required to optimize the dark mirror design; in particular, to move the reflectance cut-on out to 1.5 μ.

b. Mount Design

During the first quarter, the beamsplitter mount was designed and the CsI substrate dimensions established. CsI substrates and beryllium mounts have been ordered and upon receipt will be handled to form a test beamsplitter. This beamsplitter will be thermal cycled and subjected to the expected vibration levels to establish the integrity and stability of the beryllium mount and the effects of low temperature bond stresses and G-loadings on the optical figure of the substrate. On completion of these tests and completion of the substrate cooling fixture (discussed in Section e), a CsI substrate will be coated and the engineering model beamsplitter assembled and tested.

c. Bonding Elastomer Evaluation

Of the nine materials and material catalyst combinations which were originally under evaluation, only one; namely, DC 93-500 (a space grade material) shows promise as a bonding material for the beamsplitter substrate. RTV 630, RTV 630/655, DC 61106, and Sylgard 187 have been found to have glass transition points above 200°K. RTV 560 and RTV 566, while satisfying the low temperature requirements, require moisture to cure, even with the RTV 9811 catalyst. Further testing will be primarily confined to the DC 93-500 and RTV 630 (for reference). Also, evaluation of the RTV 566/9811 as a backup material will continue with major emphasis on establishing the humidity levels required to affect full cure. It is hoped that a suitable curing technique can be found which will not damage the hygroscopic CsI.

Figure 2-46 shows shear stress (at .004 inch deflection) as a function of temperature for the various materials. As discussed in the first quarterly report, the goal is to obtain a shear stress less than 5 psi at 200°K for .004 inch shear displacement. Reaching this goal will require increasing the bond line thickness. Tests are presently underway to evaluate bond line thickness of .025 inch and .033 inch. There are two major problems with increasing the bond line thickness; namely, angular stability over temperature and lowering of the resonance frequency of the substrate bond. At .015 bond line thickness, the resonance is around 300 Hz. At .030 bond line thickness, the resonance should drop to around 100 to 150 Hz, which is dangerously close to the projected 160 Hz resonance of the instrument on the support tube. Further testing will establish the criticality of these problems.

d. IR Beamsplitter Coating Design

During this quarter, additional work was done on optimizing the discrete and graded IR beamsplitter coating designs. Figure 2-47 represents the status of the discrete step beamsplitter coating design. The dashed curve in the upper graph represents the original linearly stepped design. The solid line represents the refined version. The index stepping in the refined version is faster than in the original. Additional improvements were made by changing the structure of the equivalent layers shown schematically in the figure. The one period (three layer) type reported previously was replaced with a two period (five layer) type in order to reduce the effect of dispersion of the resulting equivalent index. Since these five layer equivalent films contain, in some cases, very thin layers, it was necessary to establish the sensitivity of the design to errors in the thickness of the layers that might occur during deposition. An error analysis of the refined discrete step beamsplitter, with the maximum excursion of transmittance (ΔT) used as the parameter of comparison, produced the results in Table 2-7 . The results show that the coating is relatively insensitive to deposition errors; this was one of the primary concerns with this type of coating. On receipt of the substrate cooling fixture from the model shop,

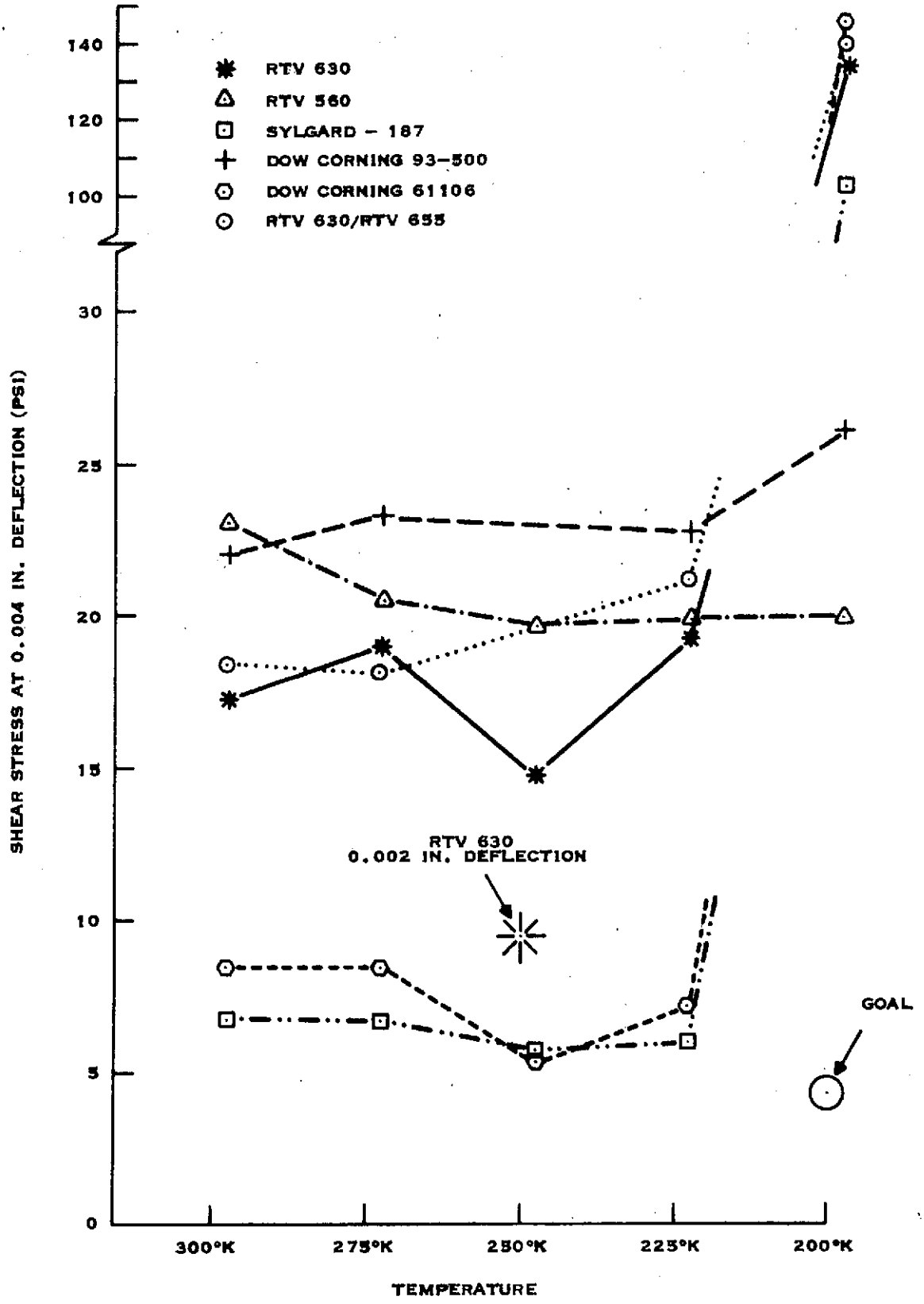
RTV 630
RTV 560
SYLGARD – 187
DOW CORNING 93–500
DOW CORNING 61106
RTV 630/RTV 655
140
120
100
30
25
20
15
10
5
0
SHEAR STRESS AT 0.004 IN. DEFLECTION (PSI)
RTV 630
0.002 IN. DEFLECTION
GOAL
300°K
275°K
250°K
225°K
200°K
TEMPERATURE

Figure 2-46

DISCRETE STEP BEAMSPLITTER

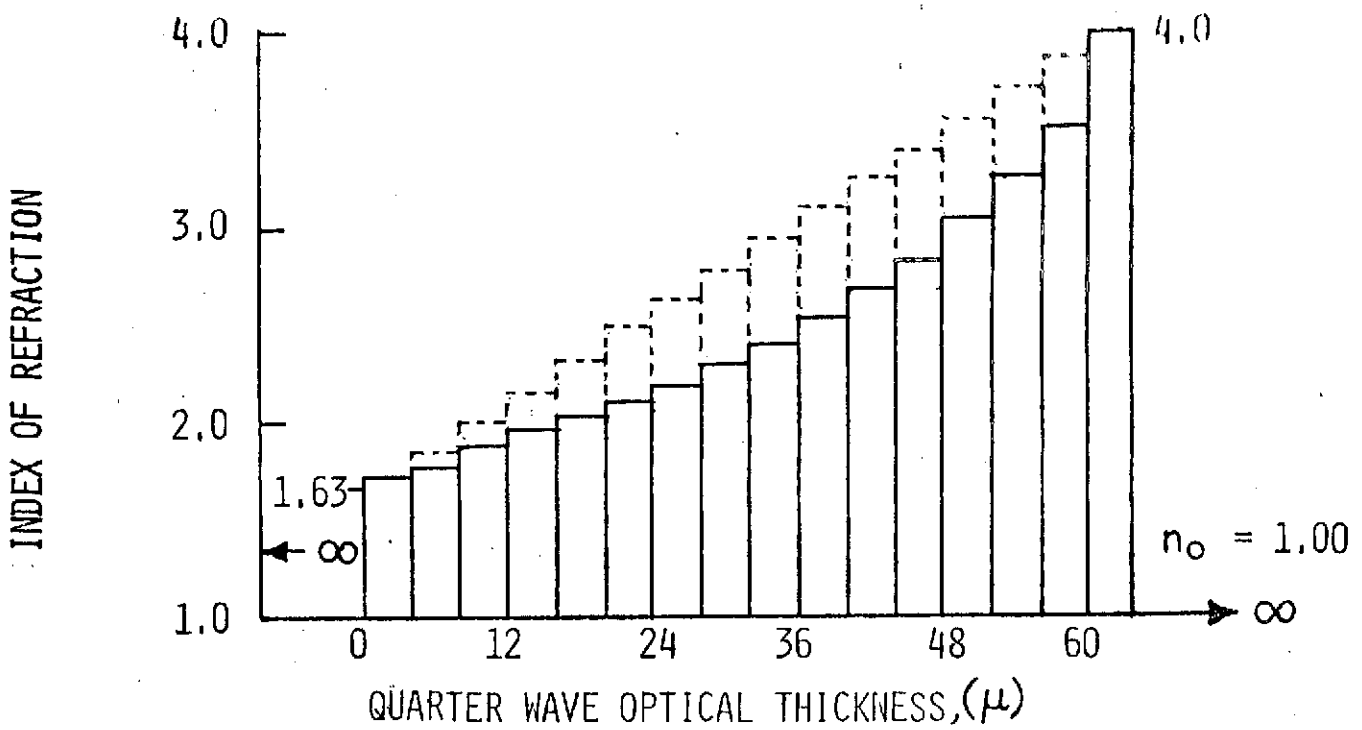

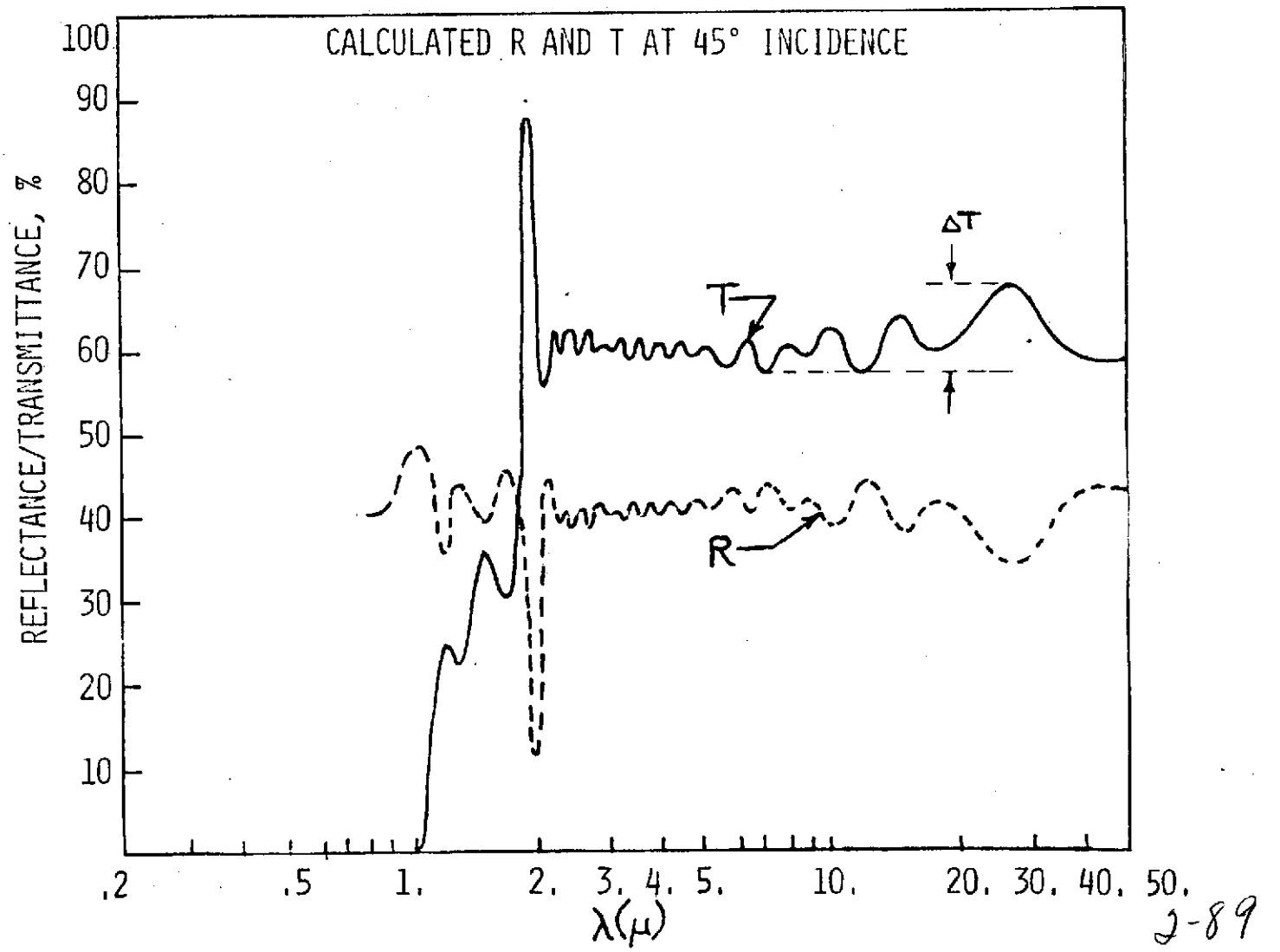

2-89

FIGURE 2-47

TABLE 2-7

RESULTS OF DISCRETE STEP COATING DESIGN ERROR ANALYSIS

RANDOM ERROR IN LAYER THICKNESS, %	ΔT_{AVE}* %	REMARKS
0.0	8.6	Nominal design
5.0	9.2	All layers varied
10.0	10.9	All layers varied
25.0	9.4	Varied only thin (< μ.4 QWOT) layers

* THIS IS THE AVERAGE VALUE OF THE MAXIMUM EXCURSION OF TRANSMITTANCE (ΔT) FROM 2.5 μ TO 50 μ FOR NINE SEPARATE CALCULATIONS IN WHICH THE RANDOM ERROR IN THICKNESS OF THE LAYERS VARIED WAS MAINTAINED AT THE PERCENTAGE OF THEIR NOMINAL VALUE SHOWN IN COLUMN 1.

a series of tests will be run to 1) establish the optimum substrate temperature for deposition of the discrete step beamsplitter coating; 2) produce test samples of the discrete step coating for thermal cycling to establish the low temperature integrity of the coating; and 3) finalize the design of the discrete step coating which will be used on the engineering model beamsplitter.

With respect to the graded index beamsplitter, the original design was intended to have a quarter wave optical thickness of 150 μ. During the thermal control tests of last quarter, a graded beamsplitter of 150 μ quarter wave optical thickness (QWOT = 4nt) was deposited using power control. The results of that deposition are shown in Figure 2-48 . The losses exhibited (1-R-T) are due to several causes. First, scatter in the short wavelengths; second, excessive germanium content; and third, PbF_2 long wavelength absorption. The latter two of these losses could be minimized by reducing the total thickness of the coating.

The need to optimize using thinner films has directed the effort toward improving the performance of a 100 μ QWOT graded beamsplitter. Work with the fast gradient technique has produced the desired results. The maximum excursion in transmittance (ΔT) in the 2.5 μ to 50 μ region has been reduced from 12.9% by changing from a linear to a fast gradient. In addition, the ΔT has been further reduced to 8.7% by varying the thickness of the other germanium layer. Figure 2-49shows the various grading types and the results of errors in the nominal fast gradient design.

One question still needs to be answered before the preliminary graded index design can be finalized; namely, the ratio of materials at each position in the coating to create the required graded index. Work has just begun to establish indices as a function of material ratios. This work will be completed in the first part of the next quarter. On completion of this work and after establishing the feasibility of the material deposition control technique (discussed in the next section) all further work on the IR beamsplitter coating will be confined to the discrete stepped coating. Since there would be significant expense involved in designing, fabricating,

MEASURED REFLECTANCE AND TRANSMITTANCE FOR A GRADED INDEX BEAMSPLITTER PRODUCED DURING THERMAL EVALUATION

(VARIED INDEX BY CONTROLLING POWER, DEPLETED ONE MATERIAL BEFORE COMPLETING RUN)

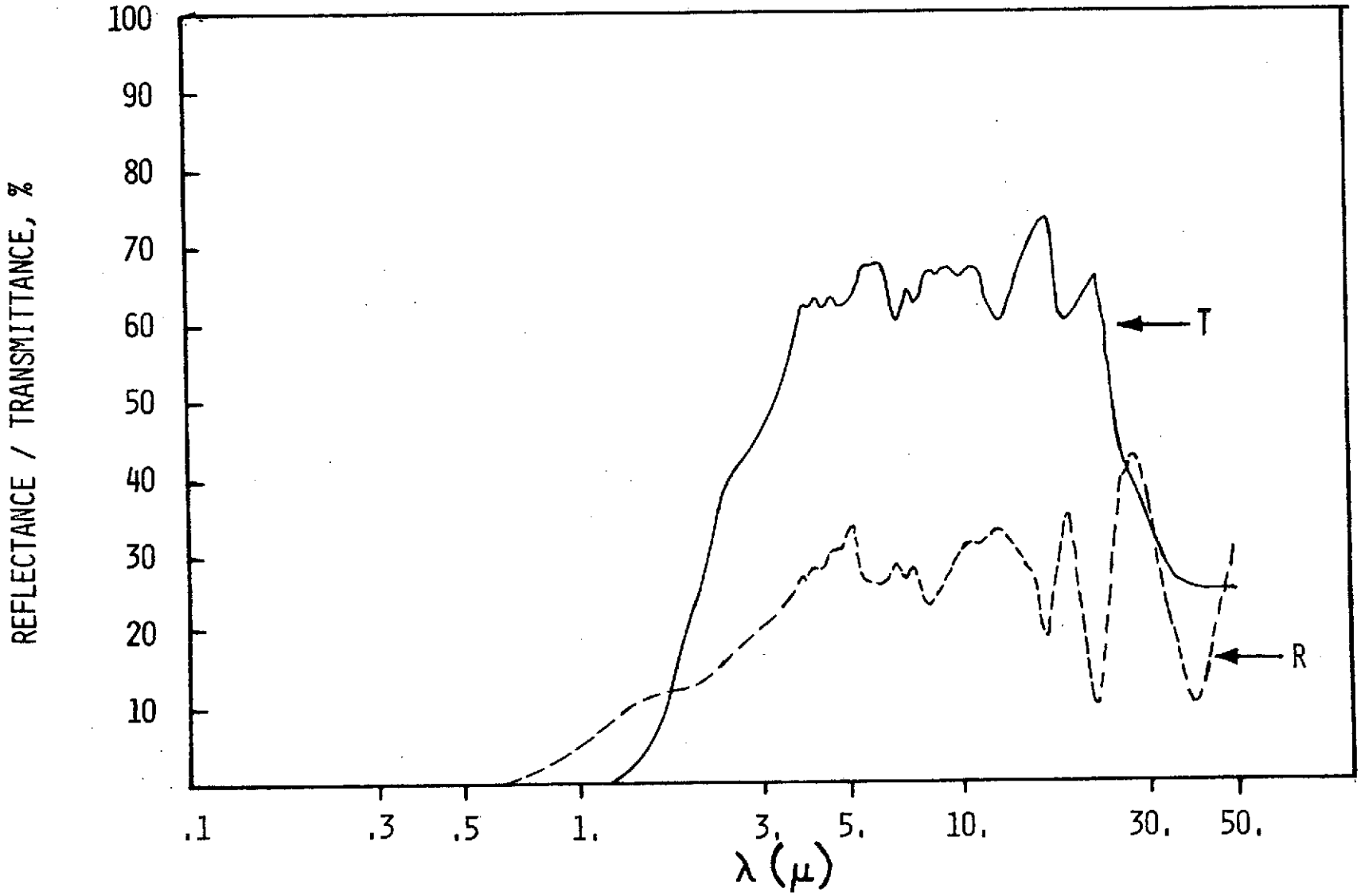

FIGURE 2-48

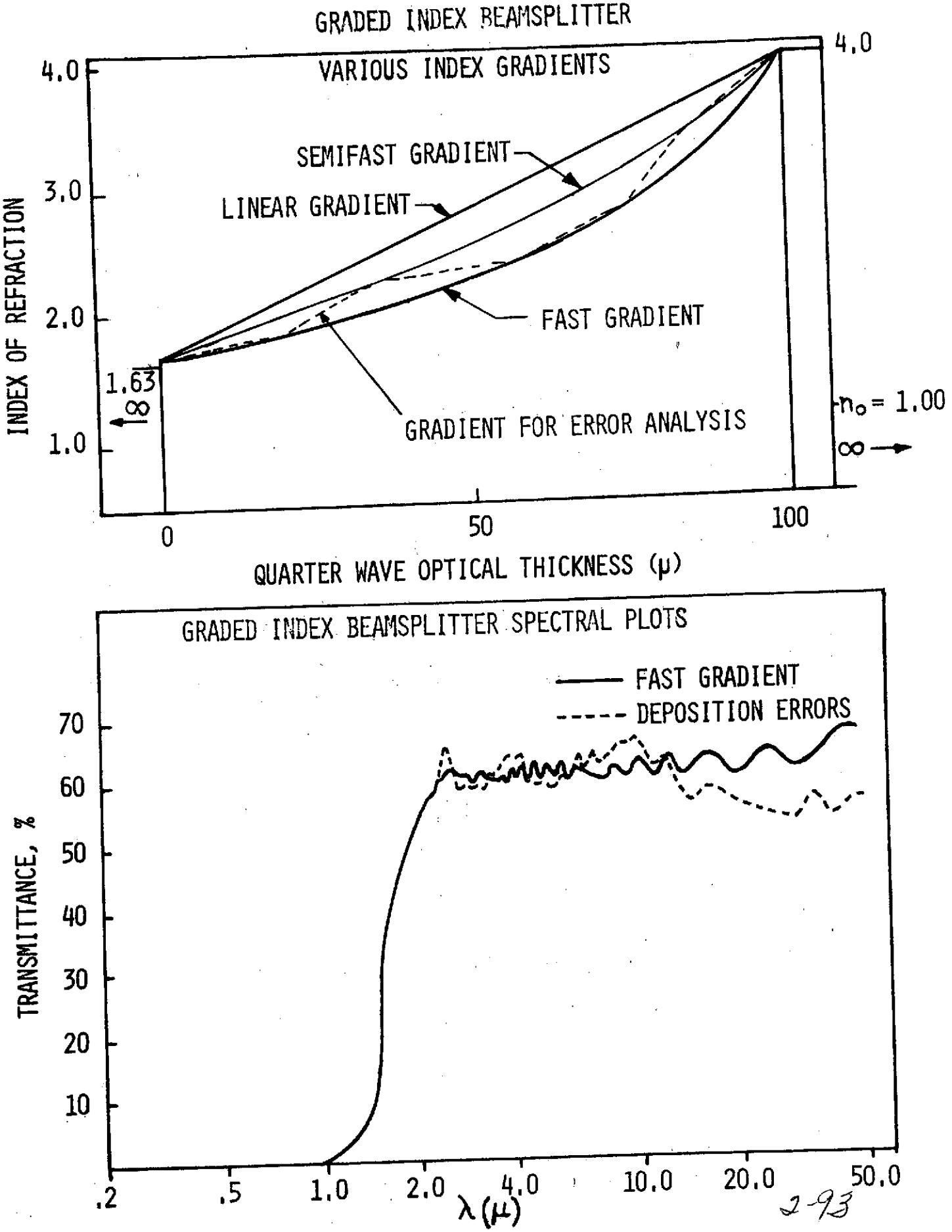
GRADED INDEX BEAMSPLITTER
VARIOUS INDEX GRADIENTS
SEMIFAST GRADIENT
LINEAR GRADIENT
FAST GRADIENT
GRADIENT FOR ERROR ANALYSIS
INDEX OF REFRACTION
4.0
3.0
2.0
1.0
1.63
1.8
n_o = 1.00
∞
0
50
100
QUARTER WAVE OPTICAL THICKNESS (μ)
GRADED INDEX BEAMSPLITTER SPECTRAL PLOTS
FAST GRADIENT
DEPOSITION ERRORS
TRANSMITTANCE, %
70
60
50
40
30
20
10
.2
.5
1.0
2.0
4.0
10.0
20.0
50.0
λ(μ)
2-93

FIGURE 2-49

and testing of gradient control fixturing, no further work will be done on the graded index coating until it is established that a satisfactory discrete step coating cannot be deposited and thermal cycled without failure.

e. Optical Coating Deposition Techniques

As in the first quarter, a major portion of the beamsplitter effort has been spent on developing the techniques for cooling and controlling the temperature of the CsI substrate during deposition of the IR beamsplitter coating. Further testing in the second quarter has established that the substrate temperature can be satisfactorily controlled. Figure 2-50 shows the basic configuration of the cooling fixture which will be used for production coating. Design of this fixture is complete with fabrication to start immediately. The unanswered question is "What temperature do we control to?" It is anticipated that the substrate will be held in the range of 60°F to 100°F. Above 100"F, we will distort the substrate during coating and/or introduce excessive stress which will eventually distort the substrate during assembly and thermal cycling or in vibration testing (as proved during the beamsplitter development for IRIS MM'71). Below 60°F, there are indications that large grain structures will form on condensation of the coating materials which could lead to excessive scattering at the shorter wavelengths (2-4 μ). An example of this can be seen in Figure 2-48 where the data shown is for a coating which was deposited while the substrate temperature was held between 30°F and 60°F. On receipt of the cooling fixture from the model shop, the proper substrate temperature during coating deposition will be established to optimize the properties of the discrete step IR beamsplitter coating.

During the second quarter, work was begun on establishing the techniques for controlling the material deposition rates in order to create a graded index IR beamsplitter coating. The results for controlling the deposition rates for KRS-5 and PbF_2 are shown in Figure 2-51 . Figure 2-52 is a schematic representation of the test fixture used. While the results show that a relationship

SUBSTRATE COOLING FIXTURE

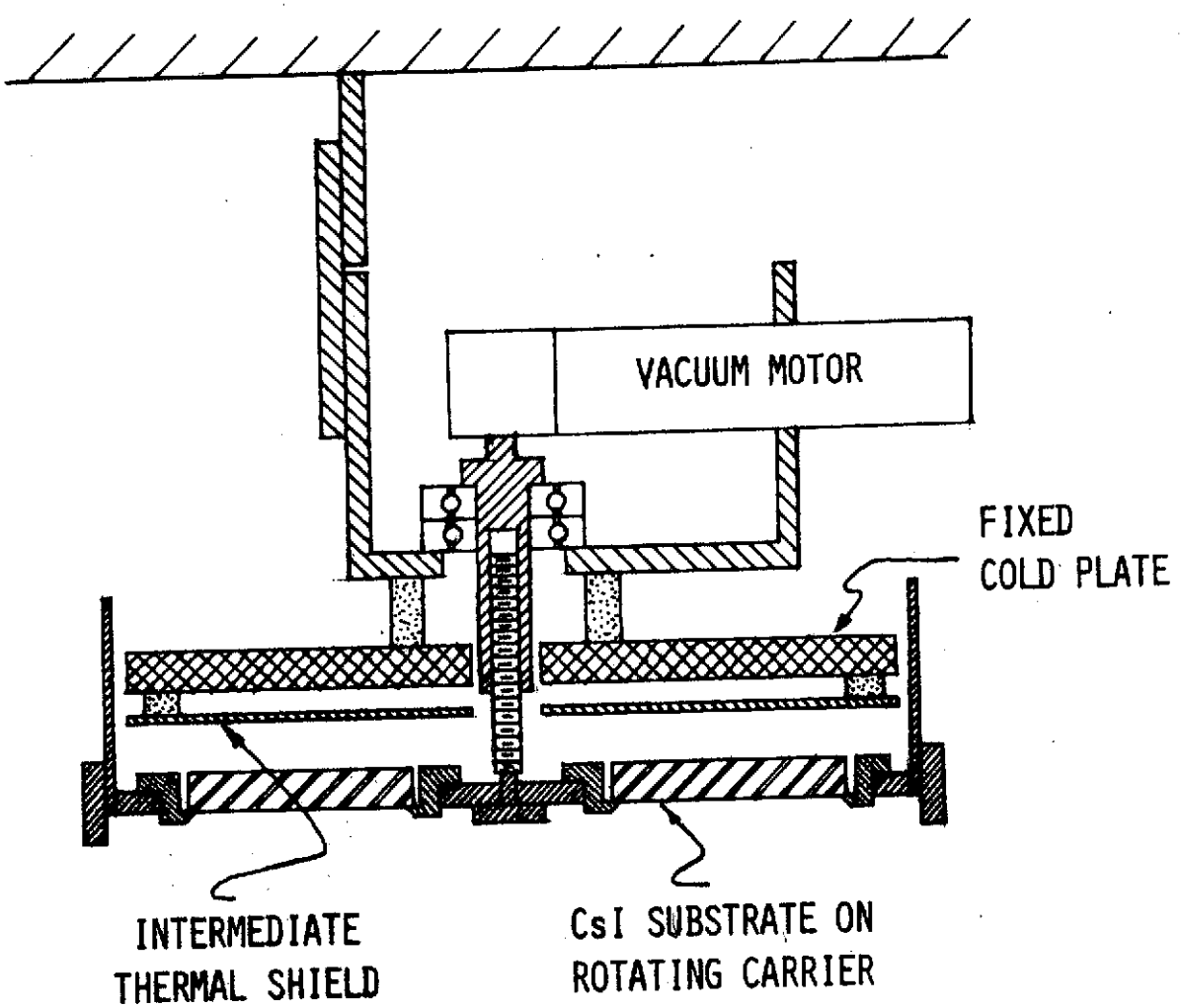

Figure 2-50

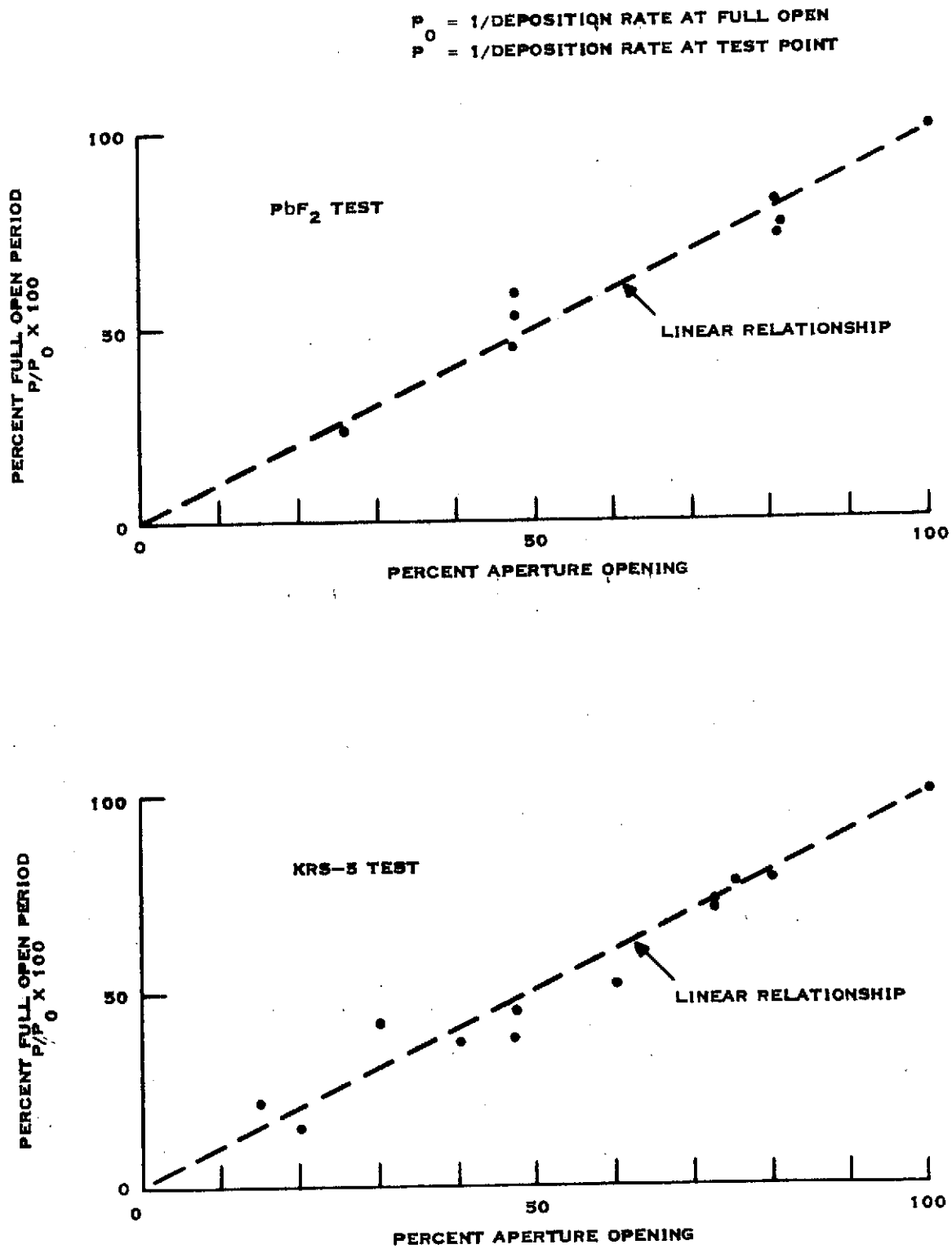

Grading Technique Test Results

Figure 2-51

EVAPORATION RATE CONTROL

TEST FIXTURE

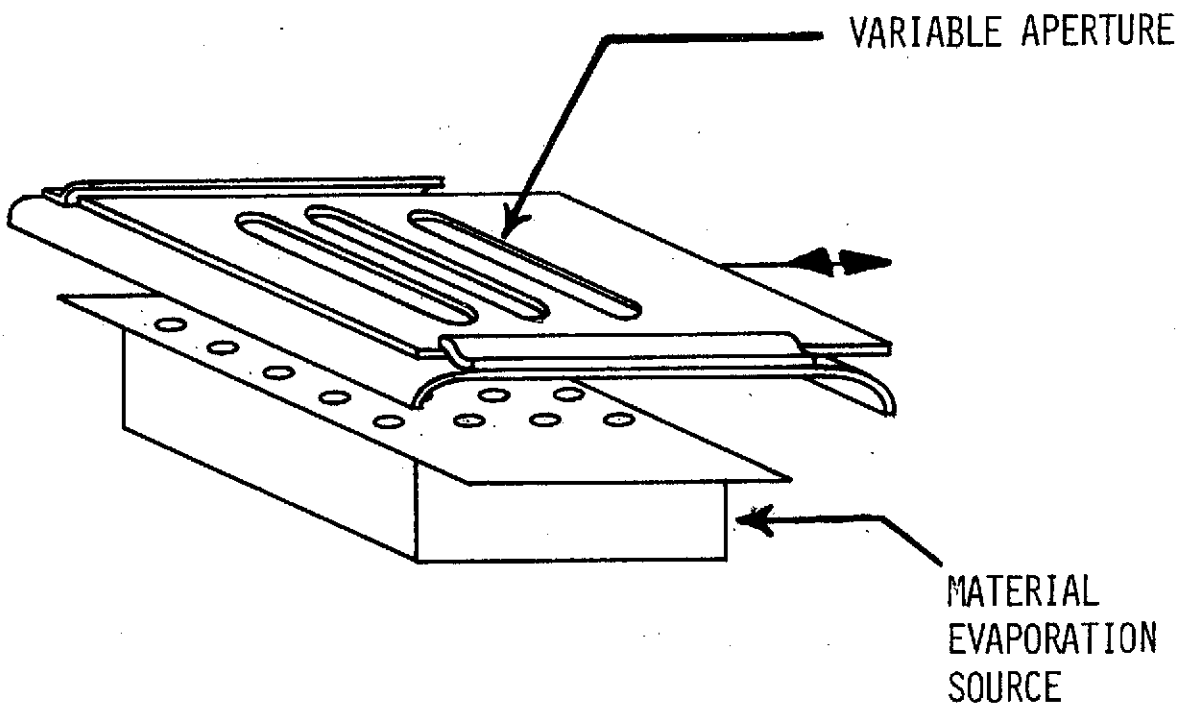

Figure 2-52

can be established between aperture opening and deposition rate, an equally important parameter is the stability of the source evaporation rate.

The stability rate versus time of deposition was tested for both PbF_2 and KRS-5 with the rate control test fixture in place full open. Figure 2-53 shows the results for the PbF_2 test. The results for KRS-5, plotted in Figure 2-54, were inconclusive, since two tests produced differing results. The differences in the two runs were thought to be due to the change of rate versus power input. If the test deposition is started carefully and a long burn-in period is used to bring the KRS-5 up to deposition temperature, the result is a more stable run. Further testing is scheduled to test the theory stated above. Preliminary work with germanium indicates that the evaporation rate of this material can be controlled by varying the power input to the evaporation source.

f. Dark Mirror and Dichroic

The results of some of the latest work on dark mirror design is presented in Figure 2-55 . The measured results are for films, representing modified published designs, deposited in an attempt to achieve a sharper reflectance cut-on. As the data indicates, we have been able to achieve a relatively sharp cut-on and maintain high reflectance at 2.0 μ; however, to date, we have not been successful translating the cut-on point out to 1.5 μ. The next step in the dark mirror effort is to complete the calculation of the optical constants of thin metal films and with this data, attempt to design and deposit multilayer films with a sharp reflectance turn-on around 1.5 μ.

One of the problems with the earlier dark mirror designs was the fact that the energy not reflected was transmitted. Thus, these earlier films would not have been compatible with a beryllium substrate as the transmitted energy would have been reflected at the beryllium surface back into the instrument. For the films shown in Figure 2-55 , the energy not reflected is absorbed; thus, these designs are compatible with a beryllium substrate.

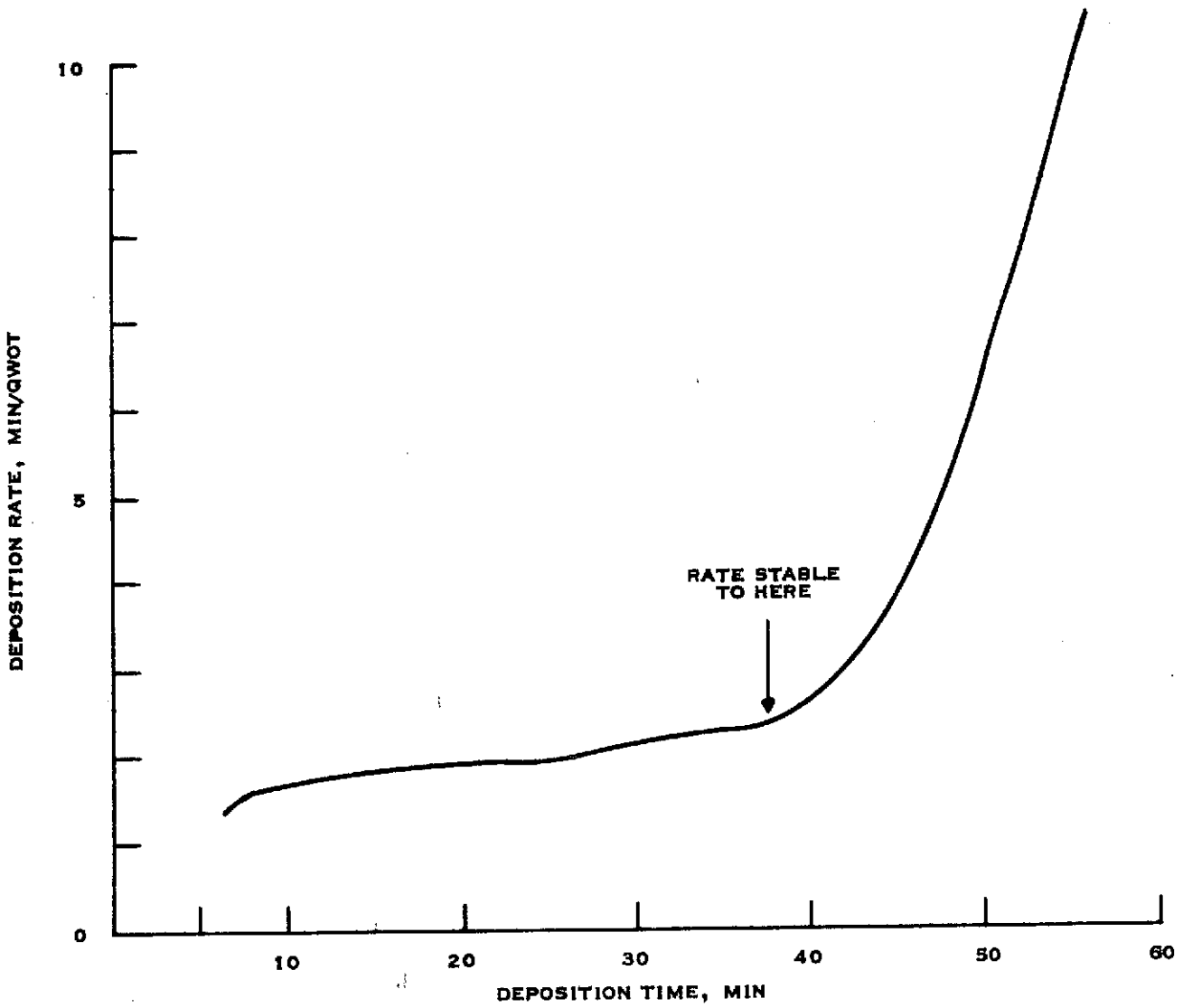

TOTAL DEPOSITION FROM SINGLE SOURCE = 3.24μ PHYSICAL THICKNESS
QUARTER WAVE OPTICAL THICKNESS, TOTAL = 22μ
TOTAL DEPOSITION TO STABLE POINT = 2.66μ, 18μ QWOT

PbF_2 Rate Stability Test

Figure 2-53

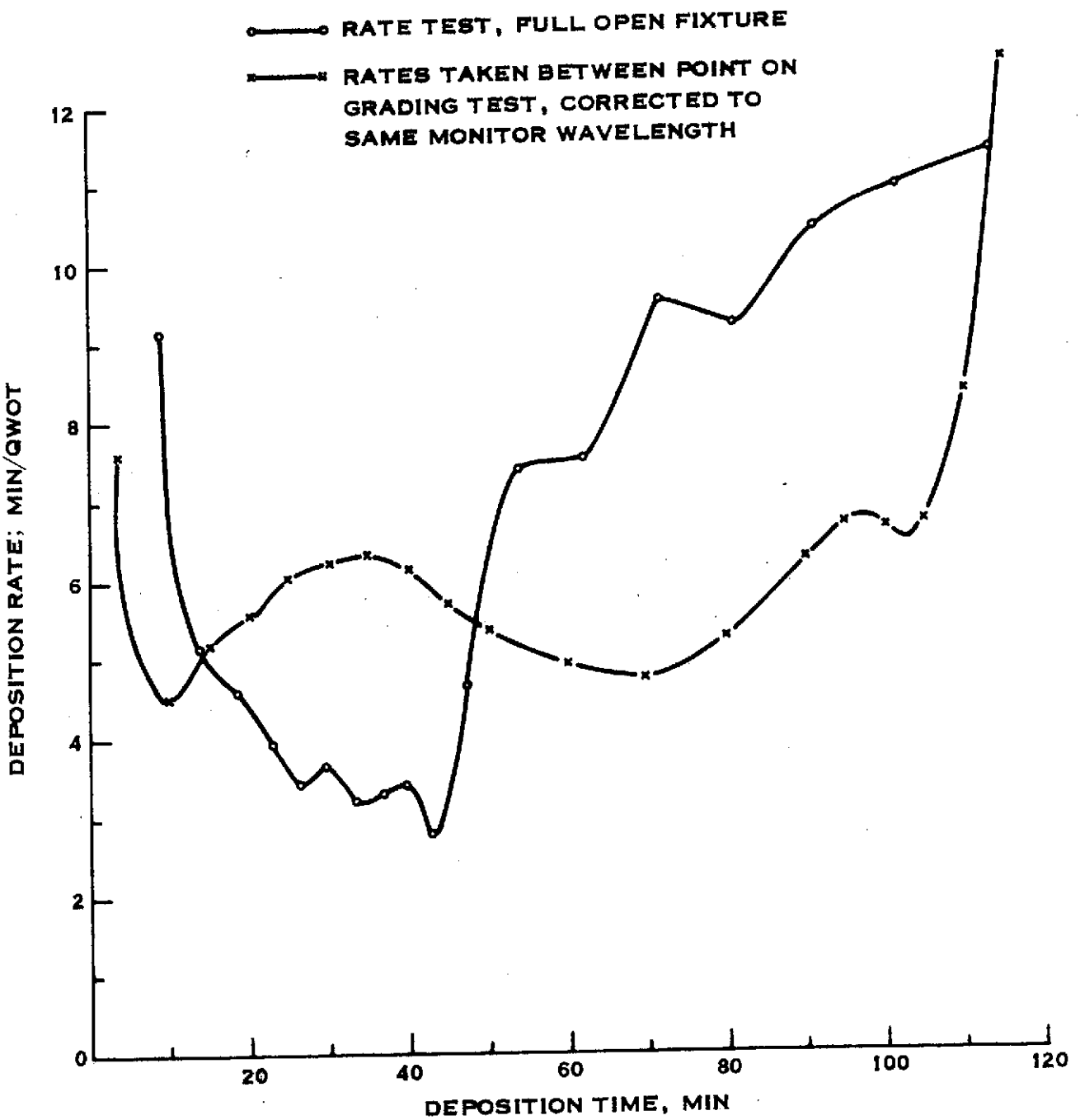
RATE TEST, FULL OPEN FIXTURE
RATES TAKEN BETWEEN POINT ON GRADING TEST, CORRECTED TO SAME MONITOR WAVELENGTH
DEPOSITION RATE; MIN/QWOT
DEPOSITION TIME, MIN
0
2
4
6
8
10
12
20
40
60
80
100
120

Figure 2-54

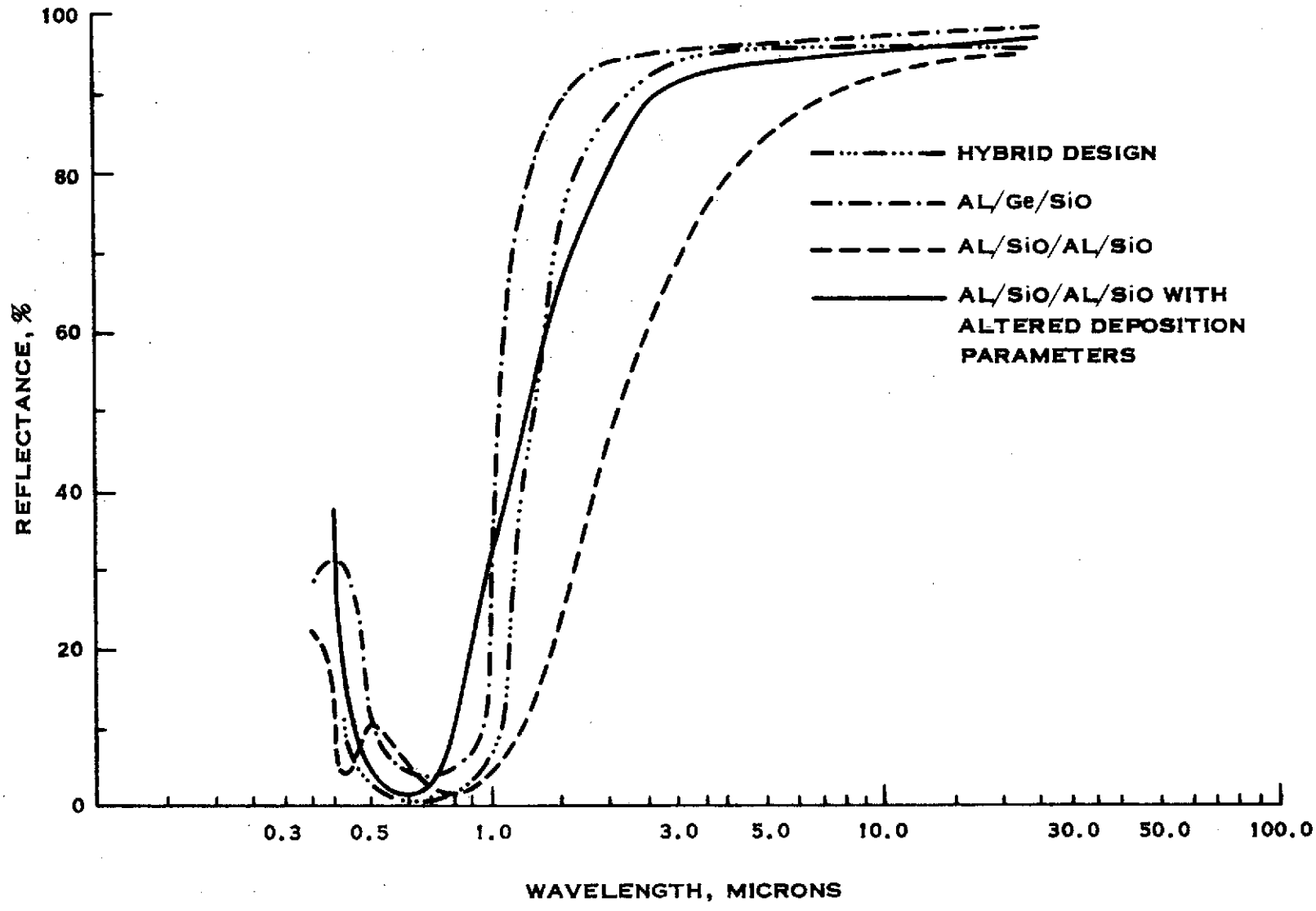
100
80
60
40
20
0
REFLECTANCE, %
0.3
0.5
1.0
3.0
5.0
10.0
30.0
50.0
100.0
WAVELENGTH, MICRONS
HYBRID DESIGN
AL/Ge/SiO
AL/SiO/AL/SiO
AL/SiO/AL/SiO WITH ALTERED DEPOSITION PARAMETERS

Figure 2-55

The work on a suitable dichroic has been resumed analytically using new data for the optical contants (n and k) for thin gold layers. Figure 2-56 shows a comparison between a single surface dichroic coating designed with this dispersive data and a vendor supplied dichroic with an additional coating applied to the second surface to flatten visible and near IR spectral response. However, further data indicates that there are adhesion problems between the thin gold layers and the dielectric layers. Since extensive development efforts would be required to resolve this problem, it is recommended that the vendor supplied dichroic be purchased and a second surface coating applied to produce a suitable dichroic.

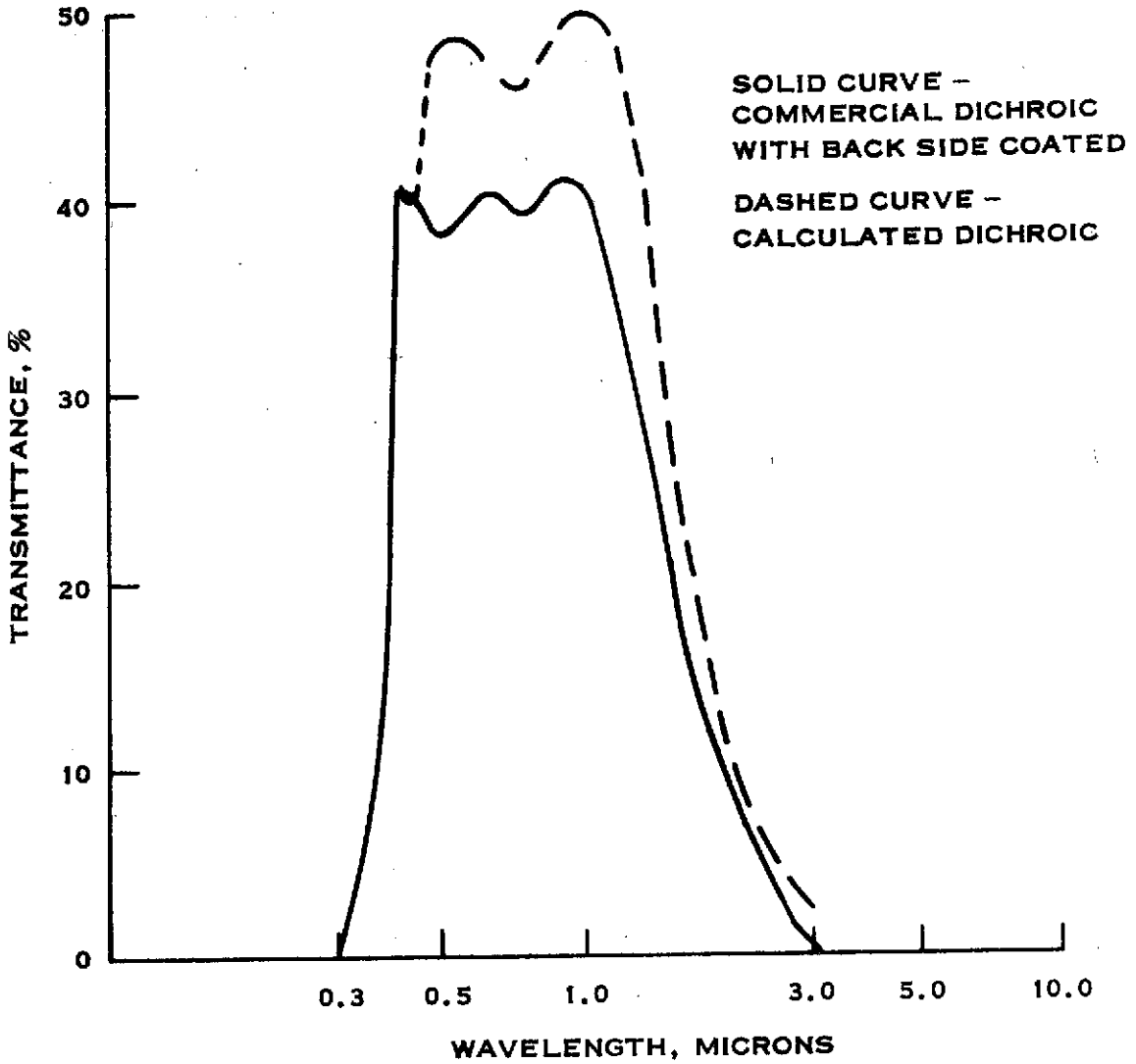

Comparison of Dichroic Performance

Figure 2-56

4. Telescope Assembly

At the end of the last reporting period, the telescope assembly was out for quotations. The resulting quotations identified several areas in the telescope design which presented technical and cost problems. The telescope design has since been upgraded to eliminate as many of these problems as was compatible with the design requirements.

The foremost technical, and yet unresolved, problem involves providing the primary mirror with a low scatter optical surface. It was learned that neither polished bare beryllium nor optical coatings of aluminum are compatible with low scatter surfaces. Based on this fact and environmental evaluation tests performed by TI on polished nickel plated beryllium, the decision was made to nickel plate the mirrors before polishing in order to provide a low scatter substrate. However, the problem with the aluminum optical coating has not been completely resolved. By using an electrodeposited gold coating, a durable low scatter surface can be attained, but the lower reflectance of gold as compared to aluminum, for wavelengths less than 6000A, will result in the loss of signal in this wavelength region. This non-reflected energy also results in an additional thermal load whenever the sun shines upon the primary mirror. In order to provide thermal control for this load, additional electrical power will be required when this load is not present.

At present, the American Beryllium Company in Sarasota, Florida is identified as the supplier of machined beryllium parts for the IRIS Telescope. Applied Optics Center, in Burlington Massachusetts, appears to be the best choice for nickel plating, polishing, assembly, and testing of the telescopes. Both of these vendors have signed agreements to contract with Texas Instruments, contingent upon NASA/GSFC approval. The tentative agreement with Applied Optics Center assumes a gold overcoat. Present engineering activity is directed towards finding ways to accomodate the thermal impact of the gold primary mirror coating.

5. Instrument Calibration

The MJS system is currently being designed with a single instrument mounted calibration system such as is shown in Figure 2-57 . The system is to be sighted 20° off of the main instrument boresight, with a ± 10mr FOV nominally boresighted with the UVS calibration system.

Two such systems had been under consideration previously, one for the radiometer, and the other for the short wavelength region of the IRIS. Solar radiation was to provide the energy for the calibration, but close inspection of the effect of adding solar radiation to the IRIS signal indicated that only a very small amount could be allowed without effecting the dynamic range adjustment in the IRIS. This arises from the fact that while solar energy is entering the instrument through a calibration system as shown in Figure 2-57, the telescope is viewing deep space. The resulting interferogram is then a combination of the cold deep space target and the solar input. Since the energy associated with these two sources does not lie in the same wavelength region, and is not "chirped" to the same extent by the uncompensated beamsplitter, the peak interferogram signal is strongly affected by the presence of solar energy. The results of the above discussion led to a single calibration system for the radiometer channel, which will provide some signal into the IRIS also, in the 2.5-6.0 um region.

The following discussion outlines the considerations taken in actually sizing the collection aperture for the radiometer channel. The calibration is designed to begin at 4.5 A.U., and to generate a signal equal to approximately 80% of the maximum signal expected during the Jupiter encounter.

The maximum signal at Jupiter is expressed as Sig.(MAX) = $\frac{\text{Solar Const.}}{\Pi}$ (Jup) x AΩ x Albedo x Spectral Efficiency, and the signal provided by the collection aperture of the calibration system by

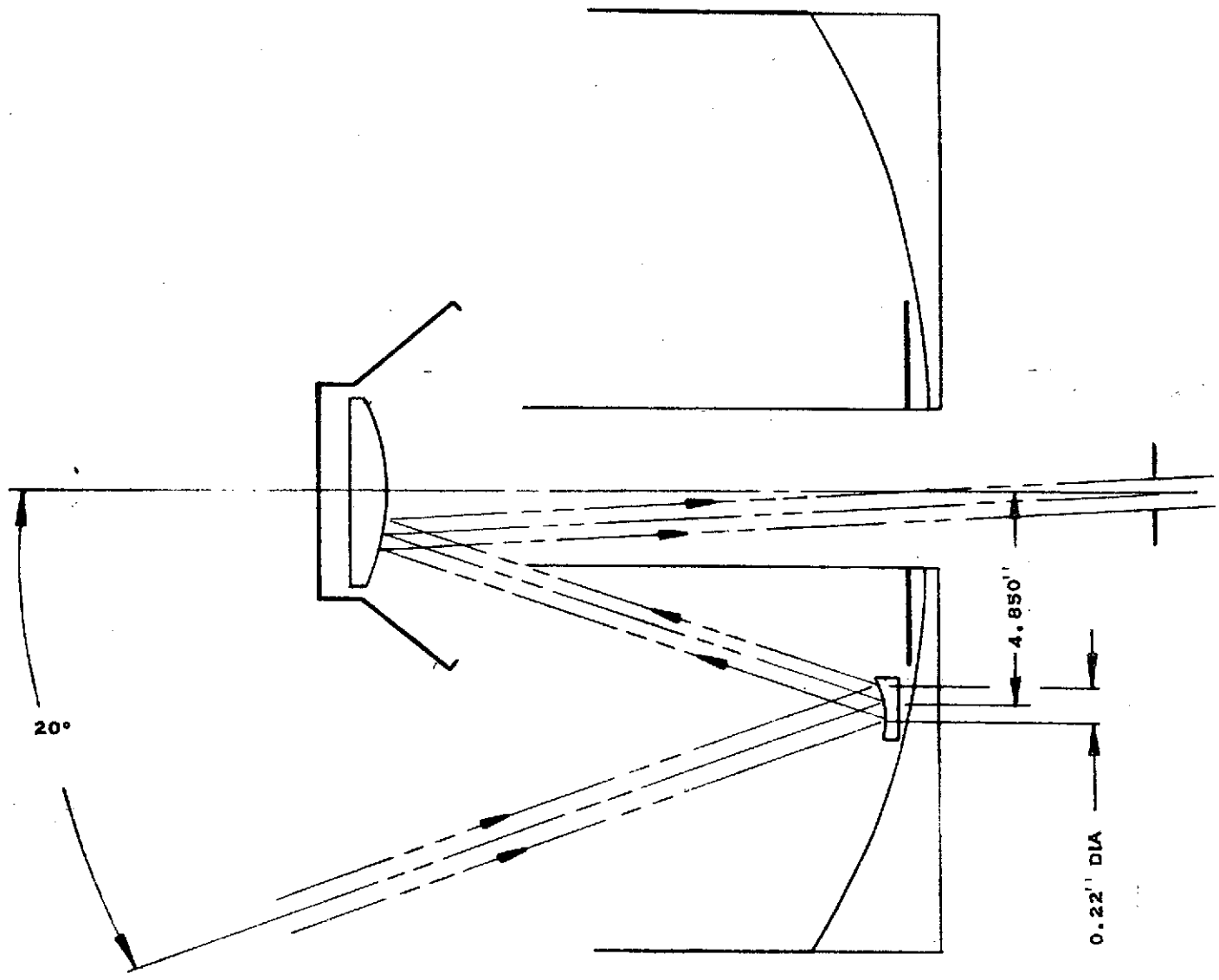

SINGLE MIRROR CALIBRATION

Figure 2-57

Sig. (CALIB) = Solar Const. (4.5 A.U.) x A^1 x Spectral Efficiency,

where $A\Omega$ is the product of the unobscured telescope aperture and its solid angle,= $A\Omega = 2.37 \times 10^{-2}$

Albedo is the maximum expected at Jupiter, Albedo = 1

Spectral Efficiency is the spectral response of the radiometer system

A^1 is the collection aperture (not necessarily the size) of the calibration mirror

If Sig. (CALIB) = .8 Sig. (MAX),

then

$$\text{Solar Const. (4.5 A.U.)} \times A^1 = .8 \frac{\text{Solar Const.}}{\pi} \text{(JUP.)} \times A\Omega$$

$$A^1 = \frac{\text{Solar Const (JUP.)}}{\text{Solar Const.(4.5 A.U.)}} \times \frac{.8}{\pi} \times 2.37 \times 10^{-2}$$

Solar Const (JUP) = 4.8×10^{-3} w/cm^2 (JPL)
Solar Const (4.5 AU) = 6.68×10^{-3} w/cm^2

Therefore $A^1 = \frac{4.8}{6.68} \times \frac{.8}{\pi} \times 2.37 \times 10^{-2} = 4.34 \times 10^{-3}$ cm^2

Since $A^1 = \frac{\pi}{4} D^2$, D = 7.4×10^{-2} cm. An effective collection aperture of 0.074cm will be used to design the radiometer calibration mirror.

The details of the collection mirror, both optical and mechanical, are currently being worked out and incorporated into the telescope design.

6. Test and Alignment Fixtures

A preliminary investigation into the fixtures necessary to align and test various subsystems of the IRIS instrument was performed during this reporting period. A list of these fixtures and their uses is given below:

a. Instrument Mount Assembly Alignment Fixture

To align the instrument support tube and its end caps during the bonding of these parts.

b. Reference Channel Interferometer Alignment Fixture

To align the two optical subassemblies with the moving mirror during assembly of the reference interferometer.

c. Radiometer and IRIS Detector Alignment Fixture

To align the radiometer and interferometer detectors with their collectors during assembly.

d. Interferometer Alignment Fixture

This fixture will be used to align the fixed mirror in the Michelson Interferometer with the beamsplitter and moving mirror.

e. IRIS Instrument Alignment Fixture

This fixture will be used to align the dichroic mirror, radiometer, and interferometer to the telescope assembly to complete the integration of all the subassemblies.

f. Instrument Mount Assembly Test Fixture

This fixture will be used to check the stability of the instrument mount assembly during launch vibration and cool down.

g. Instrument Thermal-Vacuum Test Fixture

This fixture, used in a thermal vacuum chamber, will simulate the environment in which the instrument will actually be used.

h. Instrument Calibration Targets

These targets will be used to calibrate the response of the radiometer and interferometer.

i. Instrument Vibration Fixture

A fixture which simulates the mounting configuration (and of the scan platform to the instrument) is rigid enough to prevent amplification of the input vibration in the frequency range of the launch vibration input. The fixture will allow vibration in three axes.

j. Electronics Vibration Fixture

A fixture which simulates the scan platform mounting configuration of the electronics package and power supply package. This fixture will allow vibration in three axes.

k. 200°K Alignment Test Fixture

This fixture will be used to check the alignment of the instrument at the 200°K operational temperature.

l. Field of View Check Fixture

This fixture will provide a means of mapping over the response of both the radiometer and interferometer.

7. Interferometer and Radiometer

a. Dichroic Mirror and Radiometer

The configurations of the dichroic mirror and radiometer are shown in Figure 2-58.

The dichroic mirror subassembly consists of a beryllium housing, which bolts directly onto the back of the telescope support, a dichroic mirror with its mount, and alignment wedges.

The dichroic mirror is used to separate the optical energy into two wavelength regions; the spectrum from 0.3 μ to 2.0 μ is transmitted to be collected by the radiometer and the 2.5 μ to 50. μ region is reflected into the interferometer.

The alignment wedges are used to adjust the angular position of the dichroic mirror such that the reflected energy is projected along the optical axis of the interferometer.

The radiometer consists of a beryllium housing, a thermopile detector and mount prealigned to an ellipsoidal collector and a preamplifier.

The relatively loose angular requirements of the radiometer permit machining of the housings interfaces to tolerances such that the radiometer can be bolted directly onto the rear of the dichroic mirror housing without angular adjustment. The lateral positioning is achieved by oversized bolt holes at the housings interface.

b. Interferometer Subassembly

The configuration of the interferometer has undergone two significant changes since the last reporting period. The first is that the alignment wedges between the collector and detector mount and the detector assembly to optics housing have been eliminated. The second is that the pyroelectric detector has been replaced by a thermopile detector. The latest configuration is shown in Figure 2-59.

It should be noted here that a significant change in the preamplifier package should be anticipated due to the detector change.

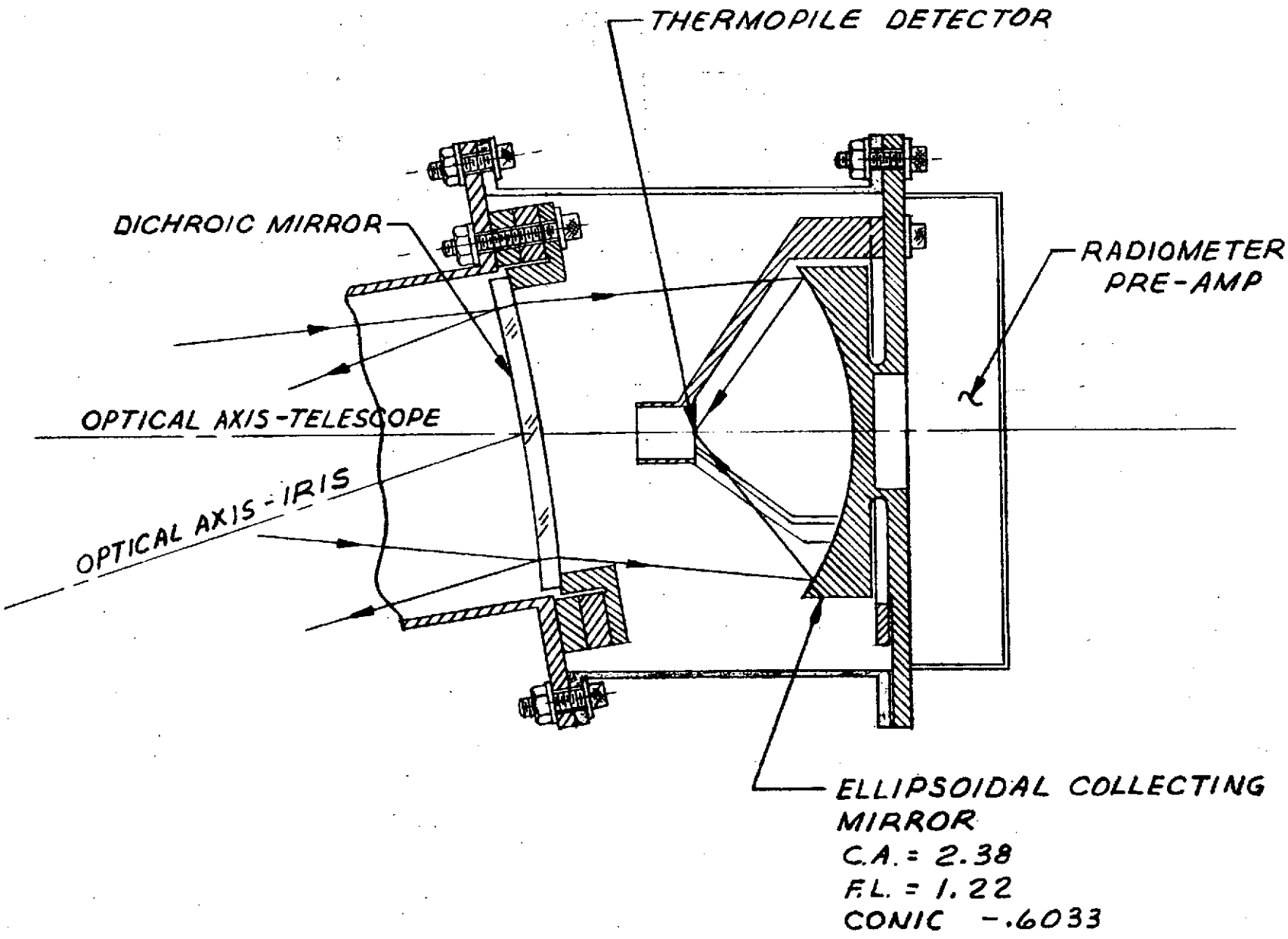

DICHROIC MIRROR AND RADIOMETER CONFIGURATION

FIGURE 2-58

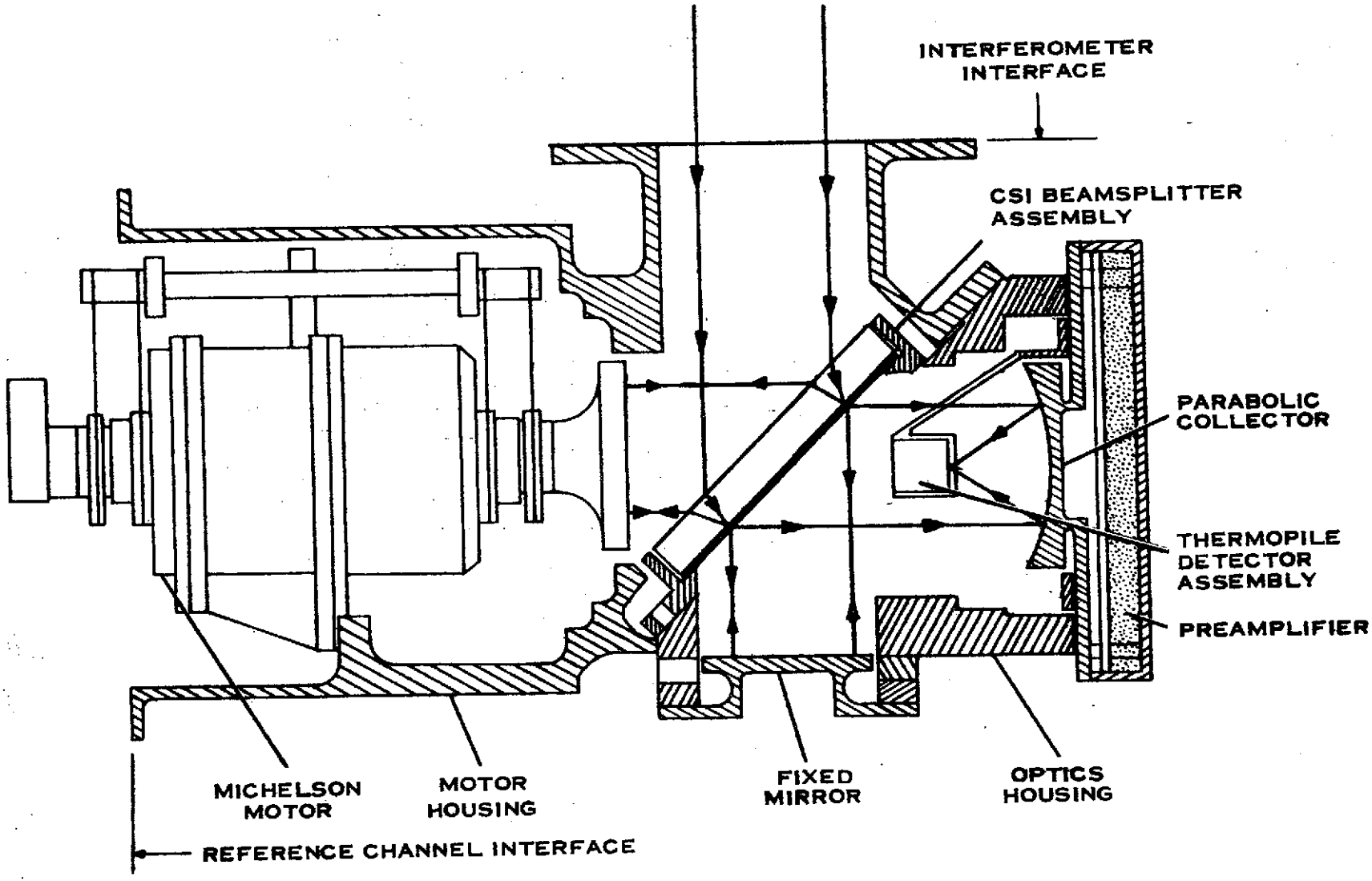

INTERFEROMETER CONFIGURATION

Figure 2-59

To utilize the thermopile detector in the interferometer requires a detector preamplifier transformer, which at present has not been completely defined. However, it is expected to require several times the space and weight allocated for the preamplifier package shown.

Reference Channel Interferometer Subassembly

The configuration of the reference channel interferometer has undergone extensive redesign. The new configuration is shown in Figure 2-60.

To increase mechanical stability in order to insure holding optical alignment during cool down to 200°K, the optics mount containing the beamsplitter, fixed mirror, and optical filter was redesigned to attach directly to the Michelson motor housing, thereby reducing to a minimum the number of mechanical interfaces between the critical optical elements of the interferometer. The less critically aligned elements (the neon sources, collimating optics, collecting optics, and silicon detector) are mounted in an assembly which is attached to the reference interferometer housing.

Access to the optical components is afforded by the use of a cover which contains the preamplifier and the source driver and is attached to the reference interferometer housing.

Not shown in Figure 2-60, and yet to be designed is the radiation spot shielding, used to protect the silicon detectors of both the interferometer and start position sensor.

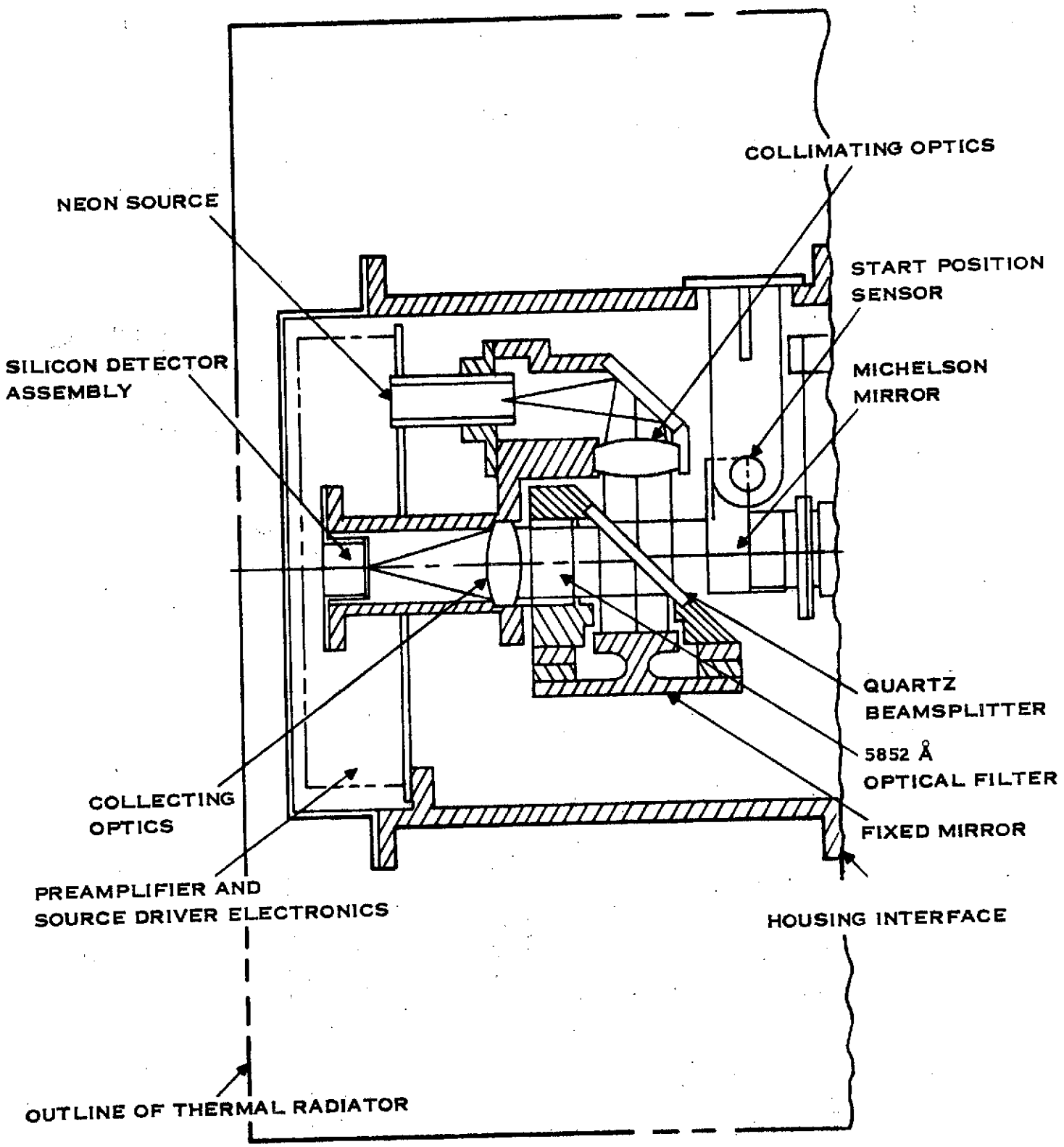

MJS IRIS REFERENCE CHANNEL

FIGURE 2-60

8. IRIS Mechanical Configuration

The current mechanical design parameters describing the IRIS instrument, electronics box, power supply, and related hardware are listed in Table 2-8 . The basic configuration of the instrument is shown in Figure 2-61 , and the electronics box and power supply on the scan platform are shown in Figure 2-62 . It should be noted that the optical centerline of the telescope will be aligned to the instrument mounting plate (to platform) within 0.2 milliradians of cone half-angle.

a. Instrument Support Tube

The design and fabrication of the advanced composite structural support tube for the IRIS instrument is currently out for quotations. A copy of the specification (877095) is enclosed in Appendix A. The apparent candidate composite materials are listed in Table 2-9 along with a relative comparison of single fiber properties. The matrix combination under initial consideration is shown in Figure 2-63. Preliminary analytical results of a tube design are anticipated by the middle of November 1974.

b. Telescope Dust Cover and N_2 Purge

Some preliminary numbers have been calculated by NASA Goddard which indicate the strong sensitivity of the IRIS telescope optics to dust particle contamination. This information is summarized in Table 2-10 for the condition where the scattered noise is on the order of the NER of the radiometer. A related problem is the moisture protection of the cesium iodide beamsplitter and general internal optical elements of the IRIS housing. A nitrogen purging scheme is being examined and it may be combined with a flexible "bag" type cover for the telescope dust protection. A possible scheme is shown in Figure 2-64, in which the bag cover is tied to the spacecraft shroud and jettisoned about 250 seconds after liftoff. Nitrogen flows into the optics housing and out into the bag during ground handling and prior to liftoff. A volume change rate of one to two per hour may be required. This corresponds to about 5 cubic feet per hour of room temperature dry nitrogen gas.

TABLE 2-8 MECHANICAL PARAMETERS

INSTRUMENT OUTLINE	21.75" OD X 29.70" LONG (STATIC) 22.0" OD X 29.70" LONG (DYNAMIC)
INSTRUMENT MASS PROPERTIES	17.6 LBm $I_{xx_{cm}} = 600\ lb_m\ in^2$; $P_{XY_{cm}} = -72\ lb_m\ in^2$ $I_{yy_{cm}} = 420\ lb_m\ in^2$; $P_{XZ_{cm}} = -30\ lb_m\ in^2$ $I_{zz_{cm}} = 600\ lb_m\ in^2$; $P_{YZ_{cm}} = 60\ lb_m\ in^2$
INSTRUMENT RESONANCES ON TUBE	160, 185 Hz
CONE LIMITATION ON S/C PLATFORM	94° (100° Goal)
ELECTRONICS BOX	4" X 8.5" X 13", 15.0 POUNDS
POWER SUPPLY	1.8" X 5" X 6.5", 2.8 POUNDS
CABLES	4 INTERCONNECTING: POWER (1), 6" INSTRUMENT (3), 10"
INSTRUMENT/PLATFORM	
a. THERMAL GRADIENT	200K TO 313K MAX. (ΔT, 203°F)
b. MECHANICAL ALIGNMENT	0.2 mr, CONE HALF-ANGLE

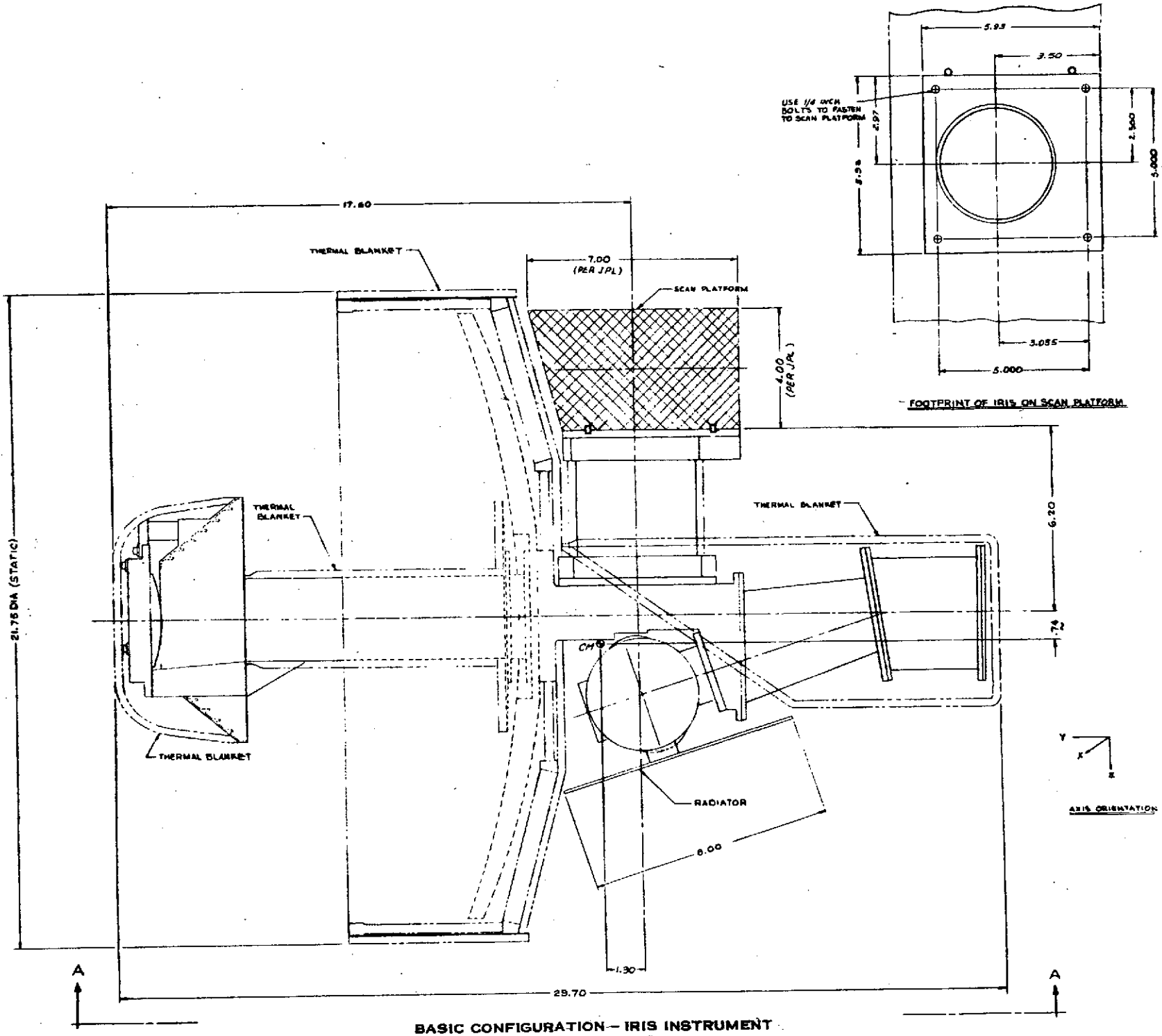

BASIC CONFIGURATION – IRIS INSTRUMENT
FIGURE 2-61

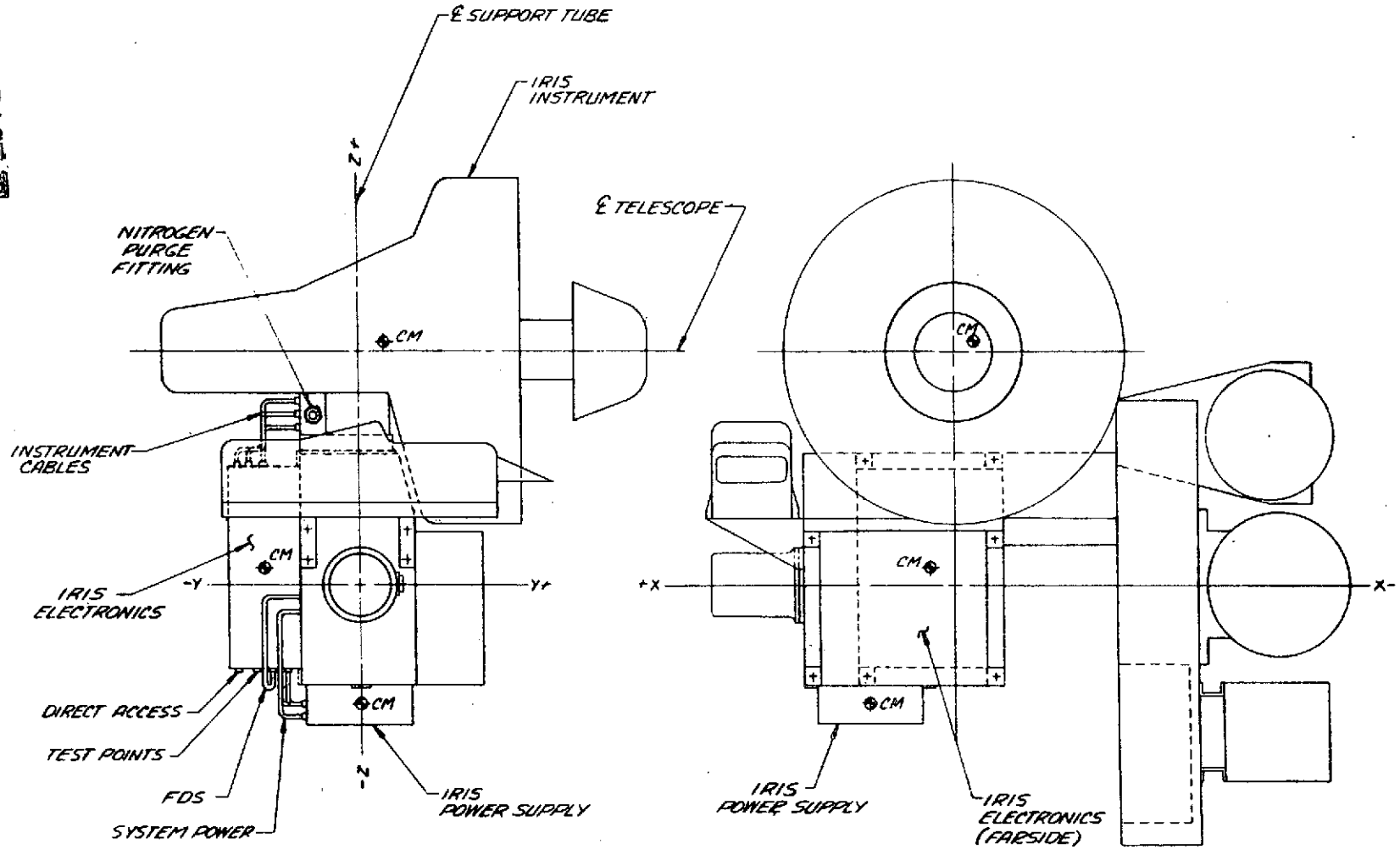

IRIS/SCAN PLATFORM PRELIMINARY CONFIGURATION

FIGURE 2-62

TABLE 2-9 COMPOSITE MATERIAL PROPERTIES

ASSUMPTIONS: SINGLE FIBER
PARALLEL DIRECTION
ROOM TEMPERATURE

MATERIAL (MFG)	TENSILE MODULUS (PSI)	THERMAL CONDUCTIVITY (BTU FT/FT^2 °F HR)
S-GLASS (OWENS-CORNING)	12.5×10^6	7.2
KEVLAR 49 (DU PONT)	19×10^6	0.3
BORON 4 (AVCO)	60×10^6	16
GRAPHITE GY-70 (CELANESE)	75×10^6	60
EPOXY	-	0.1

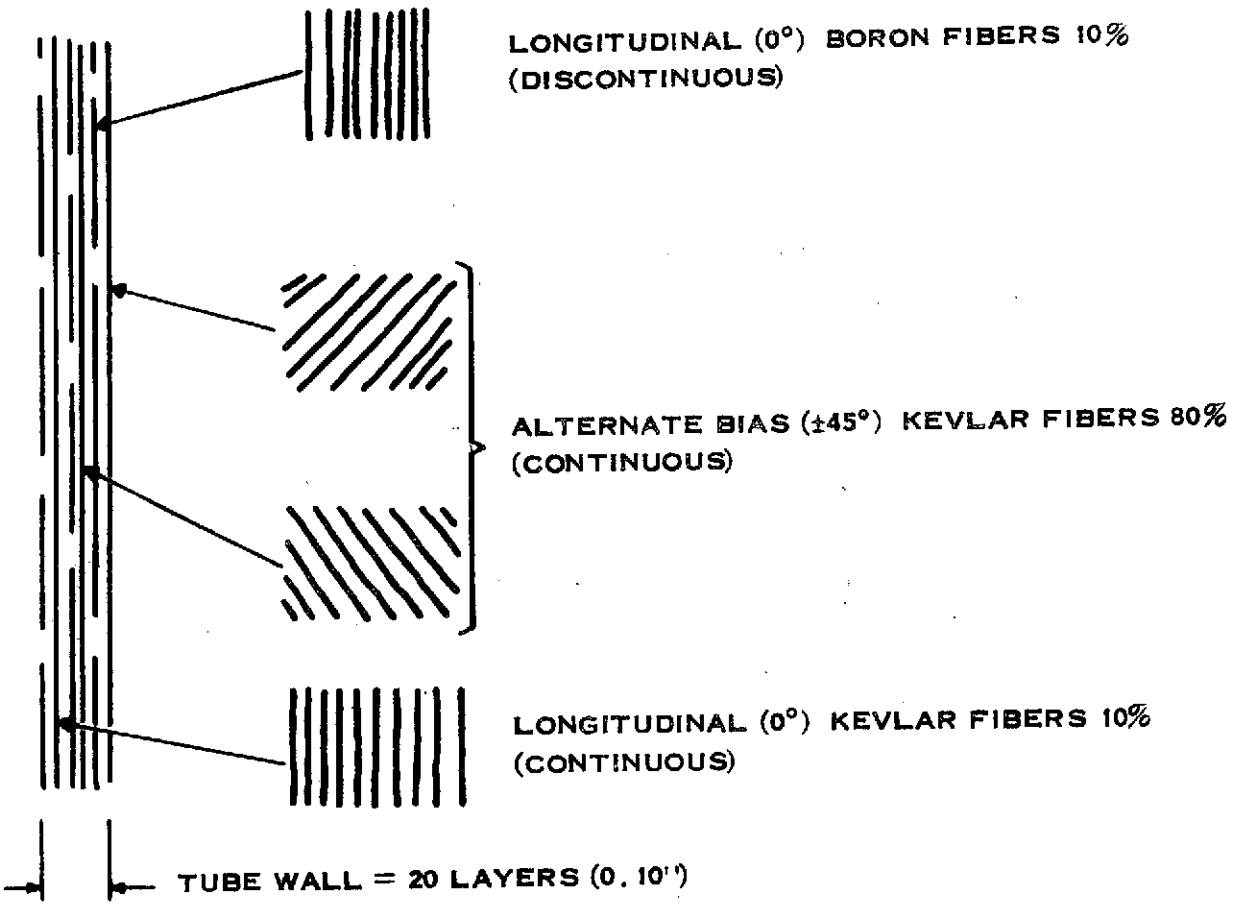

INSTRUMENT SUPPORT TUBE
PROBABLE ADVANCED COMPOSITE MATRIX
(SCHEMATIC REPRESENTATION)

FIGURE 2-63

TABLE 2-10 TELESCOPE DUST COVER AND NITROGEN PURGE

A. TELESCOPE DUST SENSITIVITY:

CONDITIONS:

1. SOLAR FLUX INCIDENT ON PRIMARY (1700 cm^2)
2. PARTICLE SIZE = 10μm, RADIUS
3. ACCOUNTING FOR FORWARD AND BACKSCATTER:
   REFLECTION/DIFFRACTION/TRANSMISSION FACTORS
4. FOR SCATTERED NOISE $\leq$ NER (RADIOMETER)

DUST AREA $\leq 5 \times 10^{-2}$ cm^2

CONCENTRATION $\leq$ 10 PARTICLES/cm^2

B. NITROGEN PURGE:

- FOR MOISTURE PROTECTION OF HYGROSCOPIC CESIUM IODIDE BEAMSPLITTER.
- FOR DUST PROTECTION OF ALL OPTICAL ELEMENTS AND INTERNAL CRITICAL COMPONENTS, I.E., MICHELSON MOTOR, ETC.

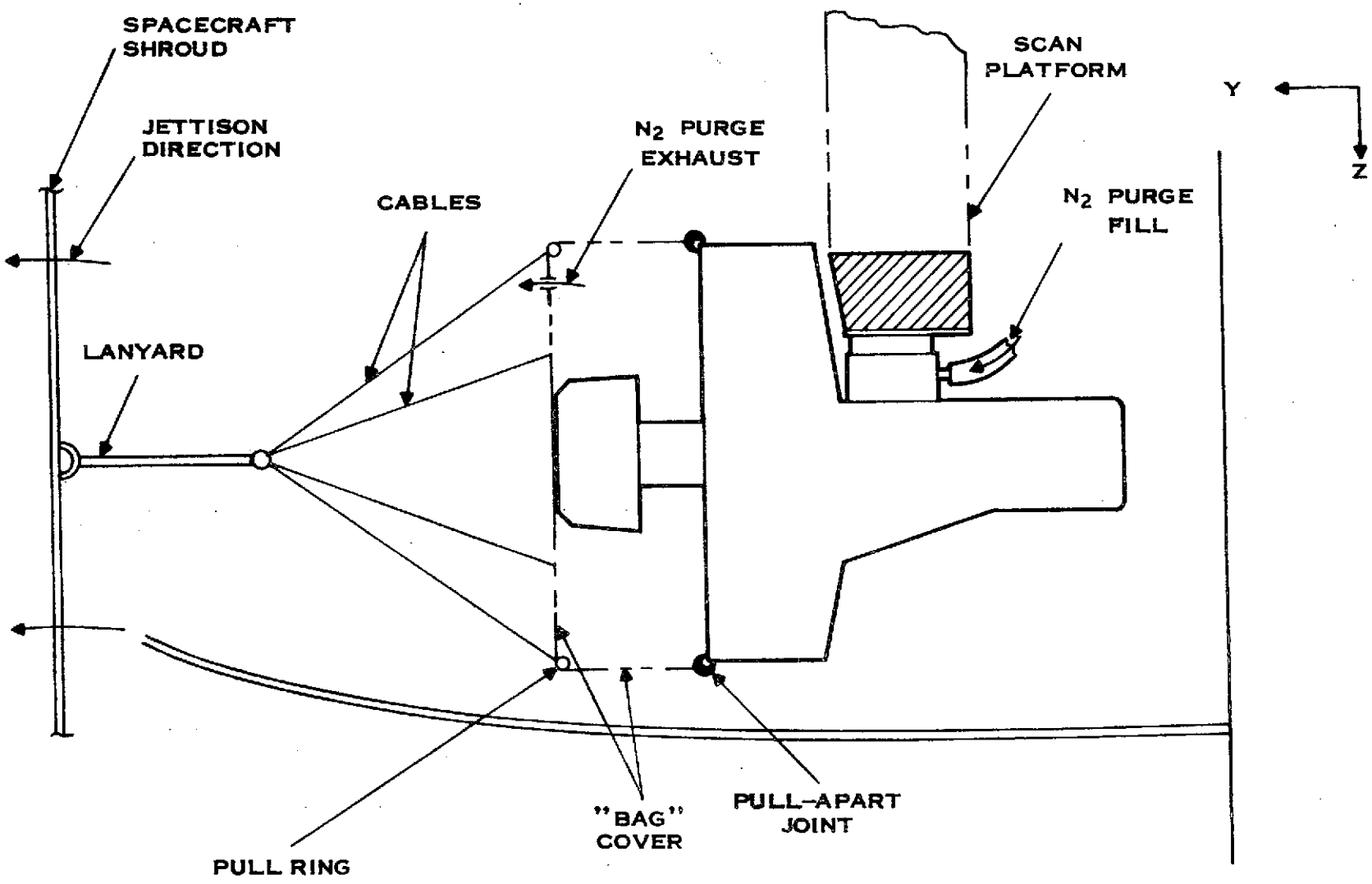

DUST COVER REMOVAL SCHEME

FIGURE 2-64

Although this scheme does not totally satisfy the dust protection desired through all rocket firings before scan platform deployment, it does point out the necessity of the spacecraft and perhaps vehicle engineering in working with TI to design a satisfactory dust protection scheme.

c. Thermal Blankets Fabrication

The preliminary geometry of the seven thermal blankets required by TI for the IRIS instrument are shown in Figure 2-65. These layouts have been submitted to JPL for comments and recommendations. JPL will supply these blankets to TI for the engineering model, proof test model, thermal model, and two flight models.

d. MJS IRIS Mass Estimate

The latest estimated mass distribution for the IRIS system is shown in Table 2-11. Included in the IRIS instrument subtotal value are mass allotments for radiation hardening : 300 grams for the interferometer detector transformer and, 100 grams for a spot shield of the motor position detector, and 100 grams for a spot shield of the radiometer detector. The electronics module mass estimate includes 225 grams for spot shielding of components. Note that the total mass estimate in the specification column of 35.5 lbm does not include any allotments for radiation hardening. A tentative agreement between TI and JPL to exchange the 0.9 pounds mass in the instrument subtotal (for stiffening the interface plate with the platform) for the 1.0 pounds of interconnecting cables will reduce the latest total mass estimate to 38.21 lbm.

e. IRIS Instrument Transit Case

TI is currently receiving bids for the transit case described in Table 2-12. This case will be used to transport the telescope assemblies as purchased from the vendor as well as the entire instrument when it is shipped between TI and JPL.

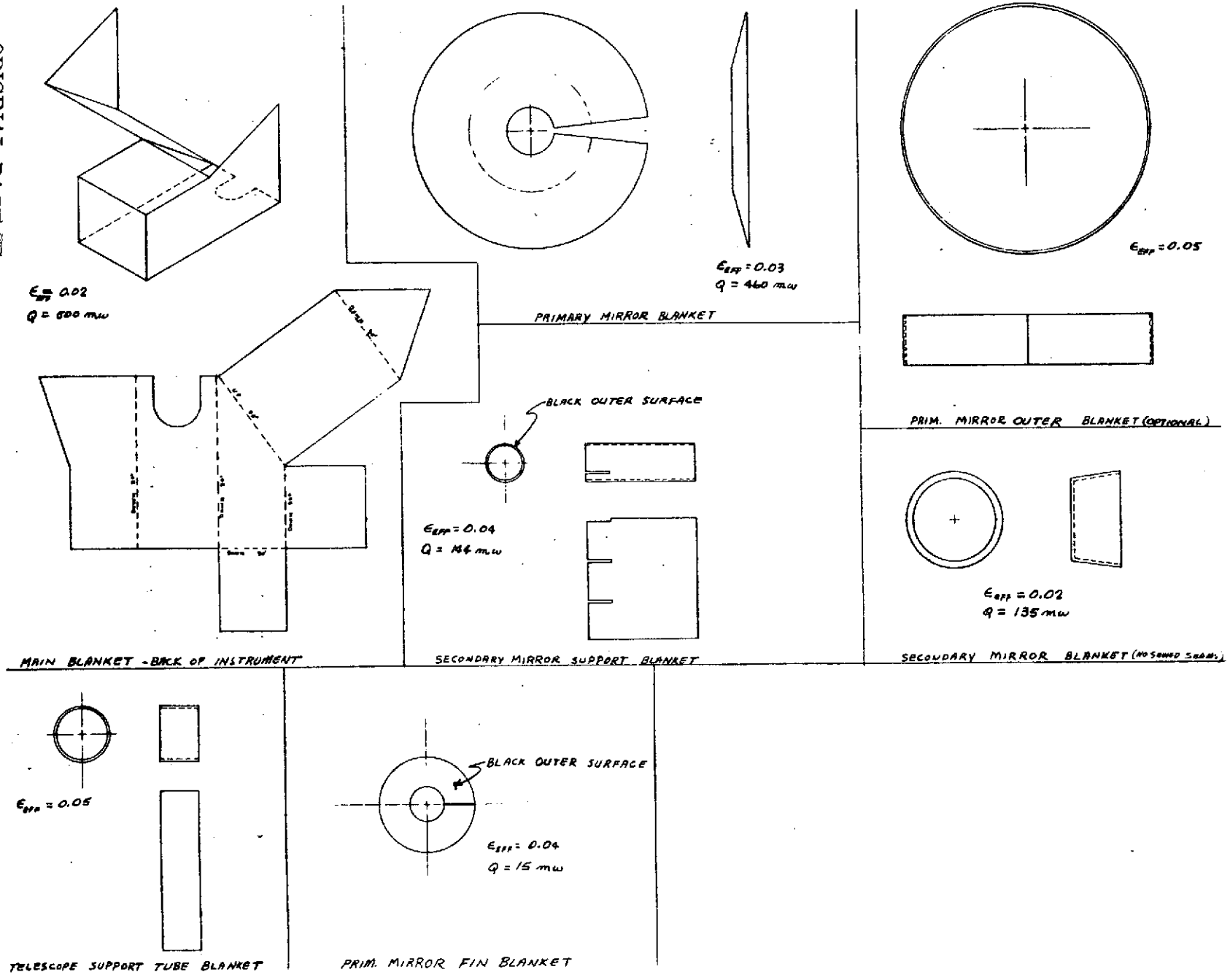

FIGURE 2-65 THERMAL BLANKETS – PRELIMINARY GEOMETRY

TABLE 2-11 MJS IRIS MASS ESTIMATE

ITEM	PRESENT ESTIMATE INCLUDING RADIATION	IMPACT	SPECIFICATION VALUE
TELESCOPE ASSEMBLY	8.14 lbm	(3.70Kg)	
INTERFEROMETER	6.97 lbm	(3.16Kg)	
RADIOMETER	.69 lbm	(.31Kg)	
THERMAL BLANKETS	1.30 lbm	(.59Kg)	
MISC HARDWARE	1.60 lbm	(.73Kg)	
IRIS INSTRUMENT(SUBTOTAL)	18.70 lb	(8.49Kg)	21.51 lbm(9.76Kg)
ELECTRONICS MODULE	15.5 lbm	(7.04Kg)	9.9 (4.49Kg)
POWER SUPPLY	2.8 lbm	(1.27Kg)	3.1 (1.41Kg)
INTERCONNECTING CABLES	1.0 lbm	(.45Kg)	1.0 (.4Kg)
TOTAL	38.0 lbm	(17.25Kg)	35.5 (16.11Kg)
CONTINGENCY	1.21lbm	(.55Kg)	
TOTAL MASS ESTIMATE =	39.21lbm	(17.80Kg)	

TABLE 2-12 IRIS - TELESCOPE/INSTRUMENT TRANSIT CASE

REQUIREMENTS:	TELESCOPE SUPPORTED AS ON SCAN PLATFORM
	SHOCK PROTECTION PROVIDED
	GAS AND DUST TIGHT
	NITROGEN PURGE PROVISION
	SIGHT WINDOW

PROPOSED CONTAINER:

DIMENSIONS	23" x 24" x 32"
MATERIAL	.090" THICK-6061-T4 ALUMINUM
LATCHES	5
HINGES	3
HANDLES	2
FINISH	NASA BLUE PAINT

9. Thermal Design

A thermal model of the optics zone has been constructed. Optics zone heater powers have been determined using this model. The telescope thermal model described in the last quarterly report has been revised to include the effect of interaction with the optics zone. Structural members used to attach the primary mirror sun shade and the secondary mirror baffle have been included in the present model. Results showing worst case cold temperature gradients over the primary mirror have been obtained for a range of possible mirror emissivities and primary mirror blanket effective emittances. Relationships between flash-off temperature and total heater power have been determined. Transient temperature response of the three instrument zones during flash-off and cool-down has been investigated.

a. Heat Load Factors

The radiant heat fluxes and the optics electronics powers presented in the first quarterly report remain unchanged. Updated information on system design has resulted in changes for values associated with heat transfer between the scan platform and the IRIS instrument. Heat transfer down the boron-epoxy support tube was given as a maximum of 400 MW for a scan platform temperature of 313°K. Although the support tube conductance has not been accurately determined as yet, more recent property data shows that heat transfer down the tube for a 313°K scan platform will be 950 MW.

Calculations for heat transfer along electrical cables connecting the scan platform to the instrument have also been revised. First quarter efforts were based on an assumed total of 60 wires, each 20 inches long. Present calculations based on more recent design information assume 70 wires, each 15 inches long. Heat transfer down the wires for a 313°K scan platform has increased from 464 MW to 650MW.

b. System Thermal Models

The thermal models for the telescope and the interferometer zone have been refined to increase accuracy.

1. Telescope

The telescope thermal model has been improved to include the effect of structures connecting the primary mirror sun shade and the secondary mirror baffle to the main system. Thermal interaction with the interferometer and radiometer zone has also been described with more certainty. A schematic of the 52 node network used to model the telescope is shown in Figure 2-66.

The lumped mass thermal model of the telescope was used in conjunction with an analytical model to define worst case cold temperature gradients across the primary mirror for a range of mirror emissivities and mirror blanket effective emittances. Results of this analysis are shown in Figure 2-67. The range of mirror emissivities shown, .025-05, is conservatively high for a polished mirror surface. The range shown for blanket effective emittance, again .025-.05, should span performance expected from blankets in this application. The curve labeled "Design Case" on Figure 2-67 is for mirror and blanket emittance of .025 and .035, respectively. At this condition the calculated maximum mirror gradient of .18°K is within the design goal of .2°K. Maximum gradient varies from .15°K to .28°K for the range of emissivities shown in Figure 2-67.

2. Interferometer and Radiometer

The level of thermal modeling for this zone of the instrument has become significantly more detailed since the first quarterly report. A schematic of a 30 node model for this zone is shown in Figure 2-68. Although much more detail is needed to accurately describe radiometer temperatures and internal component temperatures in the IRIS instrument, this model describes gross system effects. A 22 node reduction of the model shown in Figure 2-68 has been paired

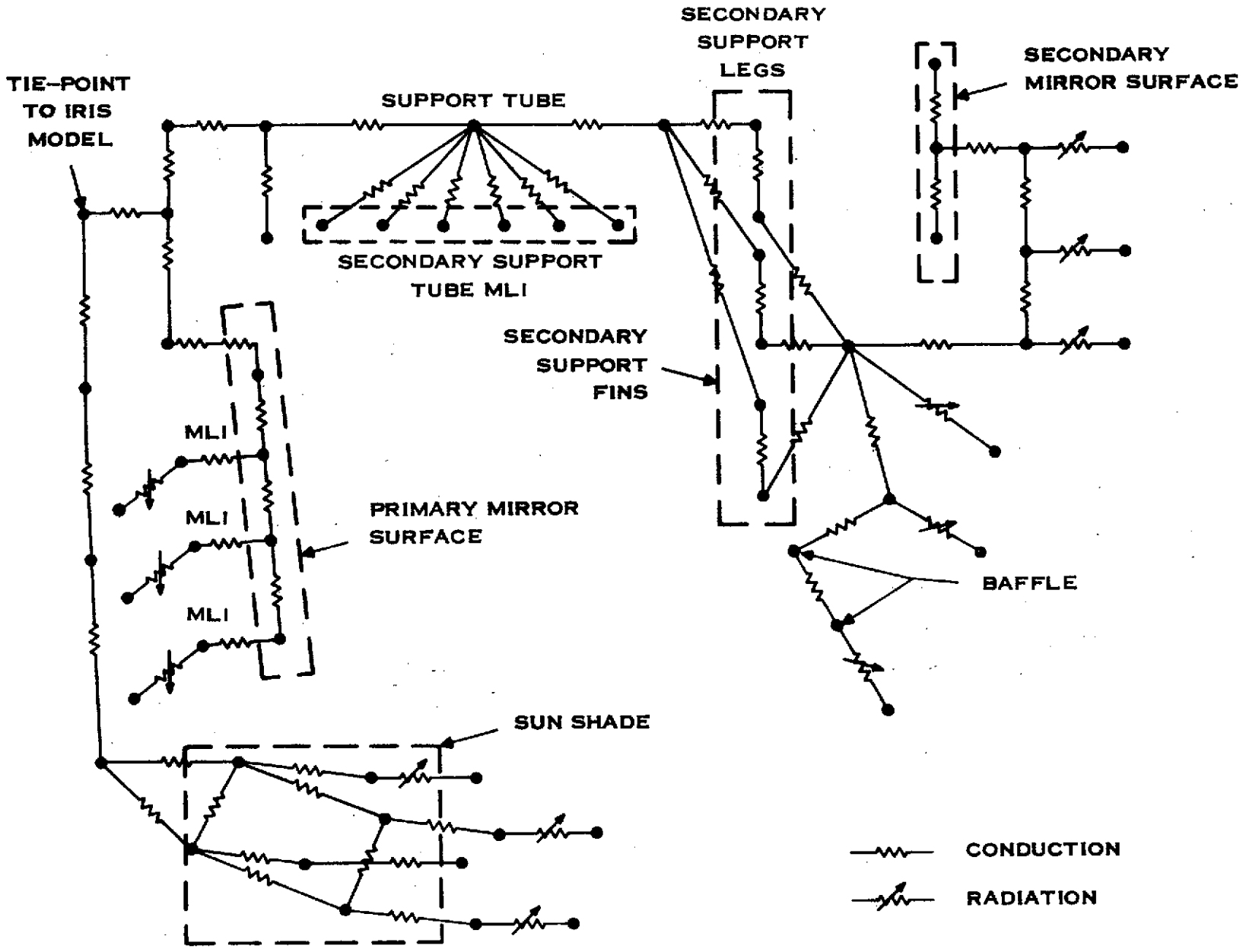

TELESCOPE THERMAL MODEL

FIGURE 2-66

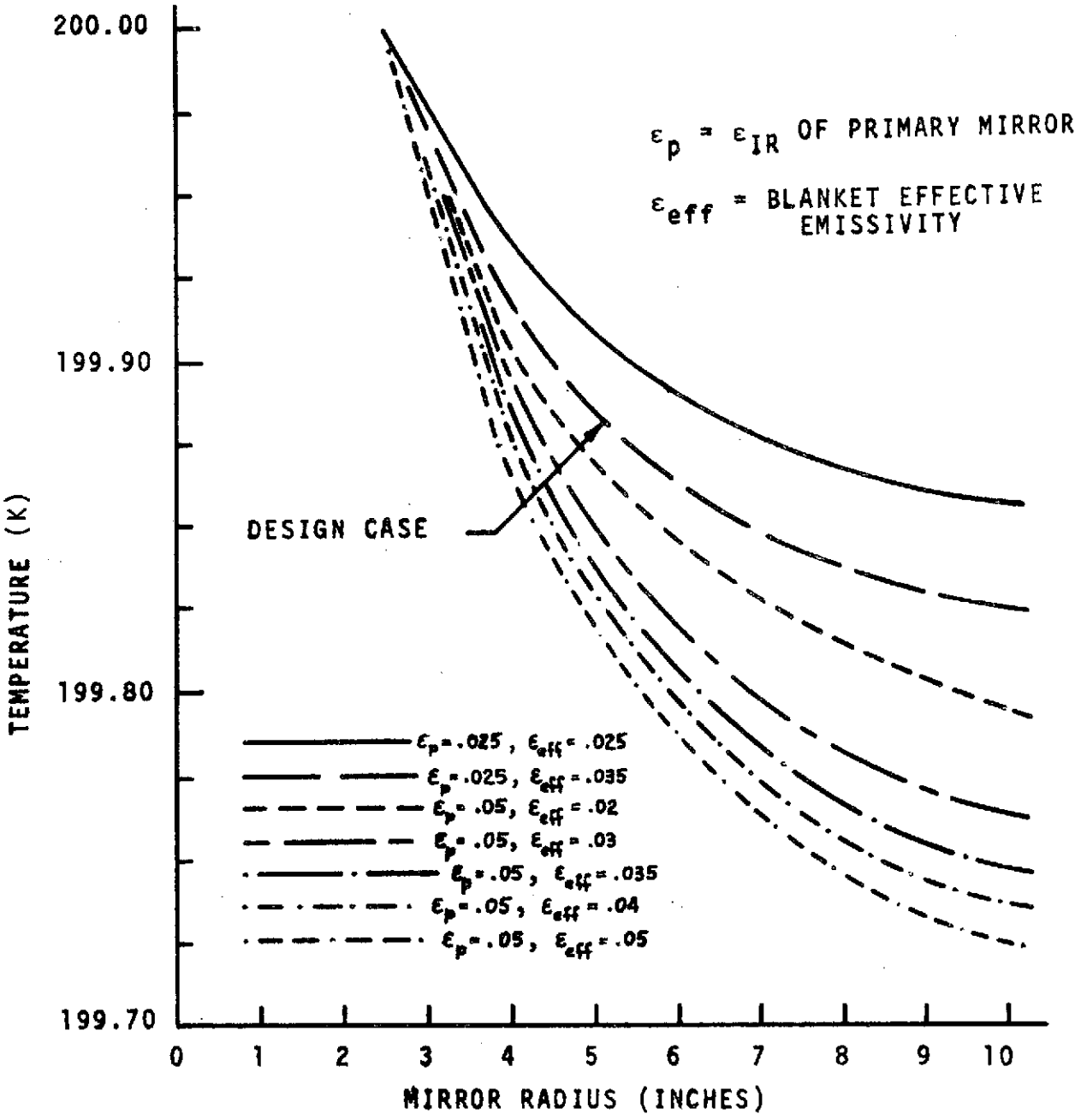

PRIMARY MIRROR TEMPERATURE DISTRIBUTION
WITH VARYING MIRROR AND BLANKET EMITTANCES

FIGURE 2-67

9-10-74, JP, 0744

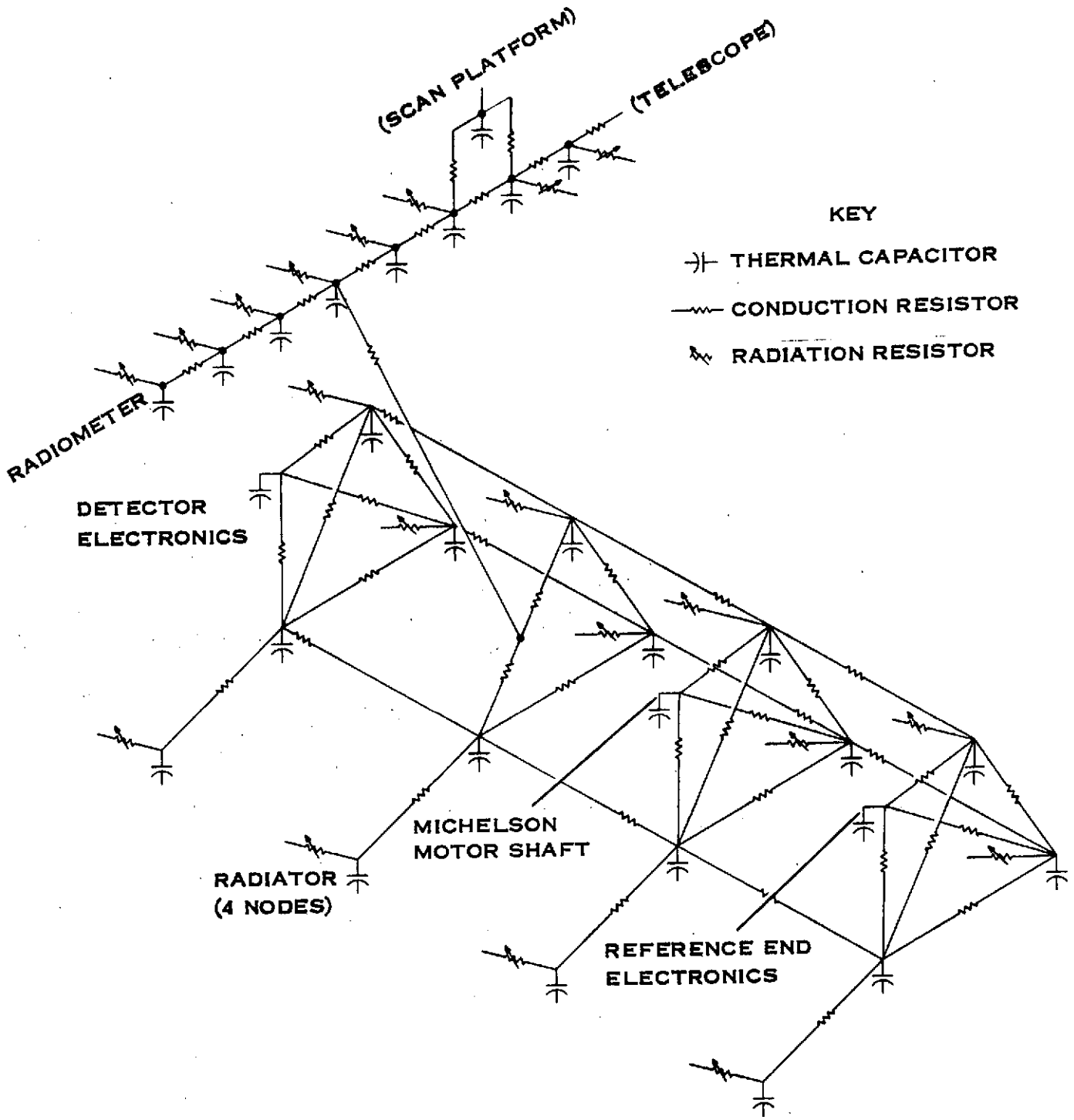

FIGURE 2-68

IRIS AND RADIOMETER THERMAL NETWORK

with the telescope model shown in Figure 2-66 to describe total system operation and to define system heater requirements.

c. System Heat Balances

An important use for the system thermal models described previously has been to predict heater powers needed within each zone to maintain thermal control. Heater powers as well as other heat terms are shown in the heat balances of Tables 2-13,2-14 and 2-15.

1. Primary Mirror

The primary mirror results shown in Table 2-13 are for a mirror solar absorptance of .08, an IR emittance of .05, and a blanket emittance of .035. The required heater power varies from 165 MW to 1.236 watts. The mirror properties given above are conservative for the worst case cold condition, especially the IR emittance of .05 which is large for a polished mirror surface. Thus, the worst case cold heater power of 1.236 watts should be conservatively large for the configuration modeled. However, the indicated hot case heater power of 165 MW does not give a suitable design margin. Since these calculations were for an optimistic mirror solar absorptance of .08, possible with bare aluminum but not with gold or silicon-monoxide overcoated aluminum, the design for this zone of the instrument may have to be changed to provide additional radiative power. This possibility is presently being investigated.

2. Secondary Mirror

A heat balance for the secondary mirror zone is shown in Table 2-14 . Heater power for this region can be seen to vary little from cold to hot conditions, ranging from 1.218 watts to 1.320 watts. The high margin of heater power at worst case hot conditions suggests that some conservation of power may be possible by reducing zone radiative power.

TABLE 2-13 PRIMARY MIRROR HEAT BALANCE

CASES: STEADY STATE, WORST CASE HOT AND COLD

GAINS AT 200K (WATTS)	WC HOT		WC COLD	
SOLAR LOAD (α_s = .08)	.724		0.00	
CONDUCTION FROM IRIS ZONE	.461	.626	.115	1.351
HEATER	.165		1.236	
TOTAL	1.350		1.351	

LOSSES AT 200K (WATTS)		
RADIATION FROM MIRROR, FRONT ϵ = .05	.787	.789
RADIATION FROM MIRROR MLI ϵ_{eff} = .035	.563	.562
TOTAL	1.350	1.351

TABLE 2-14 **SECONDARY MIRROR AND BAFFLE HEAT BALANCE**

CASES: STEADY STATE, WORST CASE HOT AND COLD
HEATERS ON SUPPORT FINS

GAINS AT 200K (WATTS)	WC HOT	WC COLD
REFLECTED SOLAR IMAGE	.008	0.00
BLANKET LEAKAGE	.137	0.00
HEATERS	1.218	1.320
TOTAL	1.363	1.320

LOSSES AT 200K (WATTS)		
RADIATION FROM MIRROR MLI ϵ_{eff} = .05	.105	.105
RADIATION FROM BAFFLE MLI ϵ_{eff} = .05	.089	.084
CONDUCTION FROM FINS TO SUPPORT TUBE	.222	.231
RADIATION TO OTHER ZONES AND TO SPACE	.947	.900
TOTAL	1.363	1.320

TABLE 2-15 IRIS & RADIOMETER HEAT BALANCE FOR JSI—JUPITER MISSION

HEAT GAINS AT 200°K	WC HOT 20° TO SUN	WC HOT SUN ON RADIATOR	WC COLD
OPTICS ELECTRONICS	1.34		1.34
INSTRUMENT SUPPORT STRUCTURE	0.95		0.57
ELECTRONICS CABLES	0.65		0.39
DIRECT SOLAR LOAD	—0—	0.26	—0—
PLANET ALBEDO	0.09		—0—
PLANET IR	0.93		—0—
SPACECRAFT BUS			—0—
SPACECRAFT ANTENNA			—0—
TOTAL GAINS	3.96	4.22	2.30
LOSSES AT 200°K			
FROM RADIATOR (540 cm^2)	3.92	3.92	3.92
THRU THERMAL BLANKET	0.33	0.33	0.33
TO TELESCOPE	0.68	0.68	0.35
TOTAL LOSSES	4.93	4.93	4.60
IRIS & R NET HEAT LOSS	0.97	0.71	2.3
RADIATOR HEATER CAPACITY	3.00	3.00	3.00
RADIATOR HEATER DEMAND, %	32%	24%	77%

3. Interferometer and Radiometer

A heat balance for the interferometer and radiometer zone showing a detailed breakdown of thermal interaction with the rest of the system is shown in Table 2-15. Results for worst case hot and worst case cold conditions show required heater powers of .97 watts and 2.30 watts, respectively. With an assumed nominal heater power of 3 watts, these values indicate a heater duty cycle of 32% to 77%. This figure also shows results for the case of direct solar flux striking the OSR radiator surface. The OSR material was assumed to have a solar absorptance of .01 and an IR emittance of .8. Although the current restriction is that the radiator not "see" the sun except for brief periods, these results show that thermal control should be possible at Jupiter with solar flux on the radiator.

d. Flash-Off Modeling

The present system will have two "flash-off" heaters, one in the Interferometer-Radiometer zone and the other on the primary mirror, for the purpose of raising system temperatures high enough to drive any condensed contaminants from the optics elements. The thermal models described previously have been used to define heater powers needed during this "flash-off" process. Required heater power vs system temperature is shown in Figure 2-69 . It can be seen that a system temperature of 300°K can be reached with a total heater power of 32.4 watts.

A flash-off heater is not located on the secondary mirror zone, so temperatures in that region will be lower than the control temperature. The temperature differential will vary from 5°K at a 200°K system temperature to 20°K at a 300°K system temperature.

e. Transient Modeling

The thermal models described previously have not been used for detailed transient investigations. Instead, a nine mode model using information obtained from the more detailed models has been used to predict system transient behavior. Transient results are shown in Figures 2-70 , 2-71 , and 2-72 .

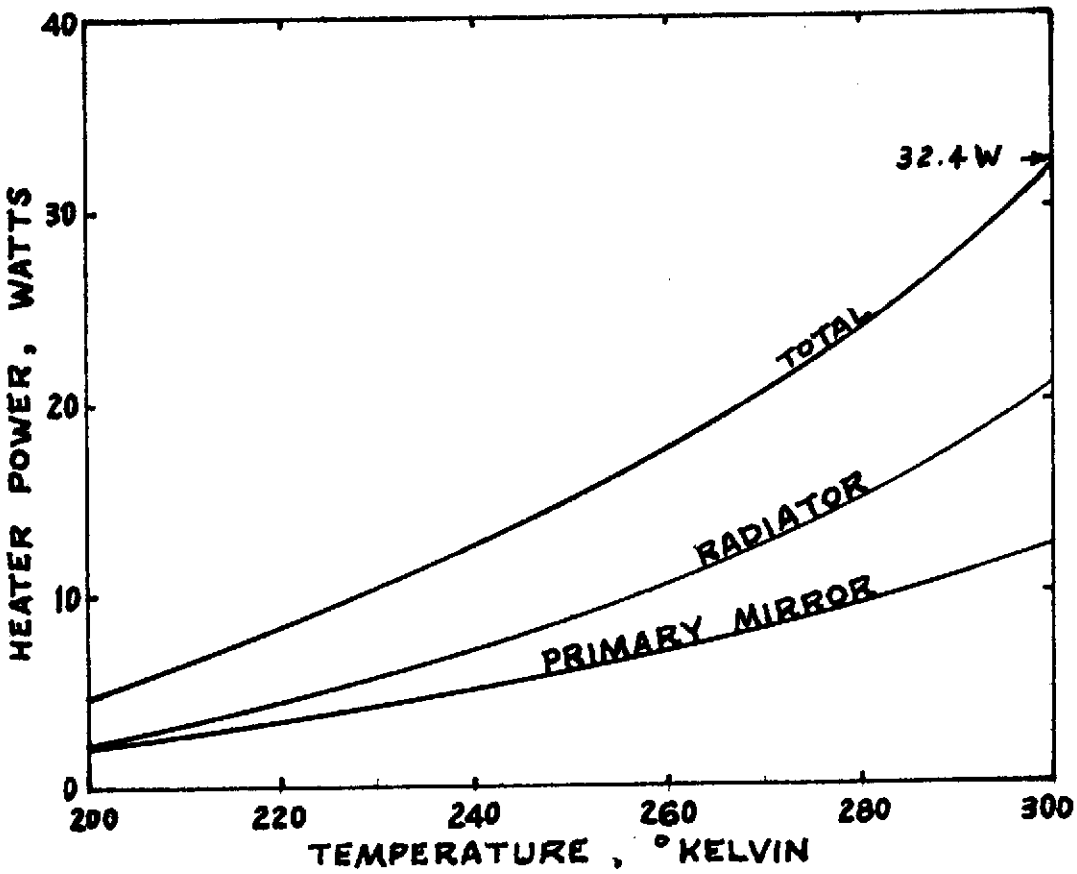

FLASH-OFF HEATER POWER REQUIRED vs. TEMPERATURE

FIGURE 2-69

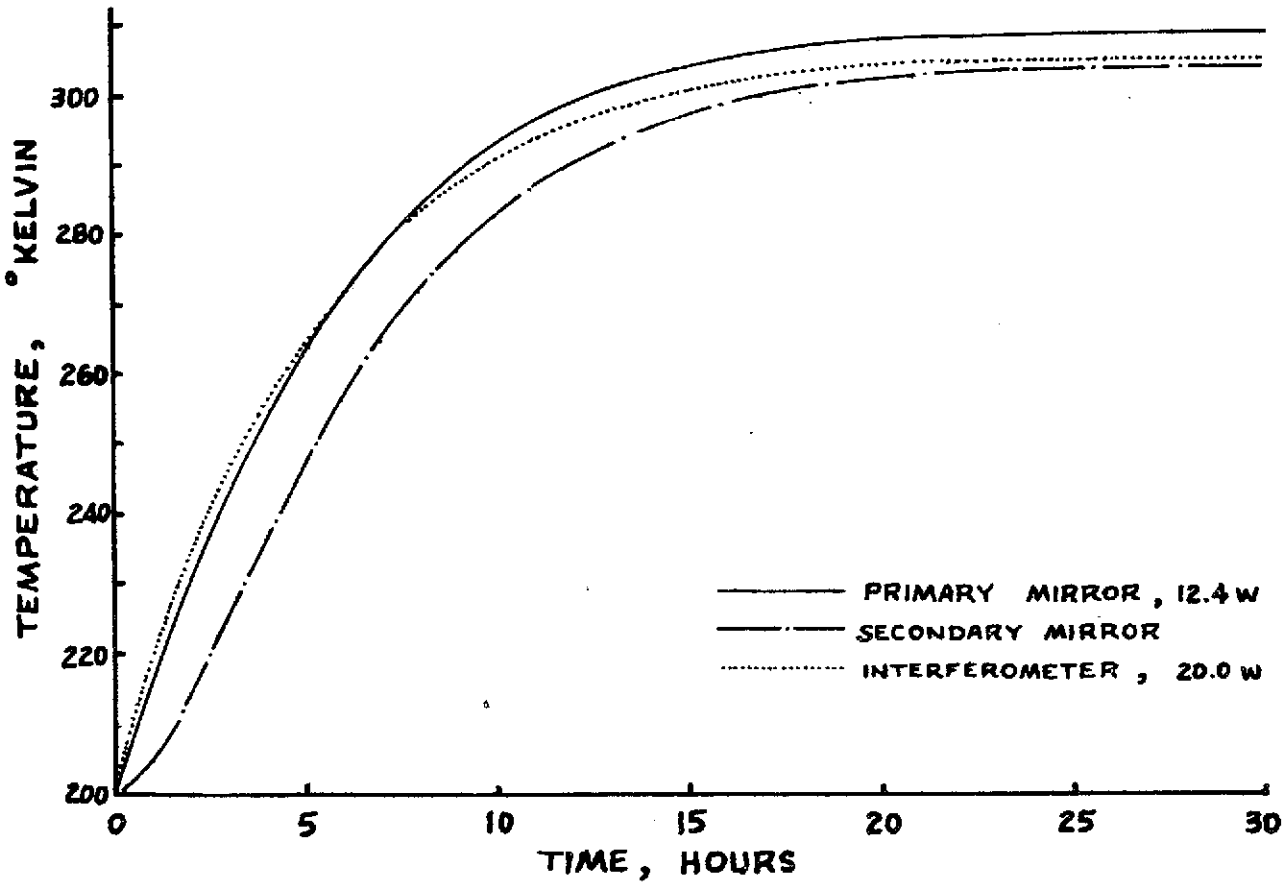

TEMPERATURE RISE IN FLASH-OFF

FIGURE 2-70

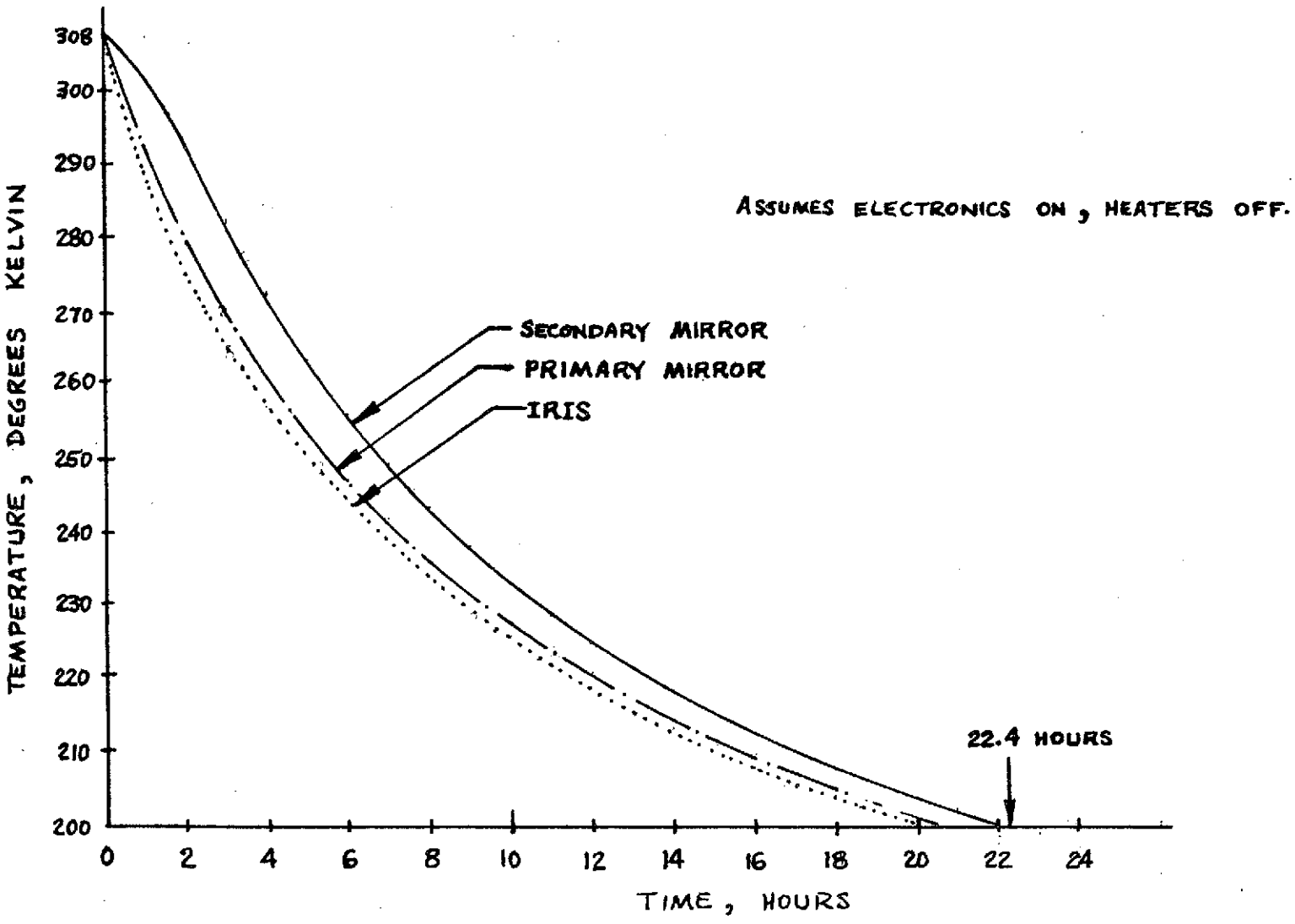

COOLDOWN FROM 308 °K TO 200 °K

FIGURE 2-71

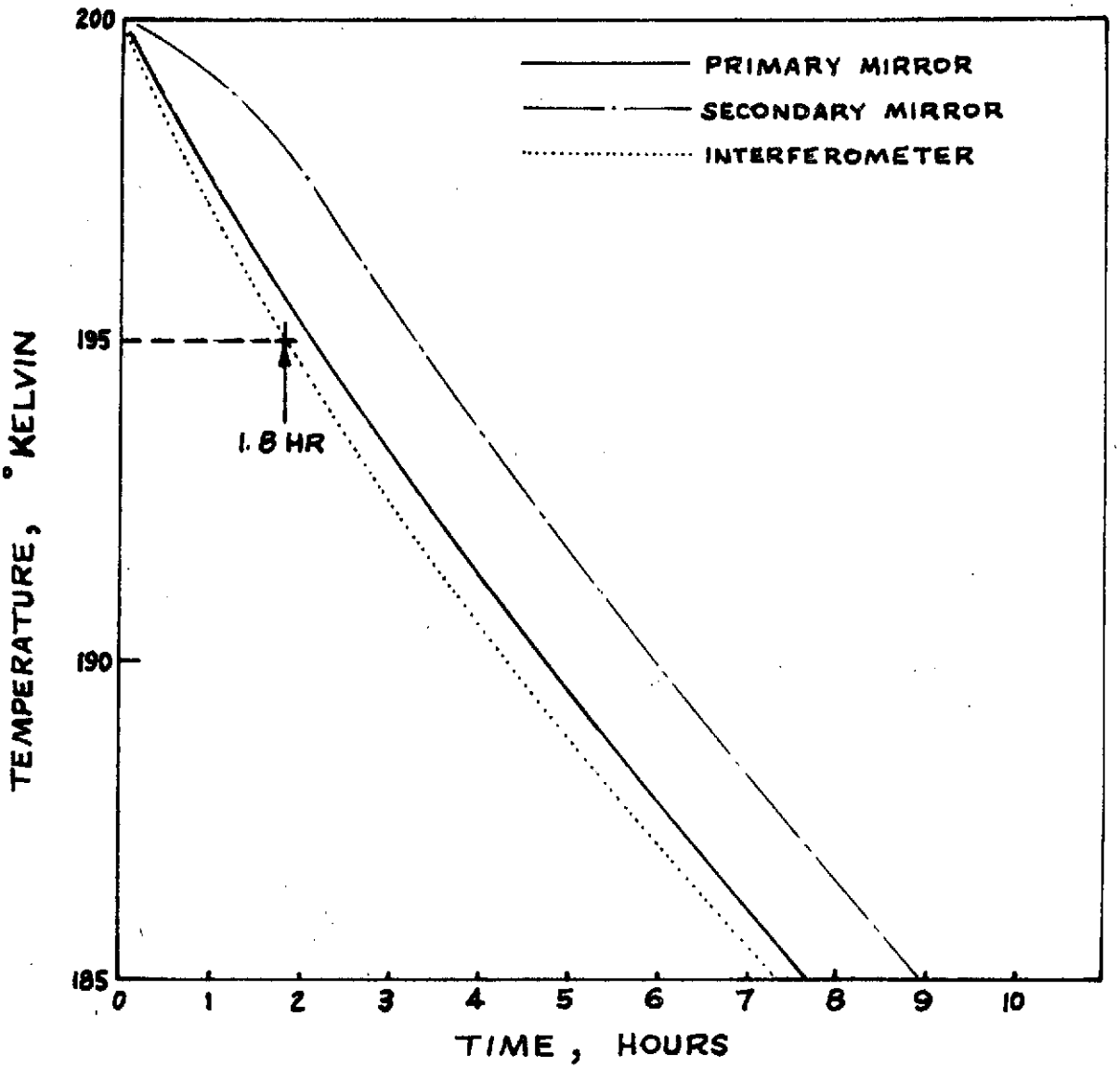

COOLDOWN FROM 200 °K
FOLLOWING HEATER SHUTOFF

FIGURE 2-72

Response during a flash-off operation is shown in Figure 2-70. Although differences in individual zone response are indicated, the model used to obtain these results was not detailed enough to accurately predict such effects. The gross response of the total system can be seen, however. The system has adjusted to the flash-off heater power and reached 300°K within 15 hours.

The maximum allowable temperature for the system is 308°K. Transient response of the instrument as it cools down from the maximum temperature is shown in Figure 2-71. The case shown is for that of no solar inputs and no heater power. Approximately 22 hours are required for the system to reach the operational temperature of 200°K.

Spacecraft requirements may dictate that the systems heaters be shut off for short time periods. Transient response of the system as it cools from 200K with no heater power is shown in Figure 2-72. A critical system component, the interferometer beamsplitter, has a lower temperature limit of 195°K. Figure 2-72 shows that in less than two hours without heater power the system will cool to 195°K.

10. Electronic Packaging

Figure 2-73 shows the relationship (schematically) of the three major packages of the IRIS, with their interconnecting cabling. The electronic module assembly and the power supply assembly will be discussed in this section of the report. Design layouts have been completed on both assemblies and piece part designs have been prepared for drafting.

The electronic module is shown in Figure 2-74 . This assembly measures 8.5 in x 13.0 in x 4.0 in (exclusive of the mounting lugs) and will weigh approximately 15.5 lbs.

> Note: The contract Statement of Work gives the size as 8.5 in x 11.5 in x 3.5 in and a weight of approximately 9.9 lbs. The increase in size reflects the increase in circuitry required for radiation; the increase in weight reflects additional weight for spot shielding of components as well as a reallocation of the total mass between the three assemblies of the IRIS.

The construction takes the form of a machined aluminum base and drawn aluminum cover. The assembly is electrically and thermally bonded to the scan platform at the mounting lugs.

The electronics is packaged on six multilayer printed circuit boards, mounted on eleven spacers, and bolted to the base plate. (The centrally located thru-bolts will also extend through the cover). Multilayer boards provide a high component density capability, necessary to meet the weight and volume restrictions. Packaging of this type has been successfully utilized on a recent program for GSFC (RAMS) in which densities of 4 CMOS flat packs per sq. in. and up to 6.5 discrete components per sq. in. were achieved.

Connector brackets, mounted to the base plate, carry the interface connectors at either end of the assembly. The power supply connector, FDS interface connector , direct access connector and a test point connector are at one end, and the instrument interface connectors at the other. (See Figure 2-73)

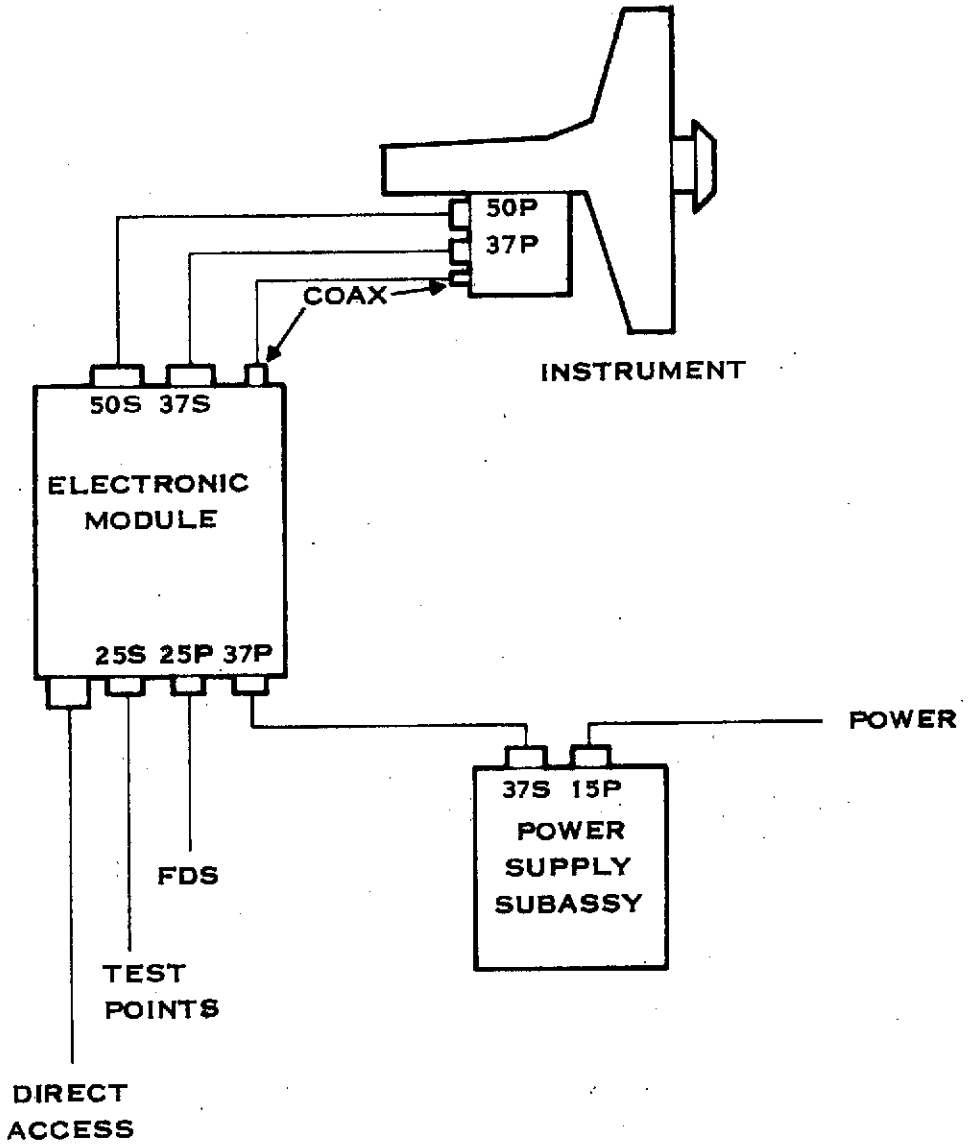

CONNECTORS: COAX: M39012/60-3001 SERIES SMA 50 OHM
DIRECT ACCESS: DS311-14-19S
ALL OTHERS: CANNON RECTANGULAR
(ST 10091/ST 10092)

IRIS CABLES

Figure 2-73

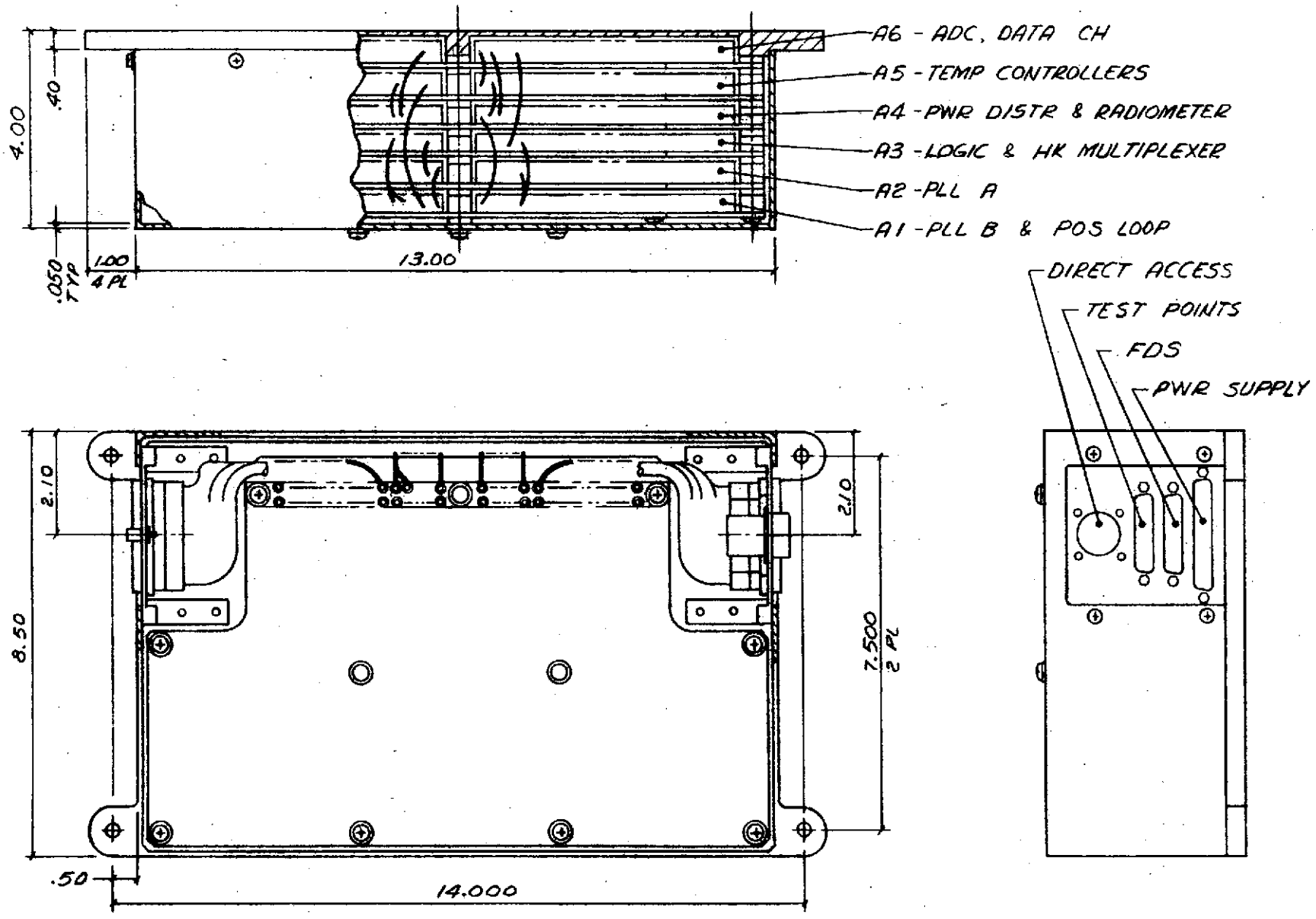

ELECTRONICS MODULE

FIGURE 2-74

Internal harnessing is dressed along the edge of the circuit boards and terminated to swagged terminals. Board-to-board connections are hand wired between the terminal rows. The power will be fanned out from the power distribution boards by separate wires to each of the other boards. Maintaining the harnessing along this single edge of the boards provides for facility of initial assembly and ease of trouble shooting maintenance by permitting the boards to be fanned out similar to pages of a book.

There will be some components mounted directly to the inside of the aluminum base. These are the housekeeping thermistor, FDS temperature sensor, and the replacement heater.

The electronic board assemblies have been arranged in the housing with the most radiation sensitive assembly next to the base plate, the second most sensitive next, and so forth. This provides increased shielding, by virtue of the layers of printed wiring boards above the more sensitive assemblies. This arrangement is, from the base plate up, as follows:

2039A2A6 ADC Data Channel
A2A5 Temperature Controllers
A2A4 Power Distribution and Radiometer Channel
A2A3 Logic and Housekeeping Multiplexer
A2A2 Phase Lock Loop A
A2A1 Phase Lock Loop B and Position Loop

Discrete shielding will also be provided for the ADC reference diodes. These will be housed in a small CRES box of .10 in. wall thickness, mounted to the ADC board.

A thermal analysis of the assembly, calculating the resistive paths, through the boards and spacers to the base and mounting lugs show, conservatively, that the highest component temperature will not exceed 21°C above the scan platform temperature. Specific components, dissipating a significant amount of heat, will be mounted to provide a low resistance direct path to the base to stay within the 21°C rise.

There are two Michelson motor driver transistors on the A1 board and two stud mounted transistors on the power distribution board. These will be mounted on aluminum plates bonded to the board at an aluminum spacer, and thermally bonded to the spacer, which provides a direct aluminum path of low resistance to the base cover.

Dynamically, board spans between spacer anchor points have been kept to a length to provide resonant frequencies around 400 Hz. At scan platform test level inputs, this will limit response excursions to less than .03 in double amplitude. The assembly low resonant frequency compared to the extremely high frequency transient pyrotechanic shock pulse results in a very low dynamic load factor, indicating board response of less than 100g. The electronics contain no sensitive components such as crystals or relays and this low response will not damage any elements.

The power supply module is shown in Figure 2-75 . This assembly measures 6.5in x 5.0in x 1.8in (exclusive of mounting lugs) and will weight 2.80 lbs.

> Note: The contract Statement of Work gives the size as 6.5 in x 6.5 in x 2.5 in and a weight of 3.10 lbs. This reduction is due to redesign of the chassis structure and a change in transformer form factor to reduce the depth of the chassis.

The construction takes the form of an aluminum chassis with an aluminum cover. The assembly is electrically and thermally bonded to the scan platform at the mounting lugs.

The electronics are packaged on two double-sided printed circuit boards, mounted by aluminum spacers to the base. The transformers are epoxy adhesive bonded to the chassis base and anchored with screws. The replacement heater will be bonded inside the chassis base. The electronics have the same type conductive path to the base as the electronic module assembly and less power dissipation, therefore component temperatures will be within the 21°C rise as calculated for the electronic module.

The board spans are shorter in the power supply and the mass of the boards lower, resulting in a higher resonant frequency and lower board response when compared to the electronics assembly.

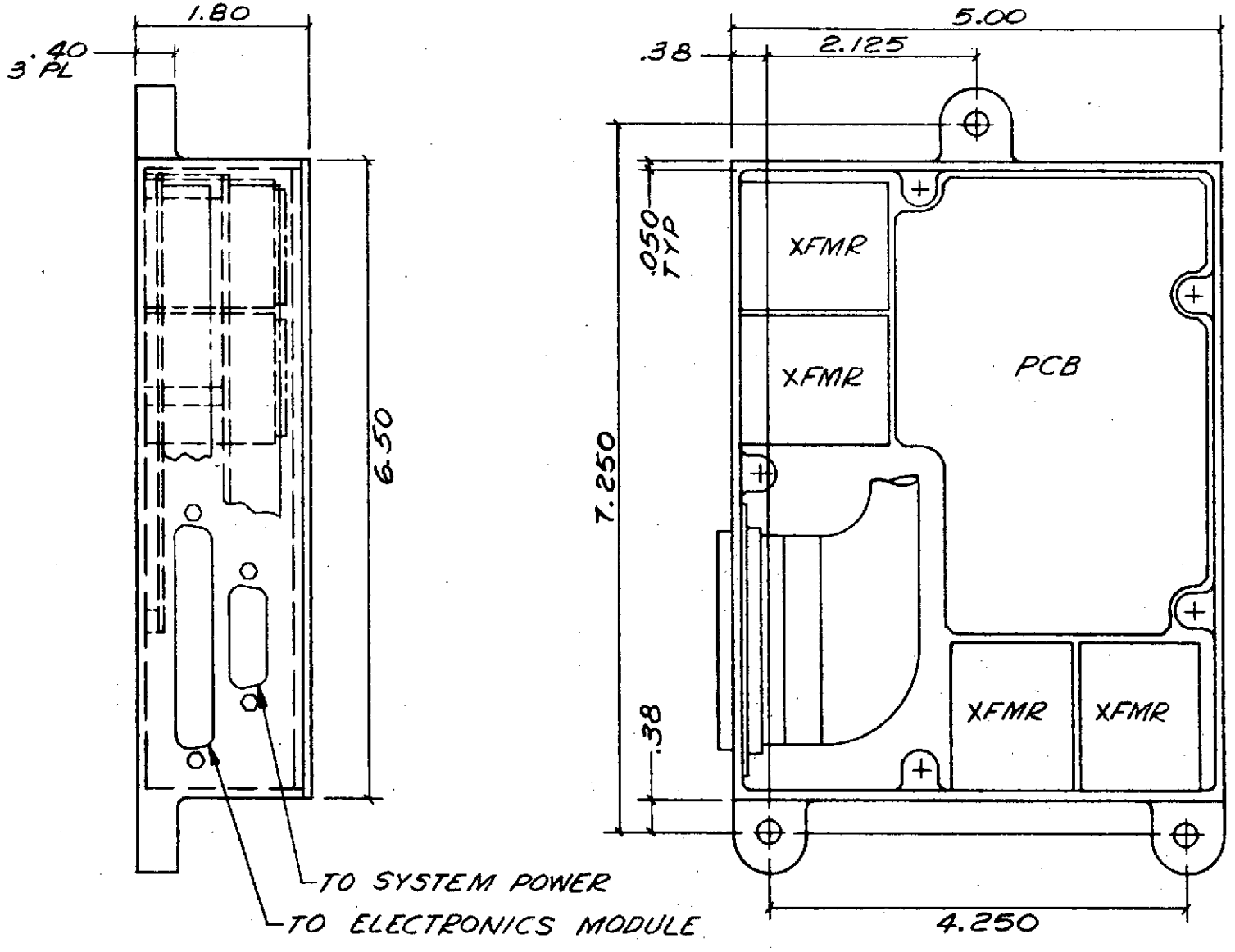

POWER SUPPLY

FIGURE 2-75

C. RELIABILITY

1. General

The reliability effort during the first two quarters of the MJS IRIS program has been oriented toward the planning of reliability tasks to be performed during the program and the guidance of design effort through reliability trade-off studies, part selection, and application assistance.

2. Reliability Program Plan

The reliability program plan was submitted for review on 26 June 1974. GSFC comments on the plan were received via Technical Direction Number 4, dated 16 August 1974. As a result of that directive, two changes were incorporated into the reliability plan; (1) the formal documentation of the stress analysis, exclusive of the worst-case study on the power supply circuits, was eliminated, and (2) the submittal date for NSPARs was changed to 20 working days before placing an order for the parts. A response to the Technical Direction describing these changes and Texas Instruments position on the remainder of the comments contained in the directive was submitted to GSFC on 5 September 1974. These points were also discussed and agreed upon with the cognizant GSFC parts engineer during the Preliminary Design Review.

3. Component Selection and Application

A major portion of the reliability effort to date has been devoted to part selection, preparation of part specification drawings, and preparation of non-standard part data for submittal to GSFC. Parts have been selected, where possible, from GSFC PPL-12. When certain applications would not allow the use of parts listed in that document, selection was made from other part sources, primarily JPL PD 618-211 APL.

At the present time, 16 non-standard parts have been selected for use in the IRIS design. NSPARs have been submitted to GSFC for 7 of these devices and the remainder are in various stages of

preparation and will be submitted in the near future.

4. Part Screening Specifications

Individual screening specifications have been created for the 7 non-standard parts for which NSPARs have been submitted. Screening specifications for the remainder of the non-standard parts and several other standard parts are currently in work. Screening specifications for the non-standard parts have been or will be submitted as attachment to the appropriate NSPARs. Screening specifications for standard parts will be submitted for GSFC review on an "as completed" basis.

5. Derating Rules

Reliability derating rules, in accordance with Appendix B of GSFC PPL-12, have been distributed to all designers. Any deviations from these rules will be discussed with the cognizant GSFC parts engineer.

6. Stress Analysis

The stress analysis effort has recently been initiated and several circuits have been reviewed. The analysis will be performed on all other circuits as designs are completed.

7. FMECA

The Failure Mode, Effects, and Criticality Analysis to be performed on the IRIS system will be initiated during the next quarter. This analysis will be performed by the circuit designers with the aid of the reliability engineer. As part of the FMECA, a worst case analysis of the IRIS power supplies is currently underway. Results of this analysis will be submitted to GSFC as an attachment to the FMECA report.

D. QUALITY ASSURANCE

Quality Assurance Engineering supported the preliminary design review of 10-12 September 1974.

During individual discussions with Texas Instruments Quality Assurance Engineering, DCASO Quality Assurance Engineering, and GSFC Quality Assurance Engineering, the Quality Assurance Program Plan was discussed. In response to verbal comments and negotiations, an Engineering Change Notice was initiated to revise the plan. This change is currently being incorporated into the document.

Quality Assurance Instructions (QAIs) 160-2, Incoming Inspection Requirements; 360-6, Assembly Inspection Requirements; 960-1, Stocking, Handling, and Kitting Requirements; and 1060-4, Material Review Procedure have been reviewed and signed by Texas Instruments personnel. With the exception of QAI 960-1, these documents have been forwarded to GSFC representativies for information. Other Quality Assurance activities performed during the reporting period are outlined below:

- Contacted GSFC Quality Assurance Engineering in an effort to obtain a revision to the letter of delegation. The letter was interpreted by DCASO representativies to be applicable to the entire project, however, discussions with GSFC indicate that the delegation is effective only for Engineering Model, Proof Test Model, and Flight Systems. Confirmation in writing has not been received from either DCASO or GSFC.

- Initiated the review of assembly work orders which will control the assembly and inspection efforts on the Bench Checkout Equipment.

- Performed a review of the Engineering Drawings (41) and the Engineering Changes Notices (23) which were initiated during the period for conformance to quality requirements. This review included approximately six (6) process specifications.

- Performed review of the requests for purchase in order to assure the project quality requirements were satisfied.
- Attempted to resolve problems associated with DCASO interpretations of Texas Instruments authority and/or material review authority relating to both "use as is" and "scrap" dispositions.
- Attended a meeting in the Texas Instruments PCB shop where specific project problems were related and discussed. This meeting was intended to familiarize appropriate personnel with project goals and requirements.

SECTION III

PROGRAM MANAGEMENT

A. ORGANIZATION

Figure 3-1 depicts the present program organization. No deletions in key personnel have occurred, nor have any major organizational changes been made through the first two quarters of the program. The current organization reflects a peak in design personnel assigned to the program on a full time basis. Additional project manufacturing personnel have been assigned due to increased engineering model hardware activity.

B. SCHEDULES

Program schedules are summarized in Figures 3-2 through 3-8. Figure 3-2 is an overall program schedule summary. No changes in overall program milestones have been made since the last report. The subsystem PDR was completed on 12 September 1974. During the next quarter, the first BCE is scheduled for completion along with the bulk of engineering model procurement and fab activities.

Figures 3-3 through 3-6 depict a more detailed schedule of engineering model activities. The first of these is a schedule for the electronics package which primarily consists of six multilayer printed circuit boards. As shown, half of these boards have been released for layout. The remaining boards have been rescheduled for release on 1 November. Completion of the logic and HK Mux board layout was revised as the result of a design change which was necesary after initial release. This design change expanded the delay generator capacity in order to accomodate the new Butterworth electronic filter discussed in Section II.

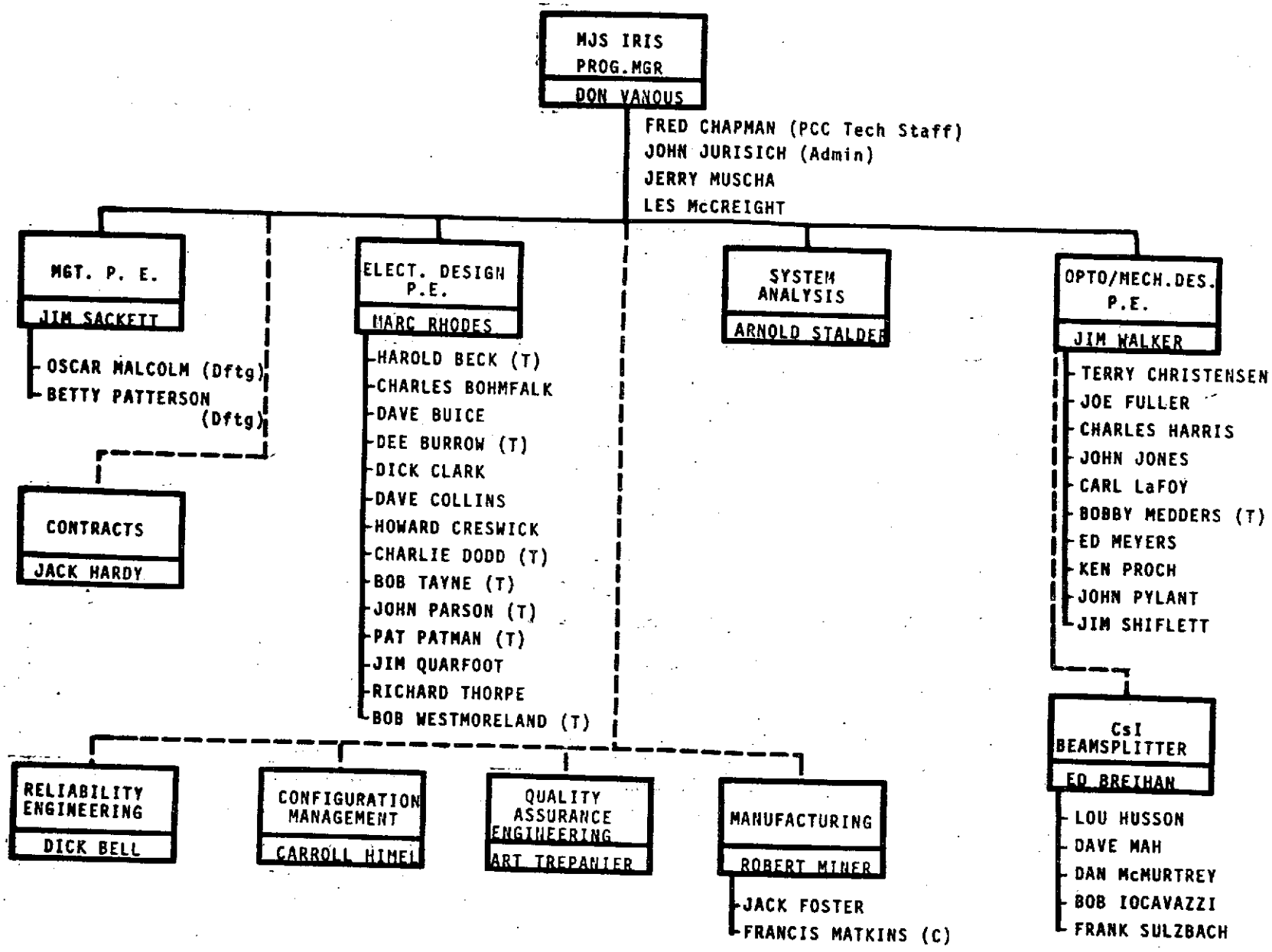

PROGRAM ORGANIZATION

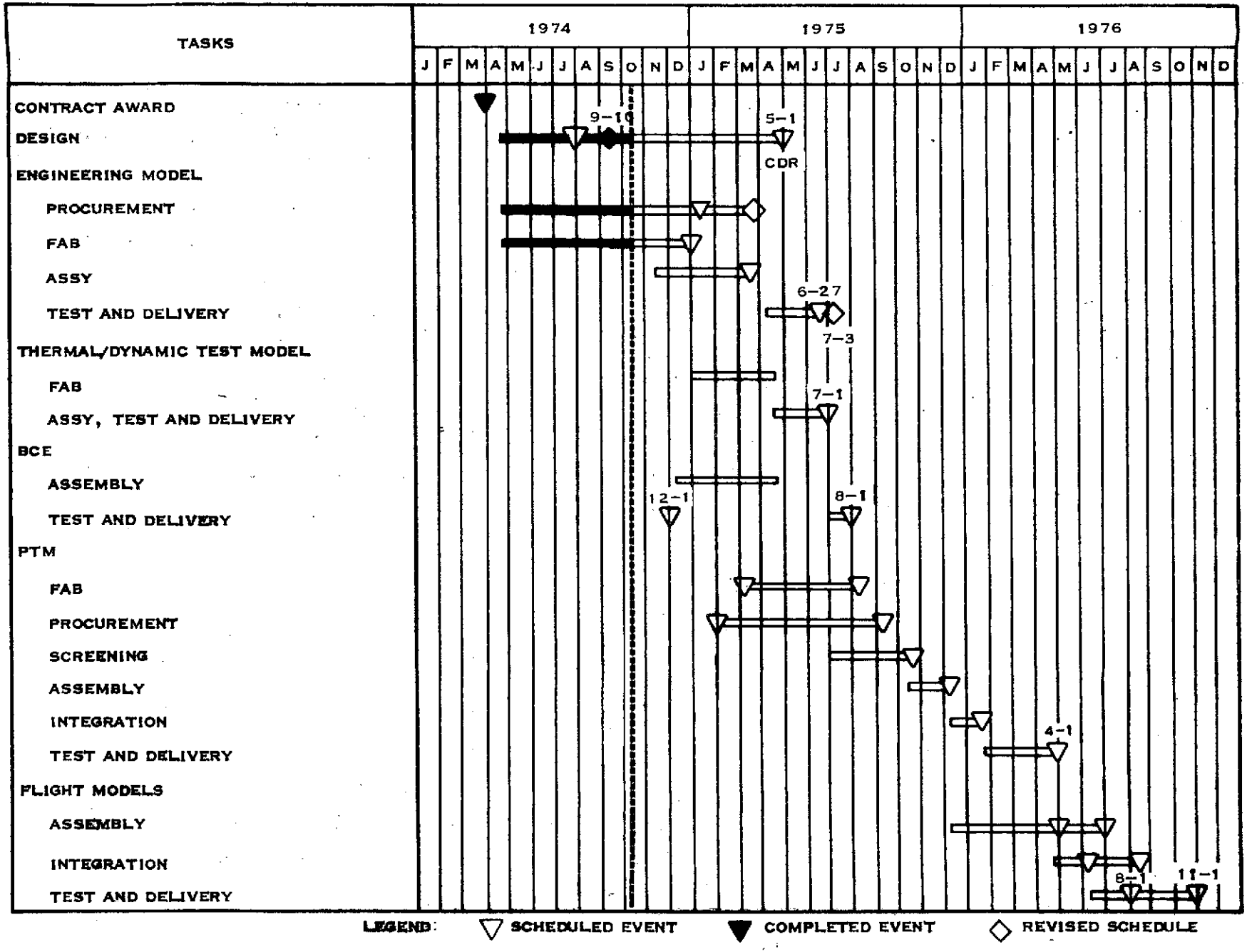

SCHEDULE

STATUS DATE 10-12-74

FIGURE 3-2

SCHEDULE CHART TI-13802-B

TEXAS INSTRUMENTS

PROGRAM	PROGRAM MANAGER	STATUS DATE
MJS-IRIS ENG.MODEL	DON VANOUS	10-2-74

IDENT. NO.	TASKS
●	DESIGN AND BREADBOARD
A3	LOGIC AND HK MUX
A6	ADC & DATA CHANNEL
A2	PHASE LOCK LOOP A
A1	PLL B & POSITION LOOP
A5	TEMPERATURE CONTROLLERS
A4	PWR DISTR.& RADIOMETER
●	MULTILAYER BOARD LAYOUT
A3	LOGIC & HK MUX
A6	ADC & DATA CHANNEL
A2	PHASE LOCK LOOP A
A1	PLL B & POSITION LOOP
A5	TEMPERATURE CONTROLLERS
A4	PWR DISTR.& RADIOMETER
●	MULTILAYER BOARD FAB
	A2, A3, A6
	A1, A5, A4
●	PARTS PROCUREMENT
●	MLB ASSEMBLY & TEST
●	PACKAGING FAB & ASSEMBLY
0	ELECTRONICS BOX & ASSY
	& TEST WIRING, ASSY & QC
	SUBSYSTEM INTEGRATION

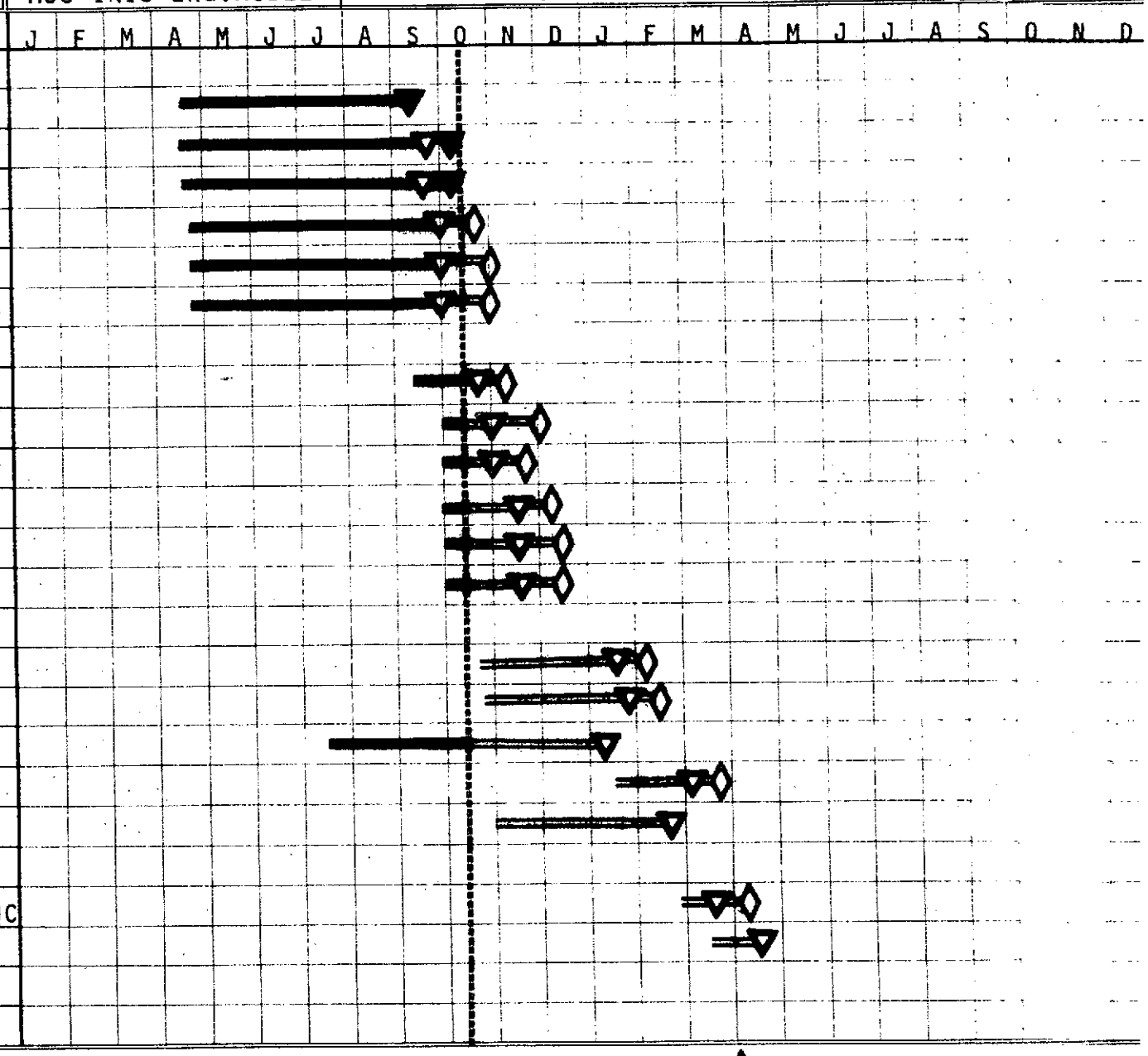

ELECTRONICS PACKAGE (A2)

LEGEND: ▽ SCHEDULED EVENT ▼ COMPLETED EVENT ◇ REVISED SCHEDULE

FIGURE 3-3

Layout completions have been revised to reflect expected release dates. While these revised dates do reduce schedule contingencies, primarily in the multilayer board fab times allocated, no change to the overall engineering model delivery schedule appears warranted at this time.

Figure 3-4 depicts the schedules for the power supply package and the instrument electronics. As shown, the design of the power supply electronics was completed slightly behind schedule. Full schedule recovery has been attained in the PCB layout process. The design of the instrument electronics is progresssing satisfactorily. Barring unexpected problems relating to radiation effects, which might be uncovered in continuing radiation test and study activities, the design of the instrument electronics should be completed by 1 November.

Figure 3-5 describes the progress of the various mechanical design areas. Negotiations for the fabrication of the telescope were consumated during the later part of September, as planned, and material procurement for fabrication is underway. Michelson test motor fabrication activities have been completed, however, the assembly schedule for the test motor has been revised due to late delivery of the CoSm magnets. The remaining Michelson motor schedules are revised accordingly. Similarly, schedules for the beamsplitter and dichroic activities have been modified to be more consistent with materials procurements.

The instrument berryllium housings design is nearing completion and engineering procurement is expected to begin in early November. Aluminum mock-ups of the more critical parts will be fabricated in parallel to identify possible design problems well in advance of the completion of the beryllium parts. The aluminum parts are also planned for use in the TCM.

SCHEDULE CHART TI-13602-B

TEXAS INSTRUMENTS

PROGRAM: MJS-IRIS ENG MODEL

PROGRAM MANAGER: DON VANOUS

STATUS DATE: 10-12-74

IDENT. NO.	TASKS
A3	POWER SUPPLY PACKAGE
	DESIGN & BREADBOARD
	PCB LAYOUT
	PCB FAB
	PARTS PROCUREMENT
	TRANSFORMER FAB
	SUBCHASSIS FAB & ASSY
	ASSEMBLY, WIRING & QC
	UNIT TEST
	SUBSYSTEM INTEGRATION
A1	INSTRUMENT ELECTRONICS
	DESIGN & BREADBOARD
	PCB LAYOUT
	PCB FAB
	PARTS PROCUREMENT
	DETECTOR PROCUREMENT
	ASSEMBLY & UNIT TEST
	INSTRUMENT WIRING & ASSY
	SUBSYSTEM INTEGRATION

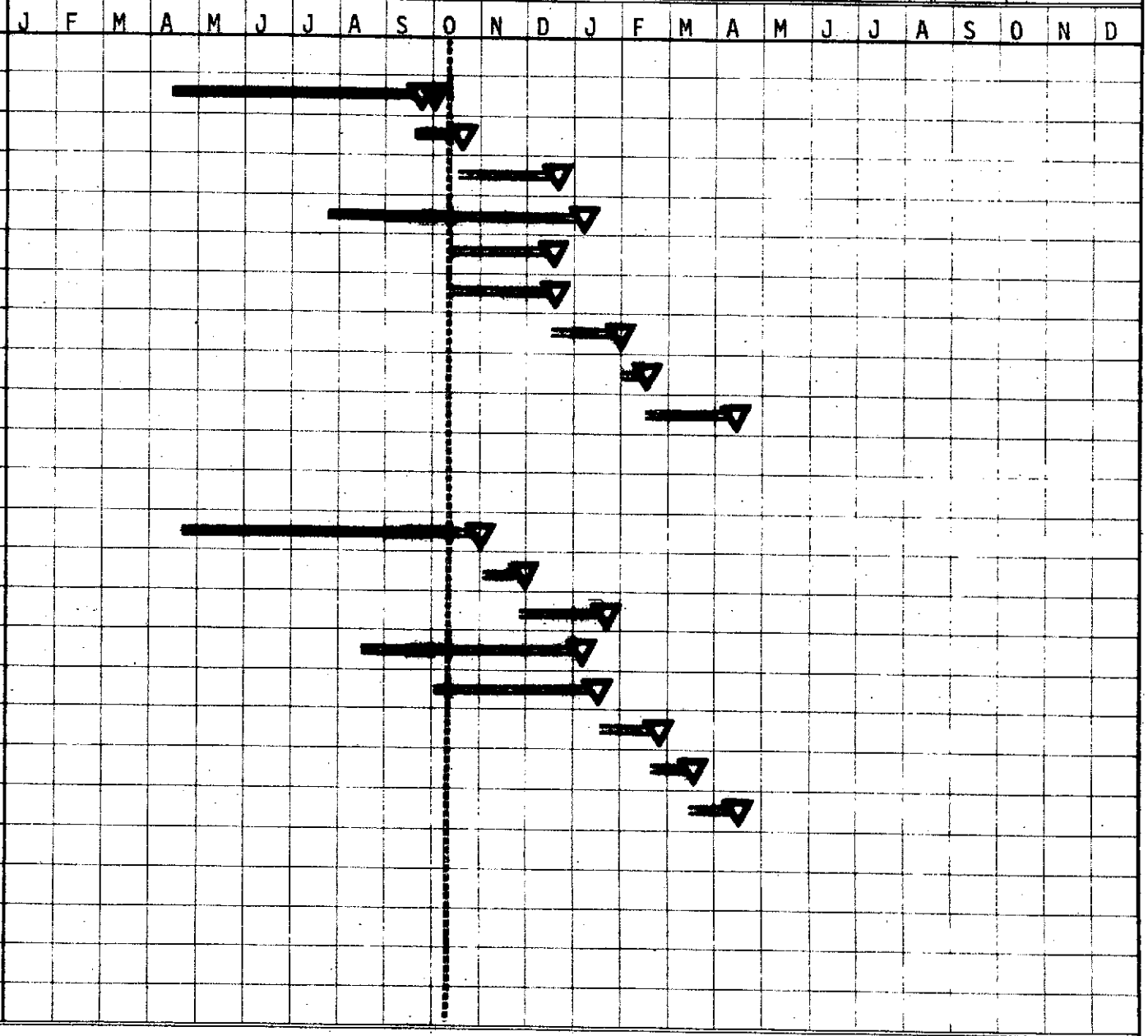

POWER SUPPLY & INSTRUMENT ELECTRONICS

LEGEND: ▽ SCHEDULED EVENT ▼ COMPLETED EVENT ◇ REVISED SCHEDULE

FIGURE 3-4

SCHEDULE CHART TI-13802-B

TEXAS INSTRUMENTS

PROGRAM	PROGRAM MANAGER	STATUS DATE
MJS-IRIS ENG MODEL	DON VANOUS	10-12-74

IDENT. NO.	TASKS
●	TELESCOPE
	FABRICATION
	POLISH, COAT, ASSY & TST
	TI ACCEPTANCE TEST
●	MICHELSON MOTOR
	TEST MODEL FAB
	TEST MODEL ASSY
	TEST & EVALUATION
	ENG MODEL FAB
	ENG MODEL ASSY & ALIGN
	ENG MODEL UNIT TEST
●	BEAMSPLITTER
	FIXTURE DESIGN & ASSY
	MOUNT DESIGN
	CsI & MOUNT PROCUREMENT
	TEST UNIT ASSY & TEST
	EM UNIT ASSY & TEST
●	DICHROIC
	COATING DESIGN
	ENVIRONMENTAL TEST
●	HOUSINGS
	DESIGN
	AL MOCK UP FAB
	EM PROCUREMENT
●	ELECTRONIC BOXES FAB

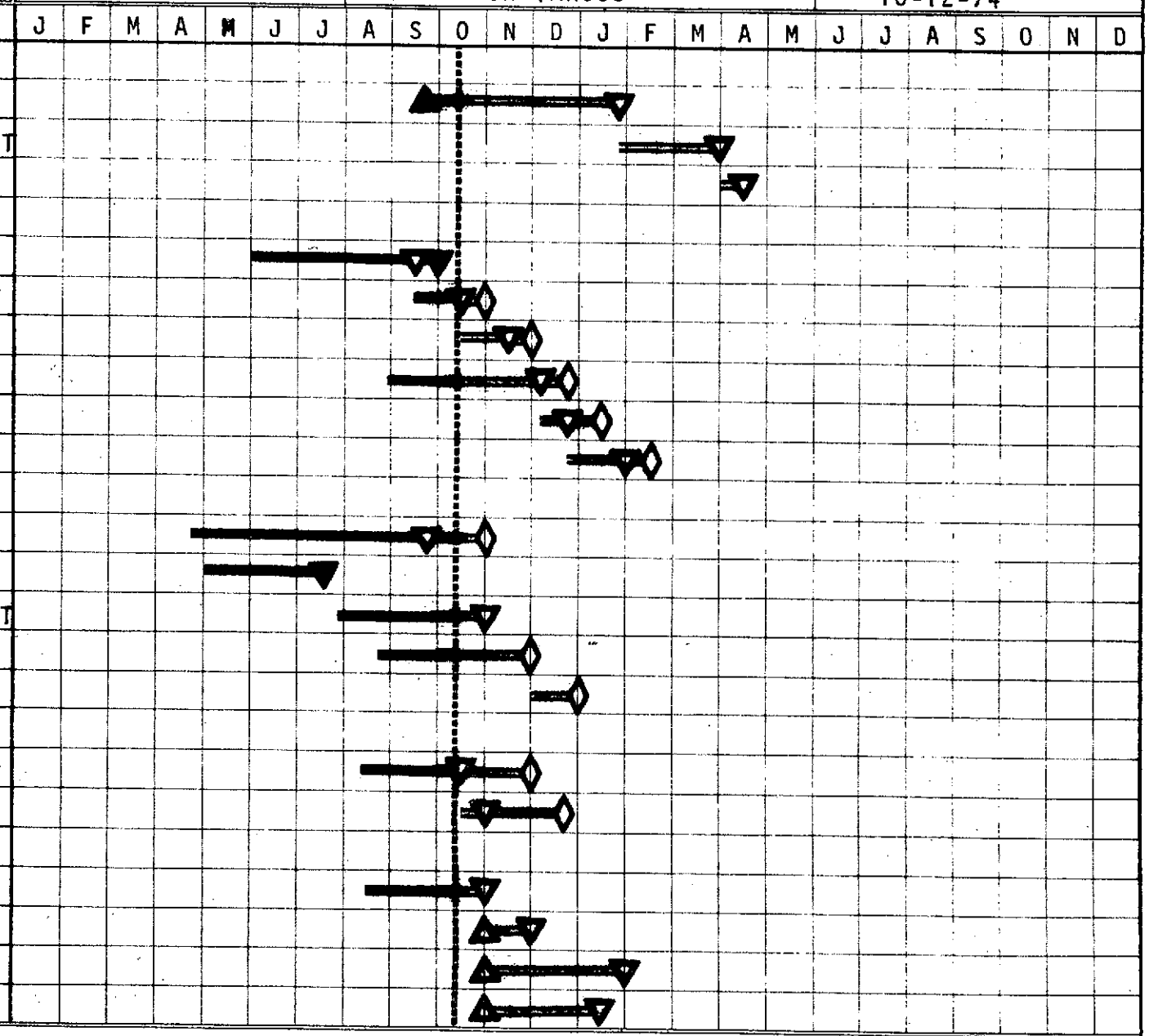

LEGEND: ▽ SCHEDULED EVENT ▼ COMPLETED EVENT ◇ REVISED SCHEDULE

FIGURE 3-5

Although the design of the electronics and power supply subchassis has been completed, release for fabrication is being deferred until early November when the electronics designs should be fairly firm.

The final engineering model schedule, Figure 3-6, shows the manner in which the three elements will be integrated with the power supply being completed first. The breadboard system will be used to allow partial subsystem integration tests to be conducted at various stages of the assembly and test operations. The telescope will be integrated with the subsystem after a month of full system integration testing and formal testing is scheduled to begin with cold alignment tests in the latter part of April 1975.

Figure 3-7 indicates the current progress made in the BCE and other test equipment areas. The BCE activities continue to progress on, or ahead, of schedule. Detailed definition of the calibration and test fixture equipment is currently in process. Detailed schedules for these various pieces of hardware are also being formulated as definition is derived.

The final schedule, Figure 3-8, depicts major data and GFP milestones. The October financial report had not been submitted as of 12 October, but is planned for submittal prior to the 22nd. The last BCE has not been received as of yet. Flight connectors were received in early September, however subsequent design modifications have changed the connector requirements.

SCHEDULE CHART TI-13802-B

TEXAS INSTRUMENTS

PROGRAM	PROGRAM MANAGER	STATUS DATE
MJS-IRIS ENG MODEL	DON VANOUS	10-12-74

IDENT. NO.	TASKS
	POWER SUPPLY ASSY & TEST
	ELECTRONICS BOX ASSY & TST
	INSTRUMENT ASSY & TEST
	SUBSYSTEM INTEGRATION TST
	TELESCOPE INTEGRATION & ROOM TEMP EVALUATION
	COLD ALIGNMENT
	VIBRATION TESTS
	THERMAL VACUUM TESTS AND CALIBRATION
	RFI TESTS
	CLEAN UP AND DELIVERY

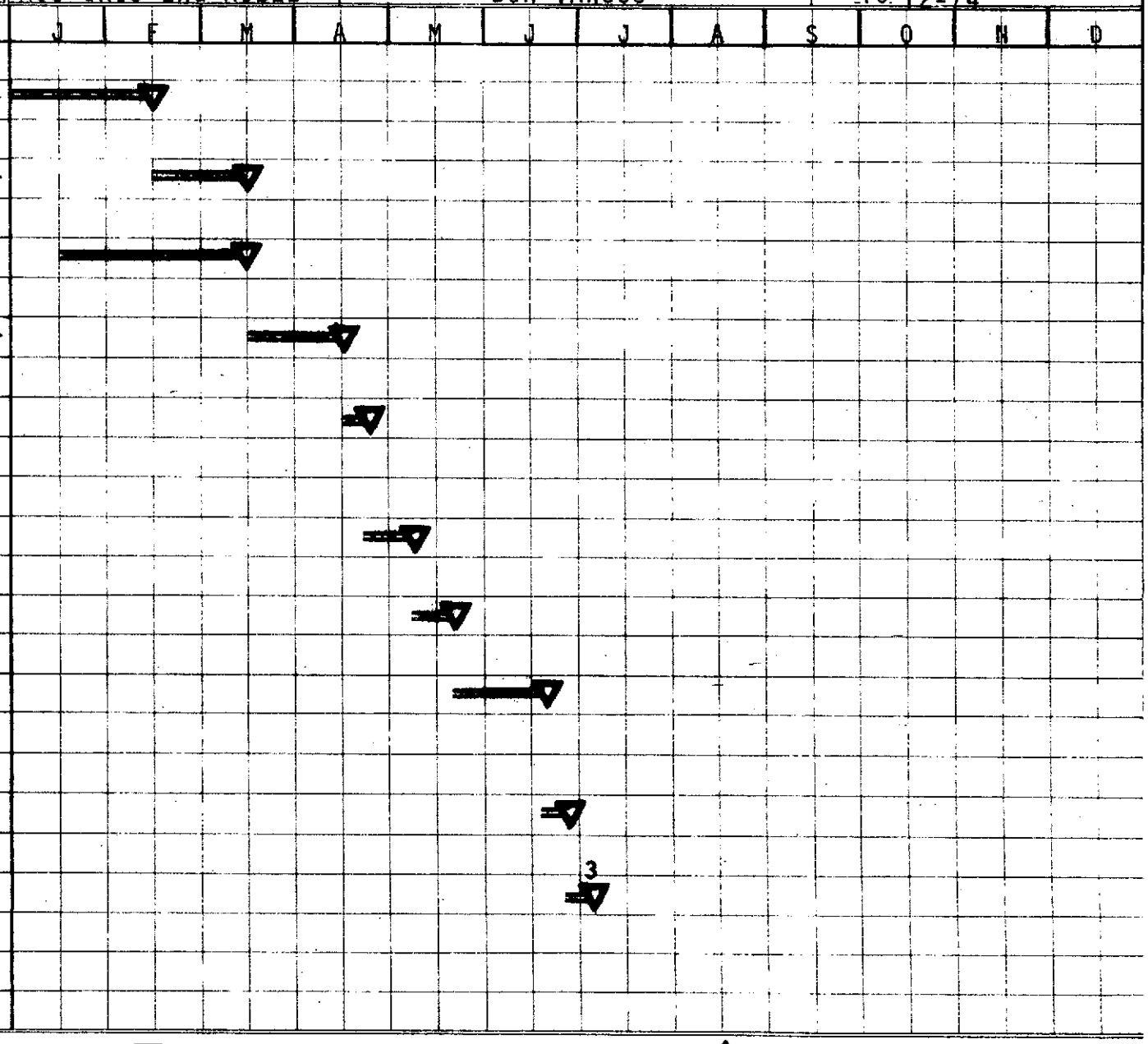

1975

LEGEND: ▽ SCHEDULED EVENT ▼ COMPLETED EVENT ◇ REVISED SCHEDULE

FIGURE 3-6

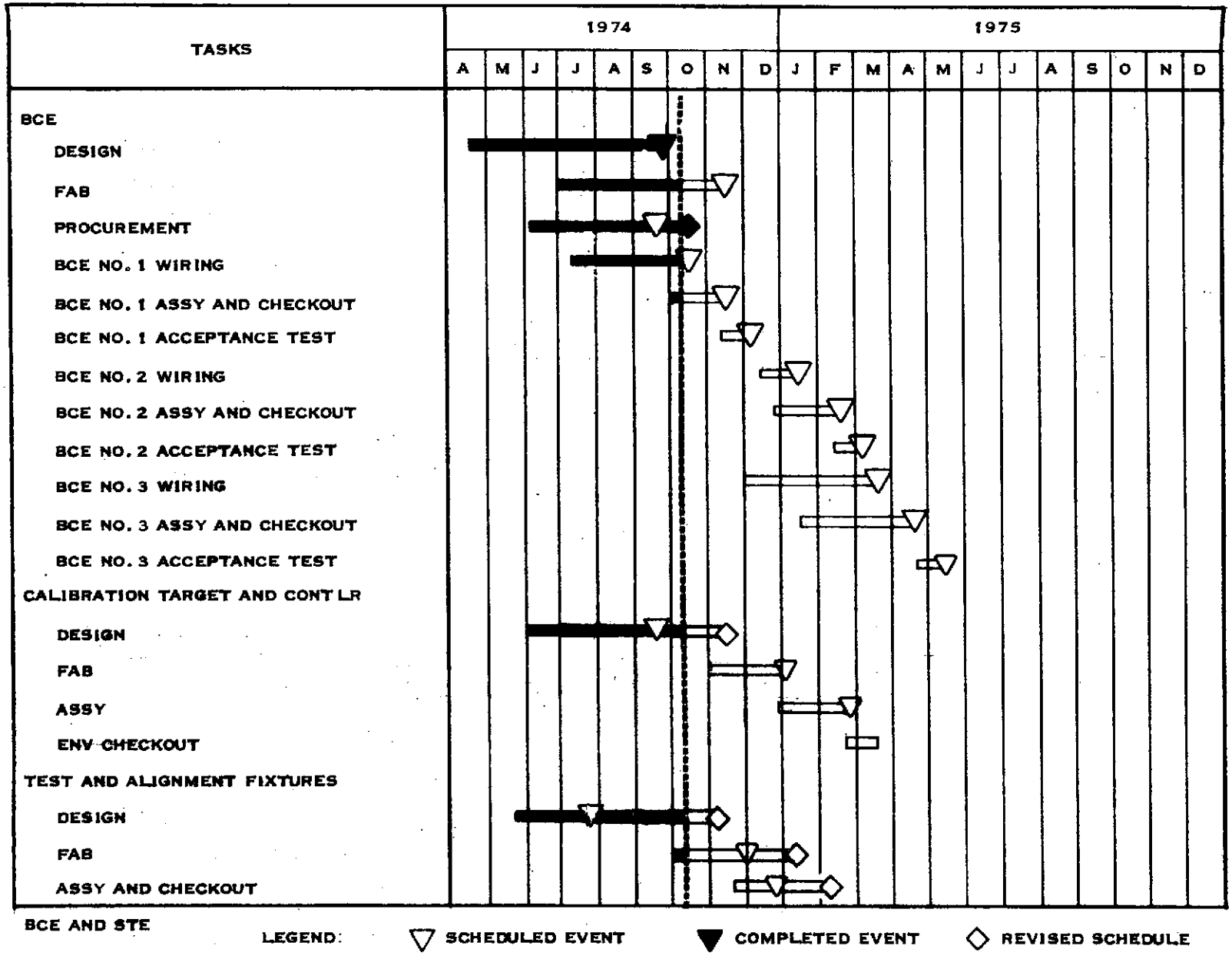

SCHEDULE

FIGURE 3-7

STATUS DATE 10-12-74

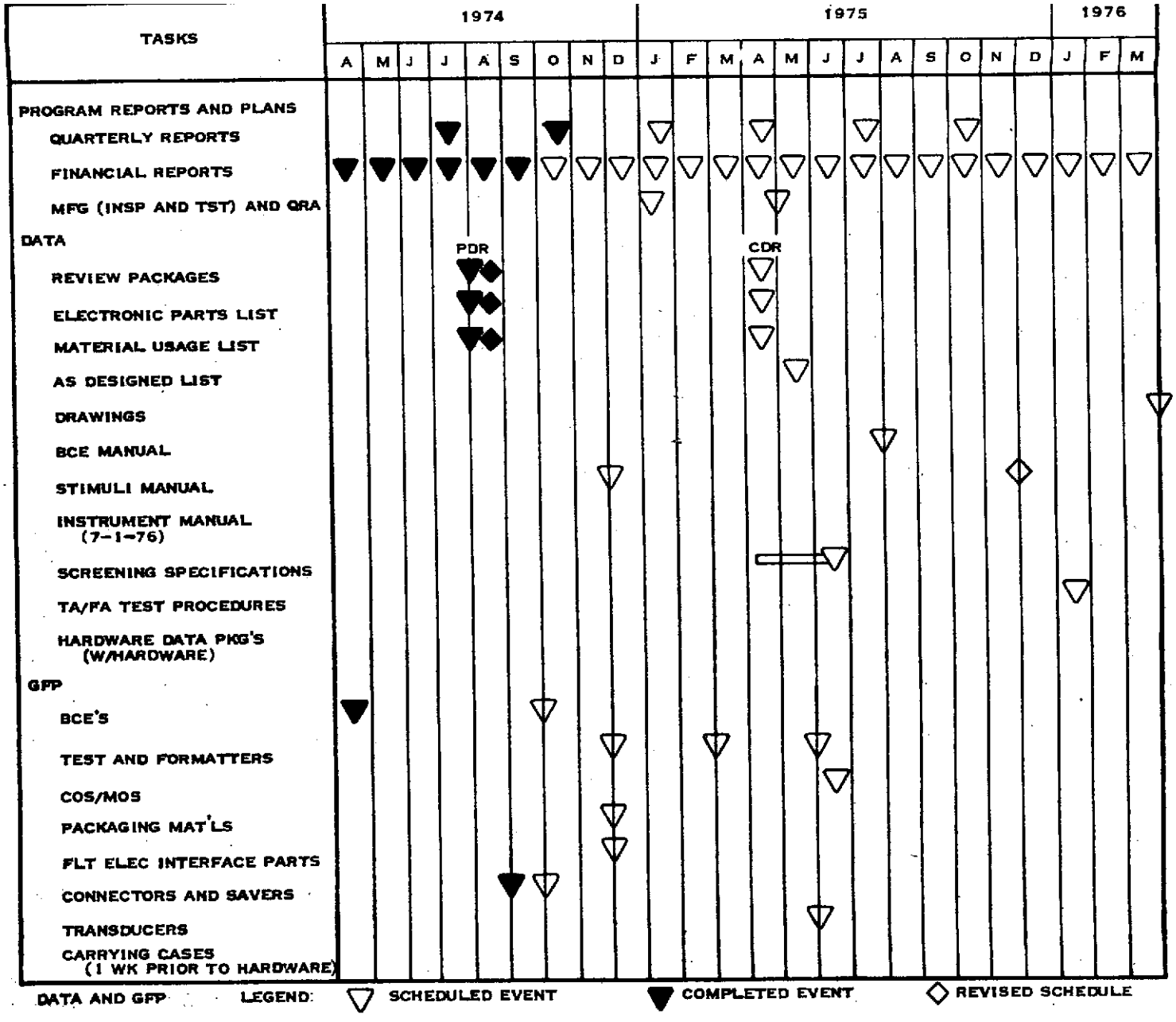

SCHEDULE STATUS DATE 10-12-74

FIGURE 3-8

C. POTENTIAL PROBLEM AREAS

Radiation continues to loom as a potential problem. Program schedules and resources dictate the commitment of detail designs for the engineering model prior to the conclusion of on-going radiation studies and tests. While the most conservative radiation designs practicable have been employed, some concern remains over the dynamic effects to be expected at the Jovian flux rates. As previously stated, the impact of future design changes on program schedules will be directly related to the elapsed time involved in identifying, and agreeing upon,such changes.

Parts procurement remains a potential problem. The late delivery of the Michelson motor magnets is an example of reduced emphasis and concern on the part of parts vendors in meeting their commitments for non-commercial, low volume orders. This trend is seen as continuing, and perhaps being aggravated by the economic environment as business concerns are pressured to concentrate on their more profitable product lines.

A fairly large number of GFP part types is being used in the subsystem to reduce cost and/or radiation design burdens. Many of these parts will be mounted on multilayer printed circuit boards which are extremely intricate, and thus, lengthy in their design and manufacture. Descriptions of the GFP parts to be mounted on these boards have been received. Any future changes to these parts could have a severe impact on program schedules and costs.

A second potential problem associated with GFP is their delivery schedules. It was suggested during PDR that rescheduling of instrument assembly flows may be required to accomodate the projected delivery dates for GFP parts. While such departures from the optimum manufacturing flow are sometimes necessary, they usually entail some schedule and cost impact. Furthermore, "work-arounds" involving certain critical parts, or a number of different types, can be virtually impossible to implement without significant program impact.

Texas Instruments has been requesting cost quotations from beryllium fabrication vendors on parts representative of those being designed for the instrument optical housings. The quotations received indicate that a large percentage of the costs for these parts will be that of the bulk beryllium material. Texas Instruments has recently been advised of a general price increase of 28% for raw beryllium. The impact of this increase will not be fully accessible until the quotations on the optical housing designs are received in November.

SECTION IV

NEW TECHNOLOGY

No data are applicable for this section

SECTION V

PROGRAM FOR THE NEXT REPORTING PERIOD

During the next quarter, most of the engineering model detail design will be completed. All major mechanical piece parts will have been released for fabrication, and the Michelson motor and beamsplitter test models will have completed environmental testing. All electronics PCB boards will have completed layout, and been released for fabrication. The vast majority of engineering parts are scheduled to have been received, and the first BCE will have been completed.

Ancillary design and manufacturing activities dealing with the calibration targets and various test, alignment, and assembly fixtures will also be a major effort during the next period.

SECTION VI

CONCLUSIONS AND RECOMMENDATIONS

A. CONCLUSIONS

The instrument design has continued to progress satisfactorily. No new major design problems were uncovered during the Preliminary Design Review, nor were any major redesigns deemed warranted.

Progress in the opto-mechanical area was initially paced by the telescope development. This development has since advanced to the point of final refinement as the engineering model unit fabrication cycle has begun. The resulting reduction in telescope design effort has allowed increased emphasis on detail optical housing design. A major milestone in the beamsplitter area was accomplished as extensive materials studies and tests were culminated in the identification of a suitable beamsplitter bonding material. Other areas of mechanical design, including thermal and Michelson motor, have progressed in a manner consistent with the overall instrument development.

In the electronics area, the last quarter has seen significant progress as a number of critical designs, including the interferometer data channel, have been completed and released for hardware layout. Design completions for all remaining electronics, other than the interferometer preamplifier, appear imminent.

While the instrument development is proving to be extremely difficult and complex, it is generally felt that the technical problems are under control. This is allowing extensive planning to be undertaken to ensure a smooth and cost effective program transition from the design phase to the engineering model manufacturing phase.

B. RECOMMENDATIONS

As previously discussed, the extensive use of GFP parts poses at least two significant potential problems; schedule, and the parts specifications themselves. With regards to schedule, it is recommended that delivery schedules for each GFP part type be forwarded to Texas Instruments for concurrence or impact assessment. With respect to the parts specifications, it is recommended that all GFP parts drawings be closely controlled and that all proposed changes to these drawings be reviewed by Texas Instruments prior to incorporation. Table 6-1 reflects Texas Instruments understanding regarding GFP parts specifications. Any descrepancies should be reported immediately.

A problem somewhat similar to that of the GFP parts drawings, which was pointed out in the PDR, exists with the various JPL Functional Requirements documents pertinent to the IRIS subsystem. As more and more IRIS detail designs are committed to hardware manufacture, it becomes increasingly unlikely that changes to the FR's affecting the subsystem would not entail some design and/or cost impact. Therefore, it is recommended that all Functional Requirements changes pertaining to the IRIS subsystem also be submitted to Texas Instruments for review and assessment prior to their adoption.

Finally, one problem which was not addressed during PDR, nor covered in Action Items, deals with the FDS interfaces. It is Texas Instruments current understanding that a total of two signal ground returns have been allocated for the FDS/IRIS interfaces. This allocation no longer appears compatible with the IRIS instrument performance requirements. Therefore, it is recommended that an additional Action Item be assigned jointly to JPL and Texas Instruments to identify an acceptable grounding arrangement for the FDS/IRIS interface.

TABLE 6-1 MJS-IRIS GFP LIST (AS OF 12 OCTOBER 1974)

JPL NO.	REV. LTR.	DEVICE	COMMENTS
ST11498-246	B	HARRIS HD-9-246-2 Tripple Line Trans Interface	14 Lead Flat Price (TO-86) Per Fig. 1 of ST11498, unformed leads 1.0 inch overall
ST11499-101H	C	LM101AH OP AMP	TO-99 Package Per Fig. 1
ST11499-108H	C	LM108H OP AMP	TO-99 Package Per Fig. 1
ST11499-111H	C	LM111H COMPAR.	TO-99 Package Per Fig. 1
ST11499-723H	C	LM723H REG	TO-100 Package Per Fig. 1a
ST11565	C	Capacitor, Fixed, Glass Type 1	Leads must be solerable type
ST11592	A	Diode, Sil. Fast Rec. 4 AMP (UTR)	
ST11715	B	Diode, Zener, Sil. 3.3 to 12V, 400 mw	Leads type D, Mil-Std-1276
ST11735	B	Fuse, Axial	
ST11868	B	Microcircuit, Digital (CMOS)	Leads to be Per Fig. 1 and Fig. 3
ST11872	A	Resistor, Fixed, Film Microcircuit Module	Leads trimmed and formed Per Fig. 1
PT40015	A	Diode Hi Speed Sw.	1N4148
PT40147-BC1042-2	B	4 Diode Array	Leads trimmed and formed per Fig. 1B

TABLE 6-1 MJS-IRIS GFP LIST (AS OF 12 OCTOBER 1974) (CON'T)

JPL NO.	REV LTR	DEVICE	COMMENTS
PT40263	A	Capacitor, Chip	Case Size 2, with silver ribbon leads
DS311	D	Conn. Circ. Wall Mtg.	
DS8828	B	Boot, Putting, D Series Conn.	Shall have been outgassed in vacuum oven
ST10028	D	Strap, Cabling	Shall have been outgassed in vacuum oven
ST10046	A	Stud, Rect. Conn.	
ST10049	C	Nut, Captive Wash. Lkg.	
ST10062	C	Insert, Thd'd, Capped	
ST10063	C	Insert, Thd'd, Open	
ST10091	D	Conn. Electr. Male Contact, Rect. NM	
ST10092	E	Conn. Electr. Female Contact, Rect. NM	
ST10737	A	Clamp, Cable, Nylon	Shall have been outgassed in vacuum oven
ST10762	A	Grommet, Universal	Shall have been outgassed in vacuum oven
ST11250	B	Spot Terminal	
ST11478	A	Wire Stranded, TFE	

TABLE 6-1 MJS-IRIS GFP LIST (AS OF 12 OCTOBER 1974) (CON'T)

JPL NO.	REV. LTR.	DEVICE	COMMENTS
ST11479	A	Cable, Hook-Up, TFE Shld'd and Jacketed	
ST11481	A	Cable, Hook-Up, TFE Twisted Pair, Shld'd and Jacketed	
MIL-C-39014B	N/A	CKR -- Capacitor	Does not specify lead material. Soldering heat test indicates solderable leads as is required
MIL-C-3902C Admendment 6	N/A	CHR01 Capacitor	Type C solderable leads
MIL-R-39008/B	N/A	RCR07 Resistors	Para. 3.5.1 "All terminals shall be suitably treated to facilate soldering"
MIL-R-55182E	N/A	RNC Resistors	Type C solderable leads

APPENDIX A

SPECIFICATION
FOR
MJS'77 IRIS SUPPORT TUBE

APPLICATION	
NEXT ASSY	USED ON

REVISIONS			
LTR	DESCRIPTION	DATE	APPROVED

SPECIFICATION
FOR
MJS-77 IRIS SUPPORT TUBE

REV																																	
SHEET																																	
REV STATUS OF SHEETS	REV																																
	SHEET																																

UNLESS OTHERWISE SPECIFIED
DIMENSIONS ARE IN INCHES
TOLERANCES:
ANGLES ±1°
3-PLACE DECIMAL ±.010
2-PLACE DECIMAL ±.02

INTERPRET DWG IN ACCORDANCE WITH STD PRESCRIBED IN MIL-STD-100

MATERIAL:

DR DATE
CHK
ENGR 10/3/74
APPD
CONTR NO.

DESIGN ACTIVITY RELEASE

TEXAS INSTRUMENTS
INCORPORATED
GOVERNMENT PRODUCTS DIVISION DALLAS, TEXAS

TITLE
SPECIFICATION, MJS-77 IRIS, SUPPORT TUBE

SIZE	CODE IDENT NO.	DRAWING NO.
A	96214	877095 A/a

SCALE	REV	SHEET
		1 of 12

TI-9923-A

SPECIFICATION
MJS-77 IRIS SUPPORT TUBE

1. OBJECTIVE

Provide support in the design and fabrication of an advanced composite structural support tube for a spaceborne scientific experiment. This activity is in support of the Mariner Jupiter Saturn 1977 (MJS-77) Interferometer and Radiometer (IRIS) program now under contract to Texas Instruments (TI).

2. SCOPE

Texas Instruments' proposed general configuration of the IRIS optical instrument support tube is shown in the following drawings:

TI	877100	MJS-77 IRIS INSTRUMENT OUTLINE DIMENSIONS
TI	877160	INSTRUMENT MOUNT

The basic design goal of this support tube is to provide a very stiff (low stress during launch) structural mount for the instrument to the spacecraft scan platform while maintaining near perfect optical boresight alignment of the instrument to other scientific experiments mounted on the platform. In addition, the tube must provide efficient thermal isolation between the subcooled instrument (-99.4°F) and the room temperature platform, and also the tube must survive high levels of electron and proton radiation.

TI will analyze the tube and end flanges with a finite-element computer model. The tube will be modeled as a "shell" composed of quadrilateral flat plate elements, having orthotropic properties (i.e., longitudinal and circumferential).

The instrument mount flanges (items 5 and 6 in TI 877160) are made of Brush Wellman I70-A optical grade beryllium and the platform mounting plate and inside flange (items 2 and 4) are made of 7075-T6 aluminum. These flanges will be modeled with elements having isotropic properties.

TI requires vendor support in establishing realistic design values for the orthotropic mechanical properties of a composite matrix material to be used for the instrument support tube. These values shall be developed on the basis of the design requirements of Paragraph 3 and the nominal performance goals of Paragraph 4. An iteration process between TI and the consultant will likely be necessary to optimize the support tube design.

The effort required by the vendor can be divided into three phases:

Phase I. Design and Analysis

A. Analytical design and optimization of the support tube material shall include discussion of tradeoffs in fiber materials, binders, wrap geometries, volume fractions, fabrication techniques, etc. In addition to summarizing predicted values for the orthotropic macroscopic mechanical properties discussed in Paragraph 4, the analysis shall present the derivation of these macroscopic properties from the microscopic properties, including stresses in the components of the composite and their stress/strain relationships individually. Also included shall be a prediction

of the temperature dependence of the various mechanical properties under consideration, a discussion of the structural failure mechanisms, fatigue characteristics, and SN (strength vs. cycles) information.

B. A final technical report summarizing the results of the analysis shall be submitted to TI.

C. A specification and drawings sufficient to fabricate the support tube shall be submitted to TI.

D. A proposed test plan to measure the properties discussed in Paragraph 5 shall be submitted to TI for approval. This plan shall include test procedures, equipment, configuration of test samples, test measurement accuracy, and repeatability of test results.

Phase II. Testing

A. Fabricate test samples of the proposed tube material.

B. Send one set of samples to TI for radiation bombardment and returned to the vendor for comparative testing.

C. Make measurements of the properties discussed in Paragraph 5.

B. A report summarizing the test results shall be submitted to TI.

Phase III. Fabrication

Fabricate support tubes as per Phase I and II in quantities of 6 and 12.

3. DESIGN REQUIREMENTS

The following conditions and assumptions are the basic "constants" in the design of the support tube.

3.1 Mission Lifetime - The MJS spacecraft will be launched in mid-1977. Some IRIS flight hardware will be assembled in 1975. The spacecraft requires approximately two years to reach the planet Jupiter and another two years to reach Saturn. Thus, the IRIS support tube must function for a minimum of two years on the ground (pre-launch) and about four years in space.

3.2 Support Tube Geometry - The mechanical configuration of the instrument support tube is shown in drawing TI 877100 with the dimensions:

3.25 inches	-	"free" length between flanges
4.00 inches	-	maximum outside diameter
0.10 inches	-	nominal wall thickness

3.3 Thermal Gradient - The design temperature differential (in space) between the scan platform at 104°F maximum and the instrument housing at - 99.4°F is 203.4°F. This gradient is assumed to occur along the 3.25 inch "free" length of the support tube.

3.4 Beryllium Interface - The IRIS instrument structure is made entirely of Brush Wellman I70-A optical grade berrllium. The instrument mount flange (items 5 and 6 in TI 877160), which interfaces between the support tube and the instrument structure, is made of the same beryllium material. After launch, the instrument (and this flange) subcools from room

temperature to its operating temperature of 200°Kelvin (-99.4°F). A thermal stress analysis between this flange and the tube will be included in TI's structural model. In order to remain optically stable and aligned, the instrument structure (and the flange) is being designed to stress levels below the microyield strength (MYS)* of the I70-A material.

The following isotropic mechanical properties are assumed for the beryllium instrument mount flange:

E (tensile modulus) = 44×10^6 psi
G (shear modulus) = 21.5×10^6 psi
MYS (microyield strength) = 3.0 KSI
ν (Poisson's ratio) = 0.024
α (thermal expansion coefficient) = 6.3×10^{-6}/°F, @300°K(80.6°F)
= 5.4×10^{-6}/°F, @ 250°K(-9.4°F)
= 3.9×10^{-6}/°F, @ 200°K(-99.4°F)

3.5 Mechanical Alignment - During the mission, the optical centerline of the instrument telescope must remain within 0.02 milliradians of cone half-angle from its original pre-launch position. This requirement imposes the following three constraints. First, the design and selection of material for the tube must include consideration of achieving a microyield strength (as defined in Paragraph 3.4) above the stress levels expected during launch; second, the composite fibers must be oriented symmetrically to avoid any thermally-induced rotation or twisting of the tube; and

* Microyield Strength is defined as the stess required to produce a permanent strain of .1 microinch/inch (or 10^{-6} strain) under short-duration loading.

finally the long term creep characteristics due to thermal stresses in the tube material must prevent any significant angular tilt of the instrument during the four year mission period.

3.6 Instrument Mass Properties - TI's structural analysis of the support tube is based upon the following instrument mass properties (at its mass center) cantilevered on the tube (reference TI 877100):

Total Instrument Mass:		17.6 lbm
Mass Moments of Inertia:	$I_{xx_{cm}}$	= 600 lbm in^2
	$I_{yy_{cm}}$	= 420 lbm in^2
	$I_{xx_{cm}}$	= 600 lbm in^2
Products of Inertia:	$P_{xy_{cm}}$	= -72 lbm in^2
	$P_{xz_{cm}}$	= -30 lbm in^2
	$P_{yz_{cm}}$	= 60 lbm in^2

3.7 Launch Environment - TI's structural design of the instrument and support tube is currently governed by the test levels of sinusoidal and random vibration as specified at the spacecraft platform mounting plate.

3.7.1 Sinusoidal Vibration

Frequency (Hz)	Acceleration Level
5 to 23	1.02 cm (0.4 in) D.A.
23 to 100	8.0 Grms (11.3 g peak)
100 to 2000	4.5 Grms (6.36 g peak)

(Sweep rate is 2 octaves/minute, up and down, in any direction.)

3.7.2 Random Vibration - See Figure I for levels assigned to "other assemblies". The instrument will be capable of 3 minutes of random vibration exposure in each of three axes.

3.8 Space Environment -

3.8.1 Vacuum - During the four year exposure to deep space vacuum, the instrument support tube must not outgas compounds which would cause contamination of optical surfaces or degradation of its intrinsic mechanical properties.

Wherever possible, materials used shall be selected from those having established records of acceptable performance in a space environment.

3.8.2 Electron Radiation - The instrument support tube must survive the following levels of electron particle radiation without degradation of its mechanical properties:

3×10^8 e/cm^2/sec	(Flux)
1×10^{13} e/cm^2	2 MeV equivalent (Fluence)

3.8.3 Proton Radiation - The instrument support tube must survive the following levels of proton particle radiation without degradation of its mechanical properties:

2×10^8 p/cm^2/sec	(Flux)
7×10^{12} p/cm^2	20 MeV equivalent (Fluence)

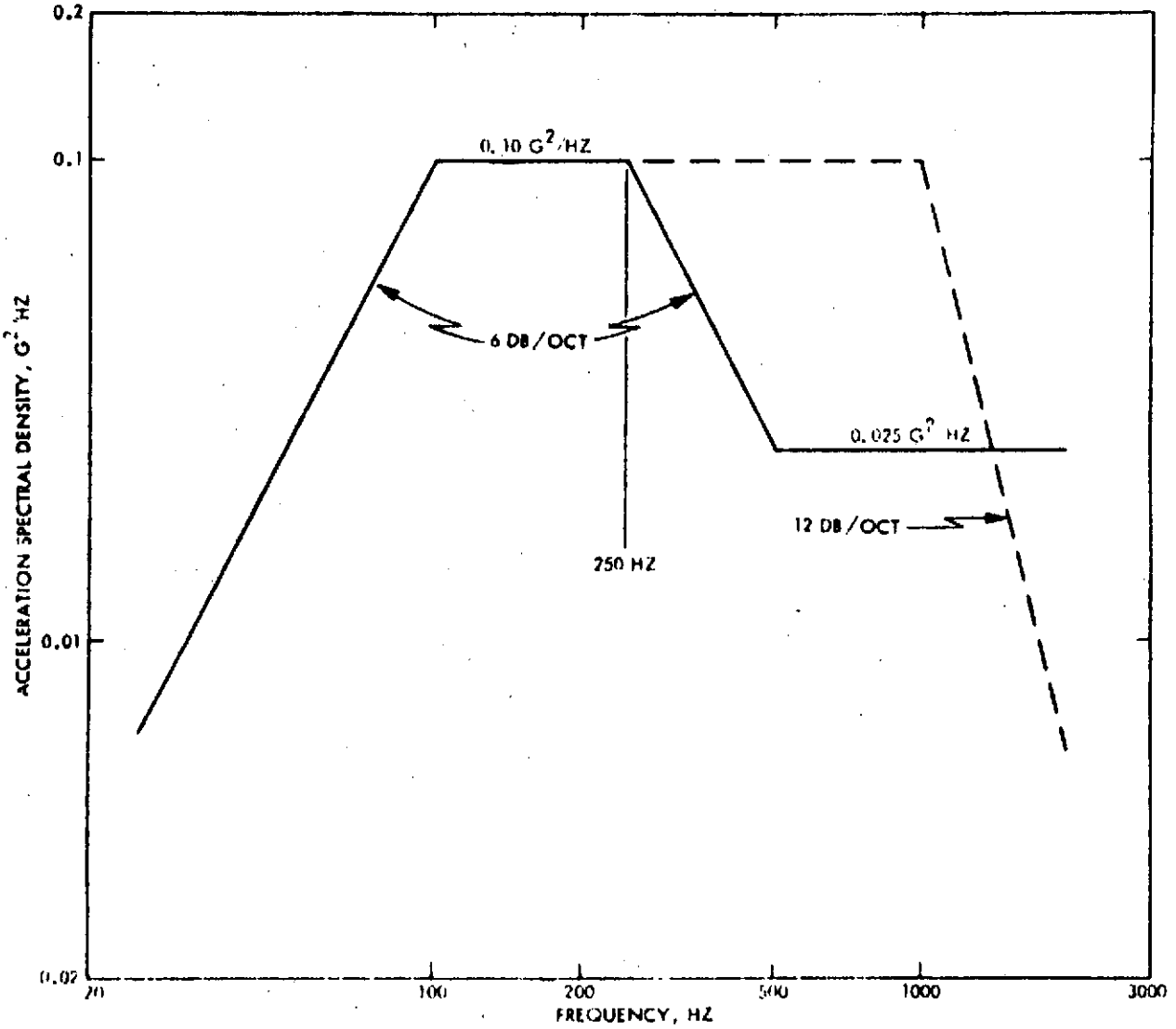

——— BUS AND PROPULSION MODULE ASSEMBLIES AND SYSTEM (OVERALL 8.3 G_{RMS}).

– – – OTHER ASSEMBLIES (OVERALL 11.1 G_{RMS}).

ROLLOFF IS 24 DB/OCT OR GREATER ABOVE 2000 HZ AND BELOW 25 HZ.

STANDARD ACCELERATION DUE TO GRAVITY – 980.665 CM/S^2.

Figure 1. Random Vibration Spectra

4. PERFORMANCE REQUIREMENTS

The following orthotropic material properties are the basic "variables" in the design of the support tube. The values indicated are current nominal design numbers (at room temperature) which satisfy the general structural, thermal, and optical goals of the IRIS instrument.

4.1 Structural Parameters

(ℓ = longitudinal; c = circumferential)

Tensile Elastic Modulus	$E_\ell = 5 \times 10^6$ psi
	$E_c = 3 \times 10^6$ psi
Shear Modulus	$G_{\ell c} = 3 \times 10^6$ psi
Poisson's Ratio	ν_ℓ = TBD
	ν_c = TBD
Microyield Strength[1]	MYS_ℓ = 30 KSI
	MYS_c = 30 KSI
Macroyield Strength[2]	σ_{y_ℓ} = TBD
	σ_{y_c} = TBD
Ultimate Tensile Strength	σ_{ult_ℓ} = TBD
	σ_{ult_c} = TBD
Thermal Expansion Coefficient	α_ℓ = TBD
	α_c = TBD
Critical Damping Ratio (Tube assembly)	$C/C_{cr} = 0.025$

1 Stress corresponding to 10^{-6} strain

2 Stress corresponding to 2×10^{-3} strain.

4.2 Thermal Parameter

Longitudinal Thermal Conductivity (goal) k_ℓ = 0.4 Btu ft/ft^2 hr°F

4.3 Electrical Parameter

Longitudinal Electrical Conductivity* γ_ℓ = TBD

(*isolation is desired)

5. MATERIAL SAMPLES TESTING

Upon approval by TI to conduct the testing of material samples, the vendor shall fabricate test specimens and proceed according to the following tentative test schedule:

Step 1. - The vendor shall measure the following mechanical properties on radiated and non-radiated samples at room temperature (75 ± 10°F). Sufficient samples shall be tested to show repeatability of each property measurement:

a. E_ℓ, E_c, G_{ℓ_c}, ν_ℓ or E_ℓ, E_c, ν_ℓ, ν_c

b. α_ℓ, α_c

c. MYS_ℓ, MYS_c

d. σ_{y_ℓ}, σ_{y_c}, σ_{ult_ℓ}, σ_{ult_c}

e. k_ℓ

f. γ_ℓ

Step 2. - The same as Step 1, except properties to be measured at 250 ± 10° Kelvin.

Step 3. - The same as Step 1, except properties to be measured at 200 ± 10° Kelvin.

Step 4. - The same as Step 1, except properties to be measured at 150 ± 10 Kelvin.

Step 5. - The same as Step 1, except properties to be measured at 100 ± 10 Kelvin.

6. QUALITY ASSURANCE PROVISIONS

6.1 Data Certification - All data and/or materials produced and delivered on this contract shall be processed under the cognizance of the vendor's quality assurance organization. The quality assurance organization will assure that data and/or material fulfills the contract requirements. Accuracy and completeness of requirements will be attested to by quality assurance personnel.

6.2 Equipment Calibration - All measurement standards and equipment used to accumulate data for this contract shall be calibrated and traceable to standards maintained by the National Bureau of Standards. The vendor shall establish calibration intervals consistent with use, accuracy, type of standard or equipment, required precision, and other conditions adversely affecting the measurement process. The vendor shall maintain individual records of measurement standards and equipment.

APPENDIX B

MJS '77 IRIS

DYNAMIC RADIATION TESTS WITH Co^{60}

AT NASA/GSFC

7/22/74-7/31/74

SUMMARY OF TEST RESULTS -- All dynamic radiation tests were run in air using a 12-14 kilocurie Co^{60} spatially extended source. Radiation received directly from the source was probably pure gamma rays since the covering of the Co^{60} blocks beta particles. Approximately 50% of the gamma rays had an energy of 1.17 Mev and approximately 50% had a 1.33 Mev energy. All test results presented below are accompanied by a statement of the noise or signal background against which the radiation effects were measured. This is important to an analysis of the results since radiation effects at a significantly lower level than the background may have been masked. The background levels that were encountered can be generally ascribed to air currents around windowless detectors, inherent thermal and shot noise in detectors and load resistors, hum from power lines at 60 Hz, thermal differentials in the area viewed by a chopped IR detector, and imperfect radiation shielding of radiation sensitive detectors used in radiation tests on optics.

Pyroelectric Detector/Preamp (windowless)

-- Barnes Engineering 2mm x 2mm L-400 with FET

A slight increase in noise was observed at 11.6 Roentgens/min at both 10 and 100 Hz against a background of ≈ 1$\mu V/Hz^{1/2}$. At 132 Roentgens/min the noise increased to ≈ 2$\mu V/Hz^{1/2}$ with a background less than 0.5 $\mu V/Hz^{1/2}$ at 1, 10, and 100 Hz. With a similar background at 650 Roentgens/min, the noise measured was 5 $\mu V/Hz^{1/2}$ at 1 Hz, 6 $\mu V/Hz^{1/2}$ at 10 Hz, and 8 $\mu V/Hz^{1/2}$ at 100 Hz.

With a plastic cap over the detector the radiation effect at 650 Roentgens/min was the same as without the cap but the background level was only 0.1 $\mu V/Hz^{1/2}$.

Thermopile Detector (windowless)

-- Reeder $(3/4\ mm)^2$ or $(1mm)^2$, 15-20Ω

No significant increase in noise was observed at 11.6, 132, or 650 Roentgens/min with a background of $0.6nV/Hz^{1/2}$ at 10 and 100 Hz and $\approx 1.8nV/Hz^{1/2}$ at 1 Hz.

Thermopile Detector

-- Sensors C1 1mm dia., 2kΩ

No significant increase in noise was observed at 630 Roentgens/min with a background of 6-7 $nV/Hz^{1/2}$ at 1, 10, and 100 Hz.

Silicon Detector (loaded by 1MΩ)

-- Electro-Nuclear Labs PVS-020

Against a background of 0.12 $\mu V/Hz^{1/2}$ at 10 Hz and 0.11 $\mu V/Hz^{1/2}$ at 100 Hz and $\leq 5\mu V_{DC}$, 105 Roentgens/min increased the noise to 10 $\mu V/Hz^{1/2}$ and the DC level to 12mV. A radiation level of 640 Roentgen/min increased the DC level to $\geq$95mV.

Silicon Detector (loaded by 1MΩ)

-- Spectronics SD5422

Against a background of 0.10-0.15$\mu V/Hz^{1/2}$ at 10 and 100 Hz and $\approx 20\mu V_{DC}$, 180 Roentgens/min increased the noise to $6\mu V/Hz^{1/2}$ and the DC level to 7.2 mV. A radiation level of 635 Roentgen/min increased the noise to $15\mu V/Hz^{1/2}$ and the DC level to 33mV.

CsI Beamsplitter

Using some lead shielding of the PVS-020 silicon detector and with a background of $1.4\mu V/Hz^{1/2}$ at 10 and 100 Hz and $0.6\text{-}0.8mV_{DC}$ the following observations were made with the beamsplitter normal to the detector axis and 8 1/2" distant with the coated surface away from the detector:

At 530 Roentgens/min,

with 5852Å filter -- $1.5\mu V/Hz^{1/2}$, $0.7mV_{DC}$

without filter -- $1.7\mu V/Hz^{1/2}$, $1.87mV_{DC}$

(The apparent small increase in noise is within the typical errors for these narrow band noise measurements.)

Using some lead shielding of the Reeder thermopile detector and with a background of $0.6\ nV/Hz^{1/2}$ at 10 and 100 Hz and $\approx 1.8\ nV/Hz^{1/2}$ at 1 Hz, no increase in noise was observed at 480 Roentgens/min. The beamsplitter was normal to the detector axis and 7 1/4" distant with the coated surface toward the detector. The beamsplitter could be seen glowing in the dark room during this test.

No change in signal level was observed at 490 Roentgen/min against a background signal of $40nV_{RMS}$ when the detectors view of the beamsplitter was chopped at ≈32Hz. The detector-beamsplitter distance was 6 1/2" for this test.

The pyroelectric detector was also used with some shieldings to look at the beamsplitter under radiation. The beamsplitter was at 45° to the detector and ≈7" from it. At 480 Roentgens/min, there appeared to be no increase in noise from the background of $0.6\mu V/Hz^{1/2}$ at 1, 10 and 100 Hz. With the detector's view of the beamsplitter chopped at 32Hz, no increase in signal was observed against a background

of 0.22mV$_{RMS}$ at the chopping frequency. The above results were obtained both with the coated side of the beamsplitter towards and away from the detector. The field of view of the detector was moderately restricted to reduce the background during these tests.

High Purity CsI and KBr beamsplitter

A high purity CsI sample and a KBr beamsplitter were radiated along with the CsI beamsplitter at roughly 490 Roentgens/min. The high purity CsI could be seen glowing in the dark room but it appeared dimmer than the CsI beamsplitter and the light seemed to be shifted towards blue from the beamsplitter output. The KBr material was not observed to glow.

Relative Glow of CsI Samples

The relative glow of the CsI beamsplitter and high purity CsI sample were measured using a SD5422 silicon detector that was moderately shielded from radiation. The detector's mechanically chopped view of the specimen was apertured to a 0.84" diameter at the specimen. The beamsplitter specimen was ≈0.33" thick, the high purity sample was ≈ 0.51" thick. Tests were made at 400 Roentgens/min with the specimen normal to the detector axis and 5 7/8" away. Background at the chopping frequency was 1.5μV$_{RMS}$.

The signal from the beamsplitter was 110μV$_{RMS}$ at the chopping frequency (≈ 32Hz.) With the high purity sample, the signal was 60μV$_{RMS}$.

Light Emitting Diode

-- Texas Instruments SL1466

No significant changes in LED characteristics were observed in a 345 Roentgens/min environment. Parameters measured with and without radiation included the LED voltage (1.2V@35mA) and the output of a radiation shielded SD5422 silicon detector (65mVp-p) with the LED electrically chopped at 100 Hz.

Neon Bulb

--General Electric K3A

No significant change in noise was measured at the output of a shielded SD5422 silicon detector viewing the neon bulb at 390 Roentgens/min against a background of $1\mu V/Hz^{1/2}$ at 10 and 100 Hz regardless whether the bulb was on or off. The sensitivity of the detector for this test was such that electrical chopping of the neon source produced ≈7mVp-p at the detector. The ON condition of the source corresponded to a 26 mV_{DC} output of the detector against a source-OFF detector output of 0.25mV_{DC}.

The voltage across the source was ≈77V@1.76mA. Both the above characteristics applied with and without radiation. The firing voltage of the source, however, dropped roughly 3V from 113V during radiation.

Zener Diode

-- 1N829A

No increase in noise was observed at 640 Roentgens/min against a no radiation level of $60nV/Hz^{1/2}$ at 1, 10, and 100 Hz. The zener was driven with 7.5mA through a 1KΩ metal film resistor for these tests. The measured zener voltage of 6.28V was not affected by radiation.

APPENDIX C

MJS'77 IRIS
DYNAMIC RADIATION TESTS WITH Sr^{90}/Y^{90}
AT NASA/GSFC

8/8/74 - 8/14/74

THE Sr^{90}/Y^{90} SOURCE

The dynamic radiation tests were run using a Tracerlab RA-2 medical applicator (serial number 1067). According to information on the applicator storage box, the source was "Isotope SR90-112" and was "110 mc roentgen equivalent - betas per second "as of 11/2/65 .

The files on the source are now at International Chemical and Nuclear in California. Hal Carter of ICN was contacted on 8/16/74 and he described the source as follows:

> The source was originally 110 millicuries of Sr^{90} and 110 millicuries of Y^{90}. The source pellet is a disk approximately 5 mm in diameter by 1 1/2 mm thick. Going from the source to the end of the applicator is first 2 mil stainless steel followed by a 3-5 mil air gap and then 1 mil stainless steel at the end of the applicator.

Kirk King of NASA/GSFC Health Physics said computer projections were that the source was 80.7 millicuries Sr^{90} and 80.7 millicuries Y^{90} as of 30 June 1974.

CALCULATED RADIATION LEVELS

Disintegration of Sr^{90} releases a spectrum of beta particles with a maximum energy of 0.54 Mev. Disintegration of Y^{90} releases a spectrum of beta particles with a maximum energy of 2.27 Mev. Ocasionally a 1.75 Mev gamma ray is also released.

The unimpeded flux levels that are presented in the summary that follows are calculated values and are not based on measurements. The method of flux level calculation is shown below.

D = Disintegration Rate = 0.16 curie x 3.7×10^{10} $curie^{-1} sec^{-1}$
$= 5.9 \times 10^{9}$ sec^{-1}

F = Flux = $\frac{D}{4 \pi r^2}$, where r is the distance from the source (in cm)

In these calculations, both the small spatial extension of the source and curvature of the calculated area ($4 \pi r^2$) have been ignored. Also, the presence of secondary electrons and x-rays has been disregarded. Due to safety considerations, distances noted below are visual estimates.

The spectrums of beta particles from Sr^{90} and Y^{90} are shown in Figure C-1. Since a substantial portion of the beta particles have been very low energies, many will be stopped either in the stainless steel in the applicator or in the glass or metal housing the silicon chip. Thus, the actual flux level at the chip is significanlly below the unimpeded flux level.

SUMMARY OF TEST RESULTS

Silicon Detector (loaded by 1 MΩ)

Spectronics SD5422

With no radiation:

Output = +8 μV_{DC} (probably from preamp)

0.11 $\mu V/Hz^{1/2}$ at 10 and 100 Hz

With source/detector separation of 3.75 inches plus 0.18 inch to silicon chip, approximately 4.7×10^6e cm^{-2} sec^{-1}:

Output = +45 μV_{DC}

0.5 $\mu V/Hz^{1/2}$ at 10 and 100 Hz

With source/detector separation of ≈ 1/8 inch plus 0.18 inch to silicon chip, on the order of 8×10^8e cm^{-2} sec^{-1}:

Output = +8.9 mV_{DC}

8 $\mu V/Hz$ at 10 and 100 Hz

With source/detector separation of ≈ 0 inch plus 0.18 inch to silicon chip, on the order of 2×10^9e cm^{-2} sec^{-1}:

Output = +13 mV_{DC}

9 $\mu V/Hz^{1/2}$ at 10 and 100 Hz

Switching Diode (loaded by 1 MΩ)

1N914

With no radiation:

Output = -31 μV_{DC} (probably from preamp)

(V_{anode}) 0.11 $\mu V/Hz^{1/2}$ at 10 and 100 Hz

With source/diode separation of ≈ 1/16 inch plus 0.04 inch to silicon chip, on the order of 6×10^9e cm^{-2} sec^{-1}:

Output = -63 μV_{DC}

0.16 $\mu V/Hz^{1/2}$ at 10 and 100 Hz

JFET Transistor

2N5196

Test Circuit No. 1 - Gate 1 connected to ground, Source 1 connected through 10KΩ, 1% metal film resistor to ground,

Drain 1 connected through 84.5KΩ, 1% metal film resistor to +23 1/2V.

Both with no radiation and with source/transistor separation of ≈ 1/10 inch plus 0.1 inch to silicon chip, on the order of 2×10^9e cm^{-2} sec^{-1}:

$V_D = 11.1\ V_{DC}$

$V_S = 1.49\ V_{DC}$

Both with no radiation and with source/transistor separation of ≈ 1/16 inch plus 0.1 inch to silicon chip, on the order of 3×10^9e cm^{-2} sec^{-1}:

$V_D = 0.5\ \mu V/Hz^{1/2}$ at 10 Hz

Test Circuit No. 2 - same as Test circuit No. 1 except gate 1 connected to ground through $10^8\ \Omega$.

With no radiation:

$I_G = 7\ pA$ (measured both by $V_G/10^8$ and by transimpedance picoampmeter.)

With source/transistor separation of ≈ 1/16 inch plus 0.1 inch to silicon chip, on the order of 3×10^9e cm^{-2} sec^{-1}:

$I_G = 390\ pA$

Test Circuit No. 3 - same as Test circuit No. 2 except Drain 1 connected to +23 1/2V through 10KΩ, 5% carbon resistor.

With no radiation:

$I_G = 13\ pA$

$V_D = 1.1\ \mu V/Hz^{1/2}$ at 1, 10, and 100 Hz

With source/transistor separation of $\approx$ 1/16 inch plus 0.1 inch to silicon chip, on the order of 3×10^{9}e cm^{-2} sec^{-1}:

I_G = 390 pA

V_D = 70 $\mu V/Hz^{1/2}$ at 1 and 100 Hz

Note - There may have been some difference in the radiation levels between the I_G and V_D tests.

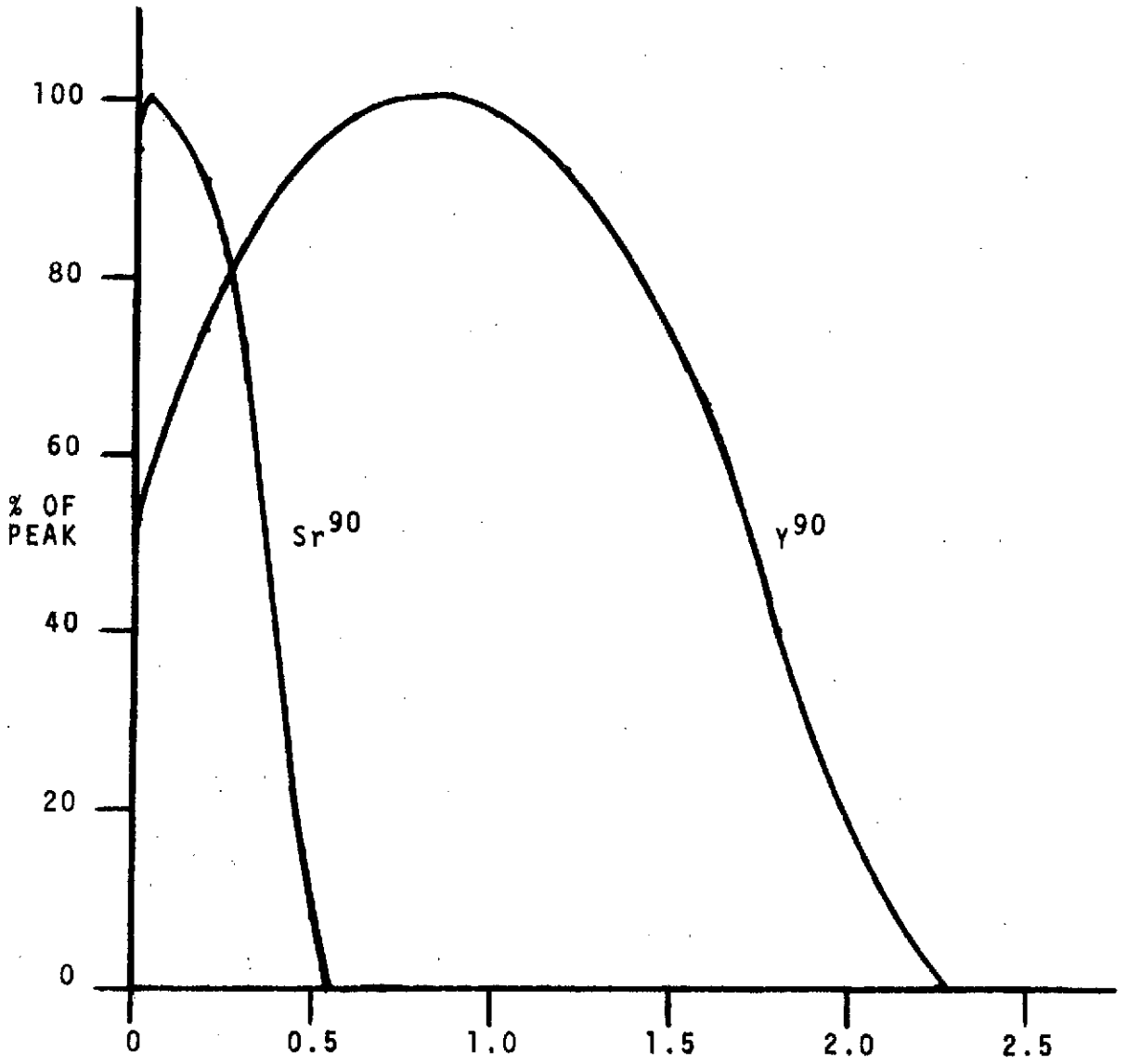

BETA PARTICLE SPECTRUMS OF Sr^{90} AND Y^{90}

FIGURE C-1

REFERENCE

Figure C-1 was derived from data presented in the following article:

Mantel, J., "Beta Ray Spectrum and the Average Beta Energy of Several Isotopes of Interest in Medicine and Biology," International Journal of Applied Radiation and Isotopes, p. 410, Vol 23, 1972.